Electrospray Ion Beam Deposition of Complex Non-Volatile Molecules

Thèse n. 5892 (2013)
présenté le 24 Juillet 2013
à la Faculté des Sciences de Base
Laboratoire de science à l'échelle nanométrique
Programme doctoral en science et génie des matériaux

École Polytechnique Fédérale de Lausanne
pour l'obtention du grade de Docteur ès Sciences par

Gordon Rinke

acceptée sur proposition du jury:

Prof. Andreas Mortensen, président du jury
Prof. Klaus Kern, directeur de thèse
Prof. Francesco Stellacci, rapporteur
Prof. Ernst Meyer, rapporteur
Dr. Leonard Grill, rapporteur

Lausanne, EPFL, 2013

Abstract

The rational synthesis of novel materials requires the control over the arrangement of matter in order to meet the desired properties for applications and devices. Ultimately, control means to define the place of each atom and determine its chemical state, as well as being able to confirm the result in a measurement. Control at the atomic level can be achieved with scanning tunneling microscopy (STM), both in imaging and atomic manipulation. The latter, however, can never be used in meso- or even macroscopic material synthesis. Self-ordering phenomena determines atomic control in material synthesis as well, observed for instance in protein folding or in molecular beam epitaxy (MBE) technology. In both cases the atomically determined arrangement of the atoms in the structure is controlled only by environmental parameters that steer the self-ordering phenomena.

In this thesis I show that electrospray ion beam deposition (ES-IBD) or ion soft-landing is a material processing technique, which combines and even extends the level of control offered by MBE. It is demonstrated that a vast range of complex organic materials including peptides and proteins is now available to ultrapure vacuum processing and moreover completely novel schemes of controlling self-ordering processes are provided.

In-situ STM is applied to investigate the structure formation of complex molecules deposited by ES-IBD on well-defined, clean, and atomically flat surfaces in ultrahigh vacuum at the greatest detail. This allows us to explore the novel control features that are intrinsic to the ES-IBD deposition process like online coverage monitoring, deposition energy control, and mass-selection to select charge states or reactive species.

The molecules studied here include organic molecular salts, dye molecules, reactive polymer building blocks, and finally peptides and proteins. Crystalline layer-by-layer as well as island growth was observed and revealed the equivalence to conventional MBE growth. On the basis of these deposition experiments the crucial influence of clusters in the ion beam for high material flux was discovered. Furthermore, it was found that the chemical state of the molecule is a key factor for the deposition result as chemical reactions can be induced or the self-assembly

behavior can be altered. Alongside the capability to handle also extremely reactive molecules, the feasibility to control chemical reactions occurring as a result of an external stimulus to a specifically selected reactive species is demonstrated.

Employing the control parameters that are specific to ES-IBD like charge state selection and deposition energy to complex biomolecules opens up new perspectives for vacuum deposition. In addition to the self-assembly governed by the molecule-substrate and molecule-molecule interaction, it was possible to actively steer the structure formation of proteins by influencing their stiffness and their reactivity through their charge state as well as by the deposition energy, parameters intrinsic to the ES-IBD method.

Hence, electrospray ion beam deposition is indeed a tool to prepare well defined surface coatings at highest level of control and complexity. To be relevant for industrial applications, the performance of the system has to be further improved, most importantly in terms of deposition rate. In general, ES-IBD enables new approaches for the growth of functional coatings but also serving as perfect sample preparation tool for the characterization of complex molecules on the atomic scale by scanning probe or more general surface science methods.

Keywords: *Electrospray, Ion Beam, Deposition, Scanning Tunneling Microscopy, Ultra-high Vacuum, Complex Non-volatile, Organic Molecules, Nanostructures, Cytochrome C, Bradykinin, Clusters, Self-assembly.*

Kurzfassung

Die wohldefinierte Anordnung von Materie ist die Voraussetzung fuer die Synthese neuartiger Materialien. Nur so erreicht man die gewünschten Eigenschaften die neue Anwendungen und neue Bauelemente ermöglichen. Ein hohes Mass an Kontrolle bedeutet im besten Fall die Möglichkeit die Position jedes Atoms genau festzulegen, dessen chemischen Zustand zu bestimmen, sowie diese Informationen mit einer Messung zu bestätigen. Diese Anforderung erfüllt die Rastertunnelmikroskopie (RTM). Sie ermöglicht dabei sowohl die Bildgebung auf atomarer Ebene als auch atomare Manipulation. Eine makroskopische Materialsynthese wird jedoch mit RTM nie moeglich sein. Um atomare Kontrolle auch bei der Materialsynthese zu erreichen werden Selbst-Organisationsprozesse ausgenutzt, wie sie zum Beispiel bei der Proteinfaltung beobachtet werden koennen oder in der Molekularstrahlepitaxie (MBE) verwendet werden. In beiden Fällen wird eine definierte Anordnung der Atome in der Struktur durch Selbstorganisationphänomene erreicht, die aber nur durch die Umgebungsbedingungen gesteuert werden.

In dieser Arbeit wird gezeigt, dass Elektrospray Ionenstrahlabscheidung (ES-IBD) oder „Soft Landing“ eine Materialsynthese-Technik ist, die nicht nur das gleiche Niveau an Kontrolle bietet wie MBE, sondern deren Möglichkeiten durch weitere Parameter deutlich erweitert. Durch die gezielte Deposition einer breiten Palette von komplexen organischen Molekülen, unter anderem Proteinen und Peptiden, wird dargelegt, dass sich diese Technik für die Vakuumprozessierung von komplexen Systemen eignet und darüber hinaus völlig neuartige Möglichkeiten zur Steuerung des Selbstorganisationsprozesses bietet.

Zur Untersuchung der Struktur von abgeschiedenen Molekülen mittels ES-IBD auf wohldefinierten, atomar sauberen Oberflächen im Ultrahochvakuum, wird in-situ RTM angewendet. Diese Technik ermöglicht die Beurteilung des Depositionsergebnisses in Abhängigkeit von den eingestellten Kontrollparametern wie Bedeckung, Depositionsenergie und Massenselektion, mit deren Hilfe bestimmte Ladungszustände oder reaktive Spezies ausgewählt werden können.

Die hier untersuchten Moleküle reichen dabei von molekularen organischen Salzen bis hin zu Farbstoffmolekülen, reaktiven Polymer-Bausteinen und schließlich

zu Peptiden und Proteinen. Kristallines Schicht- sowie Inselwachstum beweist die Äquivalenz zu herkömmlichem MBE Wachstum. Auf der Grundlage dieser Abscheidungsexperimente wurde der entscheidende Einfluss von Clustern im Ionenstrahl entdeckt, der einen hohen Materialfluss zur Folge hat. Darüber hinaus wurde festgestellt, dass der chemische Zustand des Moleküls ein wichtiger Faktor für das Abscheidungsergebnis ist, da chemische Reaktionen induziert oder das Selbstorganisationsverhalten verändert werden kann. Des Weiteren wurde nachgewiesen, dass auch extrem reaktive Moleküle mit ES-IBD deponiert werden können und deren thermische Anregung auf der Oberfläche zur chemischen Reaktionen führt.

Der Einsatz der Kontrollparameter, die spezifisch sind für ES-IBD, wie die Auswahl des Ladungszustandes und der Depositionsenergie, auf komplexe Biomoleküle eröffnet neue Perspektiven für die Vakuum-Abscheidung. Neben der Selbstorganisation, beeinflusst von Molekül-Substrat und Molekül-Molekül-Wechselwirkung, ist es möglich die Strukturbildung von Proteinen durch Beeinflussung ihrer Steifigkeit und Reaktivität über ihren Ladungszustand sowie der Depositionsenergie aktiv zu steuern.

Elektrospray Ionenstrahlabscheidung ist somit ein gut geeignetes Werkzeug, um wohldefinierte Oberflächenbeschichtungen mit höchster Kontrolle und Komplexität durchzuführen. Damit das Verfahren für industrielle Anwendungen relevant wird, muss die Effizienz des Systems weiter verbessert werden, vor allem in Bezug auf die Abscheiderate. Abgesehen davon ermöglicht ES-IBD neue Ansätze für das Wachstum funktioneller Beschichtungen, aber auch die Herstellung von perfekten Probenoberflächen mit komplexen Molekülen zur Charakterisierung auf atomarer Skala mit Hilfe von Rastersondenmikroskopie oder anderen oberflächensensitiven Methoden.

Stichwörter: *Electrospray, Ionenstrahl Deposition, Rastersondenmikroskopie, Ultrahoch Vakuum, komplexe nicht-verdampfbare, organische Moleküle, Nanostrukturen, Cytochrome C, Bradykinin, Cluster, Selbstorganisation.*

Riassunto

La sintesi mirata di nuovi materiali richiede il controllo sull´aggregazione della materia fino ad ottenere le proprietà desiderate per la realizzazione di dispositivi ed altre applicazioni. In definitiva, avere il controllo sulla deposizione significa poter determinare la posizione di ogni atomo e il suo stato chimico, oltre che essere in grado di confermare il risultato con una misura sperimentale. Il controllo a livello atomico può essere raggiunto tramite il microscopio a scansione tunnel (STM), sia per quanto riguarda la visualizzazione della superficie sia il posizionamento degli atomi. La capacità di posizionare I singoli atomi non può tuttavia essere utilizzata nella sintesi macroscopica di materiali. Fenomeni di auto-ordinamento (self-ordering) si verificano spesso, é il caso per esempio della crescita per epitassia a fascio molecolare (MBE) e del ripiegamento delle proteine. In entrambi i casi, sono i parametri ambientali a controllare i fenomeni di auto-ordinamento che determinano lo specifico arrangiamento degli atomi.

In questa tesi, mostriamo come il metodo di deposizione elettrospray a fascio ionico o ionizzazione morbida, abbreviato ES-IBD: dall´inglese electrospray ion beam deposition, é una tecnica di sintesi dei materiali che raggiunge e perfino migliora il livello di controllo offerto dalla tecnica MBE. Oltre a dimostrare che é possibile processare nell´ambiente ultra-puro del vuoto una vasta gamma di materiali organici complessi, inclusi peptidi e proteine, sono stati introdotti schemi completamente innovativi per controllare i processi di auto-ordinamento.

Tramite microscopia STM abbiamo analizzato in-situ, con massima risoluzione, la struttura di molecole complesse depositate via ES-IBD su superfici ben definite, pulite e caratterizzate a livello atomico in ultra-alto vuoto. In questo modo é stato possibile uno studio sistematico e una profonda comprensione delle funzioni di controllo caratteristiche del processo di deposizione ES-IBD quali: selezione della massa per selezionare lo stato di carica delle specie reattive, il controllo dell´energia di deposizione, e il monitoraggio in tempo reale della densità di molecole sulla superficie (coverage).

E´stata studiata una vasta gamma di molecole tra cui sali molecolari organici, molecole coloranti, unità polimeriche reattive ed infine peptidi e proteine. La

crescita cristallina riportata é sia di tipo strato per strato che crescita ad isola, dimostrando così che il metodo di deposizione é equivalente alla crescita convenzionale per MBE. Sulla base degli esperimenti di deposizione, é stato scoperto il ruolo cruciale degli aggregati (clusters) nel fascio ionico per valori alti del flusso di materiale. E´stato dimostrato inoltre come lo stato chimico delle molecole sia un fattore chiave nel determinare il risultato della deposizione poiché può indurre reazioni chimiche o alterare il meccanismo dell'auto-ordinamento. Inoltre, é stata dimostrata l´abilità di processare con questa tecnica molecole estremamente reattive e controllare le reazioni chimiche che avvengono a seguito della collisione tra ioni e molecole.

Il controllo sui parametri specifici del metodo ES-IBD come selezione dello stato di carica ed energia di deposizione di complesse molecole biologiche apre nuove prospettive per le tecniche di deposizione in vuoto. La formazione delle strutture molecolari in superficie non viene determinate solo dall´auto-ordinamento delle specie molecolari in questione ma anche attivamente modificando la rigidità e lo stato di carica delle molecole tramite il loro stato di carica e l´energia di deposizione. La deposizione per elettrospray di fascio ionico, dunque si rivela essere uno strumento per preparare deposizioni specifiche su diverse superfici con il più alto livello di controllo e complessità. Per diventare rilevante per applicazioni a livello industriale le prestazioni del sistema devono essere migliorate soprattutto per quanto riguarda la velocità di deposizione. In termini generici, ES-IBD rende possibile un approccio innovativo della crescita di strati funzionali e allo stesso tempo si dimostra uno strumento perfetto per la caratterizzazione di molecole complesse su scala atomica tramite microscopia o altri metodi di caratterizzazione delle superfici.

Parola chiave: *Elettrospray, Fascio ionico, Deposizione, Microscopio a scansione tunnell, Ultra alto vuoto, Complessi non volatili, molecole organiche, Strutture nanometriche, Citocromo C, Bradichinina, Aggregato, Auto-asemblaggio.*

Contents

Abstract (English/Deutsch/Italiano) i

Introduction 1

1 Electrospray Ion Beam Deposition - Full Control 9
- 1.1 Electrospray Ionization . . . 10
- 1.2 Components of the System . . . 12
  - 1.2.1 Electrospray Interface and Sources . . . 14
  - 1.2.2 Ion Optics . . . 16
  - 1.2.3 Beam Characterization . . . 18
  - 1.2.4 Deposition Targets . . . 20
  - 1.2.5 Software and Data Acquisition . . . 21
- 1.3 The Ion Beam Deposition Procedure . . . 22
- 1.4 Summary and Conclusion . . . 30

2 Cluster of Non-Volatile Molecules in Electrospray Ion Beams 31
- 2.1 Organic Salt Cluster Formation . . . 33
- 2.2 Declustering of Organic Salt Cluster . . . 36
- 2.3 Material and Charge Distribution in the Mass Spectrum . . . 38
- 2.4 Statistical Analysis of the Deposited Material Amount . . . 44
- 2.5 Summary & Conclusions . . . 48

3 Self-Assembly in 2D from Molecules Deposited by ES-IBD 51
- 3.1 Reichardt Dye: A Molecular Dipole . . . 53
  - 3.1.1 ESI Mass Spectrometry . . . 55
  - 3.1.2 Deposition from an Ion Beam Including Clusters . . . 59
  - 3.1.3 Deposition from a Cluster Free Ion Beam . . . 66
  - 3.1.4 Summary & Conclusion . . . 69
- 3.2 Hexayne: A Highly Reactive Molecule . . . 71
  - 3.2.1 Asymmetrical Hexayne Termination . . . 73
  - 3.2.2 Symmetrical Hexayne Termination . . . 76
  - 3.2.3 Summary & Conclusion . . . 83

4 Conformation Control of Unfolded Cytochrome C Proteins 85
4.1 Mass Spectrometry and Charge State Selection 88
4.2 The Deposition of Charge State Selected Proteins 90
4.3 Statistical Analysis of the 2D Protein Conformation 92
4.4 Landing Process of Differently Charged Proteins 96
4.5 Summary & Conclusion 102

5 The Folding of a Nine-Amino Acid Peptide on Different Surfaces 103
5.1 Experimental Procedure and Mass Spectrometry 105
5.2 The Structure of the Bradykinin on Different Surfaces 107
5.3 Sequence – Structure Correlation 110
5.4 Chemical Reactivity of the Peptide 118
5.5 Summary & Conclusion 123

Summary & Perspectives 125

Appendix A - Cluster Ion Beam 131

Appendix B - Electronic Structure of Bradykinin 139

Bibliography 141

Acknowledgment 157

Curriculum Vitae 159

Introduction

The rational synthesis of novel materials requires the control over the arrangement of matter in order to meet the desired properties for applications and devices. The properties of a macroscopic piece of material are defined by the arrangement of atoms into nano- and mesostructures as well as their mutual interactions. The atomic level manipulation and characterization of matter at dimensions below 100 nm is therefore a key requirement for improved functionalities and novel properties. These abilities are collected under the terms nanotechnology and nanoscience, which include methods and concepts for the control of matter on the nanoscale, ranging from material synthesis to characterization.

Thin film preparation methods like chemical vapor deposition (CVD) and physical vapor deposition (PVD) facilitate the growth of materials with precise control over stoichiometry and film thicknesses to the level of a single atomic layer, as it is achieved in molecular beam epitaxy (MBE).[1–3] The high level of control on the nanoscale and atomic level is accomplished by precisely controlling the parameters defining the boundaries for molecular transport, interaction and agglomeration at the surface: material flux, pressure, atmosphere, and temperature of the sample. In such an environment, self-organized growth and self-assembly of the molecular or atomic building blocks also allows for well-defined nanostructure formation.[4,5] Which of the above mentioned methods and many of their variants is finally utilized, is strongly dependent on the material. Layers or nanostrutures of semiconductors, metals, oxides, or organics require different conditions due to their different properties like vapor pressure or melting temperatures.

Among them, organic thin film materials and organic nanostructures became the focus of attention due to their low cost, light weight, flexibility and functionality[6] but also for their ability for self-assembly and self-organized growth, founded in the freedom of molecular design through synthesis. However, often organic materials do not meet the requirements for deposition and processing in vacuum. It is the nature of the organic molecules that allows for their special properties, but also impose a limitation on vacuum processing. Large molecules can incorporate a multitude of functionalities, which increases their mutual interaction and renders

them non-volatile, which means they decompose upon heating.

Alternative fabrication methods of these materials are given by solution based coating methods or printing and stamping technologies.[7] However, these methods provide less control, simply due to the fact that they require a much more complex environment as compared to vacuum processing. For instance, there is less control over impurities which might stem from the solvent or from the surfaces in the environment.

An alternative is offered by electrospray ion beam deposition (ES-IBD), a method which employs gas-phase ion beams of complex, non-volatile molecules generated by electrospray ionization (ESI) for deposition on clean substrates located in vacuum.[8–12] Evidenced mostly by scanning tunneling microscopy (STM) in ultra high vacuum (UHV), in this thesis it is shown that (ES-IBD) represents a highly controlled deposition approach, which allows to fabricate coatings and nanostructures in a similar capacity as MBE.

The possibility to grow thin, crystalline films of non-volatile molecules as well as the fabrication of molecular nanostructures is demonstrated to be analogous to conventional methods. The use of molecular ion beams moreover offers additional levers, directly needed to control the increased degrees of freedom that characterize large functional, organic molecules like proteins or peptides. In particular, macromolecular structure formation through a folding process can be steered through mechanical properties influenced by charge state or deposition energy. Moreover, the capability to deposit highly reactive or even activated species is demonstrated, which shows that ES-IBD adds a completely new level of control to the capacities of MBE and thus has the capability to create novel, functional nanostructures from highly complex and even fragile molecules.

Material and Nanostructure Growth

The origin of nanotechnology and the need to grow nanostructures may be seen in the developments in the field of semiconductor physics and micro- and nanoelectronics. The impetus was given by the compliance with Moore's law starting in the 1970s, demanding a doubling in computer chip performance every two years.[13,14] This performance improvement relies on the production of faster transistors in combination with decreasing dimensions of the devices. These requirements, which are written down in the "International Technology Roadmap for Semiconductors",[15] could only be maintained by the steady improvement of the technology for fabricating nanostructures and materials. An important part of this development was achieved by the enhancement of lithography,[16] enabling the top-down structuring of materials down to a few nanometers at present.[17]

Thin film preparation methods like chemical vapor deposition or physical vapor deposition as thermal evaporation, sputter deposition or molecular beam epitaxy, enable the growth of materials with precise stoichiometry and film thicknesses down to several nanometers.[18] These films serve as the basis for the structuring by lithography. This concept is applied most consequently in MBE, and enables by low deposition rates, a smooth growth of large flat terraces with only a few steps of atomic height. Furthermore, it is possible to abruptly change the composition at interfaces and create in this way very thin and epitaxial inorganic layers.[2,3] An ultrapure vacuum environment is thereby essential, as it ensures that contaminations and undesirable reactions are prevented and is achieved by pressures lower than 10^{-9} mbar (UHV). Moreover, it also allows the implementation of in-situ growth control techniques like reflection high energy electron diffraction (RHEED).[19,20]

Employing a high level of control on the parameters for the flux, pressure, atmosphere and temperature of the sample allows to steer the structure formation on the nanometer- and atomic scale by self-assembly and self-organized growth of materials in a bottom-up approach, which is able to produce architectures beyond the limits of lithography.[21] In general, the growth and synthesis of materials and nanostructures on substrates relies on the adsorption and mobility of atoms and molecules under the influence of the surface. The formation of nanostructures (islands or thin films) is thereby the result of the interplay between kinetics and thermodynamics.[5] When the deposition rate is low in comparison to the diffusion, the adsorbed species have enough time to move across the surface until a minimum of the surface potential energy landscape is found. In this way, equilibrium conditions are reached. If the deposition rate is higher than the diffusion, the species meet each other before reaching a low energy position, leading to the nucleation of metastable structures.

Besides inorganic materials like metals or semiconductors, small organic molecules can also be deposited in this way. The interest in molecular based materials is founded in the fact that they are relatively cheap and very flexible as their properties can be systematically manipulated through molecular design.[22,23] Due to this molecular design, their properties as well as the interaction among them can be influenced, leading to various self-assembled ordered structures on the surface. Their success is demonstrated by electronics based on organic materials, commonly in thin film structures, which are already available commercially, *e.g.* in organic light-emitting diodes,[24] organic thin-film transistors[25] or organic solar cells.[26,27] Besides these applications, many more can be envisioned when multiple functionalities can be included into the molecules. Hence, complex organic materials are potentially extremely useful. But, even more important as compared to

their inorganic counterpart, the properties of functional organic films depend on the arrangement of the molecules on the nanoscale.

Study of Molecules on Surfaces with STM

The possibilities of molecular synthesis and inspiration from biological systems has drawn attention to possible applications of functional molecules in electronics,[28] as catalysts,[29,30] as sensors, as nonlinear optical materials,[31] or as sensitizers in photochemical reactions.[32] An important step towards those applications, is the study of these molecules and their properties. In order to do this, it is desirable to investigate the molecule in an environment that supports the application as well as an atomically precise characterization method which is often important when dealing with nanosystems.

Functional molecular systems on surfaces are a promising candidate for various applications. Self-ordered, molecular assemblies on the surface, interacting with each other by non-covalent interactions like hydrogen bonding, metal-ligand interactions or also by covalent bonds, is a promising way to tailor make a functional surface. The study of the assembly, the quality and the properties of the molecules on such a surface must be performed by surface sensitive methods. Scanning probe microscopy methods, in particular, scanning tunneling microscopy[33] is often used to study these systems in real space, enabling a direct view in the molecular arrangement but also permitting information about the electronic structure[34] as well as local vibrational spectra[35] with atomic resolution. The high resolution, which also enables the imaging of single atoms, relies on a quantum mechanical tunneling current between a sharp metal tip and the sample. The alternative high resolution microscopy technique is transmission electron microscopy,[36,37] which typically is considerably more difficult and moreover may be destructive for fragile molecules during measurements. Thus, high resolution STM and its ability of spectroscopy and to manipulate individual atoms and molecules at the nanoscale is particularly useful for the study of molecules and molecular self-assembly on surfaces.

Using scanning probe microscopy methods, many studies were performed examining the properties of molecules on surfaces. For example, the structure and shape of the orbitals of single molecules like pentacene or naphthalocyanine were imaged and resolved with atomic resolution by CO modified AFM and STM tips.[38,39] Furthermore, molecular architectures were studied which were created by molecular self-assembly on the surface. These formations are often porous networks held together by hydrogen bonds,[40–42] metal coordination bonds[43–46] or covalent bonds.[47,48] Also the synthesis and study of single covalent carbon nanostructures like fullerenes,[49] graphene[50] and graphene nanoribbons[51] was performed, which

are of high interest for molecular electronics.

These achievements show that the combination of STM and self-assembly on surfaces is the perfect tool to create functional molecular structures and to explore their functionality. But the mentioned examples of molecular self-assembly on surfaces correspond to molecular building blocks which are relatively small. Thus they usually only incorporate a single functionality, usually the one which is guiding the structure formation by self assembly. In order to build structures with multiple functions for self-assembly and interaction with the environment, the molecular building blocks have to get larger in size. An example of such highly functional molecules is represented by biological systems.

Large Functional Molecules

Complex biological molecules as they can be found in nature like enzymes and proteins, are built up by 20 different available amino acids, have a size in the nanometer to micrometer range and are highly functional and complex molecular systems fulfilling various tasks. For that reason they are nanostructures by themselves in contrast to the supramolecular materials, which are rather characterized as molecules arranged in nanostructures.[52]

As an example, ribosomes are complexes with a diameter of 20 - 25 nm, which are built up of proteins and various ribonucleic acids held together by hydrogen bonds. They are the functional unit in the cell that is creating proteins according to the recipe given by a messenger RNA.[53,54] Another example are photosynthetic reaction centers, which are composed of different proteins and pigments. They convert light into usable, *e.g.* chemically bound, energy.[55] Since these complexes perform their task over and over again, they can be regarded as molecular machines.[56]

In order to understand the principles of their functionality better, it is crucial to have a molecular resolved insight into these large molecules. It is well known that their functionality is in close relation to the details of their conformation.[57,58] Thus it is necessary to understand their molecular arrangement and conformation at this resolution, ideally observing an individual molecule during its work.

X-ray diffraction (XRD) crystallography and nuclear magnetic resonance spectroscopy (NMR) are techniques, which enable the elucidation of the structure. For X-ray studies[59,60] the proteins have to crystallize into a solid whereas for NMR studies[61] the proteins are in solution. Extensive numerical simulation and data processing efforts accompany these characterization methods. Especially for XRD also the sample preparation requires much effort, if possible at all. Nevertheless, the result is the picometer precise structure of the folded, yet crystallized pro-

tein. NMR in contrast is able to resolve protein dynamics as well. Recently, the unfolding dynamics of a protein dimer could be observed with NMR, giving insight into the folding processes.[62] However, in both cases ensembles of proteins are measured, averaging the obtained data. A technique which enables the direct observation of the folding of a single protein is not available so far.

A way to study individual and large functional molecules is again given by scanning probe microscopy (SPM). In this context, biomolecules were analyzed by atomic force microscopy (AFM) at the solid/liquid interface or after deposition from solution.[63,64] These techniques have the drawback that the surfaces are not atomically clean and that there is less control over the deposition process. A deposition in vacuum, allowing high resolution at low temperatures and a clean environment, is not possible with large molecules using conventional methods like thermal evaporation. The potential of SPM for the characterization of large biomolecules was demonstrated recently with our experiment.[65] Combining in-situ STM with ES-IBD used for sample preparation, it was shown that protein could be imaged with amino acid resolution after the selective deposition of folded or unfolded species.

In summary, organic/biological materials provide advantages compared to inorganic materials like low cost, variable and tunable functionalities, or flexibility.[6] Thus they are of high interest for the integration into devices and applications but also for detailed studies and research on the molecular scale. As with increasing functionality of the molecules, they cannot be processed in vacuum anymore, a technology is needed which allows the controlled deposition of non-volatile complex molecules in vacuum. This would for instance allow the improvement of organic devices like OLEDs and displays by avoiding contamination that leads to device degradation.[66] Just as important are fundamental studies on single and self-assembled large functional molecules on surfaces with high resolution microscopy on the molecular scale that provide a thorough understanding of key principles from biology, like the structure formation by folding, and ultimately allow us to mimic them for technological applications.

Electrospray Ion Beam Deposition

A way to deposit complex and non-volatile molecules in vacuum and bridge the technology gap, is given by electrospray ion beam deposition (ES-IBD). The technique evolved from electrospray ionization mass spectrometry (ESI-MS) which, since its development in the 1980s, is a tool of paramount importance for the analysis of biological macromolecules. Due to this impact to mass spectrometry, the 2002 Nobel Prize for chemistry was awarded to John Fenn, who reported

in 1989 together with his co-authors about mass spectra of biomolecules ionized by ESI.[67] Since then the technology was improved further so that it is possible to obtain well-resolved electrospray mass spectra of biomolecules with molecular masses of several million daltons (Da), like intact ribosomes[68,69] or viruses.[70]

The deposition method ES-IBD allows for the full control of the deposition process starting from the chemical composition of the depositing molecules to landing energy and coverage control. Initially, several studies showed the deposition of ions from the gas phase in vacuum on surfaces. The first one was Cooks *et al.*[8] in 1977, presenting this method for chemical surface modification with the advantages of the high specificity and clean reaction environment. Since basically any kind of molecular ion source can be used, various species from inorganic ions[71] and clusters[72] to very small organic molecules[9] were deposited and subsequently analyzed, predominantly by means of mass spectrometry. With the emergence of ESI, the deposition of large and non-volatile molecules became possible. In this framework, DNA,[73] peptides,[74,75] proteins,[11,65] clusters[76] and dye molecules[12] were deposited.

The present base of literature shows that ES-IBD is a tool for the deposition of non-volatile and fragile molecules in vacuum under well controlled conditions. However, little information is available on the molecular structures that are formed by this deposition method. In particular, in comparison to conventional deposition methods, ES-IBD deals with hyperthermal ions in contrast to thermal atoms and molecules from thermal evaporation. This infers an energetic impact and a neutralization reaction, which can have a profound impact on the structure formation. In combination with highly resolving scanning tunneling microscopy, ES-IBD offers the possibility to understand the structure of large organic molecules with a high degree of freedom.

Thesis Outline

In this thesis I show that self-assembled molecular structures on the surface can be grown with ES-IBD and moreover, that the differences of this technique to conventional deposition methods provide additional leverage to control the structure and the arrangement at the surface.

Two-dimensional (2D) ordered systems as well as three-dimensional (3D) structures made of different molecules are observed, starting from simple non-volatile organic salts to more functional and finally to reactive molecules. For the latter, it becomes very important to have the full control over the deposition process as the chemical state of the molecules is directly connected to its behavior in the self-assembly process or to its reactivity. The deposition of single and highly functional molecules like proteins and peptides reveal a complex structure formation

by folding and the possibility to influence the conformation by the ES-IBD process itself.

The thesis is subdivided into five chapters, starting with an introduction to our home built ES-IBD system, in which the technical layout, the control parameters and the deposition procedure are described. Furthermore, recent improvements are presented, which enable the breakthrough for the highly controlled deposition.

The following chapters show how the unique possibilities of ES-IBD can be applied to molecular coatings. A mass spectrometry and AFM study of the structures formed from the organic salts sodium dodecyl sulfate (SDS) and sodium citrate (SoCit) demonstrates the capability to grow actual thin, multilayered films. In the gas phase, these molecules reveal a strong tendency to form clusters, which enable a high material flux. Upon deposition layered and 3D island growth is observed and it is shown that crystalline structures are formed. In the third chapter the growth of two different molecules is studied at high resolution by STM. Two-dimensional self-assembly is found in the initial adsorption layer on metal substrates at submonolayer coverage. Using a molecular dipole with two stable charges (Reichardt dye, RD) we show the difference between the deposition of only charged molecules and cluster ion beams containing mostly neutral molecules. The deposition of a very reactive molecule (hexayne) is possible as well. Upon self-assembly and subsequent polymerization it forms covalently bonded structures.

The fourth and fifth chapters cover the structure formation of biomolecules, specifically proteins and peptides at surfaces. We show that the conformation of the protein cytochrome c on the surface can be steered by the mass-selected deposition of different charge states and deposition energy. We find that we can influence the mechanical properties by the charge state, which yields different surface structures. This represents how ES-IBD offers additional direct control parameters for the structure formation of complex molecules. As the protein with 104 amino acids is very large, random conformations are observed. In contrast, a smaller amino acid chain, the peptide bradykinin consisting of 9 amino acids, self-assembles into ordered structures and shows different conformations as a function of the surface. Due to the ordered assembly, the single amino acids were identified with an unique theoretical approach combining density functional theory and molecular dynamic simulations. We were able to show that the different structures are related to each other by folding, which shows the potential to exploit this process for fabricating artificial molecular structures.

How the novel approach towards vacuum fabrication of highly complex organic films can be employed towards future research or even lead to commercial applications is outlined in a final concluding chapter.

1 Electrospray Ion Beam Deposition - Full Control

Gas phase atoms or molecules colliding with a surface in vacuum, may condense and become an adsorbate, many of them nucleate and eventually grow into a thin solid film. This is the simple principle of vacuum deposition, one of the most successful technologies for the preparation of surface coatings. Applications range from metal films on hundreds of square meters on window-glass to few isolated molecules or atoms placed on the surface of a metal crystal, and include key applications like the fabrication of crystalline semiconductor films.

Vacuum deposition is implemented in numerous variants, which mainly differ in the type of the gas phase particle source. By heating, thermal- or electron-beam evaporators, neutral gas phase atoms and molecules from volatile materials are created. Typically they are metals and semiconductors but the method works as well for some organic molecules.[18] Sputter sources and pulsed laser ablation uses the energy from ionized particles or light to create neutrals, gas phase ions, and clusters.[18] In contrast to thermal evaporation, these sources rely on a non-equilibrium process and can thus be used for materials with very high sublimation temperatures, low vapor pressure and even non-volatile materials like oxides. Finally, chemical vapor deposition (CVD) uses gaseous precursor molecules that are leaked into a vacuum chamber and brought to reaction on the way to or at a surface, creating a solid-phase coating.

Flux and composition of the beam as well as the surface structure, purity and temperature of the substrate, influence the growth of the adsorbate film. The success of vacuum deposition lies in the ability to control or define these process parameters. The processing in a vacuum environment ensures that contamination of the surface as well as undesirable chemical reactions are avoided. In particular, the preparation of nanoscale systems is a challenge, since already a single atom or molecule added to or taken from a nanoscopic system may alter its properties significantly. Therefore, vapor deposition in ultrahigh vacuum (UHV) is one of the

most successful approaches to fabricate thin film coatings and nanoscale systems with atomic precision.

However, with organic or biological macromolecules and nanoparticles, two large material classes are not compatible with the above mentioned approaches to vacuum deposition. Often, their decomposition threshold is below the energy needed to transfer them into the gas phase, hence they do not have sufficient vapor pressure for intact evaporation or sublimation. This poses an intrinsic limitation on the evaporation approach, which especially prevents large molecules such as polymers, dendrites, biomolecules, and synthetic functional molecules from being subject of vacuum processing.

As an alternative, soft ionization methods are capable to generate intact gas phase ions of nonvolatile and thermally unstable species. Electrospray ionization (ESI)[67] and matrix assisted laser desorption ionization (MALDI)[77] are the most prominent examples, that have found widespread applications in mass spectrometry.[78]

In this chapter the vacuum deposition experiment for non-volatile molecules is introduced. It is shown how the gas phase ions provided by an ESI source can be used for a fully controlled vacuum deposition. The starting point for the experiment are non-volatile molecules in a solution, which are transferred into intact molecular gas phase ions by electrospray ionization. As this requires ambient pressure conditions, a differentially pumped, six chamber vacuum system equipped with various ion optics is used to form an ion beam and guide it to a sample surface in UHV, where the molecular ions are deposited. The experimental setup, called electrospray ion beam deposition (ES-IBD), features a nano-electrospray source with a hydrodynamically optimized vacuum transfer, representing one of the most intense ESI sources available. Furthermore the deposition apparatus includes mass-selection, mass spectrometry as well as spatial, energy, and current characterization of the ion beam. Samples are prepared for in-situ measurements in a scanning tunneling microscope (STM), for various ex-situ methods, and for other high performance UHV based instruments, using a UHV-suitcase for transfer.

1.1 Electrospray Ionization

The work shown in this thesis builds upon the fact that molecular ions can be generated by electrospray ionization.[79,80] To generate a electrospray, a liquid containing the analyte molecules is pumped through an emitter at ambient conditions: a small capillary made of metal or silica.[81,82] Upon applying a high voltage to the solution or to the the emitter, the liquid surface is being deformed to accommo-

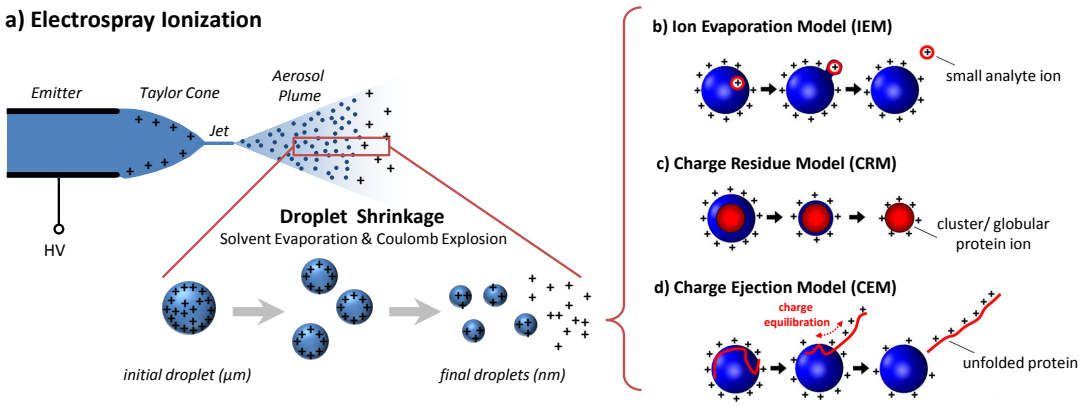

Fig. 1.1 Electrospray ionization scheme. **(a)** Instability of a liquid under the influence of a high electric field leads to charged droplets. Three different model describe the ejection of the analytes from the nanodroplets. **(b)** IEM: Ejection of small ions. **(c)** CRM: Release of globular proteins or clusters. **(d)** CEM: Ejection of unfolded proteins or polymers. (b - d from Ref. [84])

date the to the electric field formed between emitter and a counter electrode. A conical jet of the liquid at the exit of the emitter is formed, which is known as Taylor cone. In general, Taylor cones are transient objects and different regimes are known.[83] In the most simple and useful regime, the cone-jet mode, a jet of liquid is emitted at its apex that thinners due to the acceleration of this liquid jet by the electric field. The liquid stream disperses into an aerosol plume of highly charged droplets caused by electrostatic effects, the so-called electrospray (Fig. 1.1 a).

Assisted by heating, the emitted charged droplets undergo rapid solvent evaporation, causing a shrinkage. This is increasing the charge density in the droplet what intensifies the Coulomb repulsion, which is, up to a certain point, counteracted by the surface tension. At this point, the so-called Rayleigh limit, the number of charges is given by[85]

$$z_R = \frac{8\pi}{e}\sqrt{\epsilon_0 \cdot \gamma \cdot R^3}$$

where R is the droplet radius, ϵ_0 is the vacuum permittivity, and γ is the surface tension. Further decreasing of the droplet size by solvent evaporation leads to the domination of the Coulomb repulsion whereupon the droplet explodes into smaller droplets (Coulomb explosion), entering the sequence of shrinkage and Coulomb explosion on themselves. This sequence is repeated until the initial droplets have radii of a few nanometers. From these nano-droplets molecular- or cluster ions can be generated by several mechanisms: ion evaporation, charge ejection, or the

formation of charged residues.[86–88]

The models corresponding to the mentioned mechanisms are the ion evaporation model (IEM, Fig. 1.1 b), the charged residue model (CRM, Fig. 1.1 c) and, more recently introduced, the chain ejection model (CEM, Fig. 1.1 d). Their occurrence is essentially are determined by the size and the shape of the analytes contained in the nanodroplets. While light analytes, like small molecules, are brought into the gas phase via the IEM,[89] larger species, like clusters or globular proteins, are charged and released following the CRM.[90–92] Recently, MD simulations and experimental observations suggested a third plausible model that describes the charging and release of unfolded proteins.[84,88,93] Due to their elongated shape they are pulled out of the droplet. In all cases, intact ions are produced, which can now be guided into vacuum for mass spectrometry or ion beam deposition.

1.2 Components of the System

The generation of intact molecular gas phase ions from non-volatile molecules by ESI requires ambient or at least high pressure background gas to promote the reliable desolvation of the molecular ions.[94,95] Thus the idea to use ESI as a gas phase particle source for vacuum deposition immediately entails the problem of transferring an ion beam from high pressure to (ultra-) high vacuum, where it can be successfully used for a controlled deposition. Our approach is a differentially pumped vacuum system, which distributes the burden of the gas load over several pumping stages, reaching UHV at the sample position. In the several vacuum chambers that are required, ion optics must be implemented to move ions from the aperture, through which they enter the chamber, to the next chamber at highest possible transmittance. The ion optics in turn promote features that allow the control and manipulation of the ion beam.

Figure 1.2 shows a sketch of the ES-IBD apparatus. Following the ion beam it starts on the left with the ion source (ES) and ends on the right with a deposition target in UHV, which is a single crystalline sample suitable for STM characterization (S-UHV). This sample can be transferred in-situ to the STM in UHV.

The deposition apparatus consists of four major sections. The ion source and atmospheric interface (red), high pressure stages (yellow), in which a beam is formed, ultrahigh vacuum stages (green), to which the beam is transmitted, and several sample holders (blue), where the actual deposition takes place.

Six differentially pumped vacuum chambers are connected by apertures (AP) of 2 mm in diameter, through which the beam can pass from one vacuum chamber

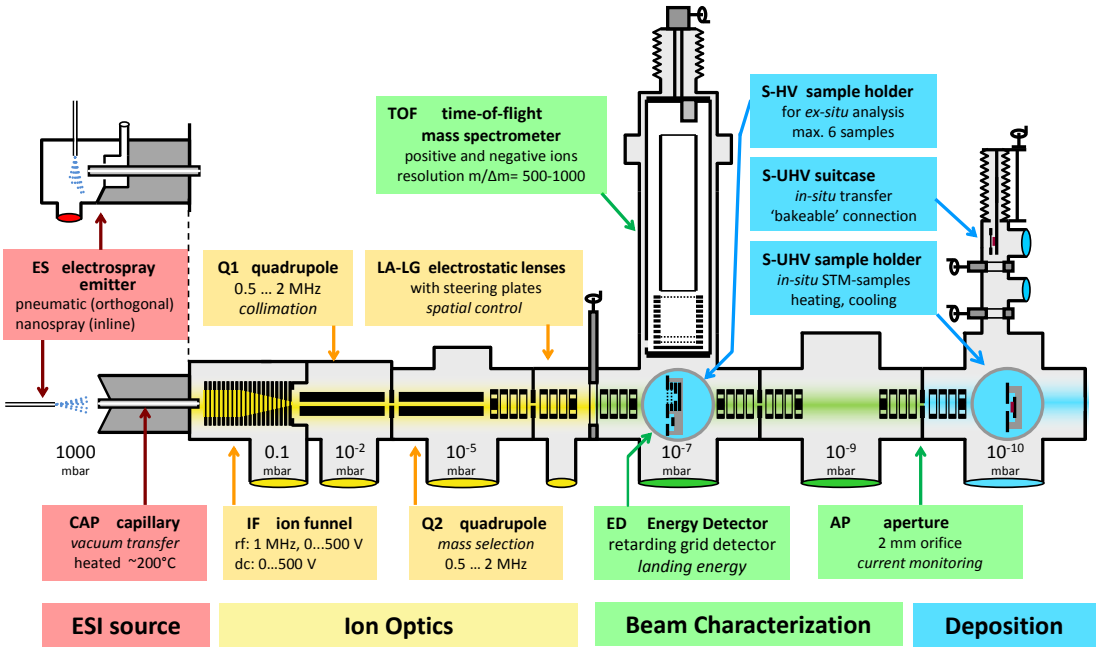

Fig. 1.2 Scheme of ES-IBD apparatus. Starting from the ion source (red), ions are transferred into vacuum entering the ion optics part (yellow) where they are collimated and mass-selected. Subsequently the beam is characterized in HV (green) by mass spectrometry and energy measurement before the ion are guided to the samples for deposition (blue).

to the next. Ion optics in each chamber are designed to transmit the ion beam to the next pumping stage. The ions enter the vacuum through a transfer capillary (CAP) and freely expand into vacuum. This expanding ion cloud is collimated by an ion funnel (IF)[96,97] in the first pumping stage and by quadrupole ion guide (Q1) in the second pumping stage. Another quadrupole Q2 in the third pumping stage is used for mass filtering of the ion beam. The ion beam is passed further downstream through several apertures by electrostatic lenses (LA...LG). The main chemical characterization tool is a linear time-of-flight mass spectrometer (TOF) in the fourth pumping stage. In this chamber also a sample stage (S-HV) is present that contains a retarding grid energy detector for the measurement of the beam's kinetic energy as well as up to six sample position for deposition in high vacuum. In the sixth vacuum chamber in ultrahigh vacuum the sample holder for deposition on single crystal substrates is mounted on a manipulator (S-UHV) for in-situ transfer into the STM. Furthermore a loadlock, to which a UHV suitcase can be connected is attached to this chamber. To operate this ES-IBD setup, a multitude of power supplies and current meters are employed. They are connected to a computer containing several digital/analog and analog/digital

converters, that controls all elements and gathers all incoming data.

Altogether, the ES-IBD setup represents a large and very complex experiment, which requires great effort in maintenance and operation, but also has the potential for a unique research. In the following, a more detailed description of the some key components is given and after that the ion beam deposition procedure is described. It is shown how the individual components act together in order to achieve the full control of the deposition.

1.2.1 Electrospray Interface and Sources

The generation of molecular gas phase ions by ESI occurs at the emitter, typically a fine capillary, through which the solution is pumped. A gas phase ion source for mass spectrometry or deposition, using the electrospray effect (or any other atmospheric pressure ionization (API) technique) requires a vacuum interface to transfer the ions from the place of their generation at ambient condition to where they are characterized or deposited in vacuum. Often ion generation and vacuum transfer, *i.e.* source and vacuum interface, are closely interdependent.

Our main ion beam deposition source uses pulled glass capillaries in the nano-electrospray[81,98] (nano-ESI) regime as emitters. This source replaced a pneumatically assisted source utilized in the beginning of this PhD project and represents the current state of art for low flow ESI-emitters. The emitters are $3 - 5\,\mathrm{cm}$ in length and have an inner diameter of $25\,\mu\mathrm{m}$, which is significantly reduced at the apex by the pulling.[81] Since they are insulating the connection to the high voltage is made via a liquid junction, which is included in a three fold PEEK liquid junction (*Upchurch Scientific*, Fig. 1.3 a). This assembly is mounted on an xyz-manipulator for precise positioning of the emitter with respect to the vacuum transfer capillary.

A successful ion beam deposition experiment requires a much larger amount of material transmitted to vacuum than a typical mass spectrometry application. To work efficiently, we therefore had to develop an improved experimental equipment. In this context, a transfer capillary with a funnel shaped inlet was designed, which allows for up to 100% transmittance (see Fig. 1.3).[99] The transfer capillary (gray) is made from stainless steel and has an inner diameter of 0.75 mm at a length of 7 cm. It is held in a copper cylinder (red) and is electrically insulated (white) from the rest of the apparatus (Fig. 1.3 a). In this way, it can be effectively heated (up to 300°C) and a voltage can be applied. The inlet region is formed in a funnel shape, which widens from the 0.75 mm inner diameter to 8 mm smoothly following a curve of 30 mm radius (Fig. 1.3 b). If the emitter apex is placed within this funnel, the hydrodynamic drag force acting on the ions induced by the gas

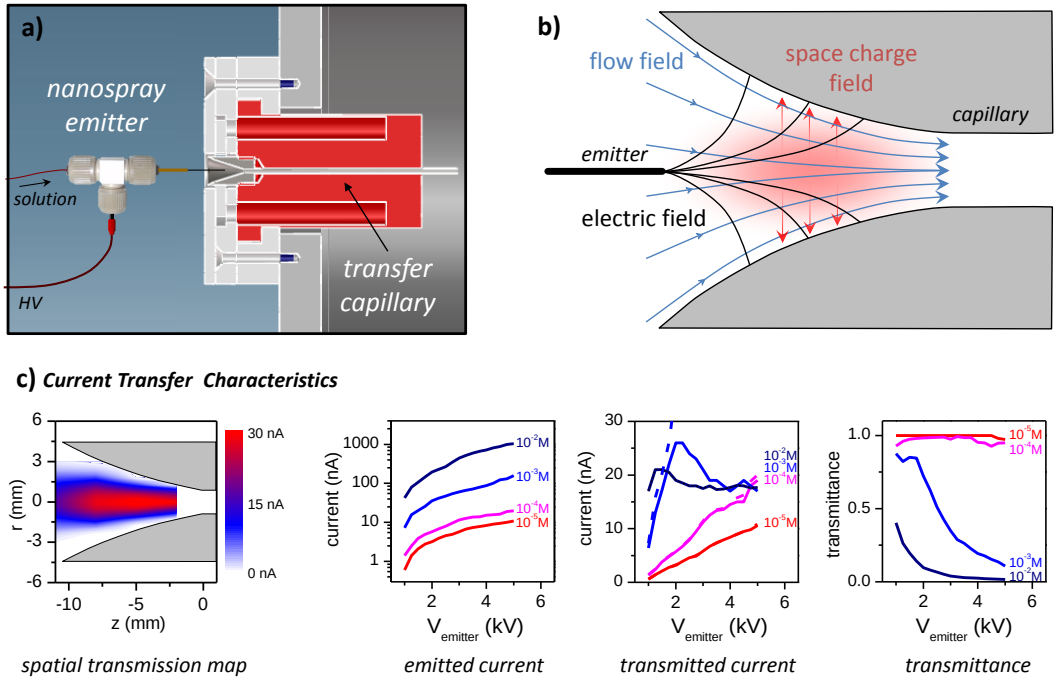

Fig. 1.3 **(a)** Hydrodynamically optimized atmospheric nano ESI interface showing the PEEK liquid junction with nanoflow tubing. **(b)** Scheme of the force fields acting on the molecular ions present in the entrance region of the transfer capillary. **(c)** Current transfer characteristics: Spatial maps of transmission as a function of the emitter position show the robustness of the collimation and current transmittance as a function of the emitter voltage shows up to 100% for currents up to 30 nA.

flow into the vacuum collimates the generated ion cloud. The robustness of this collimation by the hydrodynamic drag is seen in the spatial transmission maps as a function of the emitter position in Fig. 1.3 c). Along the radial axis the maximal transmitted current can be achieved over more than 5 mm, while away from this position in radial and axial direction the transmitted current decreases. In this way, this source reaches ion transmittance of up to 100 % into vacuum for electrospray currents of up to 30 nA depending on solution concentration and emitter voltage and is only limited by the space charge occuring in the funnel inlet (Fig. 1.3 c).[99] On the vacuum side, the completely desolvated ions together with the heated background gas, leave the capillary at approximately the speed of sound and expand into vacuum (0.7 mbar in the first differential pumping stage).

Due to the untypically large capillary diameter of 0.75 mm a significant gas load is imposed on the first pumping stage. Therefore this stage is evacuated with

a large roots pump (*Balzers Pfeiffer* WKP500A) reaching 0.7 mbar. It should be noted that this is the pressure that is read by a vacuum gauge at the chamber wall and that the pressure and gas velocity may be significantly different elsewhere, in particular following the axis of the capillary along which the gas expands into vacuum. An even more efficient pumping was not chosen for the reason that at a pressure of 1 mbar and above, the interaction of the background gas with the ions is sufficiently strong to allow the operation of radio-frequency (rf) ion optics of high adiabaticity, like the ion funnel, which have the capacity to cool a hot ion cloud and collimate it into an ion beam.[100]

1.2.2 Ion Optics

Ion Funnel

Once the ion containing gas passed the capillary it expands into vacuum, dispersing the ion cloud over a large volume. To achieve a significantly lower pressure in the subsequent chamber, however, only a small diameter aperture of 2.5 mm can connect the two chambers. In the initial implementation of the ES-IBD setup a skimmer was used to sample a part from the expanding ion cloud and pass it into the next pumping stage.[11,12] This however lead to great losses of more than 90 % of the ionic current. Therefore an ion funnel[96,101] that can collimate a major fraction of the ion cloud into an ion beam was developed to replace the skimmer.

Our ion funnel is designed as a stack of 82 disc shaped ring electrodes to which two printed circuit boards are connected. Through them rf- and dc-voltages can be applied. The electrodes, fabricated from stainless steel, are 1 mm thick and have an inner diameter of 30 mm that narrows linearly to 2.5 mm on the last third of the funnel length. They are separated by teflon washers of 0.75 mm thickness. The ion funnel is concluded by a dc-only entrance- and exit-electrodes. All electrodes in-between are connected via resistors of 1 MΩ, which allows to superimpose a dc-voltage gradient over the whole device.

Connected via capacities, the same rf-voltage is applied to every second electrode, while the opposite polarity is applied to the other half set. The rf-voltage oscillating at 1 MHz generates an effective potential, which can trap the ion cloud inside the funnel. Due to the electrode geometry in an ion funnel the trapped ions would gain a significant amount of energy from the rf-field, which ultimately would lead to their loss. However, at a pressure of 1 mbar (and above) frequent collisions with the background gas thermalize the ions, which leads to an effective collimation. The superimposed electrostatic potential gradient drags this ion cloud towards the funnel exit electrode.

Quadrupole Ion Guides

For further collimating, transporting and mass-selecting of the ions in the second and third pumping stage, two rf-quadrupole ion guides, Q1 and Q2, of identical dimensions are operated at 10^{-2} mbar and 10^{-4} mbar respectively. Their rods are 10 cm long and have a diameter of 5 mm, enclosing a trapping volume of 6 mm minimal diameter. They are connected to power supplies (*CGC Instruments* RFG10) allowing for amplitudes of up to 1 kV at the fixed frequencies of 0.5 MHz, 1 MHz, and 2 MHz, which is selected by exchanging the power stage of the amplifier.[102] A additional power supply (*CGC Instruments* HV200) is superimposing dc-voltages for each rod pair in a range of ±200 V, which are defined by a voltage offset and a differential dc-voltage. The two quadrupole ion guides are separated by an aperture of 2 mm, which can be biased independently.

The ions, leaving the ion funnel via an aperture of 2.5 mm diameter, enter the Q1 chamber together with a part of the neutral background gas. This gas load leads to a pressure of $0.1 - 0.01$ mbar in this pumping stage, which can be adjusted by changing the pumping cross section of the connected turbo pump (*Pfeiffer* TMU 262) via a gate valve. Still the collimating quadrupole requires ion-gas collisions for collimation. Nevertheless the pressure can be set lower as compared to the ion funnel, since the adiabaticity of a quadrupole is lower.[100]

This first quadrupole (Q1) is typically operated in rf-only mode, *i.e.* no differential dc-voltage is applied. At amplitudes of $50 - 150$ V, the ion beam is effectively trapped over a large m/z-range and in addition collimated by collisions with the background gas. The ions leave the Q1 quadrupole through an aperture of 2 mm diameter and enter the Q2 quadrupole in the third pumping stage at high vacuum pressure of $10^{-4} - 10^{-5}$ mbar; the pressure here depending on the pressure upstream. For all following chambers the aperture has this same diameter, which corresponds to a conductance of 1 l/s for molecular flow. The gas load entering the subsequent chamber divided by the effective pumping speed of approximately 100 l/s thus yields the pressure $p_{n+1} = \frac{1\,\mathrm{Ls}^{-1} \times p_n}{S_n^{\mathrm{eff}}}$, hence it drops by roughly two orders of magnitude per chamber.

The Q2 quadrupole is operated with amplitude values of up to 600 V and in addition differential dc-voltages are applied in order to mass-select a narrow m/z-window for the transmission. With a limited m/z-resolution $R = M/\Delta M \approx 50$ the ion guide is typically used to define a transmission window of $10 - 200$ Th rather than selecting a single ion peak with unity resolution. Leaving the Q2 ion guide, a mass-selected beam is entering the first of the electrostatic lenses. With an kinetic energy that is defined by the electrostatic potential of the Q1-Q2 aperture with respect to ground. Approximately at this location, the ion beam passes over

to high vacuum, which means that no further collisions with the background gas occur. Hence, the electric potential of this electrode is a good measure and also the defining parameter for the kinetic energy of the ion beam with respect to ground potential.

Electrostatic Lenses

The high vacuum section contains electrostatic lenses with integrated steering plates for guiding of the ion beam. The lenses consist of three concentric rings of 10 mm inner diameter to which voltages of ±200 V can be applied. One lens is attached to either side of each aperture; the first one focuses the beam through the hole, while the second one makes it parallel for further transport without losses through divergence. The steering plates in each lens can be adjusted by ±20 V in order to steer the ion beam to the next electrostatic lens or to adjust it to pass the aperture precisely.

1.2.3 Beam Characterization

Chemical Characterization by Time-of-Flight Mass Spectrometry

For the chemical characterization of the molecular ion beam, an orthogonal linear time-of-flight mass spectrometer of Wiley-McLaren geometry[103] is integrated in the HV stage. The ions enter a field-free extraction volume through a narrow aperture. With a repetition rate of $(130\mu s)^{-1}$ the ions are extracted by a push and pull pulse of 285 V and 330 V lasting 70 μs into an acceleration region of 10 cm length, which they leave at 4950 eV per charge. After a flight tube of 40 cm length the ions impinge at a fast dynode detector (*ETO* 14882). Its signal is processed by a discriminator and preamplifier, further converted to TTL pulses, and finally detected with a resolution of 1 ns by a time-to-digital card (*Blue Sky Electronics* TOF-1 TDC).

Our instrument reaches a m/z-resolution of $500-1000$, typically depending on the alignment and spread of the ion beam. A dynamic range of three orders of magnitude is typically achieved. To be more sensitive the detector voltage can be increased, however at the price of large dead time regions close to intense peaks. The instrument is, however, usually not used for classical analytical purposes since the ions to be deposited are predefined by the solution. Thus the main task of the TOF-MS is to confirm the contents and purity of the ion beam and the accuracy of the mass-selection.

During this thesis the original design of the TOF-MS was improved. The capability to detect negative ions was added by changing the fast dynode detector

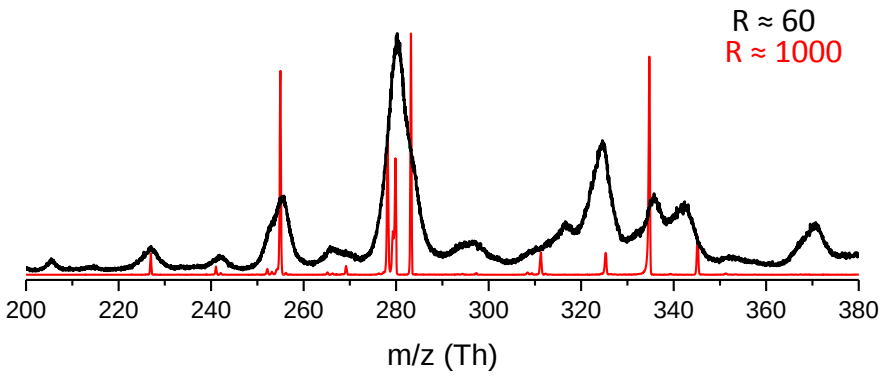

Fig. 1.4 Mass spectrum of hexanyne molecules (cp. Chap. 3.2) in negative mode before and after the improvement of the mass spectrometer. The resolution increased from R= 60 to R= 1000.

(from *ETP* 14880 to *ETP* 14882), which enabled us to perform mass-selected negative ion depositions.[104] At the same time the acceleration voltage was increased to 5 kV and the entrance slit was implemented as a narrow collimator. As a result the resolution could be improved significantly from $M/\Delta M = 50...100$ to almost 1000 (see Fig. 1.4). It is seen, that already one molecule can show a highly complex behavior which might not be noticed with low mass resolution as several peaks can be buried behind a single peak. Thus a good resolution is needed to resolve complex behavior such as chemical reaction, fragmentation, or clustering unambiguously and to deposit the corresponding ion species, which could have interesting properties.

Flux of the Ion Beam

The flux of an ion beam can be understood as an electrical current, with the molecular ions as charge carriers. To determine the material flux of the ion beam, however, one has to know the (average) charge state of the ions, a task in most cases straight forward done by mass spectrometry (see Chap. 2).

The current of the ion beam is monitored at many places in the ES-IBD apparatus for the purpose of aligning the beam through the various apertures towards the sample and most importantly, to monitor the deposition process and control thus the coverage. Since, at low ion energies, no emission of secondary charged particles occurs, the current detected by an electrometer (*Keithley* 616) directly attached to an aperture electrode or sample can be interpreted as the ion flux impinging on the surface of that electrode.

Kinetic Energy

For the deposition of the ion beam it is necessary to know the kinetic energy of the ions in order to adjust the landing energy such that the molecules stay intact during deposition. Therefore, a retarding grid detector was integrated in the HV sample holder, which allows to measure the kinetic energy of the ions and to define the deposition energy by applying a deceleration voltage to the samples accordingly. The scheme of the integrated retarding grid kinetic energy detector is shown in Fig. 1.5 a) together with the cross section of a sample position. The detector consists of an electrode on which the impinging ions are measured with the electrometer. Above this detector plate, the retarding grid is mounted, to which a voltage can be applied. A hole in the cover plate above is covered by another grid to ensure a homogeneous electric field.

In order to determine the energy, a voltage is applied at the retarding grid, which generates a repulsive electric field between the grid in the front plate. If this potential is higher then the ion's kinetic energy, the ions are repelled and hence are not detected at the electrode behind the grid (indicated in Fig. 1.5 a). When this occurs, the retarding voltage equals the kinetic energy of the ions per charge. The absolute value of the first derivative of the current-voltage characteristic $I(V_{grid})$ is the kinetic energy distribution of ion beam per charge. The usage of grids ensures that the equipotential lines are close to an ideally parallel configuration, which enables a precise energy measurement of less than 0.1 eV error.

1.2.4 Deposition Targets

For the deposition of the ion beam onto a sample, three different possibilities serving a specific purpose each are implemented. The first possibility is located in the HV stage where the mass spectrometer is placed. Here, the sample holder with the implemented energy detector is situated equipped with six sample positions (Fig. 1.5 b). These samples are mounted on the sample holder outside of the vacuum, in ambient conditions, and are intended to be used for ex-situ analysis like atomic force microscopy (AFM) or MALDI measurements after the deposition.

The second option for deposition is located in UHV in the sixth (10^{-10} mbar) pumping stage. This UHV sample holder (Fig. 1.5 c) contains only one sample alone and is directly connected through the preparation chamber to the STM for in-situ transfers. Omicron-type sample holders with different metal crystals are intended for in-situ STM measurements.

The last option to deposit onto a sample is given by the UHV suitcase. Here, a sample can be carried from another UHV setup to the ES-IBD system. After

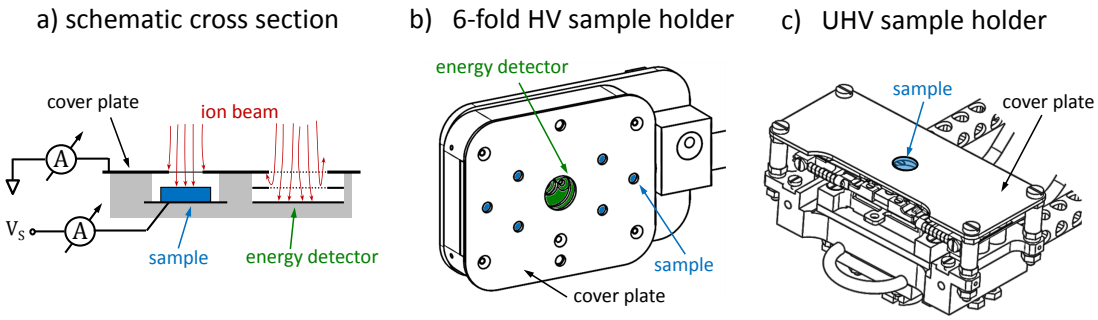

Fig. 1.5 **(a)** Schematical cross section of the sample holder and integrated retarding grid detector. **(b)** HV sample holder with six sample positions (blue) and energy detector (green). **(c)** UHV sample holder for a Omicron-type sandwich sample.

pumping and baking the connecting chamber over night, the sample is transferred from the suitcase into the deposition chamber.

All sample holders have in common, that they are mounted on an insulator with no contact to ground. Their active area is exposed to the chamber through a hole in the cover plate, which is insulated to ground as well. All of these insulated electrodes have a connection to the outside at which electrometers are connected to measure the current that is flowing during deposition when the ion beam hits the sample or cover plate.

Monitoring the ion current on the cover plate, allows the operator to direct the beam either to the different samples or to the energy detector on the HV sample holder. At the sample position the current impinging on the surface is measured by an electrometer, which is floating on a retarding or accelerating potential that is used to define the collision energy and thus the interaction strength of the ions with the surface. At the same time the amount of material can be quantitatively determined from the current that is measured, which is used to precisely define a molecular coverage.

1.2.5 Software and Data Acquisition

Because the differentially pumped beam optics column consists of almost 80 voltage terminals and at least 6 current measurement points, it is helpful to automatize the control of this system. To this end a computer program is used that can apply all needed voltages and allows the operator to manipulate them in a very controlled, intuitive way, while at the same time feedback is provided in the form of current measurements.

Five digital-to-analog cards with 16 channels $\pm$10V integrated into an industrial

PC are used to control the voltage output channels ranging from 10 kV for the TOF to 20 V for the steering plates with 16 bit precision. The current readings with a resolution of 0.5 pA of the Keithley 616 electrometers are digitalized by a ICP DAS card providing 16 double-ended channels with 16 bit resolution on the full scale of ±10 V.

All relevant terminals are displayed and can be manipulated manually or remotely as a function of other terminals as specified by the used. The whole terminal information is automatically stored as well as all the current measurements, be it the time dependent monitoring or the voltage dependent 1D or 2D sweeps.

1.3 The Ion Beam Deposition Procedure

The high complexity of the deposition apparatus, as compared for instance to evaporation methods, imposes a more elaborate deposition procedure to actually achieve the level of control that the method allows. This also means that ES-IBD is more susceptible to errors than other methods. In the following the principles of operation of ES-IBD are described following the workflow of a typical ion beam deposition experiment. The procedure can of course differ depending on the specific goal of each deposition.

Figure 1.6 outlines the main steps of the deposition process. After generating an initial ion beam the first step is its characterization by mass spectrometry (Fig. 1.6 a) followed by the mass-selection of the ion species for deposition. Next, the beam is guided to the sample holder, which is imaged by the beam to identify the deposition position (Fig. 1.6 b). Before deposition, the kinetic energy is determined as a reference for the adjustment of the landing energy for deposition (Fig. 1.6 c). Finally the ion current is monitored during deposition to determine when the desired coverage is reached (Fig. 1.6 d).

Overall this procedure allows to control all deposition parameters online, actively and quantitatively. In contrast for conventional vacuum deposition many quantities can only be determined post ex and thus extensive efforts must be made to calibrate corresponding parameters. In ES-IBD mass spectrometry and mass-selection define the purity, the current imaging allows to spatially define the deposition spot, the beam energy measurement is needed to quantitatively define the collision energy, and the coverage is controlled precisely by the current measurement.

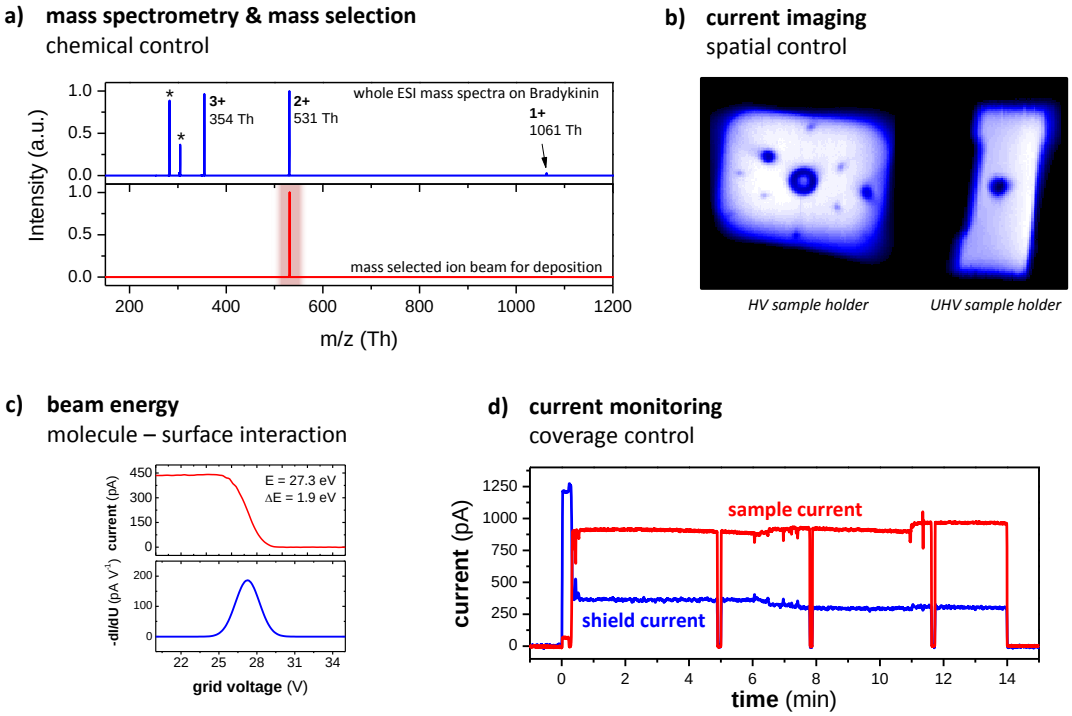

Fig. 1.6 Scheme of deposition procedure. **(a)** Analysis of beam composition and mass selection. **(b)** Thrilling the beam to the sample holder/energy detector assisted by spatial control and current imaging. **(c)** Beam energy measurement. **(d)** Current monitoring during deposition for coverage control.

Creation of the Ion Beam

Before the deposition and the adjustment of the parameter relevant to it, the ion beam has to generated staring with dissolving molecules in a solution for ESI. The solution containing the analyte, typically at a concentration of $10^{-3} \ldots 10^{-5}$ mol/l is pumped at a rate of $10 - 100\,\mu$l/h into the nanospray emitter. Typical solvents are ethanol, methanol, water, and acetonitrile. Others are intermixed when dealing with molecules that require unpolar solvents. Also small concentrations of acids (formic acid, acetic acid) or bases (ammonium acetate, ammonia) are added to enhance the ionization.

Once a stable flow is established, the emitter is brought into the proximity of the capillary entrance and the spray voltage is applied. The generated ion beam is guided to the first current monitoring aperture after the Q2 quadrupole and a first optimization is performed, in which all parameters are modified iteratively to achieve a reasonably high current, that would allow to continue with the deposition.

The ion yield is strongly dependent on the molecule. Currents up to 8 nA have been achieved after the quadrupoles in high vacuum. This current is subject to losses by mass-selection and imperfect transmission, so that usually a fraction of below 50% of it is measured at the sample. Thus, if the current is too low to proceed it is typically helpful to first adjust the mixture of solvent and additives, the flow rate and the interface parameters (polarity, voltage, temperature), since these can have a tremendous influence on the ionization yield.[105] For an overview, typical solvents, concentration and ion currents for different molecules are presented in table Tab. 1.1.

Molecule	Solvent	Concentration	Mode	Ion Current
CytC	H_2O/EtOH	$< 10^{-4}$	pos	4 nA
Bradykinin	H_2O/EtOH	$< 10^{-4}$	pos/neg	2 nA
SDS	H_2O/EtOH	$10^{-4} - 10^{-2}$	pos	2 nA
Hexayne	DCM/$CHCl_3$/MeOH	10^{-4}	neg	200 - 800 pA
Betaine	H_2O/EtOH	10^{-4}	pos/neg	2 nA/800 pA
Rho6G	H_2O/MeOH	10^{-4}	pos	6 nA
N3	H_2O/EtOH/MeOH	10^{-4}	neg	600 pA

Tab. 1.1 Table of typical ion currents, solvents and concentrations.

Mass Spectrometry and Mass-Selection

After passing the two rf-ion guides Q1 and Q2 the ion beam enters the fourth differential pumping stage through an aperture. In this chamber the TOF-MS is mounted, which is moved into the beam axis for mass spectrometry characterization. The upper panel in Fig. 1.6 a) shows a typical example of a mass spectrum, in which the molecule from solution, in this case bradykinin, is represented as ion of several charge states. In addition, contamination ions are found as well ($*$ in Fig. 1.6 a).

By superimposing a differential dc-voltage to the Q2 quadrupole, a m/z-window is selected, in this case to transmit only the doubly charged ion species at 531 Th. The TOF-MS is used to verify the successful mass-selection, which means to ensure that no other ion is transmitted. Moreover, the mass-selection parameter are optimized in order to minimize losses of the targeted ion, using the MS-intensity of the transmitted peaks as reference. After the optimization in the mass spectrum only the desired ion is visible (Fig. 1.6 a, lower panel).

That mass-selection is important to ensure a clean and defined beam is shown by the comparison of STM images of the deposition of Mn_{12} molecules on Cu(001) with and without mass-selection of the single charges Mn_{12} ion (Fig. 1.7). Applying

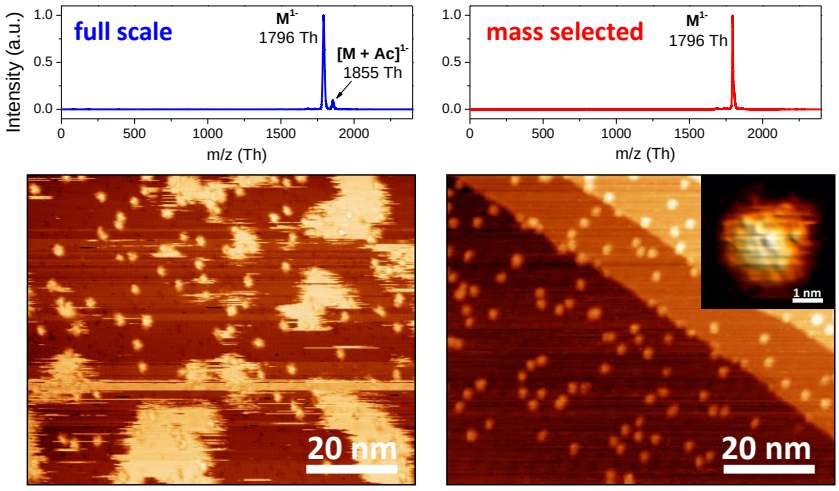

Fig. 1.7 Comparison of the deposition result of a mass-selected and a non-mass-selected ion beam for Mn_{12} molecules. Although only a small contamination peak is present, the deposition without mass-selection differs significantly.

a sharp mass-selection results in the observation of only immobilized and intact Mn_{12} molecules, observed in both STM images as 2 nm diameter lobes on the surface.[104]

Without mass-selection the mass spectrum is very clean and only a small peak is detected besides the singly deprotonated molecule. After a deposition without mass-selection, however, on the surface a large molecular coverage with very mobile species is found besides the immobilized Mn_{12} molecules.

This shows that mass selection not only removes obvious contamination, but also a background of large cluster ions can be present, that is not easily detected by mass spectrometry, yet has the capacity to convey a large amount of material to the surface. Mass selection thus ensures that only the selected species (and perhaps an isomeric contamination) is transmitted and hence deposited.

Spatial Alignment and Ion Energy Measurement

The presence of the ion beam can easily be detected by measuring its current on an electrode. Using a well focused ion beam and a set of steering plates that deflect the ion beam orthogonal to its direction, such a current measurement can be used to map the shape of the electrode. These images can be extremely useful for the alignment of the ion beam.

The images shown in Fig. 1.6 b) are such current images of the front plates of the sample holders in positive ion mode in the fourth and sixth pumping stages at

10^{-7} mbar and 10^{-10} mbar respectively (compare to Fig. 1.5). The bright regions indicate high current, hence the beam hits the sample plate, while dark regions indicate that the beam is off the plate. The shape of the plates is well represented as well as any hole in their surface. The UHV sample holder (right panel) only has a single hole, behind which the sample surface is exposed to the ion beam.

The high vacuum sample holder shows many depressions of various size and intensity. The big hole in the middle relates to the integrated current detector. (Its current detection electrode is separated into an inner and out part, which were detected separately for this measurement and the current measured on the inner electrode was added to the front plate current; hence the donut shape.) Left and right of this structure three sample positions are visible at any one side. The difference in intensity stems from the voltage applied to the sample in each position. If no voltage was applied, the sample was on ground potential, the ion beam simply passes and the hole is imaged as a big depression. The four minor depressions relate to samples to which a high positive voltage was applied to protect them from contamination by the ion beam. Since the ions enter the hole first before being deflected by the repulsive field, some of them impinge on the cover plate from the back side, which leads to reduced ion losses and hence to a less pronounced depression. Finally the two small depression at the very top and bottom correspond to two small, unused bolt holes and indicate that the resolution of imaging is approximately 0.5 mm.

The spatial imaging is done very quickly in less then one minute, usually however at a lower resolution than shown in Fig. 1.6. It allows to quickly access the position of the energy detector and sample. The required steering plate voltages are conveniently applied and adjusted by the control software, in which a cursor can be placed in the image at the respective position.

To measure the beam energy, the retarding grid in the detector is ramped, causing the beam current measured behind the grid to drop when the potential wall created becomes larger than the kinetic energy of the particles. Figure 1.6 c) shows such a measurement in the upper panel. The negative first deviate of the curve (lower panel) directly gives the distribution of the kinetic energy, in that case (27.3 ± 1.9) eV per charge. The fact that a Gaussian shape is observed shows that the ion beam was thoroughly thermalized in the high pressure rf-ion optics. The mean value moreover serves as a reference for adjusting the sample bias to define the collision energy.

UHV Sample Preparation and In-situ Characterization

Samples for deposition in UHV were prepared in-situ in a preparation chamber by subsequent sputtering with 1 kV Argon ions and annealing. Before the samples are used their cleanliness was verified by an STM imaging.

The single crystals used in this work purchased from MaTeck GmbH (Jülich, Germany) and listed in Tab. 1.2. The surfaces are prepared by three repeating cycles of Ar^+ sputtering at 1 kV (15 - 30 min) followed by annealing for 5 - 15 min at the corresponding temperature for different metals. This results in a clean surface with extended terraces. Typically a current of approximately 1.8-2.4 A is passed through the filament of the ion gun (PSP vacuum technology Ltd.) resulting in a gas discharge from which a sputtering current of 12-18 μA is extracted. This current impinges on sample surfaces with the area of about 20 mm^2. Annealing is done by electron beam heaters of the samples integrated in the samples. This design provides a very local heating, leading to a fast sample cleaning process. In this technique, electric current in the range of 2.0-2.5 A is passed through a filament beneath the sample causing thermionic electron emission. A high voltage (400 - 700 V) is applied between the filament and the sample accelerating the electrons to the backside of the sample, where the kinetic energy is converted into heat, which adds to the ohmic heat of the filament.

After the final annealing step the sample is checked with STM at RT. When it is ensured that the surface is clean and atomically flat, the sample can be transferred into the deposition chamber for ES-IBD.

Crystal	Lattice	Annealing Temp.	special Prop.
Ag(111)	hexagonal	800K	inert
Au(111)	hexagonal	900K	inert + elbow sites
Cu(111)	hexagonal	930K	-
Cu(100)	cubic	800K	adatoms
Cu(110)	tetragon.	850K	graves, template

Tab. 1.2 Table of used metal crystals with annealing temperature and properties.

Deposition

Once the deposition energy is set by applying the sample bias, the molecular ion beam is directed onto the sample surface and a deposition current is measured. In Figure 1.6 d) a net current of 1.2 nA is detected on the cover plate of which approximately 0.9 nA can be directed to the sample. After a few initial adjustments the deposition current is stable throughout the whole deposition. After few min-

utes the beam is interrupted by closing the valve before the 4th pumping stage, to verify the current measurement is free of artifacts. This is done several times during the experiment. This is usually more important for depositions of longer duration, where drifting voltages or an unstable spray could lead to an ill defined ion beam. In the presented case the deposition lasted 14 minutes, which relates to a deposited charge of 210 pAh or 0.75 μC. At a deposition area of 12 mm^2 this corresponds to a coverage of 4×10^{13} cm^{-2}, for the cytochrome c molecules used here this is approximately a monolayer for the charge state z = 14.

Since all quantities are known before the deposition, the desired coverage can be defined and a corresponding deposition charge predetermined. For that, the size of the molecule but also its charge state must be considered. It is then possible to freely and quantitatively control the coverage without the need of a calibration of the source. A computer based integration of the current allows for precise determination of the deposited charge even when the current fluctuates during the deposition, which is for instance the case when the deposition spot is randomly moved around to guarantee a homogeneous coverage.

Considering the absolute material amount, the overall deposition rate of ES-IBD is rather small. However, the efficiency of the method is extremely high if the initial amount of material in solution is taken as reference. A nano-ESI emitter operated at low flow rate can convert the major fraction of solvated molecules into molecular gas phase ions.[81] The ESI source with the hydrodynamically optimized funnel interface[99] can transmit up to 100 % of the generated ion current into vacuum. Finally, the ion optics in the following vacuum stages have transmittances in the range of $50 - 100$ %. These values agree with the experimental observation of currents of up to 6 nA on a sample holder in high vacuum, which correspond to an overall transmission of 20 % from solution to surface.

Post Deposition Mass Spectrometry

ES-IBD is characterized by hyperthermal deposition energies in the range above 2 eV per charge. This collision energy is in the same range as the covalent bonds, that hold the molecules together. While some measurement by us and other groups show that molecules and cluster survive energetic collisions up to an energy of roughly 1 eV per atom,[10,12,106,107] the intact deposition cannot be simply inferred, but rather should be confirmed, at least in cases where the morphology of the adsorbates after deposition gives reason to assume otherwise.

A chemical post-deposition characterization is preferably done via mass spectrometry, which allows a direct comparison of the desorption mass spectrum after deposition with the TOF-MS of the ion beam before deposition. Figure 1.8 shows

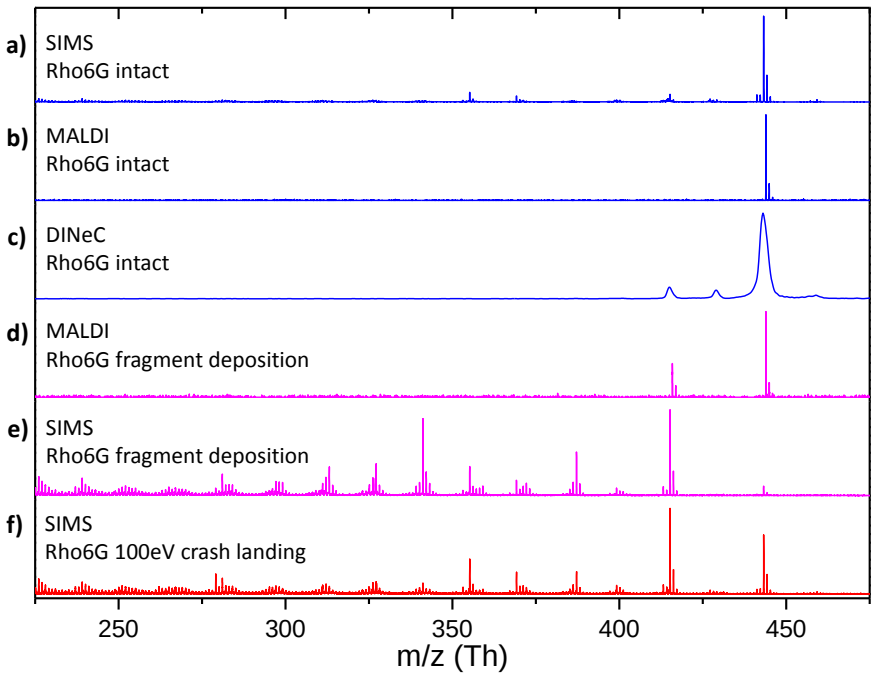

Fig. 1.8 Soft-landing and fragmentation depending on the deposition energy assessed by SIMS, MALDI and DINeC. All three techniques show intact Rho6G molecules after soft-landing, while after deposition of fragments and crash landing, fragments are detected.

examples of mass spectra of surfaces on which rhodamine 6G had been deposited under different circumstances, acquired by desorption mass spectrometry, specifically secondary ion mass spectrometry (SIMS, *TOF-SIMS 5, IonTOF* Muenster), matrix-assisted laser desorption ionization (MALDI, *Bruker Relfex IV*) and desorption ionization induced by neutral SO_2-cluster impact (DINeC).[108]

The top three panels show that the intact rhodamine 6G ion is almost exclusively detected after the deposition of intact molecules at low energy. All of the methods are thus equally suitable to desorb the intact molecules after landing. They are sensitive enough to detect even diluted amounts and further do not create a major amount of fragments.

When fragments or fragment containing ion beams are deposited (Fig. 1.8 d, e), the desorption mass spectra precisely represent the mass spectrum of the deposited ion beam. Here shown for examples of MALDI and SIMS with two differently fragmented ion beams. Finally, the fragmentation of the ions by high energy impact is detected as well in the desorption mass spectrum, here illustrated by a SIMS mass spectrum in Fig. 1.8 f).

In principle, all methods shown, are capable of determining the outcome of a

deposition experiment. DINeC however, is the most suitable method, because it neither needs sample preparation by an additional matrix molecule like MALDI, nor does it damage the surface like the impact of the Gallium ion beam in SIMS and could thus even be used on very valuable single crystalline metal samples.

1.4 Summary and Conclusion

In summary, ES-IBD enables full control of the deposition of non-volatile molecules in vacuum. It is in most cases the charged nature of the particles, which allows to control almost all aspects of the deposition in ES-IBD by electric fields. This high level of control comes at the price of a large effort, that has to be made. Nevertheless, it is justified, as ES-IBD is the only method available for controlled preparation of atomically defined surfaces in UHV with non-volatile molecules.

The major drawback of this source is still the low intensity and the fact that the source cannot simply scaled up. This hinders applications outside of academic research. However, our newly developed highly efficient hydrodynamic ion source shows that an intense ESI source is possible. After all ESI generates μA in air of which only 50 nA can be transferred into vacuum. At the level of control as shown here, a current of μA in vacuum would mean immediately a technological relevance.

In the following chapters, the capabilities of ES-IBD and the properties of the deposited layers and single molecules is demonstrated by means of various deposition parameters and molecules.

2 Cluster of Non-Volatile Molecules in Electrospray Ion Beams

Small objects, consisting of a small number of atoms or molecules are called clusters and nanoparticles. They play an important role in nanotechnology due to their special physical and chemical properties that arise from their high surface to volume ratio.[109,110] Clusters composed of several atoms or molecules have properties, strongly dependent on the exact number of constituents. The larger nanoparticle is defined as a nanometer-sized aggregate. The addition or removal of a few atoms or molecules alters neither its properties nor the size and the shape significantly.

To harness the properties of clusters and nanoparticles for applications, they must be integrated in meso- and macroscopic systems like surface coatings or thin films. While ambient processing from solution is often easy, gas phase or vacuum processes typically offer a higher level of control and cleanliness, for that a vacuum compatible gas phase particle source is required. Small gas phase clusters can be generated by condensation of vapor, expanding into vacuum.[111] These sources are one possibility to deposit clusters to surfaces.[106,107,110,112,113] However, they do not represent a general method as many possible constituents are not volatile and the cluster size is typically small. Moreover, nanoparticles that are synthesized in solution can be highly complex in chemical composition and shape.[114] Such nanoparticles offer additional functionalities, but cannot be fabricated by a gas-phase source.

In this part the capabilities of electrospray ionization (ESI) as a gas phase particle source are explored in order to integrate nonvolatile clusters and nanoparticles into vacuum processing via electrospray ion beam deposition (ES-IBD)[11,115–119] and it is shown how to control the composition and material flux. Two distinct approaches are possible: First, the generation of nanoparticle gas phase ions by electrospraying solutions or dispersions containing nanoparticles, and second, the creation of nanoparticles or clusters in the electrospray from a solution containing their constituents or precursors molecules.

Some few examples demonstrated that it is possible to ionize and deposit nanoparticles[118,120] from solutions or dispersions; also the deposition of whole viruses was shown.[70] More recently, small ligand capped gold clusters from a solution have been mass selected and soft landed in a very controlled manner.[76]

The alternative approach, the generation of charged gas phase clusters in electrospray ionization from their constituents is well documented.[121] Their components can be strongly interacting substances such as simple salts,[122] or functional macromolecules like proteins.[98] Even big micellar structures, capable of encapsulating other large molecules, were evidenced by mass spectrometry and indicates that also large nanoparticles may be created.[123] Recent deposition experiments with organic salt clusters in our laboratory showed the possibility to grow crystalline thin films from cluster ion beams.[124]

For both approaches however, it is unclear how to achieve control over the most important parameters of the deposition process, which are the distribution of size and charge state of the gas phase particles and the overall flux of material. This, foremost, requires access to the amount and distribution of material and charge in the cluster beam. With our experimental setup it is possible to determine the relation of material and charge by two independent approaches: first, in-situ time-of-flight mass spectrometry (TOF-MS) capable of detecting the distribution of cluster ions, while second, a combination of electrospray ion beam deposition and atomic force microscopy (AFM) gives quantitative access to the net deposited charge and the net amount and spatial distribution of deposited material. The first method requires an in depth analysis of the mass spectra, for the second method the morphology of the structures created by the ion beam deposition are analyzed in order to quantify the material amount.

In this study, the charged clusters of the organic salts Sodium Dodecyl Sulfate (SDS) and Sodium Citrate (SoCit) formed in an electrospray are used to demonstrate the controlled deposition of clusters and nanoparticles by ES-IBD. Moreover, SDS and SoCit are known to encapsulate and stabilize nanoparticles: SDS, for instance, is used to disperse carbon nanotubes (CNT) and SoCit to stabilize gold nanoparticles in solution.

It is found that organic salts generate clusters ranging from the smallest possible charged aggregate to nanoparticles of hundreds of molecules. Both, mass spectrometry and deposition experiments on graphite (HOPG) show that the small, low charge state ions contribute the main fraction of the charge in the beam, while heavy, high charge state ions contribute the major amount of material. As a consequence it was possible to perform well controlled depositions at high flux, achieving thin films and nanostructured island growth at the surface. Moreover,

this implies the general possibility of fabricating nanoparticle coatings by ES-IBD at a similar level of control as for molecular ions, provided that stable particles are created in the electrospray or ionized from a solution.

Unfortunately, the attempt of embedding of nanoparticles with detergents like SDS or SoCit as well as the deposition of nanoparticles from detergent-free solutions was not successful or reproducible, respectively. However, once for the nanoparticles a better understanding of the ion generation is reached, they can be handled, characterized and deposited like the ion beams that are subject of this chapter.

Methods

For mass spectrometry and deposition our ES-IBD source is used.[11,12] SDS (Sigma-Aldrich, 436143) and SoCit (Sigma-Aldrich, 71635) were dissolved in water and water/ methanol mixtures. From these solutions, gas phase ions are created by pneumatically assisted electrospray ionization at a flow rate of 16.7 μl/min. The ions are transferred into vacuum and guided through four differentially pumped stages to reach a pressure below 10^{-8} mbar at the time-of-flight mass spectrometer and sample position. On the samples ion currents of 20 - 250 pA were reached and decelerated to a kinetic energy of 2 - 5 eV per charge before deposition. The coverage is monitored via a current measurement at the sample position using electrometers (*Keithley* 616). The HOPG substrates were cleaved at ambient conditions before transferring into vacuum for deposition. AFM was acquired at ambient conditions in tapping mode directly after deposition. The images were analyzed with the WSXM software.[125]

2.1 Organic Salt Cluster Formation

Cluster ion beams of positively charged SDS and negatively charged SoCit are generated by pneumatically assisted ESI from solution and are analyzed by time-of-flight mass spectrometry to identify the clusters and study the fragmentation behavior. Typical mass spectra are shown in Fig. 2.1 (a) and (b).

The mass spectra of SDS (Fig. 2.1 a) show several series of peaks, which can be identified as SDS cluster ions. In the most pronounced series with the largest periodicity, peaks are separated by 288 Th, the mass of the SDS molecule. These peaks thus correspond to singly charged clusters of the type $Na^+(SDS)_n$, where n is the number of SDS molecules. In-between the single charged cluster peaks, additional series of lower periodicity can be observed. They are characteristic for multiply charged clusters ($z > 1$) and thus separated by fractions of 288 Th, *i.e.*

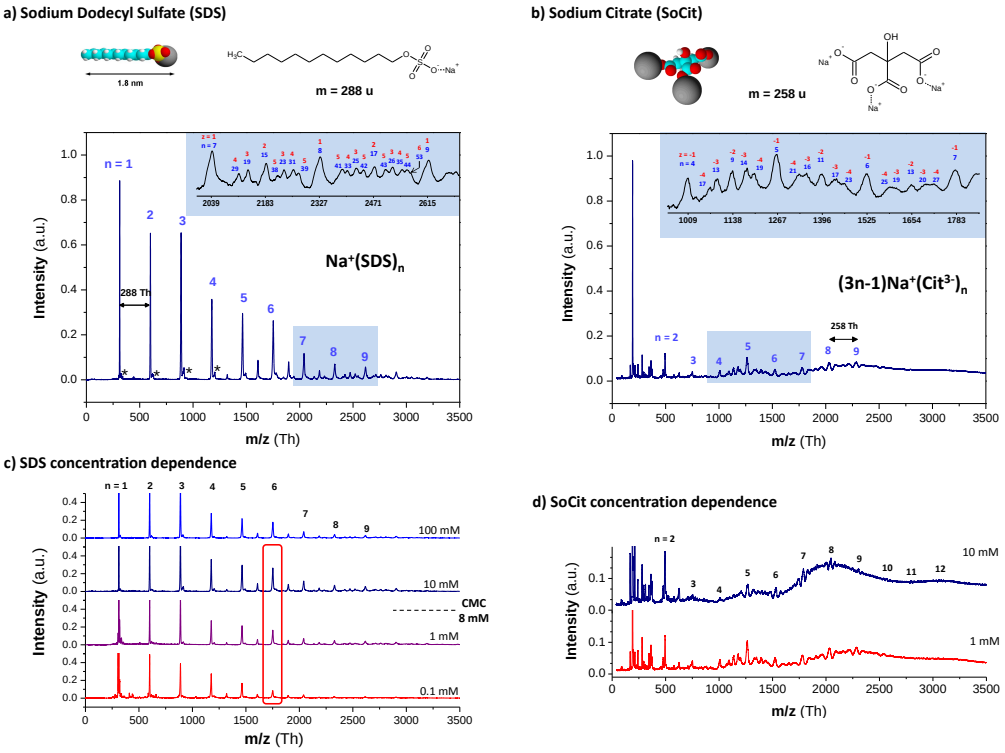

Fig. 2.1 ESI-TOF mass spectra of SDS **(a)** and SoCit **(b)**. In both spectra the single charged clusters are distinctive but the zoom-in shows that higher charged and larger clusters are also present. The spectra below show mass spectra of SDS **(c)** and SoCit **(d)** at different concentration. With higher concentration the intensity of larger cluster peaks increases.

144 Th for $z = 2$, 96 Th for $z = 3$ *etc.* The largest identified cluster consists of 53 molecules with a charge state $z = 6$. Furthermore, a small contamination of potassium is detected in the SDS solution, visible as peaks shifted by 16 Th (some are indicated by "*" in Fig. 2.1 a), which is the m/z difference of one Na^+ ion replaced by one K^+ ion in the single charged SDS cluster. Overall, the high purity of the cluster ion beam especially by the absence of solvent is verified, which is important for its application in deposition.

Similar observations can be made in the mass spectra of SoCit in Fig. 2.1(b) where the majority of peaks corresponds to cluster ions as well. The main periodic peak series is separated by 258 Th, relating to a single neutral SoCit molecule ($3Na^+$ Cit^{3-}). The peaks in the range $190 - 450$ Th correspond to the singly charged citrate molecules and to contaminants. Like in the case of SDS, peaks of higher charged, larger clusters appear in between the singly charged cluster peaks.

One parameter which can affect the cluster formation is the concentration of

the solution.[117] The influence of the concentration on the cluster size is studied by varying the solution concentration of SDS (0.1−100 mM) and of SoCit (1−10 mM) for a constant declustering potential for which fragmentation is negligible.

Increasing the concentration results in a higher relative intensity of peaks in the mass spectra of both substances at higher m/z values, while the spectra remain similar (Fig. 2.1 c and d). In the case of the amphiphilic SDS the increase of the concentration above the critical micelle concentration (CMC) of $c_{cmc} = 8.3$ mM,[126] where micelles have formed in solution, has only a minor effect on the mass spectra. Small changes are observable for instance in the intensity of low molecular weight clusters like $n = 6$, $z = 1$, which increases with concentration for $c \leq c_{cmc}$ (see Fig. 2.1 c, red box). In this concentration regime ($c \leq c_{cmc}$), clustering of SDS solute molecules is enhanced with increasing concentration due a decreasing mean intermolecular distance in the homogeneous solution. Above c_{cmc} the contribution of the low molecular weight clusters decreases and a very broad unresolved region at $m/z > 3500$ Th is seen when the mass spectra in Fig. 2.1 c) is plotted on the logarithmic intensity scale (Appendix A, Fig. A1). This intensity is consistent with heterogeneous and large SDS aggregates whose portion increases upon rising the concentration.

In water, the SDS molecules form micelles above the critical micelle concentration and can form aggregates with approximately 50 SDS molecules (14400 u).[127] The SDS molecules are aligned with their charged head groups facing towards the water, creating a water free environment inside the micelle (Fig. 2.2 a). Transferred into the gas phase these regular micelles are expected to rapidly invert into reverse micelles (Fig. 2.2 b, c). This happens because of the water evaporation

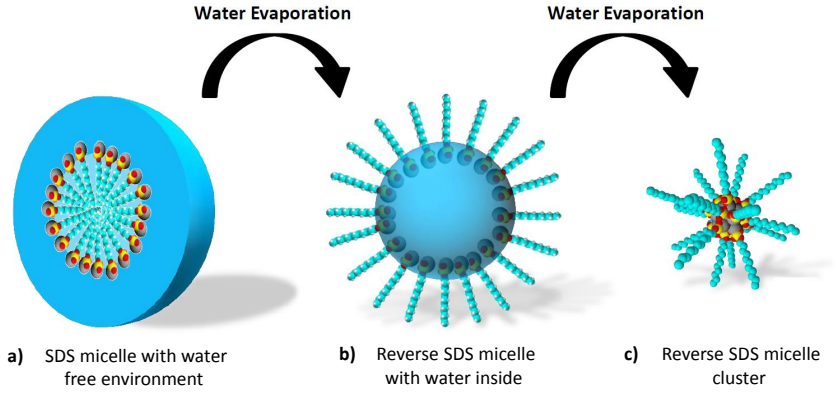

Fig. 2.2 Schematic illustration of the SDS micelle evolution from solution into vacuum. **(a)** In water the molecules form regular micelles above CMC. **(b)** transferred into the gas phase the micelle inverts. **(c)** With further water evaporation the a reverse micelle cluster is formed.

during the ESI process, shown in recent computer simulation studies on cetyltrimethylammonium bromide micelles[128] and dodecyl phosphocholine micelles.[129] In reverse micelles the charged head groups are oriented towards the core, while the alkyl tails point outwards. Alternatively, micelles may be transferred into the gas phase as a whole encapsulating water.[123] However, the mass spectra in Fig. 2.1 show only peaks for SDS without any encapsulated water so that the reverse micelle configuration can be assumed for the SDS cluster ion beams.

Furthermore, it is observed that the intensity of the singly charged SDS cluster peaks below 3500 Th decreases exponentially as the cluster size increases. This behavior is indicated by a straight line in the logarithmic plot of the mass spectra in Fig. 2.3(a). This feature shows that the cluster formation follows a so-called most probable size distribution mechanism.[130] In this case, the energy associated with the attachment of one SDS molecule to an agglomerate, does not depend on its size, which is in contrast to magic number clusters.[131]

The other applied molcule SoCit is of non-amphiphilic nature and thus does not promote the formation of micelles in solution or in vacuum. The exact shape of the clusters is therefore expected to be that of a small crystallite, strongly disturbed by excess charge and by the large surface-to-volume ratio. Similar to SDS, increasing the concentration of the SoCit solutions causes a slight shift of the relative intensity towards higher m/z values, indicative of increasing cluster size.

2.2 Declustering of Organic Salt Cluster

Fragmentation of molecules and aggregates is an inherent feature of mass spectrometry and just as effective on the final content of the cluster beam as the parameters of the ion formation like concentration or the contents of the solution. In the setup fragmentation is achieved by inducing collisions with the background gas in the first pumping stage at 0.1 mbar by adjusting the declustering potential V_{decl}, between nozzle and skimmer or nozzle and ion funnel. Upon increasing this potential, collisions become more intense and lead to fragmentation of the ionized clusters into smaller clusters, while the covalent bonds of the molecules constituting the cluster are not affected.

The influence of the declustering potential on SDS and SoCit clusters is shown in Fig. 2.3(a) for 10 mM SDS and in Fig. 2.3(b) for 1mM SoCit solutions. The mass spectra are plotted on a logarithmic intensity scale in order to emphasize the intensity above 3500 Th, which would not be visible if the spectra were scaled linearly and display the full intensity range.

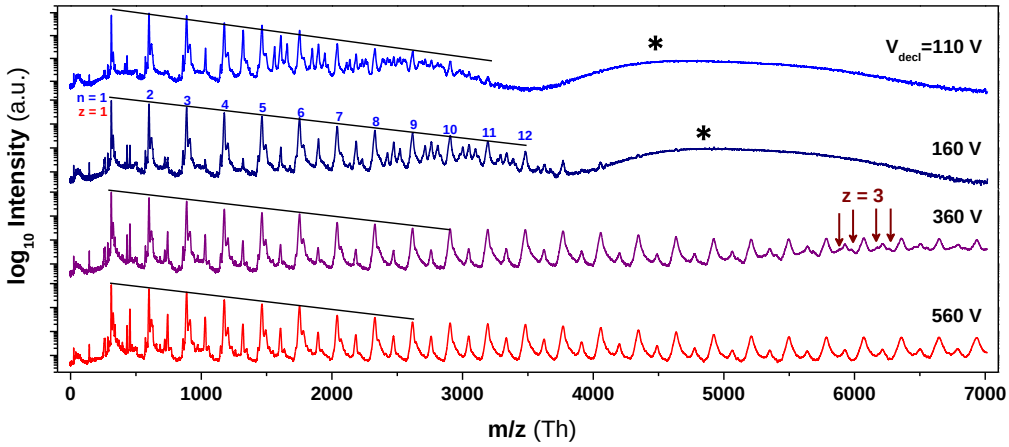

(a) SDS mass spectra for different declustering voltages.

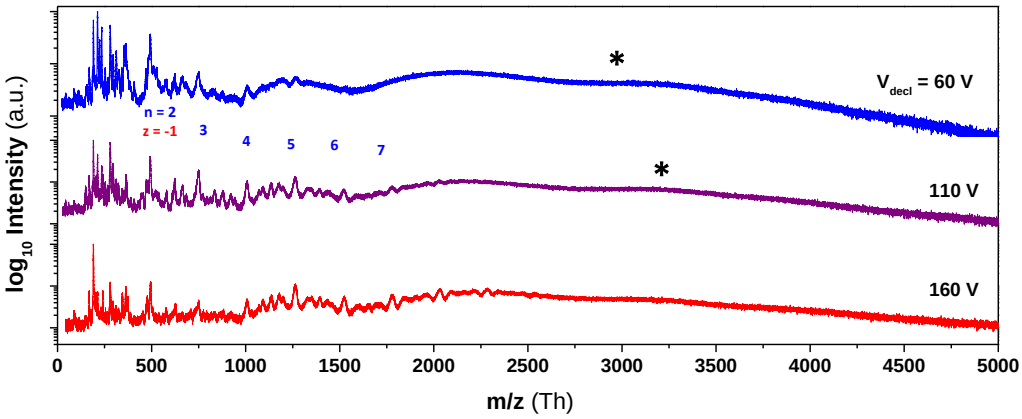

(b) SoCit mass spectra for different declustering voltages.

Fig. 2.3 **(a)** Mass spectra of positively charged SDS from a 10 mM solution at several declustering potentials V_{decl} (intensity in log-scale). Red arrows in the mass spectrum for $V_{\mathrm{decl}} = 360\,\mathrm{V}$ indicate some triple charged clusters in the high m/z-range. The straight lines illustrate the exponentially decreasing height of the single charged small cluster peaks. **(b)** Similar mass spectra of negativly charged SoCit from 1 mM solution at several declustering potentials V_{decl}. The "*" in both spectra marks unresolved regions in which highly charged clusters might be buried and thus are not resolved with our mass spectrometer.

For both SDS and SoCit the mass spectra show the most intense peaks below 3500 Th or 1500 Th, respectively. Many closely spaced peaks corresponding to high-charge-state clusters are observed in the SDS spectra for m/z values ranging from $1500-3500$ Th. In the SoCit spectra mainly single charged peaks are seen for low declustering potentials. Additionally a broad feature of low intensity without

resolved peaks can be seen in the high m/z – range between 3500 Th and 7000 Th for SDS and beyond 1500 Th for SoCit (marked with * in Fig. 2.3).

Upon increasing the declustering potential, the broad feature shifts towards higher m/z-values and eventually the series of singly charged peaks is seen in the mass spectra of both SDS and SoCit. In addition, at high m/z values, doubly and triply charged SDS clusters of low intensity can be distinguished (indicated by red arrows in Fig. 2.3(a)).

Hence, the evolution of the mass spectra as a function of the declustering voltage can be explained by big clusters ($n > 50$) of high charge state ($z > 6$). Due to the limited resolution of the instrument, the dense distribution of peaks cannot be resolved at low declustering potential. Upon increasing the potential, these clusters are fragmented into smaller clusters of lower charge state, which now may appear in the mass spectra at higher or lower m/z values around the original cluster peak. The relative abundance of the high charge state clusters is reduced since fission is more probable for high charge states as those clusters gain more energy in the electric field between subsequent collision events. Ultimately the material in the cluster beam becomes distributed into singly charged clusters as the declustering potential increases (see Fig. 2.3(a), $V_{decl} = 560V$).

The size of the clusters at the center of the unresolved feature in the SDS spectra at approx. 5000 Th corresponds to a single charged cluster with 17 molecules, or it can also be attributed to a cluster with roughly 85 molecules, if the highest observed charge state $z = 6$ is assumed. The integrated intensity of the mass spectra[a] shows that this region accounts for $j_{hi} = 9\%$ of the detected particles (Fig. 2.4). However, due to their size and depending on their charge state, the amount of material of this region can be significant and is not intuitively deduced from the mass spectra.

2.3 Material and Charge Distribution in the Mass Spectrum

Independent of charge state and size, each cluster is registered in the mass spectrometer as one count. To obtain quantitative information about the material to charge ratio of a cluster ion beam from mass spectrometry, the material and charge contribution of each individual peak must be considered separately. Because the peak series for the various charge states are partially overlapping in the mass spectra, the experimental data is fitted with a model function containing all charge states and cluster sizes. As a result the intensity of each cluster ion species is known, and the material and charge contribution can be calculated.

[a]Integrated counts, normalized to the bin width.

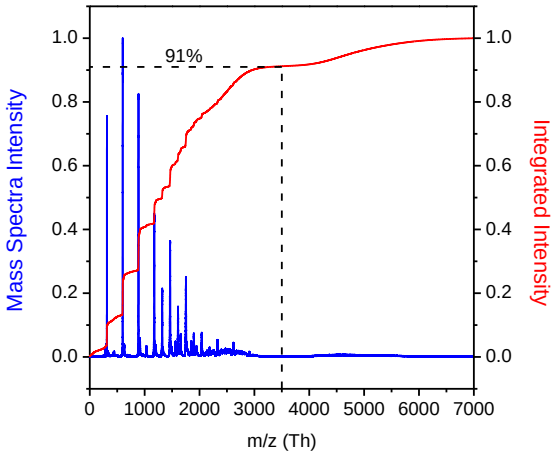

Fig. 2.4 Mass spectrum of SDS (blue) over the full m/z range containing resolved (0-3500 Th) and unresolved (3500-7000 Th) parts. The integrated mass spectrum (red curve) shows that 9% of the counts are related to the unresolved intensity.

The unresolved region of the mass spectrum has to be excluded from the fitting procedure, due to the fact that here well defined peaks are not present and thus the result would be arbitrary. Nevertheless, based on the detected intensity the results of the fitting of the resolved part can be extrapolated.

The mass spectrum is fitted in the range from 0 Th to 3500 Th with the intensity function $J(M)$, (Eqn. 2.1) with $M \equiv m/z$. This function generates mass spectra of SDS clusters of different charge states, size and intensity, by adding up all possible Gaussian peaks[b] $g(M, \frac{m_{n,z}}{z}, \frac{m_{n,z}}{zR})$ for each cluster characterized by number of molecules n and charge state z with $m_{n,z} = m_{\mathrm{Na}} \cdot z + m_{\mathrm{SDS}} \cdot n$. An envelope Gaussian distribution $J_z \cdot g(n, c_z, w_z)$ is multiplied serving as simple approximation for the intensity distribution of each charge state series.

$$J(M) = \sum_{z=1}^{z_{\max}} \sum_{n=1}^{n_{\max}} J_z \cdot g(n, c_z, w_z) \cdot g\left(M, \frac{m_{n,z}}{z}, \frac{m_{n,z}}{Rz}\right) \tag{2.1}$$

The parameters intensity J_z, the center position c_z and the width w_z are fitted for each charge state series $z = 1 \ldots z_{max}$. The difference in peak width is introduced in the model through a parameter $R \equiv m/\Delta m$, in which instrumental resolution and isotopic broadening are merged into one number that is fitted as well. To consider the low abundance peaks, the fit is performed using $\log J(M)$ as fitting function on logarithmically scaled data.

Figure 2.5 a) shows the measured mass spectrum of SDS in fair agreement with

[b] $g(x, x_0, \sigma) = \frac{1}{(\sigma\sqrt{2\pi})} \exp\left[-\frac{1}{2}(\frac{x-x_0}{\sigma})^2\right]$

the fitted spectrum for charge states $z = 1 \ldots 5$, which demonstrates the feasibility of the fitting procedure. Extracted from the fit, below the mass spectra of each charge state series are displayed individually. Summed up they yield the fitted spectrum, while the separated spectra allow to access the contribution of the different charge state to each peak. It becomes obvious that many of the heavier clusters are in fact mostly of a multiple charge state, as the intensity of $z = 1$ peaks becomes very low beyond 2100 Th.

The deviation between fit and data is owned to the relatively low abundance of high charge state peaks as well as to the simplicity of the model, in which the Gaussian envelopes are merely an estimation of the real distribution. Overall the fitted function is a good approximation of the real spectrum and allows to extract the contribution for each charge state independently to quantify its material and charge content. However, since the quality of the mass spectra does not merit a systematic study, only one typical SDS mass spectrum is discussed, nevertheless illustrating how material and charge are distributed. With mass spectra of better resolution and a refined model, a systematic study could yield further insights.

The result of the fit is summarized in Fig. 2.5 b) (see Appendix A.2 for more details). The relation between m/z-ratio and charge state of the clusters is shown in the left panel, where the center position the envelope c_z and width w_z is plotted. The m/z ratio of the clusters rises with increasing charge state z, while the width of the distribution stays roughly constant. The shaded area in the top right corner of that plot represents the resolution limit of our mass spectrometer ($R = 300$), illustrating that charge states larger than $z = 5$ can not be resolved beyond 3000 Th.

Since we know size and charge state of the clusters, the intensity parameter J_z can be used to calculate a more intuitive measures for the intensity (see Appendix A.2.2 for more details). In the right panel of Fig. 2.5 b) the relative amount of material $N(z)$ and charge $Q(z)$ are shown as function of charge state z. Stunningly, the singly charged clusters, which visually dominate the mass spectrum at linear scale, contain only 25 % of the beams material flux, compared to 45 % of the charge. In contrast, each of the higher charge states $z = 3 - 5$ contributes only $\approx 10\%$ of the charge but almost 20% of the material. Overall, the fitted mass spectrum up to 3500 Th with the resolvable charge states up to $z = 5$, has an average charge state of $\bar{z}_{lo} = 1.54$ and an average m/z ratio of $\langle M_{lo} \rangle = 1145$ Th, which corresponds to 4.0 molecules per charge in the cluster beam.

In summary, high charge states that are almost invisible in the mass spectrum contribute significantly less charge but a relatively large amount of material. This suggests that the unresolved region ($3500 - 7000$ Th), which represents only $j_{hi} =$

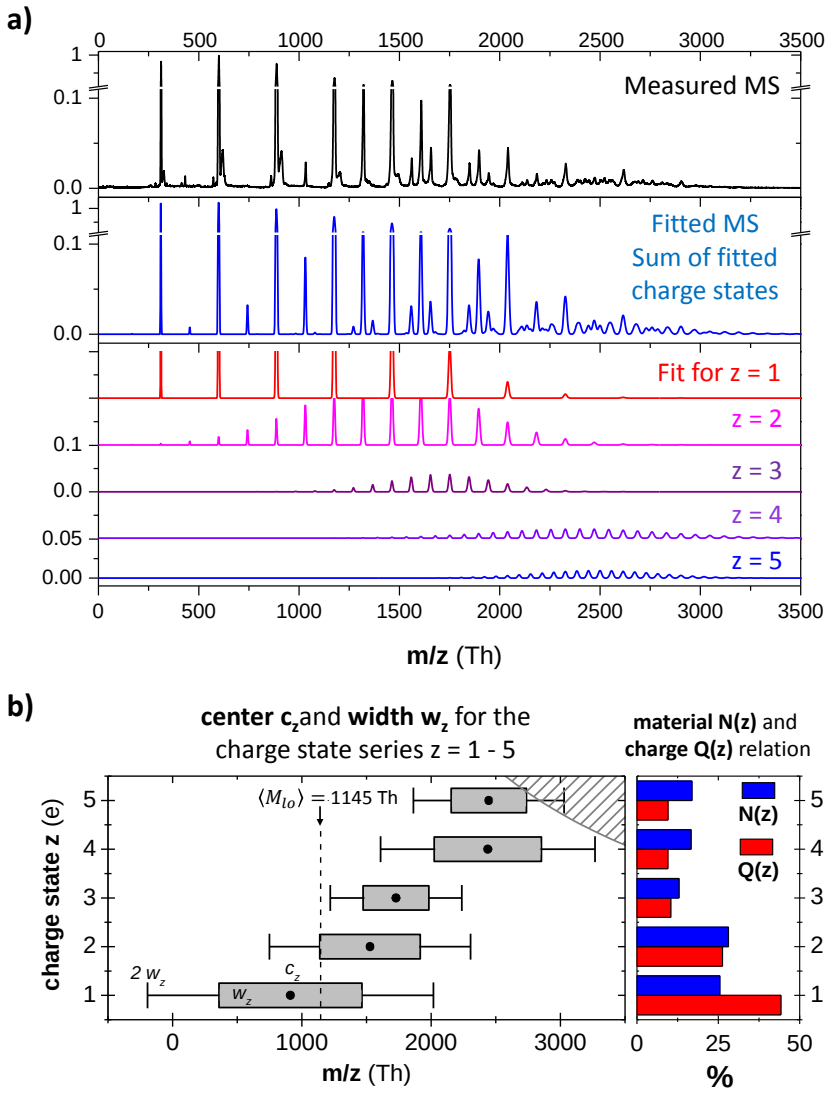

Fig. 2.5 **(a)** SDS mass spectrum (10 mM, $V_{\mathrm{decl}} = 110$ V) and best fit including charge states up to $z = 5$ (blue). Below, contributions of the charge states up to $z = 5$ shown individually. **(b)** m/z-width and center position of each charge state up to $z = 5$ as found from the fitting. The shaded area indicates the resolution limit of the mass spectrometer. The right panel show the relative material content $N(z)$ and the relative charge amount $Q(z)$ as a function of charge state.

9% of the mass spectrometric intensity, contains a significant amount of material but rather little charge, while still many ions have charge states higher than $z = 5$. This would strongly affect the average m/z-ratio of the overall cluster ion beam $\langle M_{tot} \rangle$. This value is estimated as the weighed average m/z-ratio of the resolved part at low m/z-ratio $\langle M_{lo} \rangle$ and of the unresolved part at high m/z-ratio $\langle M_{hi} \rangle$ of

the mass spectrum. The evaluation of $\langle M_{tot} \rangle$ further requires the average charge states $\bar{z}_{lo}, \bar{z}_{hi}$ and the relative intensities j_{lo} and j_{hi} (see Appendix A.2.3), which all can be measured except for $\bar{z}_{hi}$. Hence, the average m/z-ratio of the overall cluster ion beam $\langle M_{tot} \rangle$ is deduced as a function of $\bar{z}_{hi}$:

$$\langle M_{tot} \rangle (\bar{z}_{hi}) = \frac{\langle M_{lo} \rangle \cdot j_{lo} \cdot \bar{z}_{lo} + \langle M_{hi} \rangle \cdot j_{hi} \cdot \bar{z}_{hi}}{j_{lo} \cdot \bar{z}_{lo} + j_{hi} \cdot \bar{z}_{hi}} \tag{2.2}$$

In Fig. 2.6 a) this function is plotted for $\langle M_{lo} \rangle = 1145\,\mathrm{Th}$ and $\bar{z}_{lo} = 1.56$, taken from the fit of the resolved region, and $\langle M_{hi} \rangle = 5000\,\mathrm{Th}$ and $j_{hi} = 9\%$ measured from the mass spectrum (see Fig. 2.4). For the evaluation of Eqn. (2.2) the average charge states of the unresolved clusters $\bar{z}_{hi}$ were assumed to be in the range of $\bar{z}_{hi} = 1 \ldots 50$. This given range was chosen based on charge states known for large objects of comparable size like proteins.[11]

With increasing charge state $\bar{z}_{hi}$ the contribution of the unresolved part of the mass spectrum of 9% of the counts becomes more relevant and $\langle M_{tot} \rangle$ shifts significantly towards $\langle M_{hi} \rangle$. While for $\bar{z}_{hi} = 1$ the average m/z ratio is $\langle M_{tot} \rangle = 1375\,\mathrm{Th}$, it has doubled already for $\bar{z}_{hi} = 10$. Even if in the high m/z-region only background was detected, for which an intensity ratio of 1% is assumed, the average m/z-ratio $\langle M_{tot} \rangle$ doubles for high charge states.

The impact of the unresolved intensity of $j_{hi} = 9\%$ on the material transport is illustrated in Fig. 2.6 (b) showing the material fraction of high and low m/z-range as a function of the assumed charge state for the high m/z-range (solid line). For low charge states, the major share of material is carried by low m/z clusters. More likely, however, are moderate or high charge states for the heavy clusters. Already for $\bar{z}_{hi} = 3.7$, the material transport is equally divided between the low and the high m/z-range clusters. From here on the material transport fraction of the high m/z-range clusters increases to over 90% for $\bar{z}_{hi} = 50$. Supposing again an intensity fraction of $j_{hi} = 1\%$ (dashed line), which would represent the background noise, the increase is less pronounced, but still the point of equal material fraction is found for a reasonable number of charges per cluster at $\bar{z}_{hi} \approx 35$.

This analysis underlines the importance of the high m/z-region on the material transport in the ion beam. Providing that highly charged clusters are present in the ion beam, the material contribution of the unresolved region at high m/z-ranges can easily dominate, even at low relative intensities in mass spectrometry. The results from the fit show that we have to expect high charge states at the high m/z-region ($\bar{z}_{hi} > 5$), for which our estimate predicts an average m/z-ratio above 2000 Th and a material fraction of the high m/z-range of more than 60%. This discrepancy is nicely illustrated by considering the fact that a SDS cluster

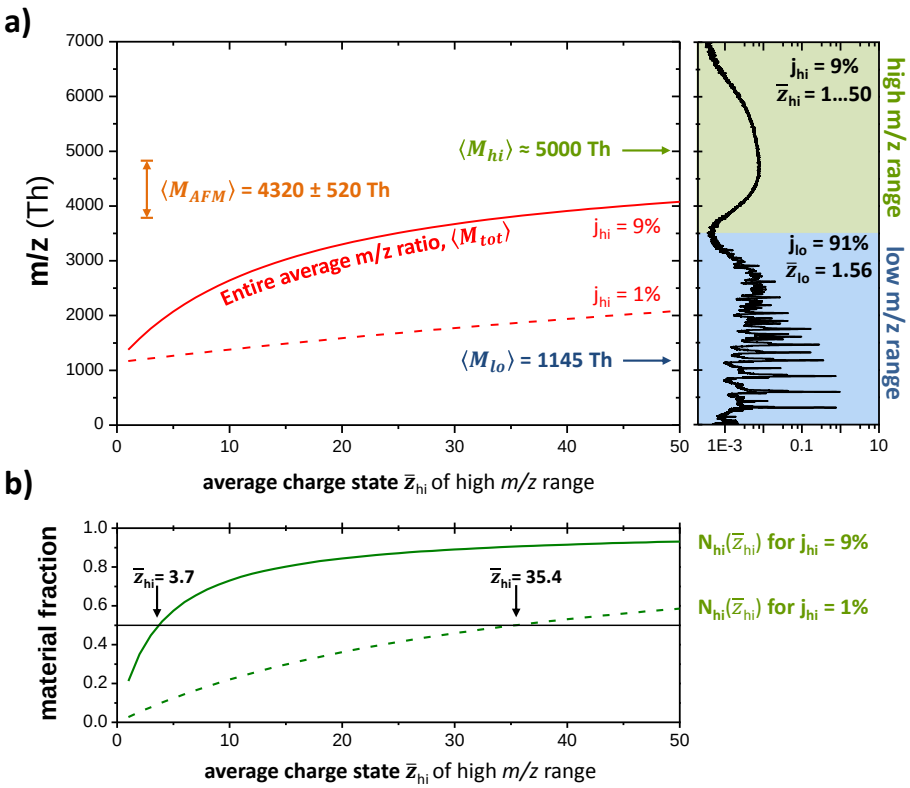

Fig. 2.6 **(a)** Average m/z ratio $\langle M_{tot} \rangle$ as a function of the average charge state $\bar{z}_{hi}$ in the high m/z-range for an intensity fraction of $j_{hi} = 9\%$ as found from the mass spectrum (solid line). For comparision $j_{hi} = 1\%$ is assumed (broken line), which would represent the integrated noise level of the MS. **(b)** The material fraction of the low and the high m/z range in dependence of $\bar{z}_{hi}$ for $j_{hi} = 9\%$ and 1%.

of charge state $z = 10$ at 5000 Th conveying approx. 85 molecules is detected as a single count in the MS, just as the single charged single $[SDS+Na]^+$ molecule.

Even though this analysis has only been done for the SDS data, it can be assumed that the mass spectra of other cluster beams like the one of SoCit can be interpreted similarly. The actual charge state distribution can, however, not be found with this method. Nevertheless, it is seen that low intensity clusters in the high-m/z range can contribute the major amount of material and thus have to be considered in cluster ion beam deposition processes. On the one hand, this can be utilized in order to enhance the material flux and to prepare high coverage samples. On the other hand contaminations that may form large highly charged clusters should be avoided by mass selection as they may not be observed in the mass spectrum but can nonetheless contribute a significant amount of material.

2.4 Statistical Analysis of the Deposited Material Amount

To test the assertion that the high m/z-region, which is almost not visible in the mass spectra, dominates the material transport, the average m/z-ratio $\langle M_{tot} \rangle$ can be measured through ion beam deposition experiments. The material amount is measured as the volume of the deposited material by AFM and the current integrated during deposition yields the net charge. This approach is entirely independent from mass spectrometry and additionally yields information about the structure of the deposited material from cluster beams at the surface. Thus it is the method of choice to validate the findings and to determine the average charge state of the high m/z-range $\bar{z}_{hi}$.

Deposition of the Molecules

Several samples of different coverage of both molecules were prepared by ES-IBD on highly oriented pyrolytic graphite (HOPG) substrates and characterized by AFM operated in tapping mode at several spots in ambient conditions. For all samples the delcustering potential was set to $V_{decl} = 110V$ for SDS and $V_{decl} = 60V$ for SoCit and the clusters were soft landed with 5 eV per charge. The deposited charge density was ranging from 120 pAh/cm^2 to 5000 pAh/cm^2. The rf-quadrupole ion guides are operated in rf-only mode so that there is a lower m/z cut-off but no upper transmission limit. In the case of SDS the lower m/z cut-off is below the first SDS cluster at 311 Th while for the SoCit the cut-off is set at 500 Th excluding the singly charged SoCit variations and possible contaminations.

On the surface the original SDS clusters are mobile and merge into larger flat aggregates, which upon increasing the coverage are stacked on top of each other (Fig. 2.7 a-d). AFM images show that these islands have a height of 3.8 nm each, which is attributed to a double layer formation of the SDS molecule having a length of 1.9 nm.[132,133] Due to the missing hydrophilic-hydrophobic interaction in vacuum, the ionic-polar interaction dominates the growth so that the molecules are arranged in an inverse membrane configuration.

Furthermore, the islands reveal a preferential growth direction at low coverage. According to the hexagonal lattice of the graphite surface, the molecules form islands with characteristic angles of 120° between them (Fig. 2.7 e). This indicates that the islands are crystalline. In order to confirm the crystallinity and molecular structure of the films, X-ray powder diffraction (XRPD) measurements were performed on SDS layers on graphite after the deposition of approximately 3600 pAh/cm^2, which corresponds to a coverage of 1.3 monolayers.[124]

In the diffraction pattern in Fig. 2.7 f), two types of Bragg reflections were

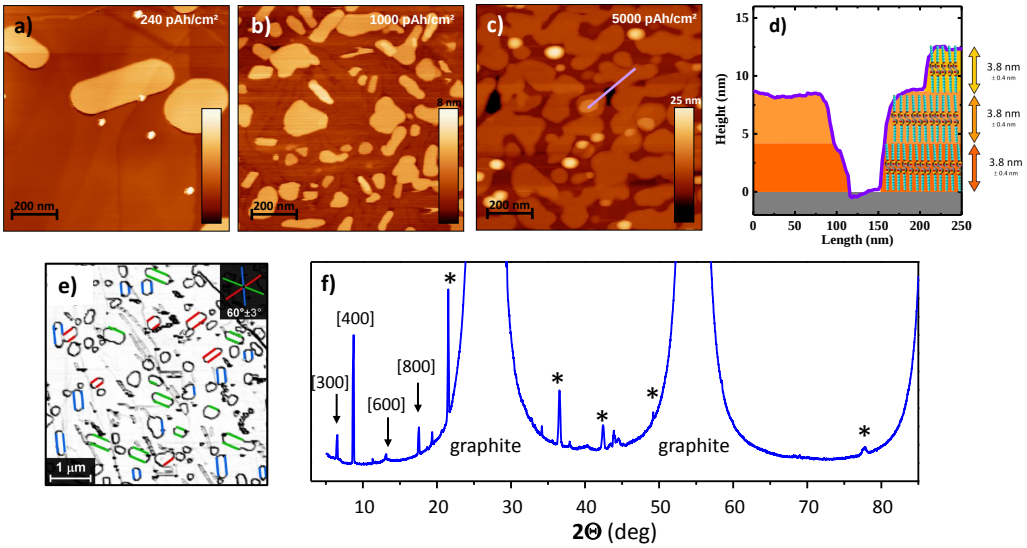

Fig. 2.7 AFM images and representative height profiles of SDS **(a - d)** shows 2D growth with several inverse double layers. **(e)** Edge filtered overview AFM-image show that the long parallel edges of the islands follow three preferential growth directions; highlighted by green, red and blue. **(f)** X-ray powder diffraction of 1.3 monolayer SDS on graphite. Reflexes of the SDS layers are visible on top of an intense signal from the graphite substrate. Most SDS peaks correspond to scattering from [h00] planes, while some reflexes contain contributions from the a- and b-axes (indicated by *).

identified: intense peaks belonging to the graphite substrate and a set of reflexes, five orders of magnitude smaller. Assuming a mixture of 90% 2H and 10% 3R graphite, the intense reflections could be satisfactorily fitted by whole powder pattern fitting (WPPF, see Appendix A.3 for details). The Bragg peaks of low intensity mostly belong to (h00) reflections, while mixed indices occur only at higher diffraction angle (marked with * in Fig. 2.7 e). Two different SDS phases with slightly different lattice parameters were identified, both showing the characteristic long a-axis of approximately 4 nm, with 0.47 nm and 0.83 nm for b- and c-axes of a nearly orthorhombic unit cell. These values are similar to the literature values on anhydrous SDS crystals grown from solution ($a = 3.91$ nm, $b = 0.47$ nm, $a = 0.82$ nm),[132,133] and are in agreement with the data obtained from the AFM measurements (3.8 nm height), confirming the crystallinity of the fabricated SDS films on graphite and their membrane-like molecular structure.[134]

In contrast, SoCit forms three dimensional aggregates (Fig. 2.8). At low coverage small round islands are found at the step edges of the graphite (Fig. 2.8 a). A further increase of the coverage, leads to more islands distributed around the

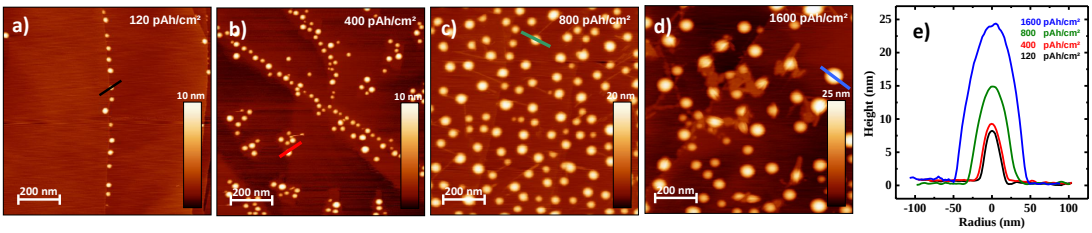

Fig. 2.8 AFM images and representative height profiles of SoCit **(a - e)** on HOPG with increasing coverage shows 3D islands which grow in size.

step edges and patches of several islands on the terraces (Fig. 2.8 b) until finally the islands are distributed homogeneously across the surface (Fig. 2.8 c). Upon doubling the coverage very large and inhomogeneously distributed islands are observed where some of them are connected by flat rods (Fig. 2.8 d). This growth sequence shows clearly that at higher coverage, islands grow at the expense of smaller ones. The flat rods at higher coverage might indicate the formation of a second crystalline phase.

In both cases upon landing the gas phase clusters dissolve and rearrange on the surface. This mobility implies the possibility to use cluster ion beams for high flux crystalline growth from molecular ion beams, as shown for SDS,[124] but unfortunately hinders us to determine the size of the individual cluster after deposition. Nevertheless, the number of deposited molecules can be estimated, and, in combination with the deposited charge, an average cluster size in molecules per charge can be deduced.

Detection of the Material Amount

The amount of deposited material was determined from AFM images of prepared samples. The topographical information of these images enables the measurement the area or the volume of the material found at the surface after flattening and subsequent flooding of the images with the WSXM software.[125] The resulting flooded area and volume of the AFM image can then be correlated to the amount of molecules (Fig. 2.9).

The quantity of deposited SDS molecules is approximated by measuring the area coverage of the double layer and relating it to the molecular footprint. This is estimated by using the anhydrous SDS crystal structure, with an average area per polar head group of 19.3 Å^2 and a lamellar thickness of 1.9 nm.[132,133] Since the layers show a thickness of around 3.8 nm, it can be assumed that they consist of double layers.[124] Thus, the number of molecules can be determine for a certain

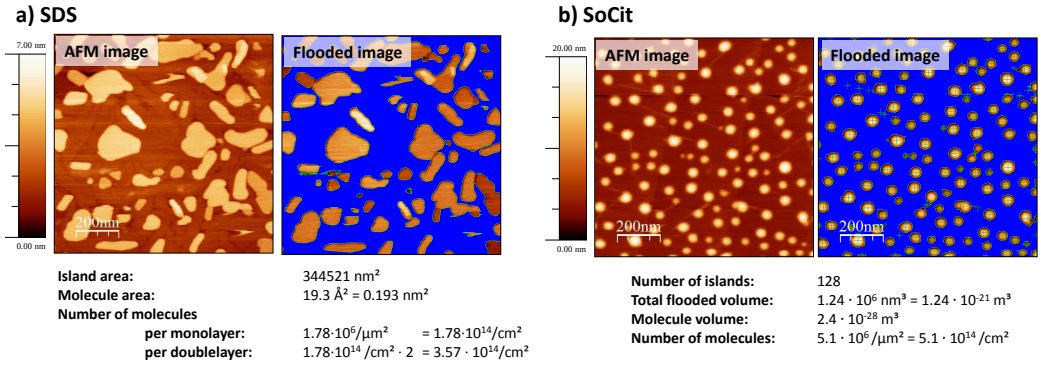

Fig. 2.9 AFM images of SDS **(a)** and SoCit **(b)**. Flooding the image with WSXM yields the total flooded volume and area from which the number of deposited molecule can be calculated.

AFM image by doubling the result of the division of the island area with the molecule area (Fig. 2.9 a).

In the case of the SoCit the volumes of the islands are evaluated. For the approximation of the amount of SoCit molecules a density of $1.8 \cdot 10^6\, g/m^3$ [135] and a molecular weight of 258 g/mol for sodium citrate, yields a molecular volume of $2.4 \cdot 10^{-28} m^3$. The number of molecules of a particular AFM image is given by the division of the flooded volume with the molecular volume (Fig. 2.9 b). For the calculation a homogeneous coverage across the whole sample with an area of 12.5 mm^2 can be assumed, which is confirmed by the AFM measurements at different spots of the sample as well as by previous studies of ion beam deposition of molecules.[12,136]

The analysis of many experiments yields a relation between the amount of deposited molecules and the deposited charge, depicted in Fig. 2.10 (a) and (b). For both molecules, the material amount increases with the deposited charge. Assuming a linear relationship, the slope of the curves corresponds to the average amount of molecules per charge, which is 15 ± 2 for SDS and 15 ± 10 for SoCit equating to an average m/z ratio of about $\langle M_{AFM}^{SDS} \rangle = 4320 \pm 580$ Th and $\langle M_{AFM}^{SoCit} \rangle = 3850 \pm 2500$ Th, respectively. A large variance of the data is seen, especially for the SoCit data. The errors can be explained by the inherently inaccurate measurement of the island volumes from the AFM images caused by finding an appropriate base plane. By comparison, the determination of the amount of deposited SDS molecules proceeds through an area measurement, which is more precise.

Comparing the estimate for the average m/z ratio $\langle M_{tot} \rangle$ to the measured $\langle M_{AFM}^{SDS} \rangle$ of about (4320 ± 580)Th, it is seen that for values of $\bar{z}_{hi} = 30 \ldots 50$,

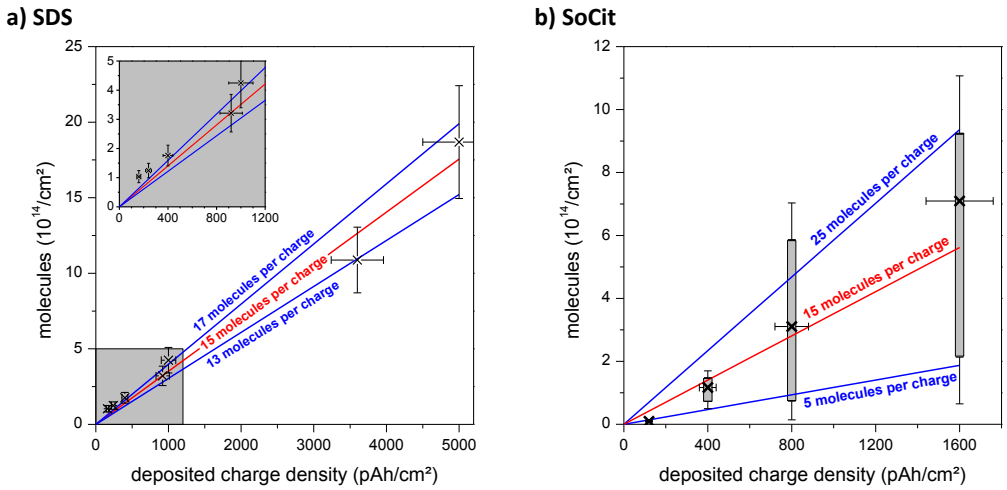

Fig. 2.10 Deposited SDS **(a)** and SoCit **(b)** molecules, calculated from AFM images, plotted against the deposited charge density. From the slope of the graphs the average cluster size in the gas phase is given.

$\langle M_{tot} \rangle$ is located in the error margin of $\langle M_{AFM}^{SDS} \rangle$ (see Fig. 2.6 a). Thus, it can be concluded that clusters with 30, 50 or even more charges are present in the upper end of the distribution. Conversely this means, that at this charge state and for an average cluster size of 15 molecules per charge, several hundred molecules compose one cluster, which then is an object with a diameter in the nanometer range and could thus be considered as a nanoparticle. Comparing this data, one has to consider that the mass spectra represent a single measurement of an ion beam, while $\langle M_{AFM}^{SDS} \rangle$ is an average value over several experiments. Furthermore, the mass spectra might be incomplete at high m/z ratios due to the instrument's limitation, so that the high m/z-range might be even larger and thus also $\langle M_{hi} \rangle$.

2.5 Summary & Conclusions

The study shows that the intuitive evaluation of the material flux of an cluster ion beam from its mass spectrum can easily underestimate a significant contribution from large clusters of low intensity at high m/z ratios. Therefore in deposition applications cluster formation provides the possibility of a high flux deposition as compared to pure molecular beams. Especially space charge effects that are often a limiting factor of ion transmission scale with increasing electrical current.[99] Hence at the space charge limit, a cluster beam carries a multiple of the material of a molecular ion beam and can thus be used for the fast growth of thin films or three dimensional islands as demonstrated here.

In the ion beams clusters with several hundred molecules were found, which should have a diameter in the range of several nanometers and thus represents small nanoparticles. The SDS or SoCit cluster ion beam can be understood as an example of a nanoparticle ion beam, which demonstrates that in principle ES-IBD processing is also applicable to this material class. Moreover, it represents a controllable route for the fabrication of nanoparticles, provided that the aggregates formed in the electrospray are stable after deposition on the surface.

When working with such ion beams one has to be aware of the footprint of nanoparticles in mass spectrometry. The mass spectra of the organic salts discussed above represent the transition from defined cluster to nanometer sized, less defined particles. Their variation in size and charge state will lead to a low intensity distribution of peaks in the high m/z range, which might not be resolved even by advanced mass spectrometers. This calls for an alternative characterization method for gas phase nanoparticles in vacuum, which would allow a controlled deposition of even large nanoparticles in vacuum and thus their integration in vacuum processes.[137–140]

In the framework of this study it was also attempted to deposit nanoparticles from solutions and dispersions. The efforts with carbon nanotubes (CNT) suspended in SDS solutions and gold nanoparticles dispersed in SoCit resulted in structures identical to those presented here for the pure SDS or SoCit solutions without nanoparticles (Fig. 2.7 & Fig. 2.8). Clearly, from such solution the salt clusters are preferably ionized and transmitted, so that in the end no Au-nanoparticles or CNTs are deposited in contrast to our interpretation in Ref. [11].

Further attempts with highly pure dispersions of CNT in ethanol and V_2O_5 and CdS nanowires in water-ethanol solutions were more successful, in the sense that structures were found which could be attributed to the nanoparticles, but often they were not or poorly reproducible. Since it was shown that in principle nanoparticles can be transmitted and deposited in ES-IBD, it is concluded that the crucial step is the controlled ionization of the nanoparticles. Therefore not only the chemical characterization by mass spectrometry is lacking, but also a better insight in the ionization and transport within the ion source is required.

3 Self-Assembly in 2D from Molecules Deposited by ES-IBD

In contrast to conventional deposition processes from the gas phase where neutral molecules at thermal energies are sublimated onto substrates, electrospray ion beam depostion (ES-IBD) relies on molecular ions at hyperthermal energies. On the one hand this results in a transient diffusion and reactivity enhancement of the molecules due to the higher energy of the molecules on the surface. On the other hand, binding interactions between the molecules are hindered due to repulsion between the charged species, if no neutralization reaction occurs at the surface. Such a neutralization reaction, however, might not necessarily be the reverse of the charging. Thus it can change the properties of the molecule.

The self-assembled growth of three-dimensional (3D) molecular structures on the basis of ES-IBD was presented in the previous chapter. Crystalline layers of non-volatile molecules as well as 3D island growth could be observed, showing that besides the properties differing from evaporation, interactions between the molecules deposited by ES-IBD on the surface occur and self-assembly is possible. In the following part, the nucleation of the molecules deposited by ES-IBD on a surface is addressed in more detail. To this end, scanning tunneling microscopy (STM) in ultra high vacuum (UHV) is used for studying two-dimensional (2D) self-assembled molecular structures at the atomic scale.

In general, two types of self-assembled molecular structures at surfaces can be distinguished: molecular assemblies held together by non-covalent intermolecular forces and molecules linked stronger by covalent bonds. Among the non-covalent interactions, hydrogen bonds and metal-ligand interactions are predominantly utilized for network formation as they are directional. Hydrogen bonds connect partial charges present in molecules functional groups in a directional fashion and are thus an important bonding motif in nature. One example for self-assembled molecular structures on surfaces relying on hydrogen bonds is trimesic acid ($C_6H_3(COOH)_3$). Upon deposition on a surface it forms a network structure

reflecting the molecule's three-fold symmetry.[141,142] In that, the three carboxylic groups of the molecule bond via hydrogen bonds to carboxylic groups of neighboring molecules and thus create a supramolecular structure with cavities.

Similar structures can also be yielded through metal-ligand interactions. In comparison to hydrogen bonds they are generally stronger and thus result in more robust entities. Moreover, the incorporation of metal centers increases the functional properties of the self-assembled structures, thus expanding their relevance for potential applications. The preparation of metal-organic coordination networks in 2D is usually done by the co-evaporation of the ligand molecule and the central metal atom in UHV. In order to function as ligand, the molecule has to feature a functional group, which can for example be a carboxylic group. A co-evaporation of trimesic acid and iron leads to the formation of various complexes with a coordination depending on the surface coverage of those two species.[143] Using this concept, metal-organic coordination networks growing over a large area and over multiple surface steps can be realized.[46] Moreover, the bonds are reversible which enables the constituents to reach the most energetically stable configuration and thus to correct errors in the structure.[144]

An even higher degree of stability can be provided by covalently bonded carbon-based networks.[145] Due to the irreversibility of the bonds, these networks are prone to defects during the growth on the surface but feature an efficient electron transport[146] which is particularly desirable for molecular electronic applications. In general, the fabrication of such networks requires a two step process, in which the precursor molecules are first deposited and then polymerized by the allocation of an activation energy. This energy can be provided in terms of temperature treatment or UV-light irradiation. As the activation barrier can be high, the utilization of catalytic properties of the surfaces is an important and often used method.

In this way, fullerenes have been fabricated by employing the catalytic properties of platinum. The deposition of complex organic polyaromatic precursor molecules by thermal evaporation on a Pt (111) surface, yielded upon annealing at moderate temperatures (750 K), a surface-catalysed cyclodehydrogenation process resulting in a transformation of the precursor molecules into fullerenes.[49,147] Another useful reaction is the Ullmann coupling.[148] The annealing of halogenated monomers at elevated temperatures on metal substrates, leads to cleaving of the halogen substituents and the monomers are transformed into surface stabilized radicals. By diffusion on the surface, they encounter and form a C-C bond through an addition reaction. A first example of this was shown by the sublimating of brominated porphyrins onto a Au(111) surface with subsequent annealing.[47] Adjusting the number of Br atoms attached to the porphyrins, allowed the steering of the

formation of dimers (1 Br atoms), chains (2 Br atoms), or grids (3-4 Br atoms). A combination of the effects of Ullman coupling and cyclodehydrogenation was use to prepare graphene nanoribbons with atomic precision.[51]

Also with ES-IBD, covalent bonds can be created by reactive landing deposition as shown by Laskin *et al.*[10,136] They utilized the kinetic energy to create bonds between peptides and a self-assembled monolayers (SAMs) on a surface which was revealed by mass spectrometry techniques.

Here, we demonstrate that ES-IBD provides the possibility of fabricating self-assembled structures held together by covalent or non-covalent bonds. Each of two different molecules used here, addresses one of two special properties of ES-IBD, which are the deposition of (1.) charged/excited molecules and (2.) fragile molecules which in both cases may be reactive.

The first molecule presented, the Reichardt Dye,[149] belongs to the group of betaines, providing a negatively and a positively charged site at the same time. It is thus of interest for studying the charging and discharging of the molecule in the gas phase and on the surface. Due to its molecular dipole, it exhibits an ordering motif, which might be observable on the surface.

The second molecular group considered, belongs to the group of alkynes and possess six triple bonds in a row (thus called hexayne), due to which it is very reactive. A clean deposition with conventional deposition methods is excluded due to the high reactivity which leads to a direct decomposition or polymerization of the molecule. The soft deposition of this very reactive molecule opens up the possibility of creating covalently bonded molecular structures after soft activation by heat or light irradiation. Subsequent self-assembly of this molecule on the surface can result in precursor structures for graphene nanoribbons with precisely defined edges for a following polymerization.

3.1 Reichardt Dye: A Molecular Dipole

The Reichardt Dye[149] [2,6-diphenyl-4-(2,4,6-triphenyl-N-pyridinio)-phenolate, *Sigma-Aldrich* 272442, referred as RD] belongs to the group of betaines. Its molecular structure exhibits a delocalized π-system and a positively and a negatively charged site causing a large permanent dipole moment of about 15 Debye (Fig. 3.1).[150] The molecule has the special property of featuring a very large negative solvatochromic effect in solution. Changing the solvent from tetrahydrofuran to methanol results in an absorption band shift of about 350 nm.[149] Polar solvents lead to a higher degree of stabilization of the ground state than of the excited state for which the transition energy increases. Therefore it is used to measure the solvent po-

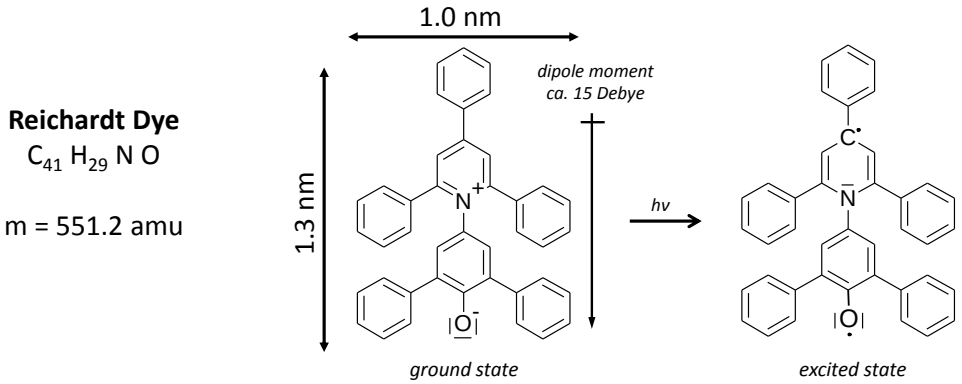

Fig. 3.1 Structure of the Reichardt Dye (RD) molecule in its ground and first excited state.[152]

larity by UV/vis spectroscopy on the empirical $E_T(30)$ scale.[151] Furthermore, the molecules are also used in chemical sensors with optical responses[152] in which the RD is immobilized in polymeric substrates,[153,154] silica,[155] and glasses[154] to obtain optochemical sensors for various vapors.

Besides its application for the above mentioned examples, it is especially interesting for ES-IBD as a model molecule due to its zwitterionic property. In order to ionize the molecule, one of the charges has to be saturated, *e.g.* by a charged adduct. Here, the questions to be addressed are whether this reaction is reversed on the surface and whether the molecule self-assembles into ordered structures. ES-IBD in combination with STM is suitable to address these questions as different species in the gas phase like clusters, fragments etc. are distinguished by mass spectrometry whereas the structure analysis of the deposited molecules is enabled by high resolution microscopy with STM.

In the gas phase we find that the molecule indeed binds any adduct offered to saturate one of its charges. In the positively charged state, it prefers to bind to protons while in the negative mode any other negatively charged ion present in the solution is used. Furthermore, in both cases clusters are formed, which can be observed in the mass spectra. In positive mode, these clusters are also perceived upon deposition of the non mass-selected ion beam onto a Cu(100) surface. This manifests itself in a huge difference between actual and expected coverage. In addition, the STM measurements show the self-assembly of the molecules into ordered structures to be dependent on the coverage. In contrast, the deposition of the mass-selected single molecule with an attached proton did not result in any immobilized structures. The molecules were highly mobile after deposition. Only upon annealing, non-covalently bonded self-assembled features were observed with basic units corresponding to a modified, reacted species of the molecule.

We conclude that a neutralization reaction is important and necessary for achieving self-assembled structures of molecules deposited by ES-IBD. In the case of the RD molecule the hydrogen adduct is strongly bonded so that neutral molecules could only be brought to the surface by the deposition of clusters. A neutralization reaction, which can be induced by an annealing of the charged species, however, resulted in a different molecular structure and thus in a different self-assembly process.

3.1.1 ESI Mass Spectrometry

For mass spectroscopy the RD molecule is dissolved in EtOH with a concentration of 0.1 mM. Due to its zwitterionic property, the charging in positive as well as in negative mode is possible and beams for deposition can be prepared as shown in the following part.

The mass spectrum of the positively charged RD molecule is depicted in Fig. 3.2. The blue spectrum shows the whole mass range of the ion beam and exhibits a strong single peak at 552 Th only. High resolution ESI mass spectrometry reveals the isotopic pattern of the molecule with four peaks occurring at distances of 1 Th, starting at 552.24 Th. The four peaks have an intensity distribution of 100%, 45%, 10% and 2%. These values fit the expected peak intensities for the molecule charged by an additional proton exactly. Other positive ions like Na^+ or Cs^+ in the form of adding salts like NaCl or CsI to the solution does not change the mass spectra, although one would expect these ions to attach to the molecule easily. As the $[RD + H]^+$ species is dominant in the mass spectra, it is also possible that the other species are not detected due to the low dynamic range of the detector. Thus the 552 Th peak was suppressed by mass-selection through a lower cut off by Q2 until 555 Th. The remaining mass spectrum measured at higher amplification is depicted in red in Fig. 3.2. Several peaks in the m/z range greater than 552 Th appear. The first three, at 574 Th, 590 Th and 684 Th respectively, correspond to the molecule with respective attachments of Na^+, K^+ and Cs^+. The peak at 849 Th represents a cluster consisting of three molecules with two sodium atoms as charge carriers. Further clusters are identified at 1103 Th, 1125 Th and 1140 Th which correspond to the molecular dimer with hydrogen, sodium and potassium as charge carriers.

The results show that the negative charge of the molecule is compensated by the attachment of positive ions. The intense peak of the protonated species $[RD + H]^+$ in the mass spectrum, suggests that it represents the most stable and preferred configuration, even after the addition of other charge carriers. This might be explained by the fact that the phenolate oxygen atom is a strong electron pair

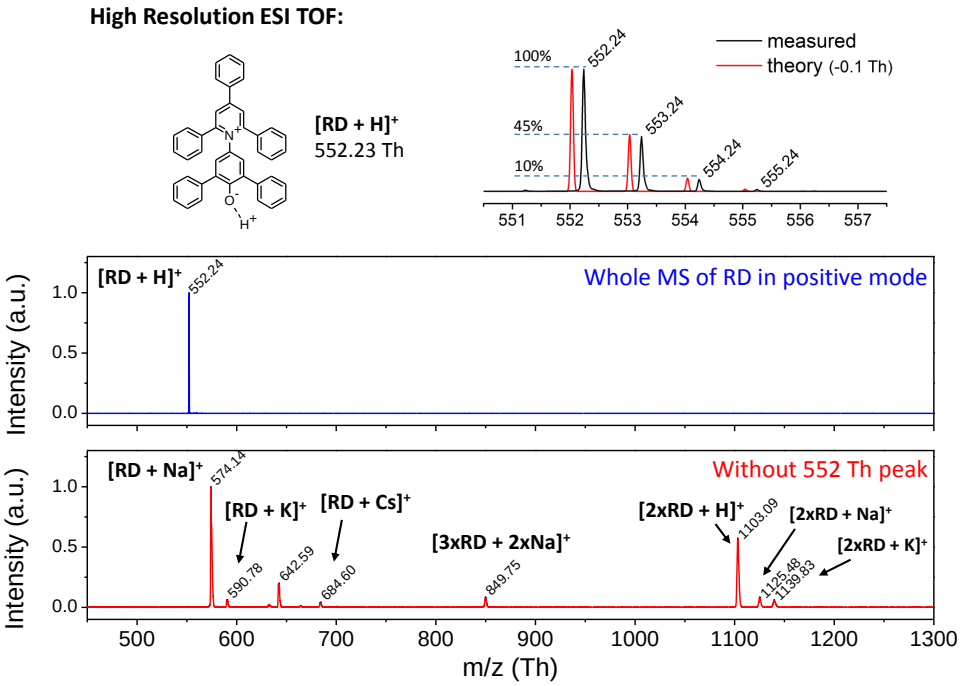

Fig. 3.2 Mass spectra of the positively charged RD molecule. The upper mass spectrum in blue depicts the full mass range showing only the single molecular peak. High resolution ESI mass spectrometry reveals the isotopic pattern of the peak. When this species is excluded by mass-selection, several other peaks are observed in the mass spectra depicted in red.

donor.[150] Thus a covalent bond between the oxygen and the hydrogen is formed, creating an alcohol. The alkali metals on the other side, undergoes a nonspecific interaction with the molecule by a ionic bond. Due to the covalent bonding between the oxygen and the hydrogen, the dipole moment of the molecule is reduced as the charged nitrogen site remains. This is in contrast to the nonspecific interaction of the alkali atoms with the molecule. Furthermore, it is observable that the molecule tends to the formation of clusters, shown by the peaks starting from 1103 Th. These peaks corresponds to dimers, whereby the most intensive peak corresponds to the one with a hydrogen attachment, demonstrating the favored bonding partner compared to the dimers with Na^+ and Cs^+. Although the mass spectra do not show any larger clusters, they might still be present but not detected in the mass spectra due to low intensity (cp. Chap. 2).

Using the molecule in negative ES-mode, different characteristics with a more pronounced clustering behavior are seen. Figure 3.3 shows two mass spectra of negative ion beams. The red spectrum depicts a solution where CsI was added to the EtOH solution while the blue spectra shows one with the addition of NaCl.

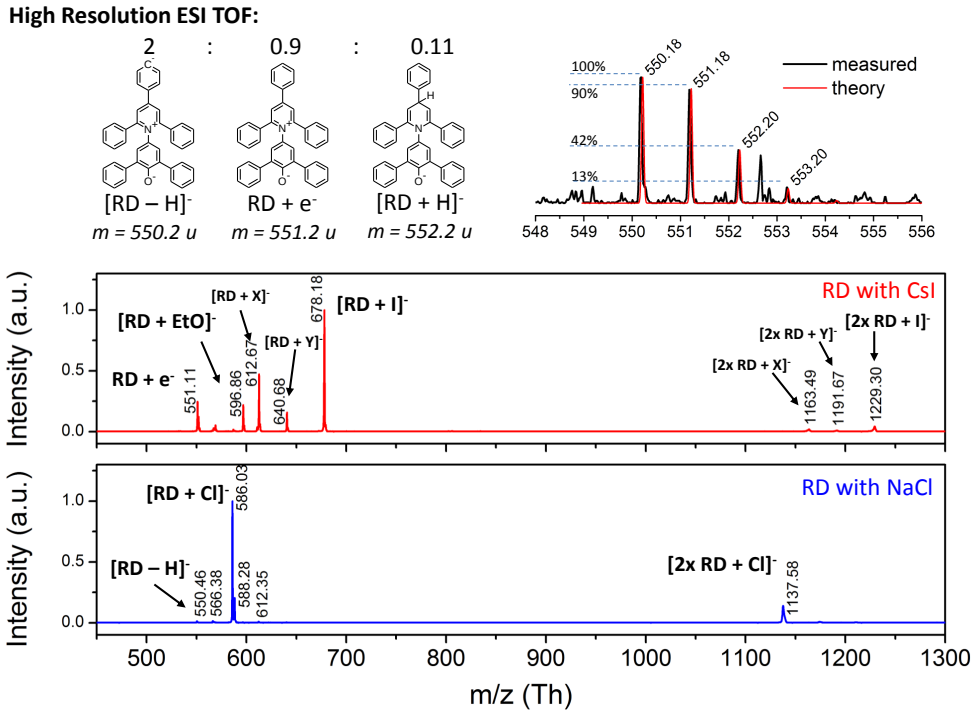

Fig. 3.3 Mass spectra of negatively charged RD molecules. High resolution ESI TOF mass spectrometry shows isotopic distribution of the single molecule demonstrating the different types of charging for the single molecule. Mass spectra of RD with additional salts show that the molecule prefers to attach adducts and tents to the formation of clusters.

In contrast to the positive ions, both spectra instantly exhibit several peaks. The peak corresponding to the single molecule around 551 Th is less pronounced in both spectra. Instead, the peaks of RD molecules with attached negatively charged iodine at 678 Th and chlorine at 586 Th are most prominent. In the mass spectra with CsI, several other peaks are observed at a m/z-ratio of 596 Th, 612 Th and 640 Th, representing the molecule with an attachment of EtO^- and two, not identified, negative ions. In the higher m/z-range dimer clusters are found which have the I^- and the two unknown ions as charge carriers.

High resolution mass spectrometry in negative mode of the single molecule peak reveals isotope peaks at 550 Th, 551 Th, 552 Th and 553 Th with an intensity distribution of 100%, 90%, 42% and 13%. The peak positions of that isotope pattern could correspond to a RD molecule that lost a proton. The expected peak abundances would be expected to 100%, 46%, 10% and 1%, which significantly differs from the observations. The assumption that different ion species are superimposed in the mass spectra enables the reproduction of the adundances. Besides

the species which is charged by the absence of a hydrogen atom, the molecule can be also ionized by an uptake of an electron, resulting in a mass of 551.2 Th, or a hydrogen atom leading to the uncharging of the nitrogen atom and thus to a mass of 552.2 Th. The latter case might be enabled when the molecule is in the excited state (Fig. 3.1) and a hydrogen atom reacts with the radical located at the pyridinium ring. In the particular case shown in the high resolution spectrum in Fig. 3.3, the abundances fit exactly when a ratio of 2 : 0.9 : 0.11 is assumed for the single molecular species without hydrogen in comparison to the one with an electron and the one with the neutralized nitrogen. It can be presumed that a mixture of these molecules is present. Thus in the red mass spectrum in Fig. 3.3, the electron charged species is dominating and in the blue mass spectrum the one missing a hydrogen atom. However, the three ionization processes described do not seem to be energetically favored as those peaks are weak in comparison with the one corresponding to species with an attached ion.

In summary, the mass spectra show that the molecule prefers a nonspecific interaction with charge carriers in order to be negatively ionized as they are the most intensive peaks in the negative mass spectra. This might be concluded from the positive charge of the pyridinium moiety, which is delocalized and partially screened by the three surrounding phenyl groups. In order to saturate the positive charge, major changes of the molecular structure are necessary to stabilize the negative charge at this position. This can be seen in the low intensities of the peaks around 551 Th.

Thus the tendency for cluster formation is also more pronounced than in the case of the positively charged ion beam. In Fig. 3.4 two mass spectra at different

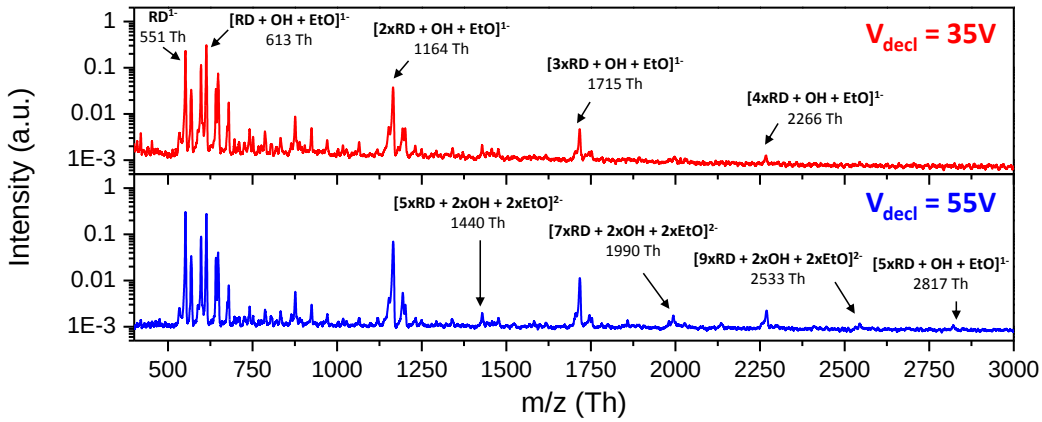

Fig. 3.4 Mass spectra of negatively charged RD molecules. With increasing declustering voltage cluster peaks appear at high m/z-ratios.

declustering voltages are shown for the molecule dissolved in EtOH and water (displayed on logarithmic-scale). As no additional charge carriers like Cl^- or I^- are added to the solution, the molecule incorporates ions like OH^- and EtO^- present in the water and the organic solution respectively. In the upper red spectrum at 35V declustering voltage, clusters up to 2266 Th corresponding to four RD molecules, are observed. Increasing the declustering voltage to 55 V, the intensities of the existing peaks increase and additional peaks at higher m/z-ratios appear, *e.g.* the doubly charged cluster at 2533 Th or the singly charged cluster at 2817 Th. Furthermore, the singly charged peak at 551 Th also increases in intensity with higher declustering voltage.

These observations show that even larger clusters than those observed in the mass spectra are present. Upon increasing the declustering voltage, large clusters at high m/z-ratios are fragmented and decay into smaller ones. Due to that, the peak intensity of the smaller clusters and the single molecule increase. Thus the molecule represents similar mechanisms for cluster ion formation as the ones described for the SDS and SoCit clusters in the previous chapter.

In conclusion, the molecule is easy to ionize due to its zwitterionic nature and high intensity ion currents are achieved. In positive mode the molecule prefers to establish a bond between a hydrogen atom and the phenolate oxygen atom since this site is a strong electron pair donor.[150] In this way, the negatively charged oxygen site is neutralized and only the positively charged nitrogen site remains unchanged. Beside the singly charged molecule, clusters are detected, including neutral molecules.

Similar characteristics are found for the molecule in negative mode. In contrast to the positively charged molecule, a saturation in this case of the positive charge, is unfavorable as major changes on the molecular structure are necessary for this reaction. Hence, the molecule prefers to attach negative ions non-specifically and has an even stronger tendency to form clusters. Fragmentation of the cluster beam showed that large cluster at high m/z-ranges are present, which are not detected in the mass spectra at low declustering voltages.

3.1.2 Deposition from an Ion Beam Including Clusters

As both ion beams, in negative mode as well as in positive mode, contain clusters, the deposition onto a surface should yield a coverage of more than one molecule per charge (cp. Chap. 2). In order to confirm the presence of clusters in the beam and to have a look at the structure, we performed deposition experiments with subsequent STM analysis. For the deposition we chose the positively charged species due to its clear and well defined mass spectra and its higher ion current

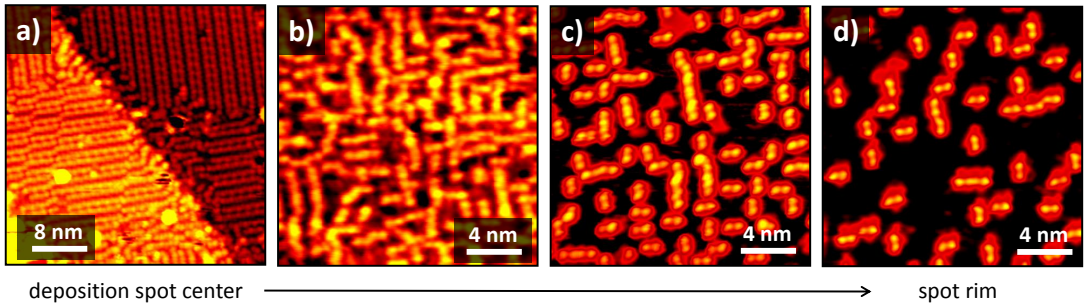

Fig. 3.5 STM images of positively charged RD molecules on a Cu(100) surface at LT (V= −1.0 V, I= 0.03 nA). **(a)** Closely packed monolayer at the center of the sample. **(b - d)** Decreasing coverage by moving towards the rim of the sample leads to single chains and isolated features.

compared to the negative mode. The mass range of the ion beam is filtered to a lower limit of 500 Th to avoid contaminants, whereas the upper mass range is not limited. This ion beam is used to deposit a nominal charge amount of 70 pAh onto a Cu(100) sample.

In Fig. 3.5, representative STM images of this sample at 40 K are shown, ordered from the center to the rim of the deposition spot. Obviously, a full, closely packed and ordered monolayer is present at the center of the sample (Fig. 3.5 a), whereas by moving towards the rim, the coverage decreases (Fig. 3.5 b-d). Along with that, the ordering motif changes from double row domains to single stripes and finally to single entities featuring two lobes, interpreted as individual molecules. The higher coverage in the center and the decay of the coverage towards the rim shows that the beam is well focused as the material distribution is expected to be Gauss distributed for ion beam deposition.[11] Furthermore, the high coverage demonstrates that clusters were contained in the ion beam. Quantitatively, the deposited charge amount of 70 pAh, composed from singly charged molecules corresponds to a submonolayer coverage of 50 molecules on an area of 20 x 20 nm^2 which would roughly equal the coverage at the rim of the sample shown in Fig. 3.5 d). Obviously, there is a huge difference compared to the observed coverage found in the center, which is only explicable by the presence of clusters. These observations confirm that although the single charged species was dominating the mass spectra, the material transport was dominated by clusters.

Self-Assembled Structures

The structures observed on the surface are clearly constructed of features having two lobes. At low coverage they are isolated and aligned along two perpendicular

directions (Fig. 3.5 d). With increasing coverage, single chains are formed following the two orientations given by the lobes, stacking up along their long axis (Fig. 3.5 b, c). Finally a compact phase consisting of perpendicular double rows is formed at highest coverage (Fig. 3.5 a).

The two lobes of the single features at low coverage reveal a distance of 0.65 nm (Fig. 3.6 a). The same distance is also observed in other single chains with four lobes and eight lobes, but additionally a separation by 0.4 nm is observed in-between (Fig. 3.6 b, c).[a] Since an individual double lobe feature reveals a distance of 0.65 nm, which is also measured within the chains at start and end, it is ascribed to a single molecule. Accordingly, the smaller distances of 0.4 nm are attributed to the junction between two molecules. By comparison to the chemical structure of the reichardt dye, 0.65 nm can be either ascribed to the distance between the nitrogen and the oxygen site (≈ 0.6 nm) or to the separation between the opposing attached phenyl rings (≈ 0.75 nm). An indication what might be present is given by notches observed in the STM images for the molecules (marked in white in Fig. 3.6 a-c). These notches are always located in the middle of two lobes on one side. Due to the symmetry of the molecule it is concluded that the lobes are located perpendicular to the molecular backbone while the notch represents the upper phenyl ring along the $N^+ \cdots O^-$ axis or the lower phenolate group. Interestingly, even in the chains this notch can be distinguished (Fig. 3.6 b, c). In the long chain these features are on alternating sites which indicates an antiparallel orientation of the molecules within the chain (Fig. 3.6 c). This hypothesis is also supported by the observation of different lobe intensities along the chain, as it reveals an alternating contrast between bright and dark for the junction between two molecules with the length of 0.4 nm (Fig. 3.6 c). Since also the single molecule provides a brighter and a fainter lobe, the alternating contrast in the chain is only explained by an antiparallel alignment of the molecules, too. Due to these observations the molecules observed at low coverage can be oriented as shown in Fig. 3.6 d, e).

However, the parallel double rows of the closely packed monolayer at high coverage reveal only an equal distance of 0.65 nm between alternating bright and faint lobes (Fig. 3.6 f). A defect in the ordered structure shows that one bright and one darker lobe can be attributed to one feature, similar to the case at low coverage. This feature is also seen at the domain borders where the structure is disturbed and breaks up into these individual features (Fig. 3.6 g). Moreover, the disturbed domain border as well as the point defect in the ordered structure show

[a] The distances are only measured in y-direction of the images. Due to thermal drift the distance is a bit larger in x-direction.

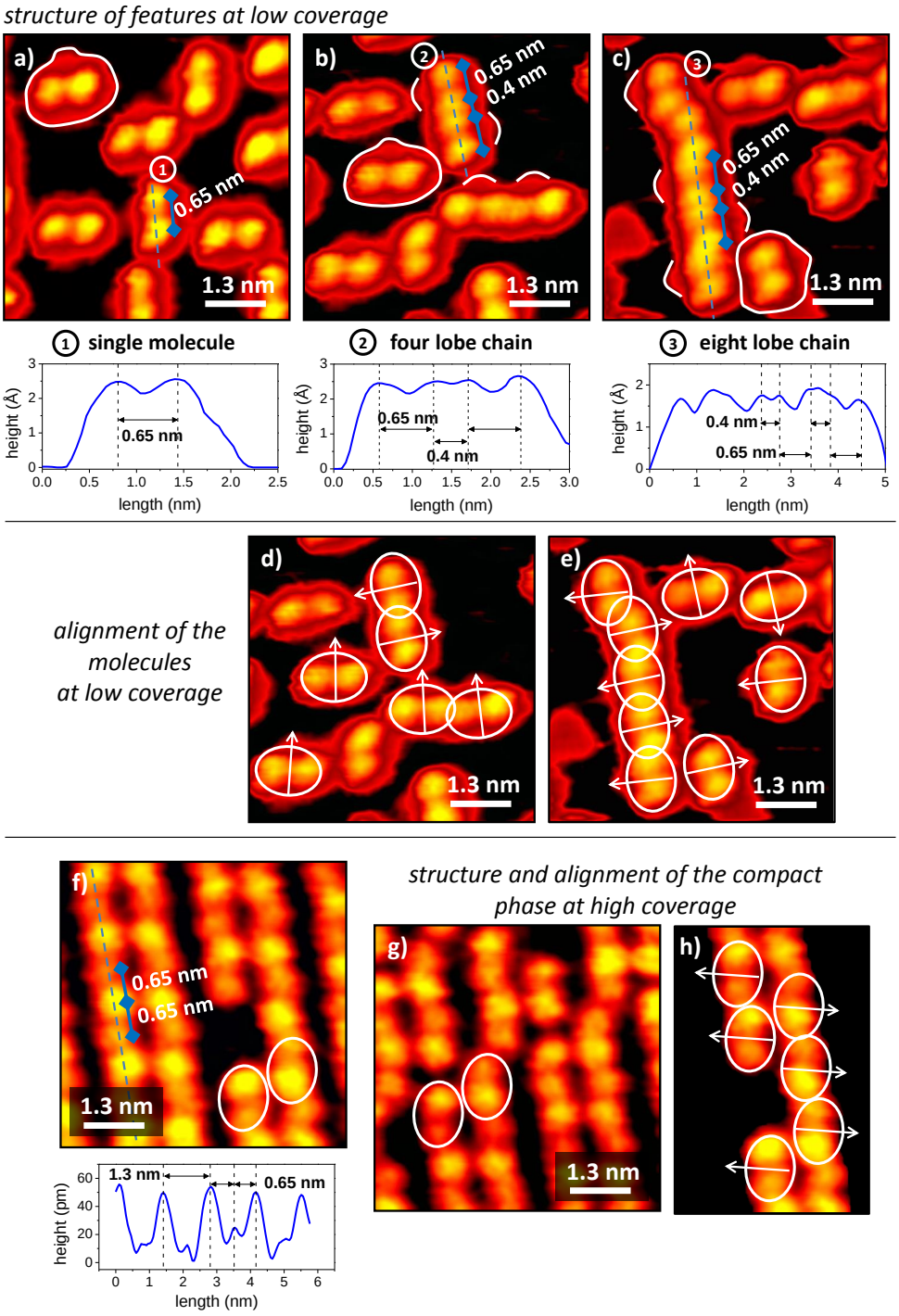

Fig. 3.6 **(a-c)** Magnified STM images of the structures at low coverage showing single molecules and chains featuring a little notch. **(d, e)** This notch enables to identify the orientation of single molecules as well as molecules within the chains. **(f-g)** Due to a different distances between the molecules in the structure at high coverage, a different orientation is presumed for the molecule in the double rows. (V = -1 V, I = 30 pA)

that two features in the double row are side by side with their brighter lobes. Hence, an orientation of the feature alignment in the double row can be given also here. Accordingly, the molecules are aligned parallel within one half of the double row, but antiparallel compared to the other half of the row (Fig. 3.6 h).

Connecting the Lobes with the Molecular Structure

Whether the two observed lobes for the single molecule can be assigned to the phenyl rings perpendicular to the $N^+ \cdots O^-$ axis is hard to judge from the STM images alone. Therefore we performed density functional theory (DFT) calculations of the molecule in the gas phase in order to determine the electronic structure and to correlate it to the observed STM contrast.

DFT calculations[b] for the molecule in gas phase were performed in periodic boundary conditions with a parallel implementation of the Car-Parrinello method[156] in the LAUTREC code.[157] Gradient-corrected exchange correlation potential PW91[158] and norm-conserving Troullier-Martins pseudopotentials[159] were used to describe the electron-core interactions. The wave functions and the electron density were expanded on a plane-wave basis set up to kinetic energy cut offs of 50 and 200 Ry, respectively. The structures were considered to be relaxed when all residual forces components on the atoms were less than 0.03 eV/Å.

From these calculations, two stable configurations A and B were found (Fig. 3.7). In the more stable configuration A, the lower phenyl rings at the oxygen site are twisted in comparison with the phenyl rings located close to the nitrogen site. The other configuration B is coined by an upwardly bended molecular backbone whereas the phenyl rings are flat and pointing down. However, both configurations show density of states along the backbone for the HOMO level and states at the oxygen site for one level below the HOMO level (HOMO-1). A superposition of those levels yields a higher density at the oxygen site, from which might be concluded that the two observed lobes in the STM images are located along the backbone, whereas the brighter lobe would correspond to the phenolate group of the molecule.

However, the calculations also show that the molecule is strongly twisted. For that reason the STM might detect primarily the topography of the molecule rather than the electronic structure. As this calculation treated the molecule in the gas phase the most stable configuration might be altered further on the surface. Therefore we calculated the molecular structure on the Cu(100) surface with DFT in order to check whether a flat geometry of the molecule is present.

[b] DFT gas phase calculations of the RD molecule were performed in collaboration with Giulia Tomba, *University of Cambridge, Department of Chemistry.*

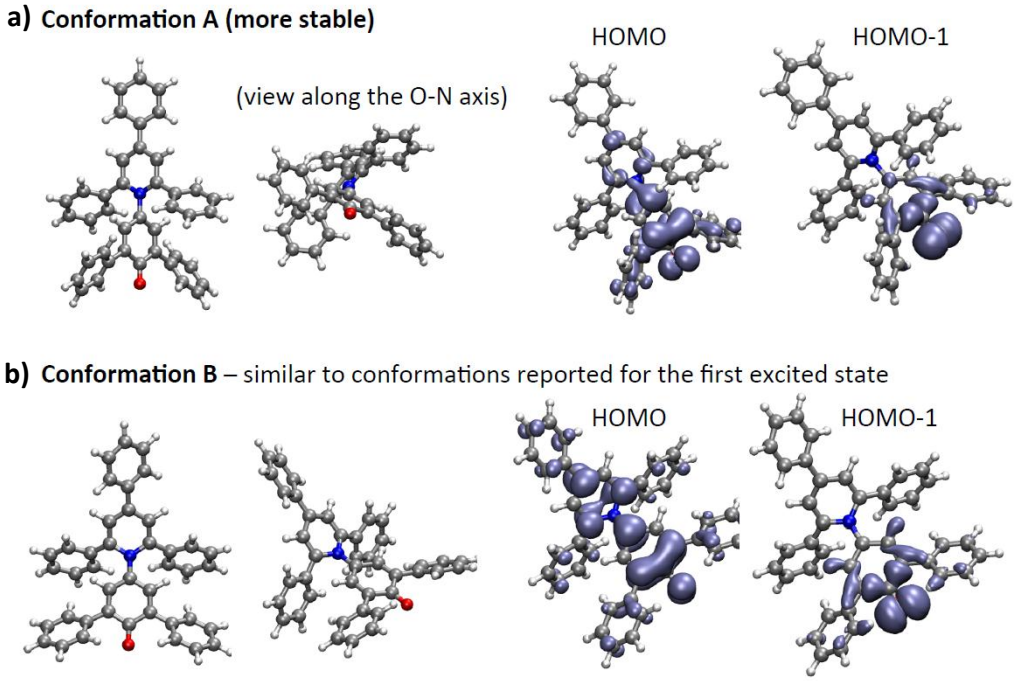

Fig. 3.7 DFT calculation of the RD molecule in the gas phase. Two stable configurations are found which both show the HOMO levels aligned along the molecular backbone.

The corresponding calculations[c] were performed with the planewave-pseudopotential package Quantum-ESPRESSO,[160] using ultrasoft pseudopotentials[161] and a GGA-PBE[162] exchange-correlation functional modified by the self-consistent DF-vdW functional,[163] to account for van-der-Waals interactions. Gas-phase and on the substrate relaxations were performed with a wave function energy cut-off of 408 eV and 204 eV, respectively. Brillouin-zone sampling included the $k = \Gamma$ point only. The adsorption was carried out only on one side of the slab, which was modeled with two layers, allowing a vacuum (adlayer-surface distance) of 10 Å. Forces were relaxed up to 0.26 eV/Å. In the presence of the surface, only forces acting on the top layer and the molecule atoms were relaxed.

From these calculations different adsorption configurations were yielded of which the most stable is shown in Fig. 3.8. This configuration is close to the gas phase configuration B (Fig. 3.7) but with the backbone flat on the surface. Furthermore, the oxygen atom is strongly interacting with the Cu surface atom causing even a little lift of the atom by 0.14 Å.

[c]DFT structure calculations of the RD molecule on the surface were performed in collaboration with Andrea Floris, *University of Cambridge, Department of Chemistry*

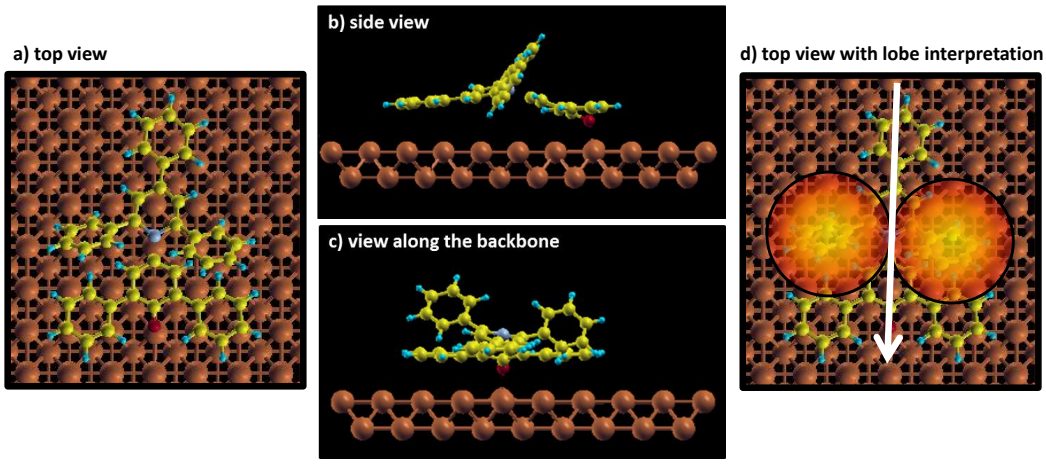

Fig. 3.8 **(a - c)** DFT structure calculation of the RD molecule on a Cu(100) surface showing the most stable configuration. **(d)** Overlay of the structure with two circles of 7.5 Å diameter representing the lobes observed in STM. The arrow indicates the orientation according to the STM images in Fig. 3.6.

As seen in the side views (Fig. 3.8 b, c) two phenyl rings on the left and right side of the molecule are twisted and point upwards while the rest of the molecule is lying flat on the surface. These upwards sticking parts might be the origin of the two lobes observed in the STM images rather than the electronic structure. For illustration, two circles were drawn onto the structure at the position of the twisted phenyl rings with a diameter of 7.5 Å, which corresponds to their separation (Fig. 3.8 d). What remains visible are the two lower and the upper phenyl ring of the structure. As they are lying flat on the surface, they are almost not detected by STM, aside from a little notch. This notch might be attributed to the lower phenolate group, as in the gas phase it provides a higher density of states for the HOMO (cp. Fig. 3.7), which are mapped in the STM images. Furthermore, even the contrast differences of the two lobes can be explained by the different height of the phenyl rings. Hence, the orientation of the lobes can be related to the molecule structure as indicated with white arrow in Fig. 3.8 d).

In summary, the deposition of a cluster beam of the RD molecule created 2D ordered structures. A high molecule density triggers the formation of domains consisting of double rows in two perpendicular directions. A lower density leads to the formation of single chains or isolated molecules. Interestingly, the mutual orientation of the molecule is different in the double row and single chain cases. The molecules in the single chains are stacked up antiparallel. In contrast, the molecules of the double rows have the same orientation within one chain, but are antiparallel to the second chain of the double row.

These observations indicate that the dipole might be intact and causes the observed self-assembly. Whether the neutral and intact dipole molecule originates from the cluster deposition or is due to a neutralization reaction of the charged molecule can not be distinguished. A cluster free ion beam deposition experiment can give the relevant evidence. The yielded structures can be compared to the ones from the cluster beam deposition and thus allow further conclusions about the molecular configuration on the surface.

3.1.3 Deposition from a Cluster Free Ion Beam

The deposition of the cluster ion beam on a Cu(100) surface in the previous section showed 2D self-assembled ordered structures with a certain orientation of the molecule. This orientation might be guided by the dipolar character of the neutral molecule. As the molecules are charged upon landing, it could mean that on the one hand a neutralization reaction of the charged molecule has taken place. On the other hand it might be also possible that these structures are only built up by the many neutral molecules which are present in the clusters. In order to distinguish the two cases, a mass-selected beam of only positively charged RD molecules is used for the deposition. Depending on the structures that are obtained, conclusions about the precise molecular configuration and structure as well as the neutralization reaction are possible.

The positive ion beam was mass selected to the singly charged molecule at 552 Th for deposition on a Cu(100) surface. To compensate for the material difference between the cluster and the mass selected beam, the deposited charge amount was increased to 250 pAh. This amount equals more than half a monolayer with 180 molecules on an area of 20 x 20 nm^2.

A representative STM image of the sample at LT is depicted in Fig. 3.9. Although the sample is at a temperature of 45 K, images characteristic for highly mobile molecules are obtained. On the terraces of the Cu(100) surface, a noisy random pattern is imaged, corresponding to molecules with a mobility on the time scale of one scan line (2D gas phase).[164] Only at the step edges of the Cu surface, some features are immobilized and imaged with round lobes. The lobes are roughly 1 Å high and are separated along the edge by approximately 1.8 nm. Beside these features, nothing else was imaged, at any of the different measuring positions on the sample.

The presence of mobile molecules at low temperature and the observation that no ordered structure is formed, indicates that charged molecules are present at the surface and no neutralization reaction took place by deprotonating the oxygen site. The mobility is caused by strongly repulsive interaction of the STM tip and

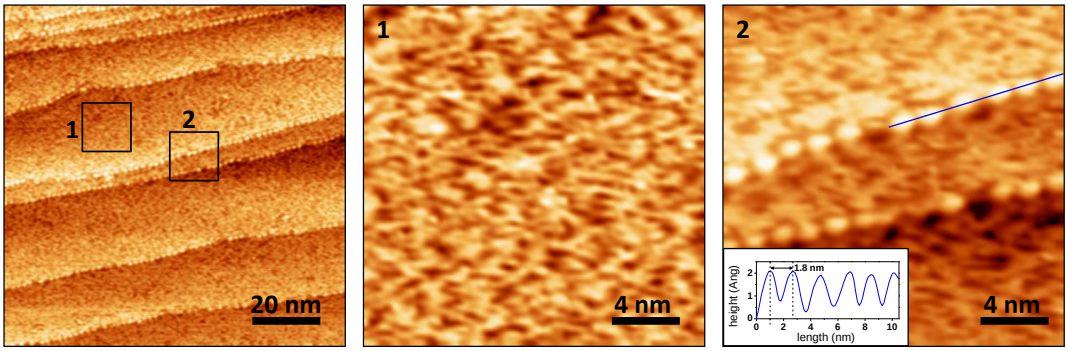

Fig. 3.9 STM images at LT of the Cu(100) surface after the deposition of the mass-selected ion beam to 552 Th. On the terraces, traces of the moving molecules are observed, whereas at the step edges single lobes with a distance of about 1.8 nm are seen.

the molecules as well as between the charged molecules which additionally avoids the formation of an ordered structure. These results thus underline the hypothesis that the structures observed after the deposition of the cluster beam, originate from the neutral dipole molecules contained in the clusters. The charged RD molecule, which is also present in the cluster beams, was not imaged due to the high mobility of the deposited molecules.

As the charge of RD molecules is caused by the attachment of a hydrogen atom bonded to the oxygen site, a deprotonation on the surface might yield the original, neutral molecule. Then, the same structures as for the cluster beam could be observed. Deprotonation can for instance be accomplished by a temperature treatment of the molecule on the surface.[165–167]

In order to perform a deprotonation of the RD molecules by temperature treatment, the sample was annealed at 120°C for 5 minutes. At RT, no structures could be observed so that the sample was cooled down to low temperatures again. In Fig. 3.10 a) it is seen that besides a 2D gas phase also a condensed ordered phase is present. The ordered islands exhibit parallel double rows, which are connected periodically (Fig. 3.10 b). The structure has an oblique unit cell and a X-like repeating unit, emphasized with a white border. This unit is also found in small chains of 2-3 elements on the terraces (Fig. 3.10 a, white arrows) in which they are connected along their axes in the same fashion as in the 2D islands (Fig. 3.10 c). In all configurations (chains and islands) the X-like feature exhibits a width of 0.73 ± 0.05 nm and a length of 1.2 ± 0.05 nm between the lobes.

Furthermore, at lower coverage near the rim of the deposition spot, the terraces are empty while the same X-motifs are found at the edges of the Cu surface. The

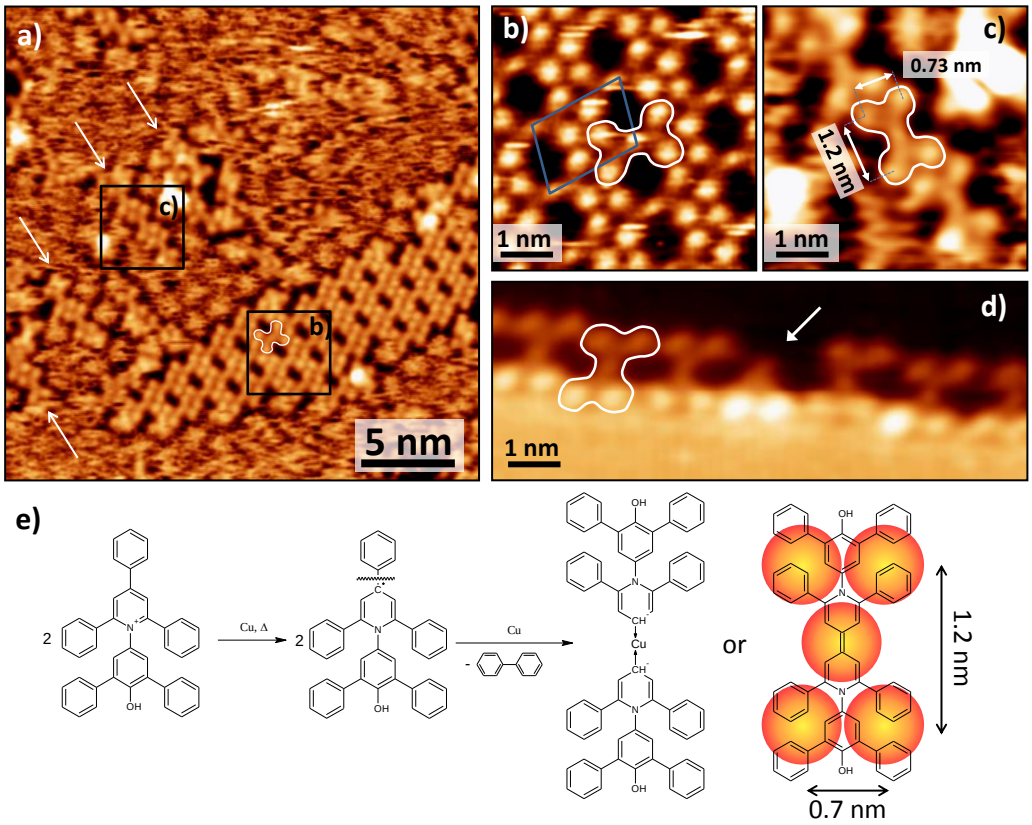

Fig. 3.10 STM images of the Cu(100) surface with the mass-selected molecules after annealing at 120°C for 5 min. **(a)** Between mobile molecules, ordered islands are found. **(b)** The islands consists of connected double rows with an X-like repeating unit which is also found as a single motif on the terraces **(c)** as well as at the step edges **(d)**. Furthermore, a single triangular structure suggests that the X-like structures is a dimer. **(e)** Proposed reaction of two RD molecules during the annealing step leading to the X-like structure.

features are ordered next to each other with their two closest lobes at the edge (Fig. 3.10 d). Between them, a triangular feature roughly half as long as the X-like feature is seen. This suggests that the X-like structure is composed of two RD molecules. Due to the triangular shape it may be believed that this feature corresponds to the single RD molecule. The two bright lobes are attributed to the phenyl rings on the left and the right side of the molecule which would also be in accordance with the lobe distance of 0.73 ± 0.05 nm. A combination of two RD molecules in order to build the X-like structure, however, yields a slightly longer structure, in the case that they do not overlap, and would require a strong interaction. Thus, the X-like unit cannot be brought into accordance with the intact RD molecule.

Instead of being deprotonated upon annealing, the molecule might be fragmented into a reactive species. Assisted by catalytic properties of the copper, the molecules are excited and cleave the upper phenyl ring, leaving a reactive site (Fig. 3.10 e). The reaction might be continued by bonding to Cu adatoms as it is known from metal organic coordination compounds.[165–167] In this way two of these fragmented molecules, with a Cu atom in the middle, would result in a X-like structure. Another possibility is that the two reactive molecules directly bond without a copper atom by forming a double bond. In this configuration, the measured distances of 1.2 nm length and 0.7 nm width of the X-like feature would nicely fit to the proposed structure (Fig. 3.10 e).

However, due to these observations, the possibility that the immobilized molecules correspond to the intact dipole species can be excluded. A final elucidation cannot be given as further investigations would be necessary. In any case, the experiment showed that there is a difference between the deposition of the cluster beam and the cluster-free beam.

3.1.4 Summary & Conclusion

The Reichardt Dye is a molecule featuring a negatively and a positively charged site and is thus a molecular dipole. For this reason, it is an interesting test molecule for ES-IBD due to the various possibilities of charging it positively or negatively. Mass spectrometry of positively charged RD molecules showed a preferred ionization by saturation of the negatively charged phenolate oxygen atom with hydrogen atoms as it is a strong electron pair donor. Nevertheless, species with other charge carriers like Na^+, Cs^+ or I^+ were also observed. These are believed to form a weak non-specific bond with the molecule. Furthermore, the molecule has the tendency to form clusters. This could be seen clearly when the molecule was charged negatively as the processes to neutralize the nitrogen via chemical reactions are less favored. Another clear sign for cluster formation in the gas phase was seen upon deposition of the positive, unfiltered ion beam. Although a submolecular coverage was aimed for, the surface showed a full monolayer which can only be explained by the deposition of large clusters. The monolayer showed an ordered structure comprised of double rows where the molecular building blocks provided a parallel alignment in the row. At lower coverage, single chains were observed which showed an antiparallel alignment within the chain. Due to that ordering motif, it is concluded that the single building block of those rows are intact RD molecules with an in-plane dipole. In contrast, the deposition of the mass-selected species with an attached hydrogen atom did not result in those structures. On the surface, only highly mobile molecules were seen, which upon annealing yielded a different kind

of ordered islands. This demonstrats that the molecule did not neutralize upon deposition and that the annealing step did not lead to the deprotonation of the molecule, but instead a new reaction occurred.

However, a clear difference between a cluster beam and a mass-selected beam is evident. In the present case, the difference was unraveled by the fact that the cluster beam contains neutral molecules which upon deposition formed a 2D ordered structures. In contrast, the charged molecules kept their charge when deposited on the surface and did not form any ordered structures. Furthermore, the findings illustrate that 2D ordered structures can be grown with ion beam deposition techniques and that ES-IBD is in this view equivalent to conventional deposition methods. The only additional requirement for self-assembly by ES-IBD are neutral molecules on the surface after the deposition, which is achieved by cluster deposition or a neutralization reaction induced by various means.

3.2 Hexayne: A Highly Reactive Molecule

While in the previous section the effect of the charging on the structure formation and reactivity was examined, a molecule class is presented which is reactive by itself and may serve as a precursor. This is to show that it is possible with ES-IBD to deposit these very reactive molecules, enabling ordered and covalently bonded systems after activation under mild conditions.

Within this context, the deposition of hexaynes, a oligo(ethynylene)$_n$ derivate with $n = 6$ repeating units is attempted (Fig. 3.11). The molecules were provided by Frauenrath *et al.* at EPFL who were able to synthesize them with different substituents.[169] The interesting possible feature these long molecules have, is that upon deposition, self-assembly into a parallelly aligned structure and subsequent polymerization results in graphene nanoribbons (GNR) with defined edges. Those are due to their special electronic property, influence by their edge determination, of high interest for nanoelectronic devices.[170,171] As shown in Fig. 3.11 two polymerization mechanisms can be envisioned, yielding a zig-zag or an arm-chair edge.[168] In this, an acetylene polymerization would result in zig-zag edges, while arm-chair edges are achieved by diacetylene polymerization. Which of these polymerization mechanism is realized, might be controlled by the substituents (R).

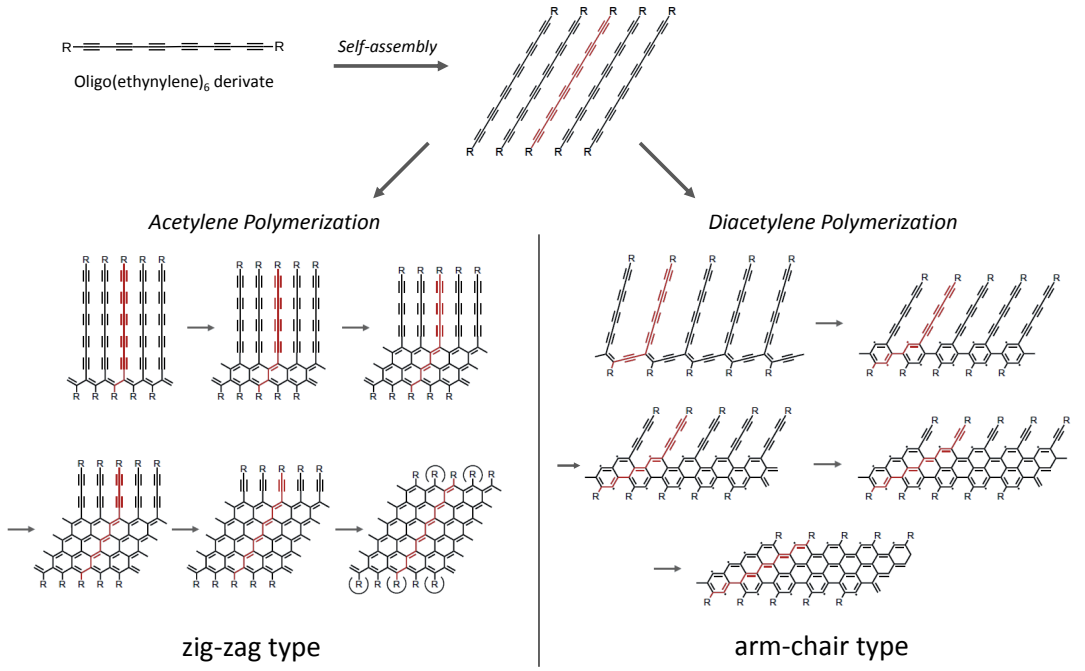

Fig. 3.11 2D polymerization mechanism of the hexaynes on surfaces yielding GNR with different edges.[168]

As indicated by the semi circle in Fig. 3.11, the substituents are very close to each other in zig-zag GNR. This means that this reaction might only occur when the substituents do not impede each other sterically. Otherwise, the route via the diacetylene polymerization is favored.

Oligo(ethynylene) derivates in the form of R–(C≡ C)$_n$–R are a group of very reactive precursors. They are thermodynamically metastable as they have an inherent reactivity leading to a rearrangement into other carbon allotropes.[172] Thus, the chemical synthesis is already challenging, in particular when the number n of repeating units is increasing. A way to stabilize those oligo(ethynylene)s is the proper choice of the substituents. This allows the fabrication of molecules with up to $n = 12$ repeating units and opens up the way for novel types of carbon materials, since additional functionalities can be provided by the substituents.[172]

The polymerization of oligo(ethynylene) derivates into nanostructures proved to be challenging, as a whole bunch of mixtures and amorphous carbon material was produced. A way to overcome this kinetic problem is the molecular self-assembly on a surface before polymerization.

So far, however, only few studies reported about the polymerization of oligo-(ethynylene)s on surfaces. One of the first reports about this was given by Takami *et al.*[173] in 1997. The evaporation of 1, 15, 17, 31-dotriacontatetrayne (DTTY) molecules onto a graphite surface in UHV led to the formation of a cloth-like macromolecule upon UV light irradiation. The reactive parts of the molecule are acetylene and diacetylene groups, which cross-link alternately by polydiacetylene (PD) and polyacetylene (PA) chains and thus create a periodic fisherman net with a defined mesh size. Unfortunately, the STM image presented by Takami *et al.* did not yield any information about how many of the PA and PD groups needed to have reacted in order to form the periodic net with the defined mesh size. Better results were achieved by Miura and coworkers.[174] The deposition of diacetylene molecules with the Langmuir-Blodgett technique yielded a self-assembled monolayer characterized by a parallel alignment of the triple bonds of different molecules. In this configuration, the molecules could cross-link upon UV light irradiation as well as by pulsing the STM tip locally above the reactive sites.

The utilization of longer oligo(ethynylene) molecules has not been shown so far. The reason for this is that the reaction at ambient conditions is hard to control since longer oligo(ethynylene) molecules are not stable enough. Therefore, UHV conditions are required to achieve the desired control, which suggests that the utilization of the ES-IBD technique, as with conventional deposition techniques, the molecules would disintegrate.

3.2.1 Asymmetrical Hexayne Termination

In the first attempt to use this class of molecules with ES-IBD, a hexayne molecule with a sugar group at one end and an alkyl chain on the other end was chosen (Fig. 3.12 a). It has a mass of 534 amu and a length of approximately 4 nm from end to end. Due to the different bonding type between the alkyne (sp) and alkyl (sp^3) chain, an angle of 120° between the hexayne and the alkyl part is characteristic for the structure at the surface. The molecule was dissolved in a mixture of DCM, MeOH and $CHCl_3$ with a concentration of about 1 mM. For the use in ES-IBD it was further diluted to 0.5 mM with MeOH and negatively ionized.

The mass spectrum of the corresponding ion beam is depicted in Fig. 3.12 b) showing several peaks between 200 - 1200 Th. The most intensive one at 533 Th corresponds to the single molecule, which is singly negatively charged by the absence of a proton, most probably at the sugar group. A second prominent peak is observed at 1067 Th and represents a deprotonated negatively charged cluster comprising by two molecules. Furthermore, both of the above mentioned species with chlorine ions as charge carriers can be identified at 569 Th and 1103 Th, respectively. As the m/z-values of the peaks correspond to the exact mass of the molecule, it can be assumed that the triple bonds of the molecule are still present and are not hydrogenated during the ionization process. The peaks below 500 Th correspond to fragments and contaminants. The two marked peaks at 356 Th and 393 Th in the spectrum show a fragment of the molecule with intact alkylene part but without the sugar group $[M - S]^{1-}$ or alkyl chain $[M - A]^{1-}$.

Thus, mass spectrometry revealed that the hexayne molecule can be transferred into the gas phase intactly and in particular without affecting the highly reactive

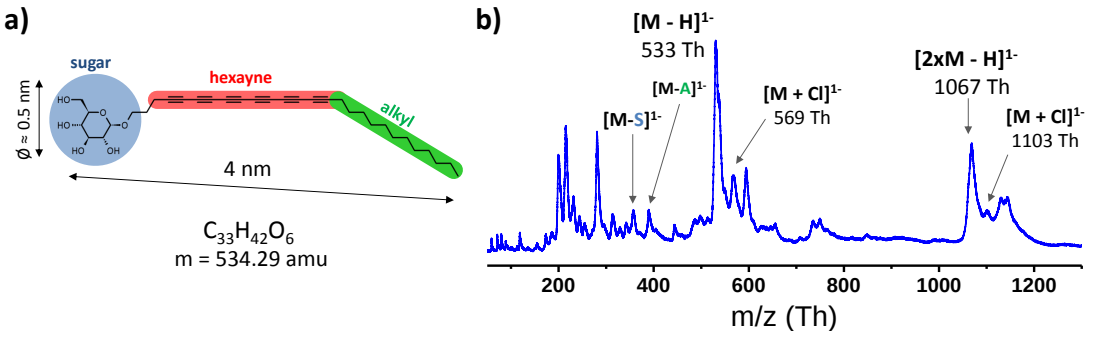

Fig. 3.12 **(a)** Chemical structure of the unsymmetrical hexayne consisting of an sugar group on one end and an alkyl chain at the other. **(b)** The mass spectrum of the molecule in negative mode shows the singly charged molecule and clusters at higher m/z ranges.

triple bonds. Furthermore, the molecule also demonstrates the tendency to form clusters. Based on this, it can be assumed that the majority of the species in the ion beam consists of the intact hexayne molecules.

Self-Assembly on Au(111)

In order to assess whether the molecules self-assemble into ordered structures, STM is used to analyze the molecules after deposition on a surface. As the beam intensity was not sufficiently high to allow mass-selection, the whole mass spectrum was used for the deposition. A total charge amount of 25 pAh was deposited onto a Au(111) surface and scanned at LT.

On the surface, besides highly mobile and undefined features, ordered islands with a striped structure were found (Fig. 3.13 a). The observed bright stripes of the islands exhibit a periodicity of about 4.6 nm. A closer look at the islands reveals further substructure. Each of the stripes consist of two rows with lobes of an approximate diameter of 0.5 nm that are distributed in a zig-zag pattern (Fig. 3.13 b). Furthermore, the structure also reveals kinked lines in between of two bright rows. The kinks are thereby antiparallel on different sides of each row.

As the kinked feature is structurally characteristic of the intact molecule, it can be concluded that the hexayne part of the molecule remains intact on the surface. In order to reproduce the island structure using the molecular shape, the bright double rows of the islands have to correspond to the sugar group of the molecule while the kinked part represents the hexayne and the alkyl chain. In the double rows, the molecules are assembled in a head-to-head fashion with their alkyl tails pointing outwards (Fig. 3.13 c). The kinks are thus pointing in opposite directions on different sides of the row. Due to the fact that at the rim of an island, no bright rows are observed and that two rows have a distance of 4.6 nm, the molecules of neighboring rows have to be interlocked. This interlocked arrangement results in the hexayne parts (red) of the molecules not being located next to each other, but instead being intermittent with the alkyl tails (green) of the neighboring molecules (Fig. 3.13 c, d). This is also seen in Fig. 3.13 d) where the lines pointing to the kink are displaced. An explanation for this can only be given by an interlocked arrangement in which the alkyl and the hexayne chains have different contrasts.

The reason for the interlocked arrangement is the size difference between the sugar head group and the tail consisting of the alkyl and hexayne chains. The sugar part of the molecule is much bulkier than the tail, hence there is space between the tails despite the head groups being packed very compactly. In comparison, the SDS molecule considered in the previous chapter (Chap. 2, p. 34), is also composed of an alkyl chain but in contrast has a small sulfate head group. Upon deposition

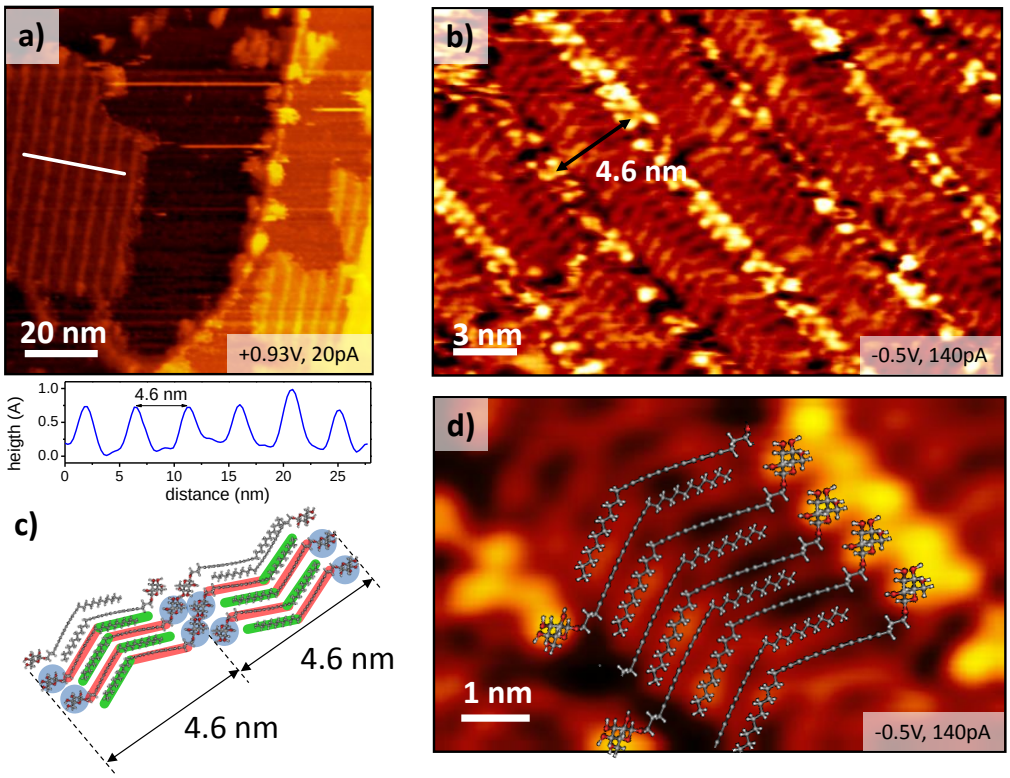

Fig. 3.13 STM images of a Au(111) surface with deposited hexayne molecules show islands with bright stripes being a distance of 4.6 nm apart **(a)**. A close-up scan on a single island **(b)** provides molecular resolution showing that the intact hexayne self assemble into an interlocked structure as sketched in the models **(c)** and **(d)**.

on a Cu(100) surface the molecule assembles into a head-to-head configuration without interlocking.[124]

Furthermore, in the STM image in Fig. 3.13 b) and d), many defects are present in the structure. This is particularly obvious in the case of the bright rows corresponding to the sugar group of the molecule. This high amount of defects can be explained by the deposition of many different species. Since mass-selection was not done, fragments like the molecule without the sugar group $[M - S]^{1-}$ or the alkyl chain $[M - A]^{1-}$ were deposited in addition to the intact molecules. On the surface, the fragments were incorporated into the islands. Two examples of how fragmented molecules are integrated into the structure are shown in the model in Fig. 3.13 d) for molecules without the sugar group.

However, the STM images reveal that intact hexayne molecules were deposited with ES-IBD and that they self-assemble into ordered island structures. The molecules thereby order into an interlocked arrangement in which the reactive

hexayne parts of parallel aligned molecules are intermitted with the alkyl part of neighboring molecules. Since the deposited mass spectrum contained fragments and contaminants, the ordered islands feature defects due to the incorporation of these fragments. However, the arrangement of the molecules into the interlocked structure prevented the reactive parts from being located next to each other. Therefore, a polymerization into ordered GNRs is not feasible.

3.2.2 Symmetrical Hexayne Termination

In order to steer the self-assembly into a configuration where the reactive hexayne parts are located next to each other, the molecule has been modified to exhibit equal substituents on both ends. Due to this symmetrical termination an interlocked structure is avoided. This molecular structure was realized with a hexayne molecule having methoxycarbonyl groups on each side (Fig. 3.14 a). Compared to the side groups of the asymmetrical molecule, the methoxycarbonyl groups are much smaller, so that the mass and the length of the molecule are reduced to 346 amu and 2.7 nm end-to-end distance.

To utilize the molecule for ES-IBD, the molecule, dissolved in chloroform, was diluted with MeOH to increase the polarity of the solution. Otherwise, the solution is too apolar for being usable in electrospray ionization. The yielded solution, with a concentration of 0.1 mM, was sprayed in negative mode.

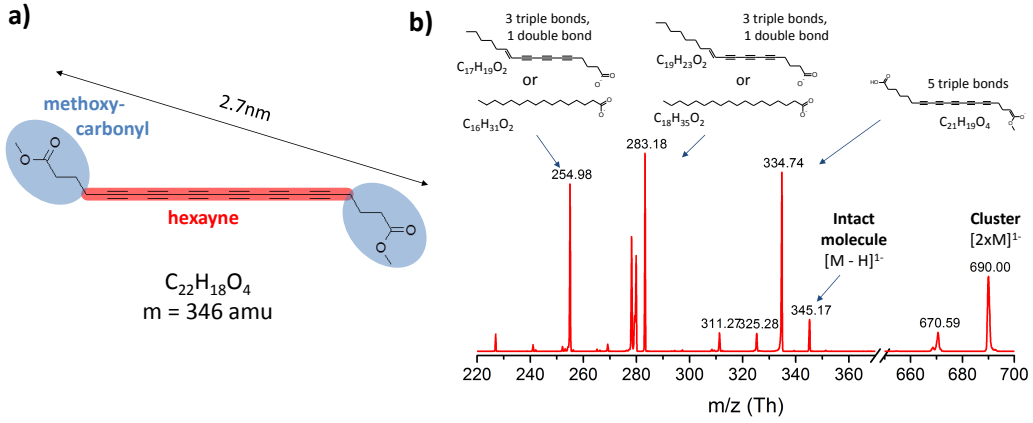

Fig. 3.14 **(a)** Symmetrical hexayne molecule with methoxycarbonyl side groups. **(b)** The mass spectrum of the symmetrical hexayne molecule in negative mode shows a high intensity and amount of fragmented molecules whereas only a less intense peak for the intact molecule is observed. The peaks corresponding to the fragment could correspond to the molecules with less than six triple bonds or even only to alkyl chains.

The mass spectrum in Fig. 3.14 b) shows several peaks ranging from 227 Th to 690 Th. The peak at 345 Th corresponds to the deprotonated molecule but has only a low intensity. Much higher intensities are found for the peaks at 335 Th, 283 Th and 255 Th, which correspond to molecules which are fragmented and have lost some of their triple bonds. At the same time, the peaks at 283 Th and 255 Th correspond to molecules, in which all triple bonds are saturated by hydrogen atoms. Furthermore, peaks at 670 Th and 690 Th correspond to single negatively charged dimers of the intact molecule and the species at 335 Th in the mass spectrum.

The high amount of fragmented molecules in the mass spectrum might be caused by the dilution with MeOH. As the side groups of the molecule are relatively small, they can not comply with the increased steric demand which is on the one hand induced by the increased polarity and on the other hand needed for the kinetic stabilization of the molecule. However, not all molecules were fragmented as also intact species are found. But the low intensity of the intact molecule peak indicates that a low ionization ability of the molecule. This circumstance might also be responsible for the fragmented molecules, as they might have formed upon charging of the intact species. Nevertheless, the intact molecule is found in a higher intensity in the cluster peak at 690 Th, indicating that are higher amount of intact molecules are available in gas phase.

Deposition on Au(111)

The mass spectrum of the ion beam from the symmetrical hexayne molecule solution revealed a low intensity of the intact molecule peak and a high amount of fragments. In order to see whether any of the species self-assembles on the surface, the whole mass spectrum was employed for deposition. By this, also fragmented molecules, which could not unambiguously be identified in the mass spectrum might be distinguished on the surface. Therefore, several samples were prepared in which a charge amount of 25 pAh was deposited onto a Au(111) surface and subsequently scanned at low temperatures.

On the surface, rod-like islands growing from the elbow sites were observed (Fig. 3.15 a). In different experiments, these islands appear with elements of different contrasts. One type of island in Fig. 3.15 b) features almost a flat island surface, while the other type exhibits a stripe-like structure on the island (Fig. 3.15 c). Furthermore, mixed island types were also found in some experiments, as shown in Fig. 3.15 d). The single rods of both island types have a width of approximately 2.3 nm. This length is too short for the intact molecule, which has a end-to-end distance of about 2.7 nm. Moreover, the substructure of the rods reveals that

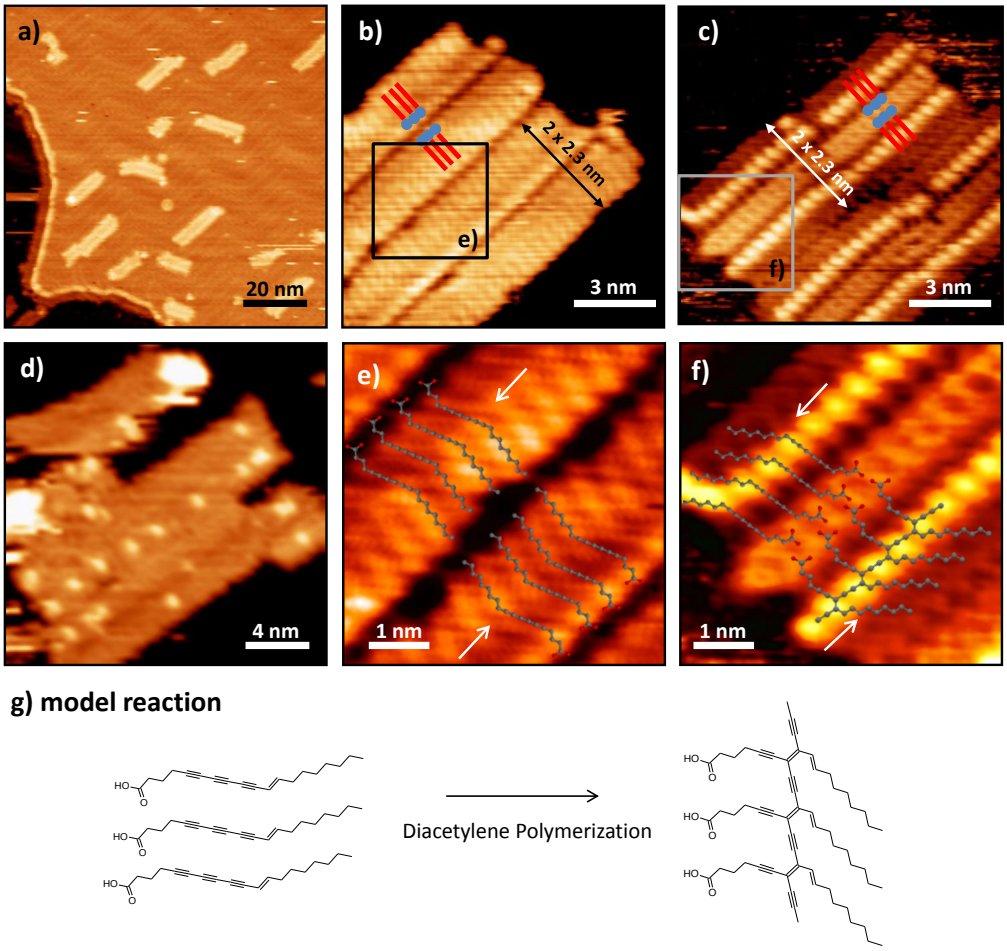

Fig. 3.15 STM images on Au(111) at LT after the deposition of the whole mass spectrum of the symmetrical hexayne solution. **(a)** Rod-like island grow between the elbow site of the Au reconstruction. **(b-d)** Two different island contrasts are observed in different experiments. In both cases the islands are built up out of rods, which consist of molecules with a head (blue) and tail (red) following the head-to-head and tail-to-tail motif. **(e, f)** Overlay of the islands with a molecule observed in the MS. **(g)** Model diacetylene polymerization of this molecule which also might cause the structure observed in **(f)**.

they are not symmetric. This leads to the conclusion that they are built up by an asymmetric molecule consisting of a head (blue) and a tail (red). Accordingly, the alignment of the islands in both cases can be assigned as a head-to-head and tail-to-tail motif as depicted in Fig. 3.15 b, c).

With a closer look on the islands, it can be seen that the building blocks of the rods feature a kink in the region of the tail (white arrows in Fig. 3.15 e, f). Such a kinked structure was already observed in the previous section for the

asymmetric hexayne molecules due to the stiff hexayne chain being followed by an alkyl chain. Therefore, the molecular building block of the islands have to exhibit this feature as well. This kind of molecular structure was observed in the mass spectrum of the deposited ion beam. The peaks at 255 Th and 283 Th are ascribed to asymmetric molecules providing an alkyne with three triple bonds and an alkyl chain. The overlay of the molecule with a mass of 283 amu with the structure in question shows a agreement for both island types (Fig. 3.15 e, f). Hence, the island structure is ascribed to the self-assembly of these molecules.

The different appearance of the islands might be related to a reaction between the molecules or of the molecule itself. In the configuration presented, the molecules are not interlocked, in contrast to the asymmetrical hexayne molecule shown in the previous section. As a result, a reaction of neighboring triple bonds is enabled, which might have been induced by the tunneling current of the STM. Through polymerization of neighboring molecules with three triple and one double bond as observed in the mass spectrum at 283 Th, a diacetylene structure can be formed as shown exemplary in Fig. 3.15 g). The overlay of this structure with the STM image reveals that the bright lobes would correspond to the sites where the double bonds are located. Thus, the bright contrast is derived from the higher conductance at this position that is due to the delocalized electrons. Additionally the higher contrast can also imply a conformational change upon polymerization in which the diacetylene group is lifted from the substrate.[174]

This polymerization scheme, however, would not explain the intermediate islands types, on which only some isolated lobes on the low contrast islands were observed (Fig. 3.15 c). Once a polymerization is initiated, it is continued and not stopped after the first step.[174] Thus these intermediate island types would rather suggest that a single molecule reacted with itself without affecting neighboring molecules. This assumption is supported by the observation that all island types were only observed at LT which is an argument against a polymerized structure. At RT, the molecules were highly mobile and could thus not be imaged which is in conflict to the fact that such large, covalently bonded structure should be immobile. Furthermore, soft annealing at an elevated temperature of 100°C for 5 minutes resulted in structures that were not reproducible. In these trials, the annealing of low contrast islands as shown in Fig. 3.15 b) resulted in islands with high contrast, in random unordered structures, in an empty surface, or in no observable change. Higher temperatures directly yielded empty surfaces, demonstrating that the molecules desorbed upon annealing due to low molecule-surface interaction. Hence, the different appearance of the islands can not be clarified without further chemical characterization.

In summary, no immobilized, symmetrical hexayne molecules were detected on the surface upon deposition of the whole mass range observed in the mass spectrum. Instead, asymmetric species which correspond to fragmented molecules, could be identified in self-assembled islands. The different contrasts of these islands might indicate that the molecules have reacted with themselves. However, the structures could not be reproduced systematically.

Mass-Selected Deposition on Cu(111)

To work with a more defined deposition, the chemical composition of the ion beam was limited by mass selection to a m/z range of 250 to 300 Th. This is the range in which the asymmetrical species are observed. Due to the mass-selection, the deposited amount of charge was increased to 100 pAh in order to compensate for the material contribution lost by excluding possible clusters. Furthermore, the substrate was changed from an Au(111) to a Cu(111) surface. This resulted in a higher interaction of the deposited molecules with the surface, which allows a higher annealing temperature without desorption of the molecule.

Although the substrate provides higher adhesion, molecules are only observed at low temperature on the Cu(111) surface, whereas at RT no immobilized structures are found. STM images of the surface at LT exhibit islands with bright stripes on top, aligned in three directions of an angle of 60°, which are in accordance with the surface directions of the hexagonal lattice underneath (Fig. 3.16 a).

Furthermore, the islands are again built up from an asymmetrical molecule, in which the position of the head (blue) corresponds to the bright stripes (Fig. 3.16 b). The islands are similar to the ones observed on the Au(111) surface depicted in Fig. 3.15 c). Besides the bright spots of the islands on the Au(111) surface, both structures on Au(111) and Cu(111) exhibit stripes in the middle where the molecular heads are located. The width of two rods (4.3 nm) is comparable to the one observed on the gold surface featuring a width of 4.6 nm. The small length difference might be due to a more compact arrangement of the molecules on copper caused by the stronger influence of that surface in comparison the gold surface.

Besides the obvious head-to-head configuration, a head-to-tail arrangement is also found in the islands on copper (Fig. 3.16 c). The change of the ordering motif is noticeable since only the head-to-head configuration produces the dominant bright strips on the islands. In the head-to-tail configuration, the coupling point between two molecules is less pronounced. Instead, the kink of the molecules is more apparent. This kink is seen for both types of islands and can be modulated by using molecules with three triple bonds, which already built up the islands on the gold surface (Fig. 3.16 d, e). Unlike the islands on the gold surface, the

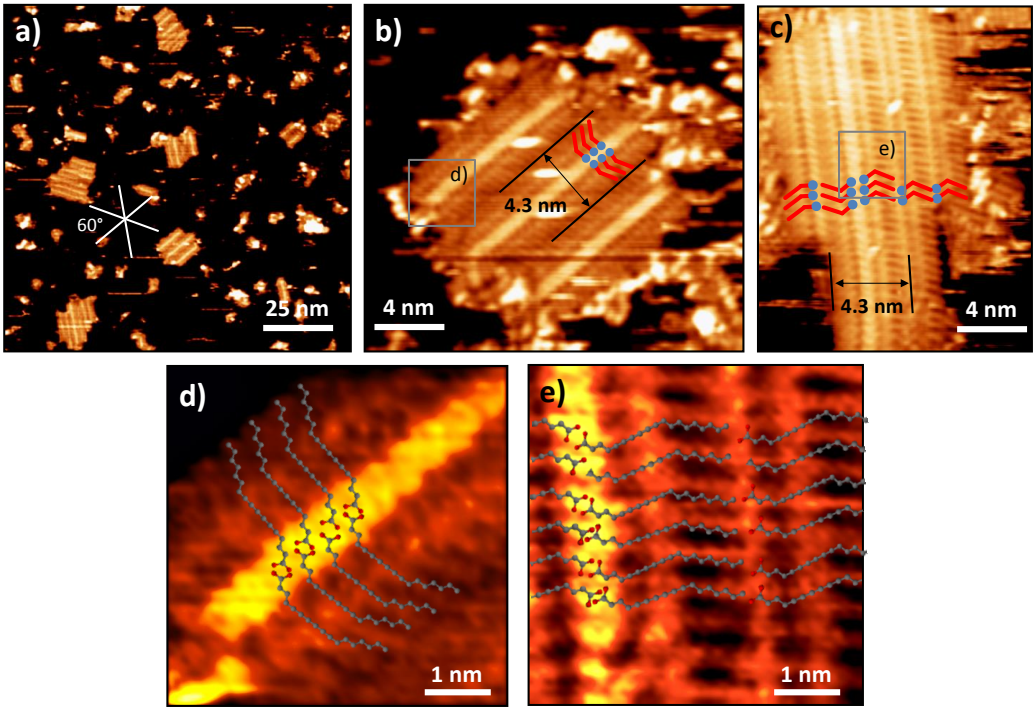

Fig. 3.16 STM images on Cu(111) at LT after the deposition of the species with m/z-ratios between 250 Th and 300 Th. **(a)** Rod-like islands in three directions are built up by molecules with a head (blue) and a kinked tail (red). **(b, c)** The arrangements of the molecule within the islands is a mixture between the head-to-head and head to tail motif. **(d, e)** Overlay of the islands with the molecule with three triple bonds shows reasonable agreement.

observed contrast of the islands on Cu(111) was reproducible and did not change. Thus it is concluded, that they did not react neither with themselves nor with each other.

In summary, the mass-selected deposition of the fragmented molecules on the Cu(111) surface led to islands with a non-polymerized structure, which was already observed on the gold surface. As the fragmented molecules of the structure seem to provide a reactive triple bond part, a polymerization might be initiated by an annealing of the sample at elevated temperatures.

Annealing of the Structures on Cu(111)

In order to accomplish a reaction between the molecules, the prepared copper samples were annealed to 150°C for several minutes and scanned afterwards at RT.

On the surface, large islands were found, exhibiting orthogonal angles and

shapes (Fig 3.17 a) showing a low interaction with the surface as the crystallographic hexagonal directions of the Cu(111) surface are not represented. Furthermore, the frayed edges of the islands reveal that the building blocks are mobile and not strongly bonded. For that reason, slight changes in the shape of the islands were observed in different images.

A magnification the islands exhibits alternating building blocks which are rotated by 90° to each other. One building block reveals two lobes with a distance of about 0.5 nm (Fig 3.17 b, c). Changing the tunnel voltage from -1.8 V to -1.3 V influences the contrast of the island, showing that the two lobes of a single feature are separated even further, by a distance of about 0.65 nm. Furthermore, it can be noticed that the features are asymmetric as one lobe is broader and higher than the other.

Besides these islands, further features were observed in the background. Areas without islands show very flat and wire-like features (Fig. 3.17 d, e, f). They were

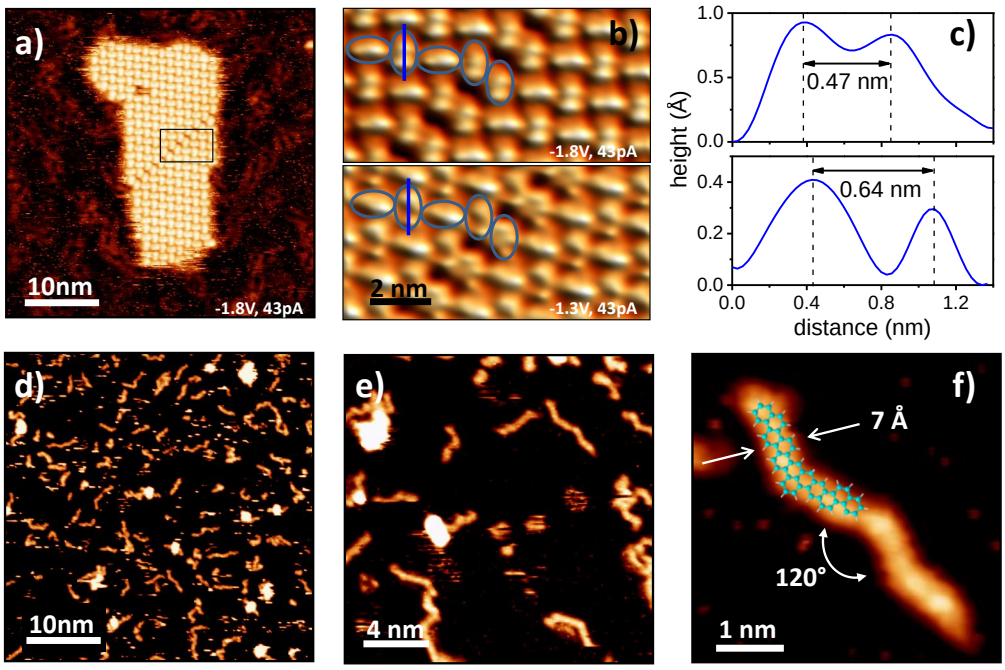

Fig. 3.17 **(a)** Cu(111) sample after annealing at 120°C exhibits large mobile islands. **(b, c)** A magnification of the islands reveal alternating building blocks with two lobes separated by 0.5 nm or 0.65 nm respectively depending on the tunneling voltage. **(d, e, f)** Furthermore, flat wire-like residues distributed randomly on the surface are observed. Due to the characteristic angle of 120° and their high stability even after annealing at 250°C, they might represent covalently bonded structures.

randomly distributed and exhibited a width of about 7 Å and an average length of approximately 5 nm. Between straight sections of the features, an angle of 120° is detected. When the sample is further annealed at higher temperatures up to 250°C, the islands disappear while the wire-like features are still present.

These observations show that the molecules are highly reactive since different structures on the surface were found after annealing. Therefore, two different processes might have taken place, resulting in the two different features.

In one of these processes, a single molecule reacted with itself into a new species. This new species is mobile and composes, together with other such molecules, the observed islands by non-covalent interactions. With increasing annealing temperature, these molecules do not react further, but instead are desorbed from the surface. The structure of the reacted molecules is difficult to determine. According to STM images they are asymmetric, which is in accordance with the deposition of the asymmetric precursor molecule. The carboxylic group of the molecule might still be present as it can provide a bonding possibly to the neighboring molecules, either by hydrogen bonds or by a metal-ligand interaction.[142,143]

The other process occuring on the surface, led to flat wire-like features. Their width of 7 Å could correspond to the width of two benzol rings in arm chair conformation as depict in Fig 3.17 f). Hence this could be a result of a reaction between the triply bonded parts of molecules. For instance, a diacetylene reaction led to the formation of one phenyl ring whereas the second ring is closed by a cyclodehydrogenation step of the double bonded carbon with a neighboring phenyl ring. In addition, the substiuents on both sides of the precursor molecule are split off.

However, an unambiguous proof for the composition of these structures cannot be given. Yet the observations show that a high reactivity of the molecules is present as a result of the deposition of the mass selected fragments of the symmetrical hexayne molecule. Furthermore, the random distribution of the structures shows that the annealing step dissolved the self-assembled structures. Thus, an initiation of a polymerization might better be performed by UV light irradiation.

3.2.3 Summary & Conclusion

In summary, the ES-IBD of oligo(ethynylene)$_n$ molecules with $n = 6$ triple bonds was shown. These molecules allow the polymerization into graphene nanoribbons with defined edges when they are parallely aligned on the surface. The first approach made towards this aim dealt with an unsymmetrical hexayne molecule featuring a large sugar group on one side and an dodecyl tail on the other side. Upon deposition, the molecule self-assembled into a head-to-head configuration

where the hexayne parts were parallelly aligned but interlocked with the alkyl tails of a neighboring head-to-head arrangement. This formation is caused by the large sugar head group, leaving enough space between the tails that other molecules can be incorporated. A polymerization between them was thus avoided.

A second hexayne molecule was utilized exhibiting a smaller head group on both sides of the hexayne part. This molecule turned out to be difficult to handle since, due to its the methoxycarbonyl side groups, the molecule fragmented either upon charging in the ionization process or when diluted in a polar solvent which is necessary for ES-IBD. Nevertheless, the intact molecule was found in the gas phase. Upon deposition on Au(111) only fragments of the molecule assembled into ordered structures. The fragments however, were asymmetric featuring a carboxylic group on the one side and an alkylne and alkyl tail on the other side. They were thus very similar to the asymmetric hexayne but in contrast had only three triple bonds and a smaller head group. Upon deposition on Cu(111), they were ordered in a head-to-head and head-to-tail manner with their reactive parts parallely aligned. The annealing of these structures yielded two completely different structured features revealing the reactivity of the species. One of the structure observed after annealing showed large mobile islands which might be ascribed to the molecule after having reacted with itself. The other structure showed randomly distributed wire-like structures as a result of a reaction between the molecules.

In conclusion, these experiments showed that the deposition of highly reactive molecules with ES-IBD is feasible. As a requirement for this, the molecule should be dissolvable and stable in polar solvent which comes along with the allocation of a functional group for ionization by electrospray ionization.

Beside the potential of fabricating self-assembled, non-covalently bonded structures with ES-IBD, the technique enables the preparation of covalently bonded systems through the deposition of highly reactive molecules. This is advantageous as catalytic surfaces are not needed for the polymerization process, such as Ullman coupling processes.[148]

4 Conformation Control of Unfolded Cytochrome C Proteins

The functionality of biological macromolecular systems is based on the molecular arrangement, in which the position of every atom as well as the precise 3D conformation of the molecular chain is relevant. This high level of complexity is the result of ordering the structures through self-assembly and hierarchy.[175] The major fraction of these function-fulfilling biomolecules are proteins, built up out of 20 available types of α-amino acids. Their chemical composition steers their conformation and along with that their functionality in their natural environment.[176] In order to understand or even to control the folding, a detailed investigation of single molecules is necessary. A way to achieve this might be given by high resolution microscopy of single biomolecules on surfaces.

In particular, the observation of the folding of the amino acid chain on all length scales represents a challenge, that could be met by scanning probe microscopy. Important details such as the atomic/amino acid configuration as well as the molecular arrangement on larger length scales could be addressed with scanning tunneling microscopy (STM). Due to the large mass of biomolecules, electrospray ion beam deposition (ES-IBD) is needed to bring them onto an atomically defined surface in ultra high vacuum (UHV), which is the precondition to achieve good results with STM. Electrospray ionization is a well established method to deposit biomolecules intact into the gas phase where their chemical composition can be analyzed by means of mass spectrometry.[177–179] Furthermore, several studies revealed that the conformation of the proteins can be preserved upon transfer from solution into the gas phase.[180,181]

Beyond that, ES-IBD might offer the possibility to directly influence the conformation of a biopolymer by controlling the interaction with the surface. Identified by ion mobility spectrometry, the charge state of the protein has been identified as a parameter, which is related to the conformation in the gas phase.[181] Low charge states provide compact structures whereas high charge states rather cor-

respond to extended shapes, due to repulsive Coulomb forces. However, the exact shapes cannot be imaged by methods like ion mobility spectrometry and there is an ongoing debate on whether the detected conformational changes as a function of charge state can be really related to the native conformations of a protein in solution.[182–184]

In an initial study, we have shown that it is possible to image the conformation of both folded and unfolded cytochrome c (CytC) from acidic and non-acid solutions on different surfaces in UHV by using ES-IBD and STM (see Fig. 4.1).[65] Mass-selecting species of low charge states of +10 to +7 from solutions of folded proteins, resulted in globular structures on different surfaces (Fig. 4.1 c). These structures with a height of about 1 – 1.5 nm correspond to the folded proteins disturbed due to missing hydrophilic-hydrophobic and surface interactions. In contrast, the deposition of the high charge state of +18 to +12 from solution with a higher pH, provided extended and randomly distributed strands on an adhesive Cu(100) surface, while on the less interacting Au(111) surface the chains refold into patches at the elbow sites (Fig. 4.1 b).

Beside the submolecular resolution of the protein, which might enable a local sequencing by scanning tunneling spectroscopy (STS), the conformation of the unfolded proteins on the adhesive Cu(100) surface can be studied. Understanding the driving force and mechanisms of the conformation on the surface might enable the steered preparation of functional coatings with amino acid polymers and can give a better idea of how proteins are folded on the surface. Great interest arose for the so called foldamers, artificial polymers with the possibility to adopt a certain configuration in 3D or in 2D on a surface.[185,186]

Here, the deposition of unfolded, stretched and compact refolded CytC on Cu(100) by using acidic solutions together with ES-IBD and charge state selection is discussed (Fig. 4.2). In contrast to the earlier study, we select a narrow window of 2-3 charge states of the unfolded proteins and deposited them. Quantitative STM image analysis by applying the worm-like chain model confirmed a correlation between the conformation and charge state of the deposited proteins. In order to rationalize the experimental findings we performed atomistic molecular dynamics (MD) simulations of the adsorption of CytC on a Cu(100) surface. To understand the main principles of the interplay between the Coulomb repulsion induced by the charge state and the conformation of adsorbed proteins, we varied the charge state of CytC in the simulations. Thus, we were able to rebuild structures found by STM on the surface and found our landing model in good agreement with these structures. Furthermore, simulations and experiments yielded the possibility to influence the conformation by adjusting the landing energy of the proteins.

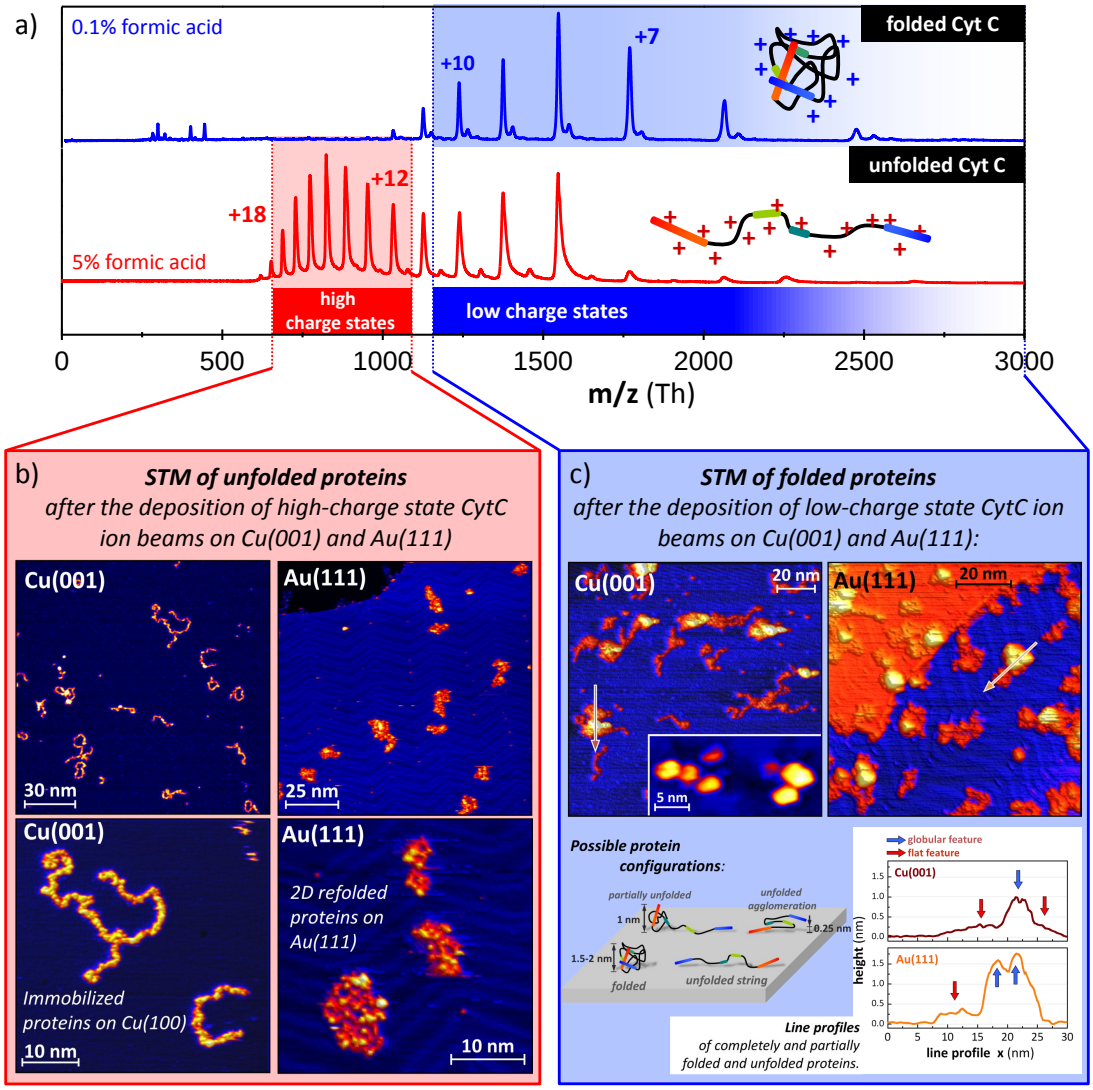

Fig. 4.1 **(a)** Mass spectra of folded and unfolded CytC of solutions with 0.1% and 5% formic acid. **(b)** STM images of unfolded CytC on Cu(001) and Au(111) showing strands and refolded patched, respectively. **(c)** STM images of folded CytC on these surfaces show globular structures with a height of 1 – 1.5 nm.

Hence, ES-IBD enables a high level control of the conformation of proteins on a surface. The addition of charge state and landing energy as control parameters in the deposition greatly extend the possibilities in comparison to conventional methods and allow to influence dimensions like stiffness and persistence length that were out of reach before.

4.1 Mass Spectrometry and Charge State Selection

Cytochome C is a heme-containing protein, consisting of 104 amino acids adding up to a molecular weight of 12384 Da (Fig. 4.2). In its natural environment, it is central to several processes in electron transfer and apoptosis.[187] The mechanism for this functionality relies on the oxidation and reduction of the iron center in the heme complex.

The solutions of CytC (Sigma-Aldrich, C2506) for mass spectrometry and subsequent deposition experiments were prepared by dissolving CytC in water/ethanol mixtures. With the addition of 5% formic acid to the solution it was ensured that the proteins were unfolded. Positivly charged gas phase ions were created with a nanospray emitter at $3-4$ kV and a flow rate of $15\mu l/h$ (see Chap. 1). After transfer into vacuum, the ions were mass-selected with the rf-quadropole Q2 in a way that only a certain narrow mass-to-charge ratio (m/z) could pass. Subsequently, time-of-flight mass spectrometry (TOF-MS) and energy detection (eV/z) in the fourth chamber at a pressure of 10^{-8} mbar ensured a defined ion beam.

For the deposition on a Cu(100) sample, which was cleaned with several sputter and annealing cycles, the ion beam was further guided through two following apertures leading to the deposition chamber at a pressure of 10^{-10} mbar. A positive voltage applied to the sample decelerated the ions for soft landing. The ion current on the sample was monitored online using electrometers (Keithley 616). After deposition, the sample was transferred in situ to the variable temperature STM (Omicron VT-STM, Omicron Nanotechnology GmbH, Germany) and was scanned at room temperature (RT).

The mass spectrum of unfolded CytC before mass-selection is displayed in Fig. 4.2 a). A series of peaks from 700 Th to 1600 Th corresponds to the protein ions with charge states from +8 up to +19. The ionic current of the whole spectrum at the TOF-MS in high vacuum is around $2-3$ nA.[99] This high ion current enables a mass-selection of even weak intensity peaks such that the remaining intensity is still sufficient for deposition. Nevertheless, there is a compromise between intensity and selectivity. This compromise is mainly due to the limited resolution of our mass-selecting quadrapole, which is restricting the size of the selection window to approximately 5 % of m_0. This does not mean that a sharp mass-selection of one charge state is impossible, but rather that it would significantly reduce the transmitted current. Despite a current of 2 nA available for the whole mass spectrum, the current would be reduced to 38 pA ($\approx 2\%$) when assuming a sharp mass-selection for the single charge state $z = 18$ out of the 12 available states (+19...+8). Together with losses occuring when threading the beam through the different chambers, the current is reduced further by approx.

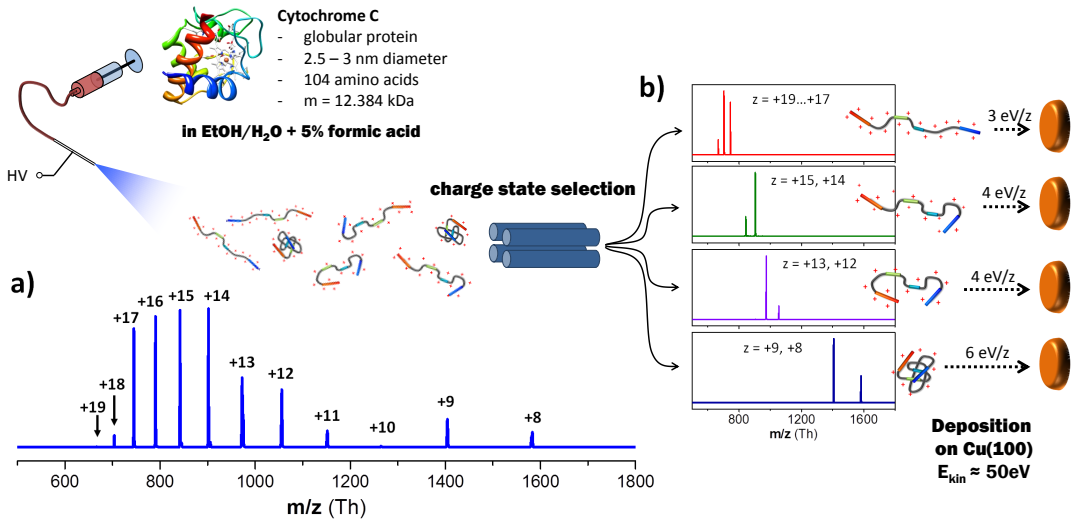

Fig. 4.2 Experimental scheme: The unfolded protein cytochrome c was ionized by electrospray. **(a)** The full mass spectra of the ion beam shows charge states from +8 up to +19. **(b)** From that mass spectra, four mass windows with 2 – 3 charge states were selected in the gas phase and deposited onto a Cu(100) surface in UHV with a constant landing energy of approx. 50 eV.

67 % to 13 pA at the sample position. Taking into account the low resolution of the mass-selecting quadropole, this current would decrease further and would be at the deposition limit for this reason.

Thus, it was optimal to select four transmission windows of two or three charge states each. These windows had a width of 100 – 250 Th and included the charge states $z = 19...17$, $z = 15, 14$, $z = 13, 12$, and $z = 9, 8$ with an ionic current of 15...130 pA at the sample in UHV (Fig. 4.2). The relative peak intensities of the selected charge states differ from the non-mass-selected spectra due to the shape of the transmission function. For later analysis, an average charge state $z_{avg} = \sum J_z \cdot z / \sum J_z$ was calculated weighting the different intensities and resulting in $z_{avg} = 8.7, 12.8, 14.2$ and 17.7.

Due to this mass-selection, a very well defined molecular ion species is achieved in the gas phase. According to the observations by Shelimov *et al.*,[180] who measured the cross section of CytC by ion mobility spectrometry, the protein expands with increasing charge state due to the Coulomb repulsion. Hence, the mass-selection enables the choice of different conformations of the molecule in the gas phase which also are related to different Coulomb energies. The deposition of these selected species is addressed in the following section.

4.2 The Deposition of Charge State Selected Proteins

In order to observe possible conformational differences of the charge state selected proteins upon deposition, the surface should avoid a reorganization due to the allocation of mobility caused by a low interaction. This was observed in the initial study where refolded CytC patches were found on Au(111) while the deposition on Cu(100) yielded extended strings and thus bearing comparison with a projection of the gas phase (cp. Fig. 4.1 b).[65] For this reason, the charge state selected proteins were landed onto a clean Cu(100) surface.

To make the different samples comparable, two parameters were kept constant. This was on the one hand the deposited charge density, which was maintained at 120 pAh/cm^2 in the different depositions. On the other hand, the landing energy was held constant at ~ 53 eV for the differently charged species. This was achieved by soft landing the molecules at a potential fitting their charge state with $\sim 6 \pm 1$ eV/z for the low charge states and up to $\sim 3 \pm 1$ eV/z for the high charge states.

The STM images of the differently charged proteins on the Cu(100) surface are shown in Fig. 4.3. For a better description of the structures, overview images are depicted for a general impression whereas close-up pictures and representative single molecule images show the substructure in more detail. On all images, unfolded immobilized proteins are found, which are randomly distributed on the surface. They have a height of about 3 Å and a length of roughly 25 ± 2 nm. This length corresponds to unfolded proteins with intact α-helices, which have a length of 26.4 nm.[65,188,189] Furthermore, some of the molecules are in contact with each other or are attached along the step edges.

Comparing the coverage in the overview images for the differently charged species, a decrease with the deposited charge state is recognized. The area coverage for the proteins deposited with the high charge state is approximately 4 % while it is 17 % for the proteins deposited with the low charge states. This can be understood as for a given charge amount on the surface, less molecules are deposited the higher the charge state of the single molecule. In particular, the size of the overview image of 70 x 70 nm^2 and a charge density of 120 pAh/cm^2 equals to 132 charges per image. This relates to seven proteins deposited with a charge state of $z = 18$ and seventeen proteins for $z = 8$ which is nicely represented in the images. Hence, this difference prooves that the mass-selection has been successful.

Apart from different coverages of the differently charged species, the conformation of the proteins on the surface is strongly affected by the chosen charge state. With decreasing charge state, the protein conformation evolves from extended to curved strands, and finally to compact patches, visualized by characteristic STM

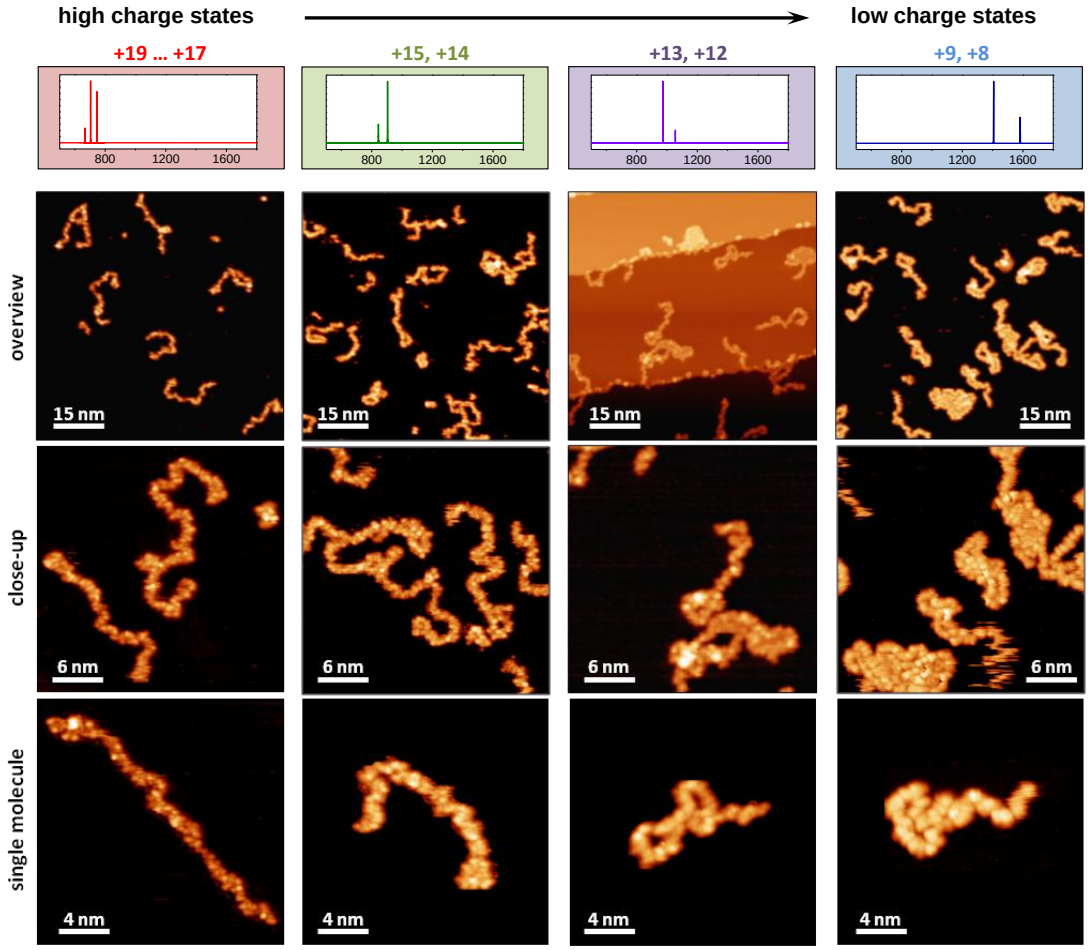

Fig. 4.3 STM images of the charge state selected CytC on the Cu(100) surface. As can be seen in the overview and close-up images, the proteins are randomly distributed featuring many different configurations. But a general trend is found as a function of the charge state of the proteins, depicted in the representative single molecule images: From extended strands for highly charged proteins to compact folded patches for low-charged species.

images of single proteins in Fig. 4.3.

In general, the conformation is distributed around an average. It is seen that for the high charge states not exclusively extended but also curved shapes are present. However, with decreasing charge state the fraction of curved shapes increase together with reducing bend radii. The molecules start to touch themselves and finally form compact patches, in which the proteins are folded very densely in two dimensions.

4.3 Statistical Analysis of the 2D Protein Conformation

On the basis of the STM images it is only possible to distinguish qualitatively between the protein conformations of different charge states. In order to quantify the conformation of the randomly distributed protein strands of a given charge state, a statistical analysis of the protein contour is necessary.

The conformation of the proteins in the gas phase is influenced by their charge state due to repulsive Coulomb interactions.[180,181] Accordingly, the repulsion also determines a mechanical stiffness of the molecular chain. Upon deposition, the conformation is obviously retained, as can be seen from the observed difference between extended strands for high charge proteins and compact patches for low charged molecules. Hence, this parameter can be used to describe and to distinguish the different and randomly distributed conformations quantitatively.

In polymer physics, the molecular stiffness is described by the so called worm-like chain (WLC) model for semi-flexible molecules. In this model, the contour of a polymer is related to its molecular stiffness in terms of the persistence length l_p (see Ref. [190] and references therein). By definition, l_p is related to the stiffness of an object and can be interpreted as the length over which the polymer is approximately straight. Thus, different values for stretched or compact folded molecules are expected. Equilibrium properties of adsorbed worm-like chain molecules can be characterized by the second and fourth moment of the ensemble-averaged end-to-monomer distance $R_2(s)$ and $R_4(s)$, respectively, which are given by[65]

$$R_2(s) = \overbrace{\left\langle (\mathbf{r}(0)-\mathbf{r}(s))^2 \right\rangle^{\frac{1}{2}}}^{measured} = \overbrace{\left(\frac{4}{3}(l_p s - l_p^2(1-e^{-\frac{s}{l_p}})\right)^{\frac{1}{2}}}^{fit} \tag{4.1}$$

$$R_4(s) = \left\langle (\mathbf{r}(0)-\mathbf{r}(s))^4 \right\rangle^{\frac{1}{4}} = \left(\frac{5}{3}\right)^{\frac{1}{4}} R_2(s)\,. \tag{4.2}$$

The first term labeled with "*measured*" describes a Gaussian distribution of the intramolecular distances between one end $\mathbf{r}(0)$ of the protein and a next monomer $\mathbf{r}(s)$ in the chain as a function of the contour coordinate s along the protein. It is directly obtained by sectioning a molecular chain into equal monomers (here in disks of 1 nm diameter) and measuring the distances between them as shown in Fig. 4.4. When these values are plotted against the contour length s of the molecule, characteristic graphs are obtained according to the stiffness of the molecule. For instance, a straight molecule is represented by a 45° line while a bent molecule reveals a truncated curve (Fig. 4.4).

The second part of Eq. (4.1) labeled with "*fit*" describes the graph which is

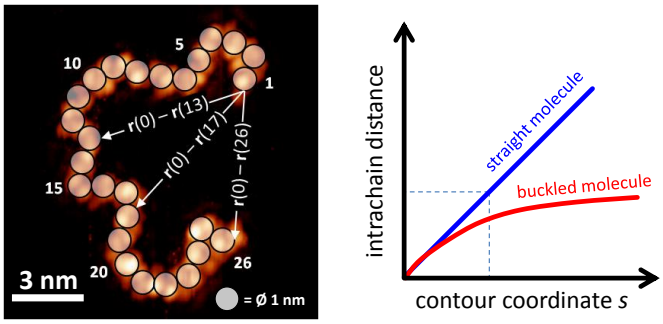

Fig. 4.4 Scheme for obtaining the end-to-monomer distances for the WLC model. Straightly aligned molecule are represented by a straight line with an angle of 45° while bent molecules are characterized by a truncated curve.

yielded according to the WLC model as a function of the persistence length l_p. The obtained data points, averaged for several molecules, are fitted with this function and a value for l_p is gained, describing the ensemble stiffness of the molecules.

For the evaluation of several samples and STM images, 50 - 100 individual, clearly identified molecules with a length of 25 ± 4 nm are considered. Proteins, which are adsorbed mainly at step edges are excluded from the analysis. These rules were applied to all datasets identically so that the obtained results are comparable to each other.

In Fig. 4.5 the second and fourth moments $R_2(s)$ and $R_4(s)$ are displayed as a function of the contour length for the four different charge state ranges, where $R_4(s)$ is shifted up by +2 nm for a better visualization. The circles represent the measured values while the solid lines denote the results calculated according to

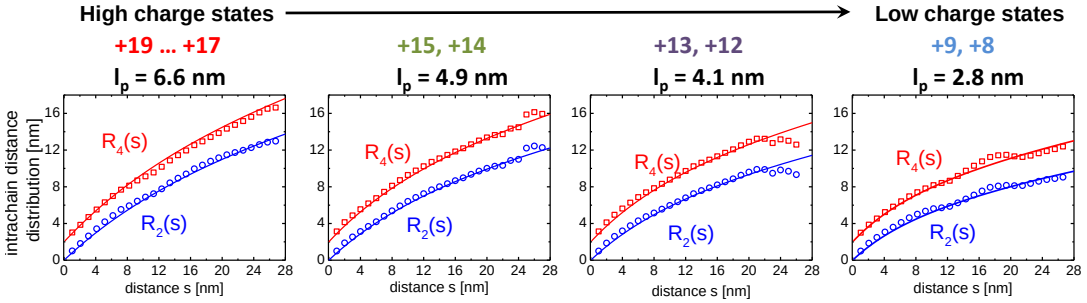

Fig. 4.5 Second $R_2(s)$ and fourth $R_4(s)$ moment of the ensemble-averaged end-to-monomer distance as a function of the contour length s (symbols) for each charge state range together with the results obtained from Eqs. (4.1) and (4.2) using the denoted persistence lengths l_p as input (lines). The $R_4(s)$ data have been shifted up by 2 nm for clarity.

Eqs. (4.1) and (4.2) using the persistence lengths labeled in the figure. Apparently, the slopes of the curves decrease with the protein's charge state. This reveals that the molecules have a more curved shape with diminishing charge state as it was observed in the STM images. The trend is quantified by the reduction of the persistence length. While for the high charge state $z = 19...17$ the persistence length l_p can be determined as 6.6 nm, it is only 2.8 nm for the low charge states $z = 9, 8$.

The resulting dependence of l_p on the average charge state z_{avg} is collated in Fig. 4.6 together with a table summarizing the obtained data points (Tab. 4.1). In the graph, the measured values of l_p (red symbols) are plotted together with the relation $l_p = 1.6\,\mathrm{nm} + 0.016\,\mathrm{nm} \cdot z_{avg}^2$ (blue line). This relation expresses the fact that the molecular stiffness of charged chain molecules is the sum of a bare (intrinsic) and an electrostatic contribution (see Ref. [191] and references therein). Accordingly, a persistence length of 1.6 nm is yielded when the protein is not charged, reflecting the intrinsic stiffness characterized by the bending rigidity and steric boundary conditions. This value can corresponds to a very compact structure on the surface as shown in Fig. 4.7 a). In this schematic illustration, the blue spheres represent the persistence length of 1.6 nm which is interpreted as the average length, over which the protein is straight. The most compact arrangement of the spheres is given by an arrangement in a hexagonal lattice. The connections between the centers of the spheres, illustrated by the black line, constitute the most compact conformation of the molecule with the given persistence length. In order to better visualize the protein in this scheme, the black line is overlaid by orange spheres representing the protein length monomers of 1 nm in diameter.

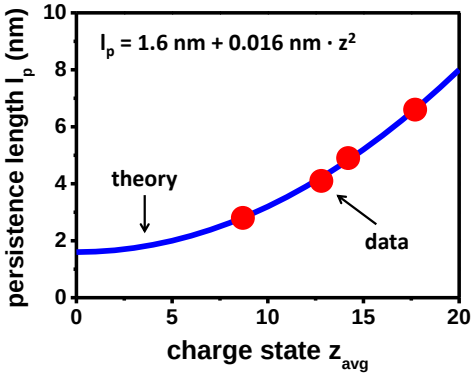

Fig. 4.6 The persistence length l_p as obtained from the STM images (symbols) together with a relation for l_p (line) as a function of the average charge state z_{avg}.

z	z_{avg}	l_p (nm)	E_{coul}(eV)
8 - 9	8.7	2.8	3.2
12 - 13	12.8	4.1	8.7
14 - 15	14.2	4.9	11.3
17 - 19	17.7	6.6	19.5

Tab. 4.1 Obtained persistence length of CytC and Coulomb energy of a linear rod as a function of the charge state z.

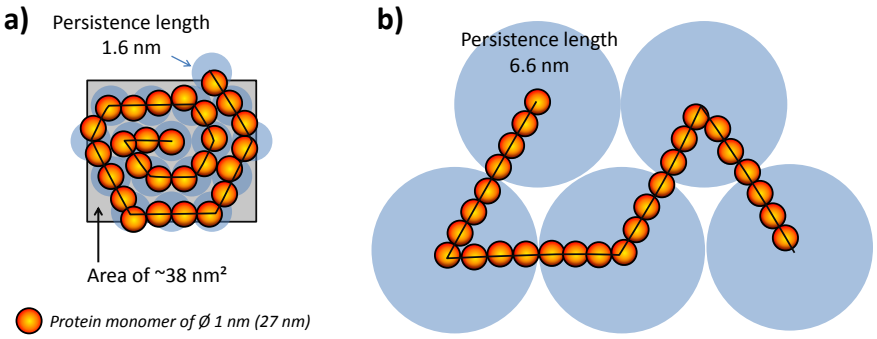

Fig. 4.7 Schematic illustration of the persistence length for a protein on the surface (blue circles). **(a)** The low value of $l_p = 1.6$ nm corresponds to a very compact patch with an area of around 38 nm^2, a value which was found for CytC deposited on a gold surface.[65] **(b)** For comparison the persistence length of 6.6 nm for the protein is depict.

For comparison, the conformation for a persistence length of 6.6 nm is shown in Fig. 4.7 b), which was measured for the highly charged proteins. Stunningly, the area corresponding to the very compact and neutral protein with a persistence length of 1.6 nm is around 38 nm^2. This value corresponds exactly to the area, which was measured for single CytC proteins deposited on the gold surface (cp. Fig. 4.10 a).[65] Hence, it can be concluded that the protein ions are discharged on the gold surface because this conformation was reached by diffusion and a repulsive interaction would have hindered a compact structure.

The relation displayed in Fig. 4.6 is fitted by a second order polynomial in z ($\propto z^2$) reflecting the Coulomb repulsion of the charges on the protein as the main driving force for the structure formation. In comparison to water, the Coulomb repulsion becomes substantially more important in vacuum, reflected by the decrease of the dielectric constant ϵ from $\epsilon_{\text{water}} = 80$ to $\epsilon_{\text{vac}} = 1$.[192,193] For a simple approximation of the Coulomb energy E_{coul} for the protein as a function of the amount of charges $z_{\max}$, a linear chain with equally distributed charges is assumed[194] and the following relation is hold:

$$E_{\text{coul}} = \int_1^{z_{\max}} \left(\frac{q^2 \cdot (z_{max} - 1)}{4\pi\epsilon_{\text{cytc}}\epsilon_0 \cdot l} \sum_{n=1}^{m} \frac{1}{n} \right) dm \tag{4.3}$$

In order to consider screening of the charge by the protein itself, the dielectric constant with $\epsilon_{\text{cytc}} = 2$ is included.[195] The values of E_{coul} for the charge states z_{avg} of CytC proteins shown in Tab. 4.1 are in accordance to the literature[180,194,195] and reveal a non-linear increase. Hence, a direct relation of charge state and conformation is shown.

In general, the statistical analysis confirms the subjective impression of the STM images and demonstrates the larger expansion of proteins with higher charge states on the surface. In some cases, however, the measured $R_2(s)$ and $R_4(s)$ deviate from the theoretical results (see in particular the low charge states in Fig. 4.5). The origin of these deviations might be ascribed to the landing process of the proteins as they are landed with a certain energy. This might induce partial backfolding or transient mobility after the deposition on the surface, that the WLC model does not consider.

4.4 Landing Process of Differently Charged Proteins

As the STM images and the analysis with the WLC model show, the gas phase conformation seems to be projected onto the Cu(100) surface upon deposition. Highly charged and stretched proteins in the gas phase are found expanded on the surface, whereas lowly charged species are more curved or even found in compact folded patches on the surface. Therefore the question arises, of how the landing process evolves.

In general, repulsive Coulomb forces between the charges have more impact on the conformation of the protein in the gas phase than in solution due to the loss of solvation effects. Furthermore, the Coulomb repulsion competes with attractive intramolecular interactions which are also stronger *in vacuo* than in solution. The free folding energy for cytochrome c in vacuum was calculated to a value of 22 eV.[196] It can be assumed that with the addition of the charge carrier H^+, this energy is further reduced since the possible hydrogen binding site is occupied by this additional hydrogen atom and no bond can be retained. For low charge states (z = 8, 9), the Coulomb energy of about 3 eV (Tab. 4.1) is relatively small and the attractive intramolecular interactions dominate the protein in terms of a compact conformation. For high charge states ($z > 17$) the repulsive Coulomb forces are in the same order of magnitude or higher than the intramolecular interactions. Thus, extended shapes are developed.[180]

During the landing process, the molecules are decelerated with an electric field to a kinetic energy of about 50 eV. As the electric field is approximately perpendicular to the sample surface, a partial alignment of the proteins might occur such that they touch the surface first with atoms located close to one of their ends. The reason for the alignment are the electric dipole moments of the proteins due to inhomogeneous charge distributions. For example, native CytC has a relatively large electric dipole moment of about 330 debye.[197]

From this perspective, the landing process of highly and low charged species can

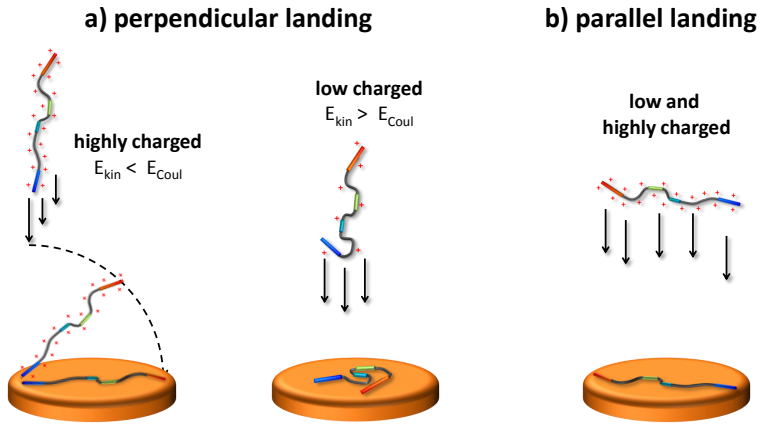

Fig. 4.8 Suggested landing processes for the two extreme cases of **(a)** nearly perpendicular and **(b)** parallel oriented proteins of high and low charge state.

be sketched in the following way (Fig. 4.8): As a result of the nearly perpendicular alignment to the surface caused by the dipole moment and the external field, the low and highly charged proteins touch the surface with one end. Highly charged molecules are considered as very stiff due to the Coulomb repulsion whereas the low charged species are relatively soft and flexible. When the kinetic energy E_{kin} of the stiff and extended proteins is in the same order of magnitude as the Coulomb energy E_{coul}, the proteins remain stretched during landing. Thus after touching the surface, they tilt to the side and remain in a extended configuration on the surface due to the high adhesion of the Cu(100) surface avoiding a refolding (Fig. 4.8 a).

In contrast, when E_{kin} is higher than E_{coul}, which is the case for the low charged proteins, the molecules are compressed after touching the surface with one end and form patches (Fig. 4.8 b). In addition, the higher amount of available hydrogen bonding sites due to the lower charge state and the closer distances of single amino acids to each other might induce more intramolecular interactions and less interactions with the copper surface. Hence, they form wiggled compact patches which is recognized in the statistical analysis and called partial backfolding.

A third option, which can not be excluded in the landing process are further landing angles in-between the perpendicular and the parallel alignment of the protein and the surface. During the ionization as well as by passing the ion optics the proteins can have gained a certain rotational energy. Depending on the rotation frequency and the velocity of the ions, the dimensions of the decelerating electric field in front of the sample surface might be too small to align the proteins. Assuming that the proteins land parallel to the surface, no difference between highly and lowly charged species should be observed, postulating that in both cases extended conformations are present (Fig. 4.8 c).

In order to understand the landing process in better, MD simulations[a] of the adsorption of CytC on a Cu(100) surface using the GROMACS software (see Ref. [129] and references therein) were performed. The energy function comprises bonded interactions such as bond stretch, bond angle, and dihedral terms as well as non-bonded interactions described by Coulomb and van-der-Waals potentials. Moreover, the positions of the Cu atoms were frozen at their crystallographic values. The proteins are transported to the surface under the influence of an external electric field such that they are soft-landed at a kinetic energy of about 50 eV. Furthermore, in the timescale of the simulations, the proteins are always partly aligned by the external electric field so that they touch the copper surface first with atoms located close to one of their ends.

In general, the precise location of the charges on cytochrome c after ESI is not known.[195,198–201] Moreover, it is not possible to perform computer simulation studies for all the charge permutations due to the huge number of ways to assign charges for CytC.[195] Here we consider protonation of all lysine and arginine residues because of their high proton affinity. For the low charge state with $z = 8$ all glutamic acid (Glu) residues and the aspartic acid (Asp) residues Asp 2, Asp 93 are deprotonated, while for the high charge state with $z = 18$ all aspartic acid residues and glutamic acid residues are uncharged except for the deprotonated Glu 104 residue. In the case of the $z = 14$ charge state, the glutamic acid residues Glu 21, 62, 69, 92, 104 are deprotonated, whereas the remaining glutamic acid residues and all aspartic acids are uncharged. Figure 4.9 displays the calculated conformations of three differently charged proteins ($z = 18, 14, 8$) using a space-filling representation together with three measured STM topographies of proteins deposited with the same charge state.

In principle, a huge conformational space is accessible to an unfolded protein in contrast to a natively folded protein. Therefore, one cannot find calculated protein conformations which agree exactly with the measured STM topographies of unfolded CytC. Nevertheless, the three calculated protein conformations shown in Fig. 4.9 exhibit characteristic features similar to the measured topographies. Decreasing the charge state from $z = 18$ to $z = 8$ increases bend angles of the proteins due to reduced molecular stiffness. From a set of images collected in additional independent simulations, the trend towards more highly bent proteins upon decreasing z is evident. In the case of low charge state CytC with $z = 8$, tight loops with 180° backfolds have been found in the MD simulations. In particular, low charged sections along the backbone act like flexible hinges, thereby decreasing

[a]The MD simulations were preformed in collaboration with Ludger Harnau, *Max-Planck-Institute for Intelligent Systems & IV. Institute for Theoretical Physics, University Stuttgart*

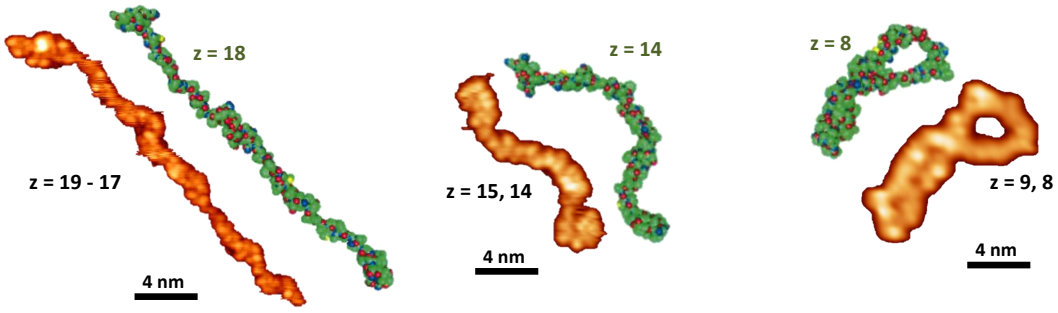

Fig. 4.9 Calculated conformations of unfolded CytC of charge state $z = 18, 14, 8$ using a space-filling representation, where the carbon, oxygen, nitrogen, sulfur and hydrogen atoms are shown in green, red, blue, yellow and white, respectively. The Cu(100) surface is omitted from the top views for clarity. For comparison three measured STM topographies for charge states $z = 17 - 19, 14 - 15, 8 - 9$ are shown.

the end-to-end distance of the protein. For high charge state CytC with $z = 18$, intramolecular repulsion between the positively charged amino acids leads to unfolding and relatively extended conformations.

So far, a fixed charge distribution on a protein during the whole adsorption process was considered. However, in principle the possibility of discharging of proteins upon contact with the copper surface has to be taken into account. To investigate a potential link between discharging of adsorbed proteins and their final conformation, additional simulations of adsorbed and uncharged CytC using the MD results shown in Fig. 4.9 as initial systems were performed. These simulations resulted in very similar protein conformations, with minor variations of the location of some amino acids.

It is concluded that, within the limits of the present MD simulations, no major conformational changes of the adsorbed proteins upon discharging is observed. This result applies specifically to the case of a Cu(100) surface due to the strong van-der-Waals interactions between proteins and this surface as compared to intramolecular protein interactions.

Preliminary simulations of CytC adsorption on surfaces with weaker protein – surface van-der-Waals interactions exhibit a two-dimensionally confined refolding upon discharging after adsorption. It is noted that these conclusions rest on classical MD simulations, which do not allow one to study proton transfers. Hence they are in no way final. Nevertheless, experimentally refolding has been already observed.[65] The deposition of unfolded highly charged CytC on a gold surface resulted in compact patches at the elbow sites of the gold reconstruction

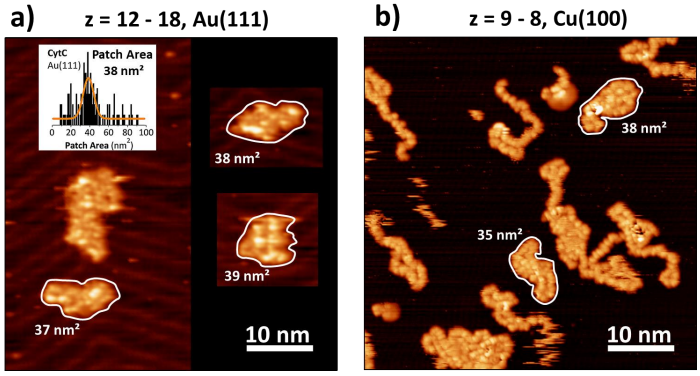

Fig. 4.10 Comparison of CytC deposited on Au(111) **(a)** and low charged CytC on Cu(100) **(b)**. In both cases patches of 38 nm^2 area corresponding to single CytC proteins are observed although their formation is governed by different processes on the different surfaces.

(Fig. 4.10 a). Thus, discharging on a metal surface after deposition is proven.

Furthermore, patches of similar sizes are also observed for low charge states on the Cu(100) surface (Fig. 4.10 b). In contrast to the patches on the gold surface they do not originate from discharging and subsequent refolding since the copper surface prevents any mobility of the proteins. Thus, these patches are caused by low stiffness during landing, induced by the Coulomb energy.

Deposition Energy Dependencies

According to the proposed landing model, the kinetic energy of the proteins in the ion beam should have an impact on the adsorption process. For a stiff protein, extended configurations are expected and have already been observed for landing energies of the same magnitude. By increasing the landing energy, augmented buckling with smaller end-to-end distances of the protein is expected. In contrast, the deposition with different energies of low charged and flexible proteins, should not result in any conformational differences. For both cases, at a certain point the kinetic energy is too large, leading to fragmentation of the molecule.[12] To address this issue, the kinetic energies were considered in the simulations as well as in experiments.

In the simulations, various kinetic energies were studied by changing the strength of the external electric field. As a result decreasing end-to-end distance of the proteins upon increasing the kinetic energy was found. In the molecular view, this can be ascribed to a reduced time available for molecular reorientations of the protein after the first contact with the copper surface.

Experimentally, the landing energy was increased as the width of the energy

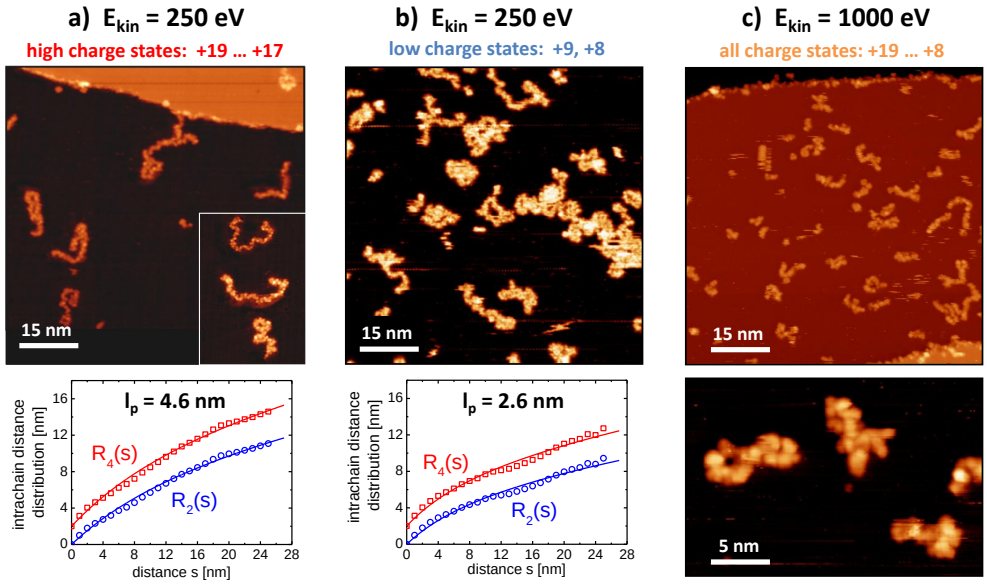

Fig. 4.11 High energy deposition of CytC on Cu(100). After deposition with a landing energy of 250 eV, intact proteins with a persistence length of **(a)** 4.6 nm for the high charge states and **(b)** 2.6 nm for the low charge states are observed. **(c)** After landing all charge states of the protein with an energy of 1000 eV only fragments are observed.

distribution in the beam is the limiting factor for lower energies. In preliminary deposition experiments of the highly charged and low charged CytC with 250 eV landing energy, results consistent with the simulations were obtained. In both cases, the persistence length decreased, revealing a smaller end-to-end distance and a more curved shape (Fig. 4.11 a, b). In particular, the persistence length of the highly charged protein exhibited a distinct change of about 30% compared to the persistence length at 50 eV landing energy. In contrast, the lower charged species revealed a similar persistence length in comparision with the low energy deposition. Upon increasing the energy to 1000 eV, only smaller fragments of the protein are found on the surface (Fig. 4.11 c).

These results support the proposed landing model, which describes the conformation of the protein as an interplay of stiffness induced by Coulomb repulsion and kinetic energy during landing. Increasing the landing energy above the persistency energy of the molecule, which is steered by the charge state, leads to more compact conformations as the molecule is compressed upon landing. For low charged molecules, this effect is less pronounced since they are already soft and adopt a compact conformation in any case. When the landing energy is too high, the proteins will fragment and smaller residues are observed on the surface.

4.5 Summary & Conclusion

In summary, we have demonstrated the deposition of differently charged and unfolded proteins from electrospray ion beams on Cu(100). STM images showed randomly distributed molecules of about 25 ± 2 nm length, which had a predominately stretched configuration for high charge states and a predominately compact folded configuration for low charge states. Statistical analysis with the worm-like chain model revealed a correlation between protein charge state and protein configuration in terms of a charge state dependent persistence length. The persistence length is a measure of the molecular stiffness, which is caused by the Coulomb repulsion between the charges on the molecule. According to this model, a landing process of the charged species is proposed, in which the proteins either remain in the stretched configuration from the gas phase or are compressed into compact patches on the surface. This process was modeled with MD simulations, which provided a large agreement between simulated structures and measured STM images of proteins with different charge states. Moreover, simulation and experiment showed decreasing persistence length with increasing deposition energy.

It is concluded that the conformation of proteins on adhesive surfaces can be steered with ES-IBD either by charge state selection or by the landing energy. Hence, ES-IBD is a tool enabling a high control of the conformation of proteins on the surface which cannot be realized by any other deposition techniques. This high control envisions the preparation of functional coatings based on amino acid polymers which are highly functional systems.

Besides the conformation of the protein, the different amino acids and their sequence is important for the functionality. With this CytC study, a high resolution of the amino acid chain is realized by STM imaging, but it was not possible to determine the C- and N-terminal or any other amino acid of the protein. This can be understood as STM can not give any chemical information and has to rely on structural arrangements. The high conformational freedom of the amino acid chain makes such reliance on structure very difficult, hence repeating and characteristic lobes on different single proteins could not be identified. However, an identification of the amino acids and their role for the surface conformation of the protein would be import for potential functional coating with amino acids. Understanding the role of certain amino acids with respect to the yielded conformation and functionality on the surface would enable the highest level of control. Therefore, amino acid interactions of proteins on surfaces have to be studied.

A way to study these interactions is the reduction of the conformational freedom by shortening the amino acid chain. The conformation of a nine amino acid peptide is examined in the next chapter as a function of different surface interactions.

5 The Folding of a Nine-Amino Acid Peptide on Different Surfaces

In nature, combining the 20 available types of α-amino acids into polymers leads to highly complex, functional molecular structures. They can be found in every organism and, after water, constitute the second most frequent compound class in the human body. In the natural environment of these structures, in aqueous solution, they take on a three-dimensional (3D) conformation. The precise 3D conformation of the amino acid chain is crucial to its functionality. The process in which the one-dimensional string of amino acids is converted into a 3D structure is called folding. It is steered by the molecular and atomic interactions of the amino acids but also through a backbone bond angle preference of the polymer and the chain entropy.[202]

A common interaction between amino acids are hydrogen bonds, which lead to the 3D folding of α-helices or β-sheets. Furthermore, coordination bonds between metals and the amino acids are possible, for example, in the zinc finger motif, where two cysteine and two histidine residues coordinate a zinc atom.[203,204] Covalent bonds in the form of disulfide bridges can also be realized, allowing further stabilization of the configuration.[205,206]

The unraveling of folding pathways with atomic resolution can provide deeper insight into the biological functionality of natural proteins and peptides. For instance, the self-assembly of misfolded peptides and proteins is of high interest as they can still fulfill a function but trigger therewith diseases like Alzheimer's, Parkinson's and type II diabetes, the so-called folding diseases.[202,207,208] Furthermore, folding of amino acid polymers on surfaces can be a way to functional surfaces, which might be utilized for technical applications in biocompatible materials,[209] catalytic model systems,[29,30] molecular electronics, or spintronics.[210] The robust and relatively simple synthesis of oligo-amino acids provides a way by which the functionality can be easily altered in well-defined, small steps by exchanging certain amino acids in the sequence from a library of 20 different α-amino

acids or even other types.

Several studies have already been performed to characterize single amino acids,[211,212] short peptides,[199,213] or synthetic oligoamines[186] on surfaces with scanning tunneling microscopy (STM). In these works, the adsorption behavior, as well as the conformational arrangement has been addressed. As a matter of course, both high resolution microscopy, and a clean environment are necessary to study these systems at the nanoscale. For larger molecules, the latter requirement is much more difficult to obtain. While some single amino acids can be evaporated onto surfaces in ultra high vacuum (UHV) and studied with STM and other conventional surface characterization techniques in a controlled environment with high resolution, larger molecules such as peptides and proteins with more than four amino acids, can only be performed at the solid/liquid interface or after deposition from solution. These techniques have the drawback that the surfaces are not atomically clean, there is less control over the deposition process, and the mobility of adsorbates cannot be reduced by low temperatures allowing the detailed analysis of the interactions between individual species on the surface. Therefore, detailed information about the adsorption process and the conformation of the deposited species is more difficult to obtain.

A method to deposit peptides and proteins in a controlled manner onto clean surfaces is made available by electrospray ion beam deposition (ES-IBD).[10–12,65] It allows the transfer of large molecules like whole viruses[70] and proteins[67] into the gas phase and to vacuum, where they are brought intactly onto atomically clean surfaces. In the previous chapter, we presented a study with high resolution STM images of Cytochrome C, a protein with 104 amino acids.[65] Randomly distributed strings are observed on a sticky, high interacting surface, while 2D randomly refolded patches are seen on a less interacting surface on which the molecules had slightly higher mobility. This showed, on the one hand that the surface plays an important role, as the conformation of the molecule can be steered by the interaction of the amino acids with each other in the chain or with the surface. On the other hand, high resolution at the single amino acid level was not sufficient to identify the N- or C-terminal of the protein or a specific amino acid. This was caused by the non-ordered and random alignment due to the protein's high degree of conformational freedom. Even the assumption that every amino acid has only two conformations available results in $2^{104} \approx 2 \cdot 10^{31}$ different possible conformations. Thus it is not surprising that so many different conformations were observed.[65]

In order to study the properties of amino acid polymers on surfaces it is thus necessary to have ordered systems on the surface, which allow the identification

of the single amino acids in the chain. One way to achieve this might be given by the length reduction of the amino acid chain. Decreasing the number to 10 amino acids reduces the conformational freedom enormously by 28 orders of magnitude by the previous approximation. This still provides a high degree of freedom for the peptide strand, hence folding should be observable.

In the following, Bradykinin, a natural peptide with a total chain length of nine amino acids and a mass of 1060 amu (Fig. 5.1 a) is studied on different surfaces deposited by ES-IBD. It consists of the five different α-amino acids arginine (Arg), proline (Pro), glycine (Gly), serine (Ser), phenylalanine (Phe), and in its natural environment it causes a higher permeability and a dilation of blood vessels in the body.[214] The peptide was soft-landed in UHV on atomically clean surfaces and studied with STM. Several conformations, starting from single isolated structures, to dimers, and hierarchical self-assemblies of dimers, are observed depending on the strength of the molecule-surface interaction. These structures provide insight into the folding processes of a single peptide on a surface. Structural motives of the species on the different surfaces and the application of a combination of theoretical modeling methods, helped to identify the different amino acids involved in the folding and adsorption process. In molecular dynamics (MD) simulations, several possible molecular structures were determined for one surface. An agreement to the measured structures was found by reproducing the experimentally obtained structures through possible folding capabilities of the modeled structures. For comparison to our STM measurements, the electronic structure was calculated by applying density functional theory (DFT) to the molecular structure fitting the experimental results.

The study shows 2D folding of peptides on different surfaces and the possibility to identify the single amino acids within the obtained structures. Hence the influence of certain building blocks on the structure and the functionality can be studied in detail. Together with the synthesis of specialized peptides, two-dimensional nanostructured peptide surfaces with unique catalytic and chemical functions can be envisioned.

5.1 Experimental Procedure and Mass Spectrometry

For the ES-IBD experiments, Bradykinin (BK, Sigma-Aldrich, B3259) was dissolved in water/methanol mixtures with 5% formic acid. Positivly charged gas phase ions were created with a nanospray emitter at $3 - 4$ kV and a flow rate of $15\mu l/h$. The ions are transferred into vacuum and guided through four differentially pumped stages to the time-of-flight mass spectrometer (TOF-MS) and

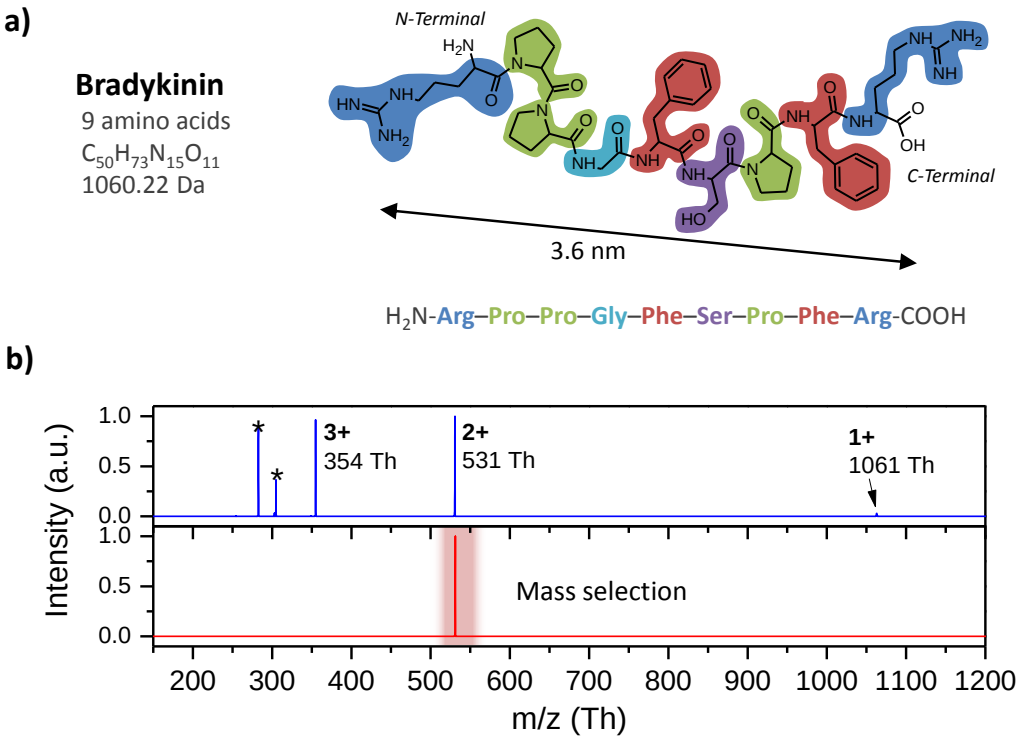

Fig. 5.1 **(a)** Sequence, mass, and chemical structure of Bradykinin. **(b)** ESI mass spectra in positive mode of Bradykinin dissolved in H_2O/MeOH showing several charge states. For the deposition, the doubly charge species was mass selected.

the energy detector in the fourth chamber at a pressure of 10^{-7} mbar yielding an ion current in the range of 500 pA – 1 nA. The mass spectrum of the positively charged BK ion beam in Fig. 5.1 b) is very clean and shows intense peaks between 200 and 600 Th. Amoung them, the doubly charged species at 531 Th and the triply charged molecule at 354 Th are observed with the highest intensity. The peaks marked with a star are unidentified contaminants or fragments. In addition, a peak of low intensity is found at 1061 Th corresponding to the intact, singly protonated peptide.

In order to have one defined molecular species on the surface, the ion beam was mass-selected. Since the single charged protonated molecule at 1061 Th is of very low abundance, the doubly charged molecule at 531 Th was mass-selected for the deposition (see Fig. 5.1 b). In this way large clusters, which may not be detected in the mass spectrum as well as low mass contaminats are excluded. As the charge state may also influence the structure formation, we chose to deposit only the charge state $z = 2$.

For soft-landing the ions were decelerated with a positive voltage applied to the

sample, resulting in a landing energy of 10 eV. Before deposition, the different samples were cleaned by several sputter and annealing cycles to ensure atomically clean surfaces. Directly after the deposition, the sample was transferred in-situ to a variable temperature STM (Omicron VT-STM, Omicron Nanotechnology GmbH, Germany) and investigated at room temperature (RT) or at low temperature (LT) of 45 K.

5.2 The Structure of the Bradykinin on Different Surfaces

In the following section, the doubly charged peptide, deposited on different surfaces and analyzed with STM is considered. The surfaces thereby are characterized by different interaction strengths and different symmetry affecting the molecule's mobility and arrangement.

The strongest interaction among the utilized surfaces is exhibited by the Cu(110) surface, which additionally provides a structural template defined by its symmetry. The atoms in the first layer are aligned in rows in [110]-direction separated by a distance of 3.6 Å, the lattice constant of copper, while atoms within a row have a smaller distance to each other. Due to this gap between the rows, deposited molecules prefer to align along the [110]-direction.[215] The next strongly interacting surface is Cu(100). It is characterized by a square lattice and is known to provide adatoms on the surface, which are not imaged in the STM.[165] The third surface ordered by interaction strength is Cu(111). It exhibits hexagonally aligned atoms at the surface and has the lowest interaction strength compared to both of the other copper surfaces. An even less interacting surface is obtained by changing the material from copper to gold. The Au(111) surface is of hexagonal symmetry as well and exhibits a so-called herringbone reconstruction; a zig-zag pattern of alternating face-centered cubic (fcc) and hexagonal close packed (hcp) surface atoms. The turning sites of the zig-zag pattern, the elbow sites, are thereby preferred anchoring positions for molecules.

Upon the deposition of the doubly positive charged peptide on the Cu(110) surface, isolated single molecules are found in STM at RT (Fig. 5.2 a). Besides some random structures with no preferred configuration, two repeating and different aligned structures are observed on the sample. Each of the two configurations are found in two orientations rotated by 180°. The first one is elongated along the [110]-direction and exhibits three bright lobes with a height of 1.5 to 1.8 Å. Furthermore, two small branches are identified in the middle part of the molecule pointing up and down in the ⟨100⟩-direction, respectively. The length of the structure is around 3.2 nm and roughly agrees with the length of the single peptide

being 3.6 nm (Fig. 5.1 a). Thus, the structure is ascribed to a single molecule. The second recurring structure on the surface is tilted by approximately 45° in comparison to the first monomer and is aligned with the long side in the [111]-direction, exhibiting three bright lobes as well. As it has a similar size and lobes at similar positions, it is also ascribed to a single peptide but with a different conformation.

The deposition of the molecule on a Cu(100) surface results exclusively in structures exhibiting two bright double lobes with a twofold rotational symmetry at RT, which are oriented along the ⟨110⟩-directions and have a height of 1.5 to 2.2 Å (Fig. 5.2 b). As these structures are roughly twice as big as the monomers observed on the Cu(110) surface and the length of one half of that feature from the bright lobes to the fainter parts is with 3.3 nm comparable to the elongated monomer, we conclude that they represent a dimer structure.

Molecules which have not formed a dimer, are mobile and are just recognized by characteristic traces with STM at RT. When the sample is cooled down to low temperatures and thus the mobility of the molecules is reduced, single immobilized entities are seen in-between the dimer structures. They are non-interacting and have no preferred orientation on the surface (Fig. 5.2 b). Interestingly, the single molecules are not interacting with the dimers nor do the dimers interact with each other. This indicates that the reactive sites of the monomers are saturated by constructing these dimers and that the dimers are strongly interacting with the surface. Furthermore it shows, that also the single molecule reacts just with specific sites of a second molecule, which are not available at the dimers anymore.

Upon increasing the mobility of the molecules by changing the symmetry of the surface to a hexagonal Cu(111) arrangement, no immobilized structures are found at RT. At low temperatures, the molecules were still mobile as features of moving molecules were observed. But in addition, immobilized features were observed arranging along the ⟨110⟩-direction of the surface (Fig. 5.2 c). These features exhibit a two-fold rotation symmetry with two bright lobes close to the rotation axis. The length of a half of that feature is about 3.1 nm and has an apparent height of 2.8 Å at the lobe. Due to that size the feature is also attributed to be composed of two molecules. Beside the single dimer structures also a few agglomerations are found at the surface in contrast to the Cu(100) sample. This shows on the one side, that the interaction between the dimer and the surface is low enough that they can diffuse and, on the other side, that the dimers in this configuration are able to interact with each other.

The lower interaction between the molecules and the surfaces is also seen in the line profiles of the entities. By comparing the line profiles of the elongated

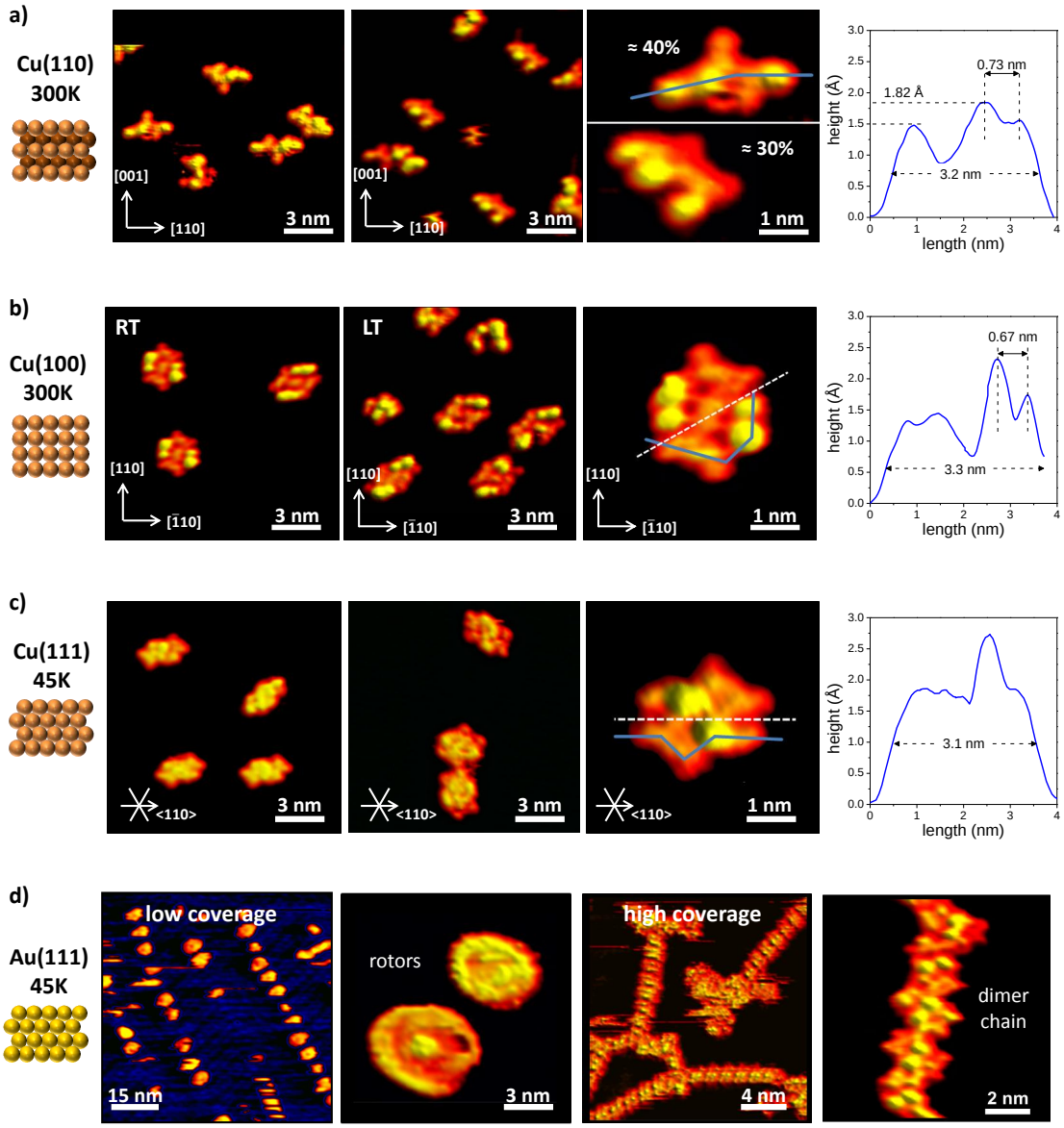

Fig. 5.2 The structure of Bradykinin on different surfaces. **(a)** Single elongated molecule along [110]-direction and tilted structure along [111]-direction on Cu(110) at RT. **(b)** Twofold rotation symmetrical dimer structure at RT on Cu(100). At LT also individual, immobilized peptides are observed. **(c)** A different dimer structure on Cu(111) at LT. **(d)** Bradykinin on Au(111) at LT. At low coverage they stick at the elbow sites and rotate, while at high coverage weakly bonded dimer chains are formed.

monomer on the Cu(110) surface and the corresponding monomers in the dimer structures on the Cu(100) and Cu(111) surfaces in Fig. 5.2, it is seen that the length decreases while the height increases with the change from Cu(110) to Cu(100) and Cu(111). This higher compactness is explained with the decreasing interaction strength between the molecules and the surface while the intramolecular interactions are becoming stronger.

Upon reducing the surface interaction even further by using an Au(111) surface, no molecular features were identified at RT, indicating a very high mobility of the molecules. At low temperatures, they start to immobilize partially at the elbow sites of the herringbone reconstruction by rotating around these positions (Fig. 5.2 d). These rotors have a radius between 2 nm and 3.5 nm and can be attributed to single peptides or dimers, which due to different anchoring groups sticking to the elbow sites,[216] generate disks of different diameters. Upon increasing the coverage, the molecules are forced to interact and form extended chains in different directions at low temperature. Interestingly, these chains are constructed from dimers of the same appearance as observed on the Cu(111) surface, since the building blocks of the chains also exhibit the two bright and characteristic lobes discussed previously.

These results show that the surface interaction plays a significant role in determining the molecular conformations on a substrate and the arrangement of the dimers. The degrees of freedom which the molecule has and the different interaction strength of the different surfaces of different symmetry, leads to five different structures of one and the same molecule. With decreasing diffusion barrier, the molecules evolve from isolated species to interacting molecules, creating self-assembled dimers and finally even hierarchically ordered chain structures.

5.3 Sequence – Structure Correlation

In order to unravel the structure of the dimer and the single BK peptide in the different conformations and to understand the driving force behind the highly specific dimer formation, the position of the single amino acids in the observed structures is important. The identification of the amino acids would enable to detect the responsible parts involved in the bonding process and identify other parts involved in possible functionalities. Knowing the effect of every single amino acid would further enable to modify the structure and the function of the peptide on the surface by exchanging amino acids in the sequence for future deposition experiments.

In the STM images the sequence of the peptides cannot be directly correlated to

the structures on the different surfaces. For example, only a number of five to six lobes are observed in the structures. Those are too few in comparison to nine amino acids of the molecule. This indicates that some lobes are composed of more than one amino acid or do not contribute to the STM image significantly. Especially, no chemical information can be derived from STM measurements, which hinders the identification of amino acids at particular positions.

However, STM allows a precise comparison of the geometry between the found structures for the monomers and the dimers and might thus help to identify the amino acids, which can be further supported by theory. Hence, a first step is a detailed look at the measured structures. Since the molecule is large and flexible, structural relationships might be established by connecting the different formations through conformational arrangements or folding processes. Furthermore, molecular dynamic (MD) simulations and density functional theory (DFT) calculations can determine the molecular as well as the electronic structure of the peptide on a surface and help thus to understand the observed features. The combination of these two approaches in the following, enables the determination of a plausible configuration of the peptide and allows the assignment of the observed lobes to the amino acid residues.

In Fig. 5.3 the two monomer and two dimer structures are shown again in the four corners of the figure. The different STM measurements can be compared to each other as the appearance of the structures is constant for a bias voltage interval between -1.3 V and -2 V and the structures shown were recorded at -1.6 V. It is noticed that all structures exhibit the same bright lobes in a characteristic pattern as mentioned in the previous section. For clarity, these lobes are labeled in the insets in Fig. 5.3 with numbers ranging from 1 to 4.

The double lobe feature of the first monomer (Fig. 5.3 a) is tagged with (1a) and (1b) and the single intense lobe at the other end is labeled with (2). Furthermore, the two less bright branches pointing up and downwards are labeled with (3) and (4). Transferred to the symmetric dimer structure on Cu(100) (Fig. 5.3 b), a similar double lobe feature is recognized oriented along the ⟨110⟩-direction. Due to the same directions in which the double lobe feature is aligned on the two surfaces and the similar distances of the lobes with 0.73 nm on the Cu(110) and 0.67 nm on the Cu(100) surface (cp. Fig. 5.2), it seems reasonable to rearrange two monomers in the structure of a dimer. Stunningly, this is possible by connecting two monomers over the branch labeled with (4) and a simple rotation by 90° of the double lobe (1a) and (1b) (see Fig. 5.3 α). This would be meaningful if the electronic structure is only dependent on the amino acid sequence and largely independent of the conformation of the peptide. From the appearance of the STM

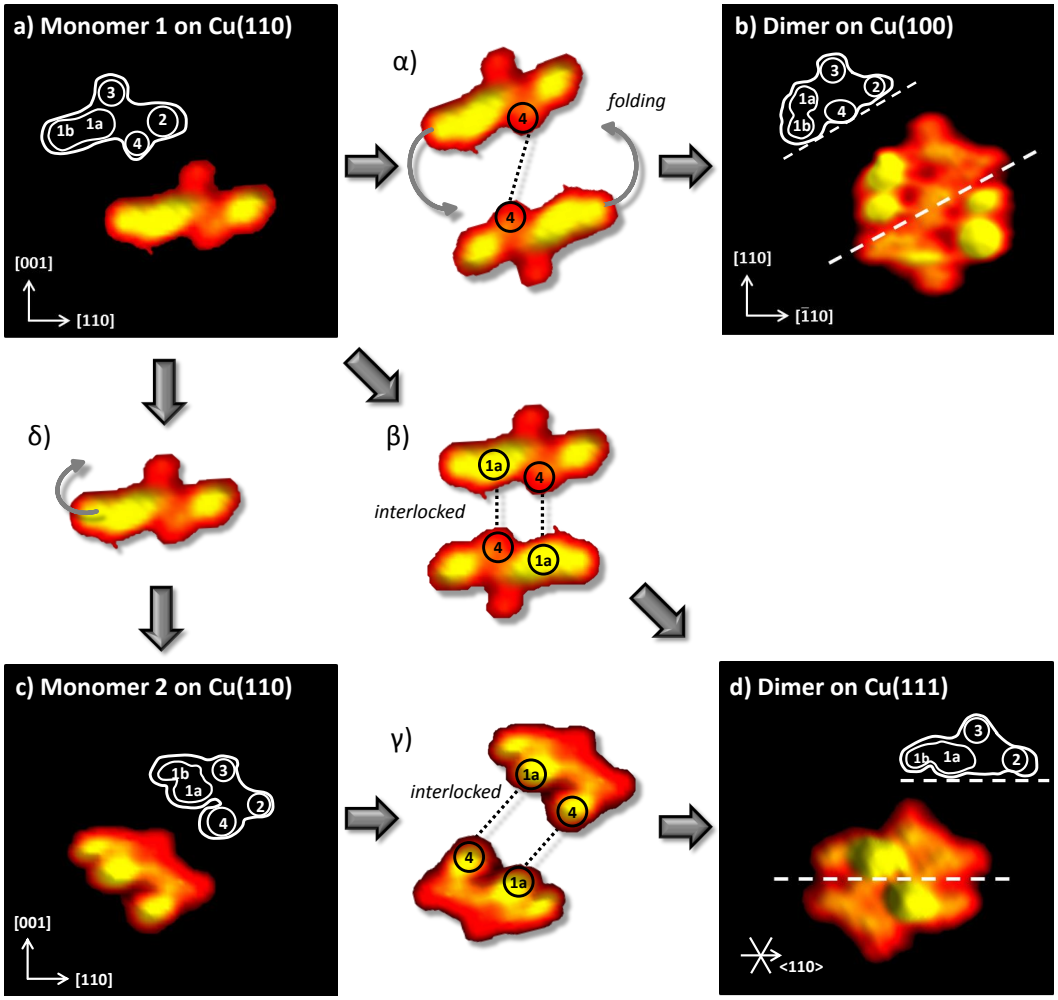

Fig. 5.3 Structural relation between the observed monomers and dimers on different surfaces. By folding and small structural rearrangements all structures can be brought into accordance.

images this seems to be the case and is confirmed in the following by electronic structure calculations.

On the Cu(111) surface the ⟨110⟩-direction is also found. The combination of two monomers as present on the Cu(110) surface along that direction by interlocking them, enables the reproduction of the dimer on the Cu(111) surface (Fig. 5.3 β). In this way, the two molecules are overlapping with their lobes (1a) and (4). Accordingly, the two bright lobes observed in the dimer, are each the overlap of the lobe (1a) of one monomer with the lobe (4) of the other monomer and appears thus even higher.

Alternatively, the dimer on the Cu(111) surface (Fig. 5.3 d) can also be constructed from the second monomer (Fig. 5.3 c) found on the Cu(110) surface. This

is somewhat simpler to visualize as the monomer itself provides the shape of the upper half of the dimer. By interlocking the lobes in the middle and at the end of one monomer with the corresponding lobes of another monomer molecule, the dimer is formed (Fig. 5.3 γ). The involved lobes can be identified as the same positions known from the first monomer, which are the lobes (1a) and (4). This can be understood by relating the structures of the two monomers to each other. Rearranging the lobe (1b) of the first monomer by moving it upwards brings the lobes (1a), (1b) and (4) to one line in the $\langle 111 \rangle$-direction (Fig. 5.3 δ). Thus, it is in the conformation of the second monomer. The only difference is that the lobe (4) is brighter in the second conformation of the monomer than the first. This might be related to a slightly different alignment of the monomer to the substrate in which this part is shifted upwards by interactions.

In summary, the peptide agglomerates are characterized by a very compact structure as well as by a great flexibility. The observation of the same lobes in a characteristic pattern for all structures enabled to relate the structures to each other by structural rearrangements. It can be assumed that the structural rearrangement observed on the different surfaces is made by bond rotation around the backbone, rather than by straining the molecules.[217,218] The fact that the characteristic lobe pattern is found in all structures leads to the conclusion that the electronic structure is only coupled to the amino acid sequence and is mostly independent of the conformation.

MD and DFT calculations

In order to assign the different lobes to certain amino acids and determine the C- and N-terminal of the peptide, theoretical calculations were performed to be compared to the structures observed with STM. In general, for STM studies the molecular arrangement as well as the electronic structure of molecules are calculated by DFT.[219,220] From these calculations STM images can be extracted for constant height or constant current mode that allow a direct comparison.

However, as the molecule utilized is composed of 149 atoms, its calculation with DFT is very demanding, especially when the surface is included. To overcome this problem we used a unique approach, combining MD simulations and DFT calculation. MD simulations are frequently applied to calculate molecular structures in force fields. In this context it is often used to refine three-dimensional structures of proteins and other macromolecules from experimental data found by NMR or XRD.[61,221,222] We apply this technique to determine the molecular structure of the peptide upon deposition on a surface by ES-IBD. This optimized structure is then used to determine the electronic structure by DFT. In this way, a comparison

to the STM images is given. As all of the observed structures can be related to each other, it is sufficient to initially treat just one surface with one structure. Therefore we will only look at the case of the dimer structure on the Cu(100) surface in this section.

MD simulations[a] of the adsorption of the peptide on a Cu(100) surface were performed using the GROMACS software (see Ref. [129] and references therein). Thereby the doubly charged Bradykinin was landed on a Cu(100) surface where the atoms were frozen at their crystallographic positions. Upon landing the molecules were discharged and relaxed.

In this way, three different, stable dimer structures were found on the surface (Fig. 5.4). The first structure (I) is very compact as the monomers are interlocked. It is the structure with the lowest energy, which is found to be stable aligned along several directions on the substrate. The second (II) and third (III) dimer structures occupy more space and the monomers are separated further from each other.

Comparing the structures, it is recognized that the functional parts containing oxygen (red) and nitrogen (blue) are encased in structure (II) while in the other two cases, they are also exposed to the outside of the dimer. This means that these dimer structures would strongly interact with other molecules or neighboring dimers on the surface. As this is not observed for the dimer on the Cu(100) surface, the formations (I) and (III) seem less probable to fit our observations. An overlay of these structures with the STM images show that (I) is too small while (III) is too large and only the second structure shows a reasonable agree-

[a]The MD simulations were preformed in collaboration with Ludger Harnau, *Max-Planck-Institute for Intelligent Systems & IV. Institute for Theoretical Physics, University Stuttgart*

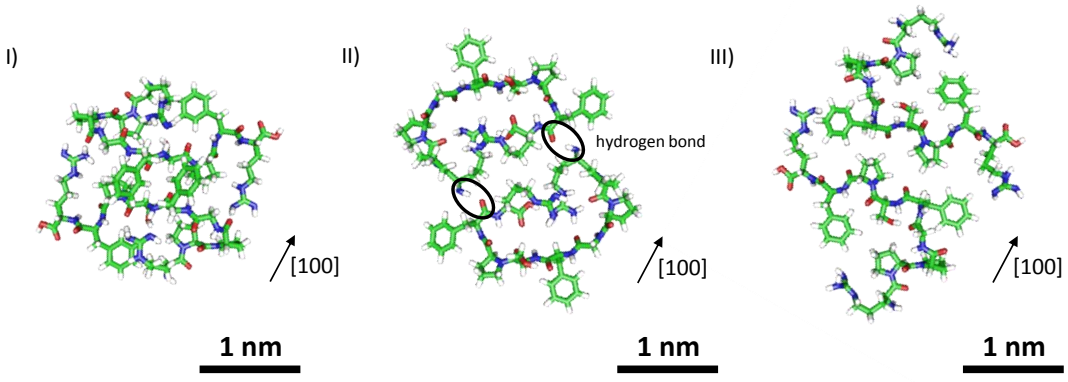

Fig. 5.4 Three possible low energy dimer structures obtained from the MD simulations. For clarity, the underlying surface is not plotted but instead the surface direction is indicated.

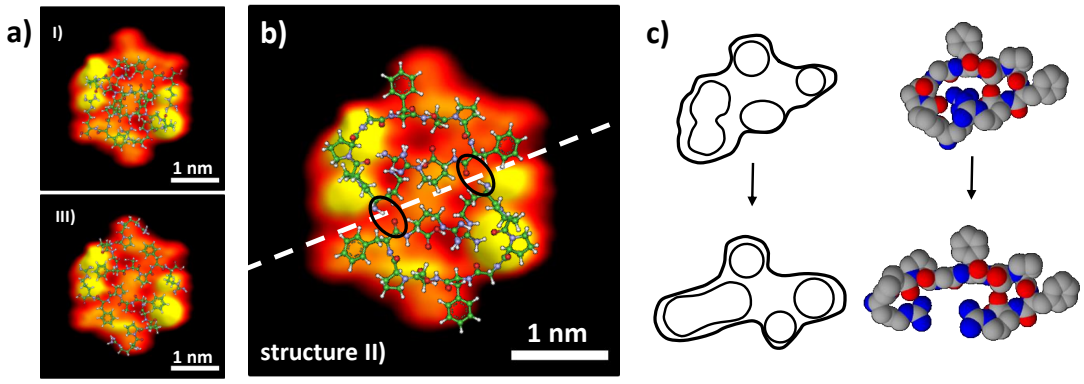

Fig. 5.5 **(a)** Overlay of the simulated structures with the STM image of the dimer shows a misfit for the structure I) and III) while a reasonable agreement for the structure II) is observed **(b)**. An important property of the monomer structure is the possible folding from an angled configuration into an elongated one, as observed on the Cu(110) surface **(c)**.

ment (Fig. 5.5). Furthermore, the monomer of the dimer structure (II) permits the folding process of its parts in a way that produces agreement with the bright lobes observed in the STM images. An important aspect for the structure determination, is that the bend monomer of the dimer structure (II) can be easily transformed into the elongated shape observed for the single peptides on the Cu(110) surface by a rotation of the corresponding part without a large rearrangement of the molecular structure (Fig. 5.5 c). this is not possible for the monomers of the other two structures (I) and (III). Thus structure (II) is the most reasonable configuration among the three simulation results. The two monomers of this structure are coupled to each other via two hydrogen bonds (N–H$\cdots$O) and van-der-Waals interaction (Fig. 5.4). According to the folding scheme presented in Fig. 5.3, this is the lobe (1b) bonding to the space between the lobes (4) and (2).

In order to verify whether the structure also agrees with the contrast measured in the STM, density functional theory calculations are performed to gain further insight into the density of states of the given Bradykinin conformation.

Calculations[b] were carried out using the ORCA 2.8 program[223] with the B3LYP functional and the 6-31G(d) basis set for the neutral molecule in its ground state. The geometry of the molecule was taken from the previous molecular mechanics geometry optimizations, in which the peptide was able to relax in the presence of a copper surface. Single point calculations excluding the surface were performed

[b]The DFT simulations were preformed in collaboration with Rico Gutzler, *Max-Planck-Institute for Solid State Research, Stuttgart*

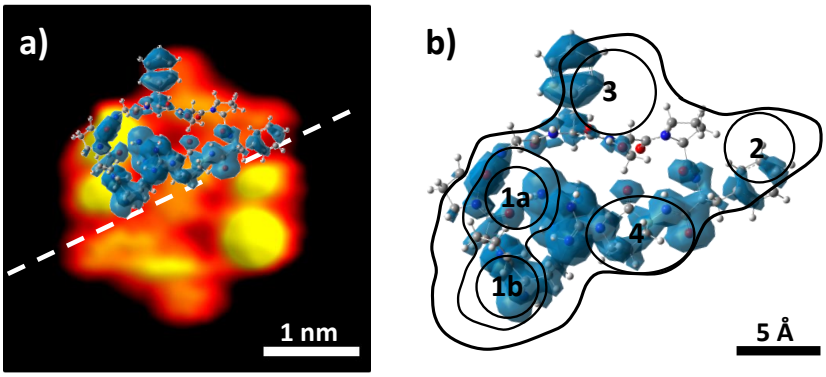

Fig. 5.6 **(a)** DFT calculation of the molecular structure obtained from MD simulations showing the 10 first occupied orbitals in blue with the structure measured with STM for negative bias. **(b)** The majority of the occupied orbitals are located in the bright double lobes ⓵ⓐ and ⓵ⓑ and in the inner lobe ④.

to find the corresponding electron density. The partial electron density presented was calculated as the sum of squared molecular orbitals for an energy interval that roughly corresponds to the applied tunneling current in a typical STM experiment. As the two monomers are equal and weak interactions between the two molecules are not expected to significantly alter their electronic structure within the dimer, only one of the two molecules in the dimer was computed.

In Fig. 5.6 a) the molecular structure obtained from the MD simulation is shown together with the 10 first occupied orbitals (blue) calculated by DFT and a STM image of the dimer on Cu(100). In the overlay (Fig. 5.6 b) it is seen that the occupied orbitals are mainly located at the position of the bright double lobe feature ⓵ⓐ and ⓵ⓑ and at the position ④ in the middle while at the positions of the fainter lobes ② and ③ less occupied orbitals are located. Hence, the intensities, which are measured with STM are in well accordance to the locations of the occupied orbitals and further verify the observed structure. However, only quantitative agreement is achieved as also the height of the molecule will influence the lobe intensity in the actual STM image. In addition, it can be not excluded that the local density of states (LDOS) does not change when the molecule becomes adsorbed on the surface. But in this case only minor changes are expected.

In summary, the MD simulations yielded three different dimer structures on the Cu(100) surface, of which structure (II) is the most reasonable configuration as it matches the observed structure in many complementary aspects: It allows certain folding movements without a complete, thus unfavorable, rearrangement of the molecular structure and agrees to the proposed folding scheme presented in Fig. 5.3. Furthermore, the reactive sites are encased and hence not exposed to the

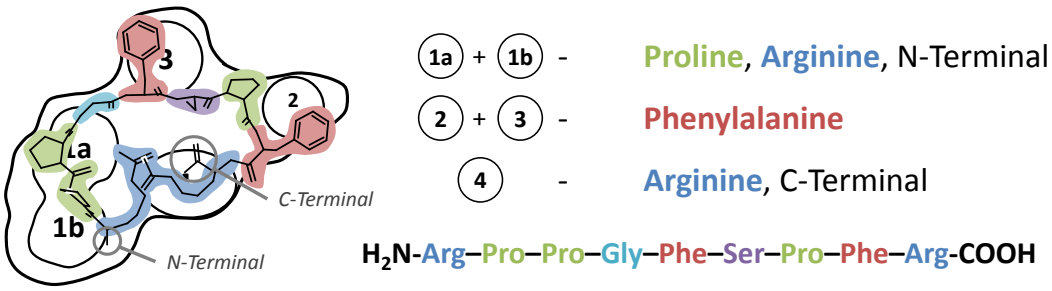

Fig. 5.7 The overlay of the contour shape of the dimer structure with the determined molecular structure allows the assignment of the amino acids to the observed lobes.

outside, which concurs to the observation that the dimers on the Cu(100) surface do not interact. Finally, the observed contrast of the dimer structure in the STM is in agreement with the calculated LDOS.

The characteristic features of the Cu(100)-dimer can be found in the single molecular structures on the Cu(110) surface as well as in the dimer on the Cu(111) surface. The observed lobe pattern can be ascribed to the same amino acids in all cases. This means that the conformation of the molecule on the different surfaces has only a minor effect on the electronic LDOS. Also the DFT calculations of the single molecule in various geometries provide essentially a similar LDOS with respect to the sequence (see Appendix B, Fig. B1). This can be understood based on the fact that the electronic features in the molecule are electronically decoupled by a non-conjugated backbone and the thus conformational changes on the nanometer scale do not affect the electronic properties of far away parts. This property is essential to biological systems, where function comes about by folding of otherwise independent parts into a functional configuration. The sp^3 backbone is highly flexible and electronically decoupling, so that the amino acid side chains can be brought to the position where they are needed. As a consequence, the determination of the single amino acids in the STM image is possible, as already in a topography image made with a simple variable temperature STM, we can determine more and less intense features belonging to single amino acids.

The observed features labeled with (1) to (4) in the shape contours of Fig. 5.3, leads to the assignment of the amino acids depicted in Fig. 5.7. In our model, the bright double lobe feature (1a) and (1b) correspond to the position of the double proline groups as well as to the arginine with N-terminal. The two fainter lobes (2) and (3) at the upper part of the monomer can be assigned to the phenylalanine groups whereas the intensity in the middle of the dimer (4) is the position of the arginine group at the C-terminal.

The molecular structure determined for the dimer has identified the position of the amino acids by fulfilling all boundary conditions given by the observations. Nevertheless, the structure model is not perfectly fitting the observed dimer structure. For instance, the lobe (1b) is not completely filled by the model structure. This might be caused by the MD structure optimization in which certain aspects cannot be considered. For example, the Cu(100) surface provides surfaces adatoms which might heave led to a Cu-complex formation, providing the binding between two monomers. However, given the size of the problem this STM structure determination method by the combination of MD simulations and DFT calculation was very successful and will serve as a blueprint for the analysis of other peptide structures. Although the structure can not be elucidated completely, it can be assumed that the positions of the amino acids are correct. What remains unclear is the bonding type between the monomers. From the MD simulations it is implicated that they are connected via hydrogen bonds and van-der-Waals forces. But as the simulation is not fitting perfectly, one could infer that also coordination bonds incorporating Cu-adatoms might have developed between two monomers.

An indication for the reactivity of the peptides related to possible Cu-coordination bonds is presented in the following section, where the peptide is deposited as negative ion onto the Cu(100) surface and decays from a dimer into a single molecular structure. A very similar structure is yielded when additional energy is provided by temperature treatment for positively charged molecules deposited on Cu(111). This suggests that Cu-coordination bonds are formed and in turn means that in the structures shown until here the incorporation of Cu adatoms is improbable.

5.4 Chemical Reactivity of the Peptide

In the previous experiments the peptide was deposited as double charged positive ion (positive mode), which means that two H^+ ion are attached to the molecule in the gas phase. We expect that upon deposition the protons are released and the molecule is in a neutral configuration on the surface. However, the molecule can also be deposited as negatively charged species (negative mode). In this case, the molecule is deprotonated, most probably at the C-terminal where a negatively charged carboxylic group would remain or at the OH-group of the serine group. For the neutralization, a reaction with a hydrogen atom or another electron accepting bonding partner is required. To what extent this influences the configuration of the peptide on the surface is addressed in the following.

For this experiment the same solution as used for the depositions in positive

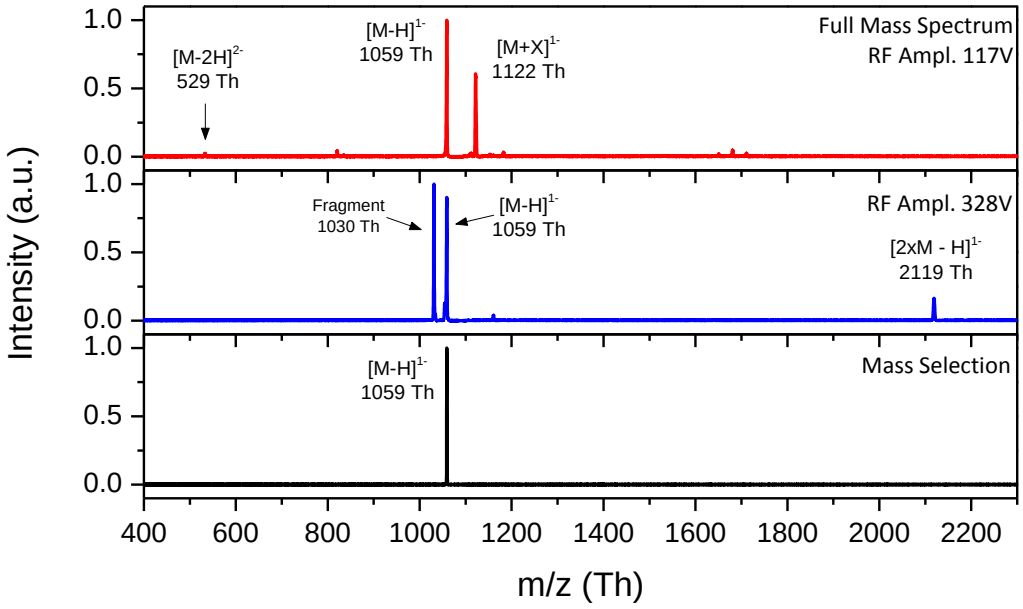

Fig. 5.8 Mass spectrum of negatively charged Bradykinin. The upper full-range mass spectra shows the intact, single deprotonated molecule at 1059 Th and a doubly charged molecule at 529 Th (red spectrum). Increasing the fragmentation potential leads to fragmentation and reveals cluster formation (blue spectrum). For the deposition the single deprotonated peptide at 1059 Th was mass-selected (black spectrum).

mode is prepared, however without formic acid. The mass spectrometry of this solution in negative mode is shown in Fig. 5.8. The upper mass spectrum reveals an intense peak at 1059 Th corresponding to the intact and deprotonated Bradykinin. Furthermore, also the doubly charged species is observed at 529 Th with a very low intensity. Increasing the RF amplitude voltage of the ion funnel leads to fragmentation of the molecule and a peak at 1030 Th appears corresponding to a fragment of the peptide (blue spectrum). Additionally a singly charged cluster at 2219 Th corresponding to two molecules is observed showing again the presence of larger clusters at lower fragmentation potentials. In contrast to the positive mode only two charge states are found. This can be understood as only the COOH-group of the arginine and the OH-group of the serine can be deprotonated. In order to ensure a defined ion beam for the following deposition on Cu(100), the singly charged species at 1059 Th was mass-selected (black spectrum).

In Fig. 5.9 STM images of the Cu(100) surface at RT after the deposition of the single negatively charged peptide are shown. Directly after deposition, dimer structures are found identical to those already known from positively charged

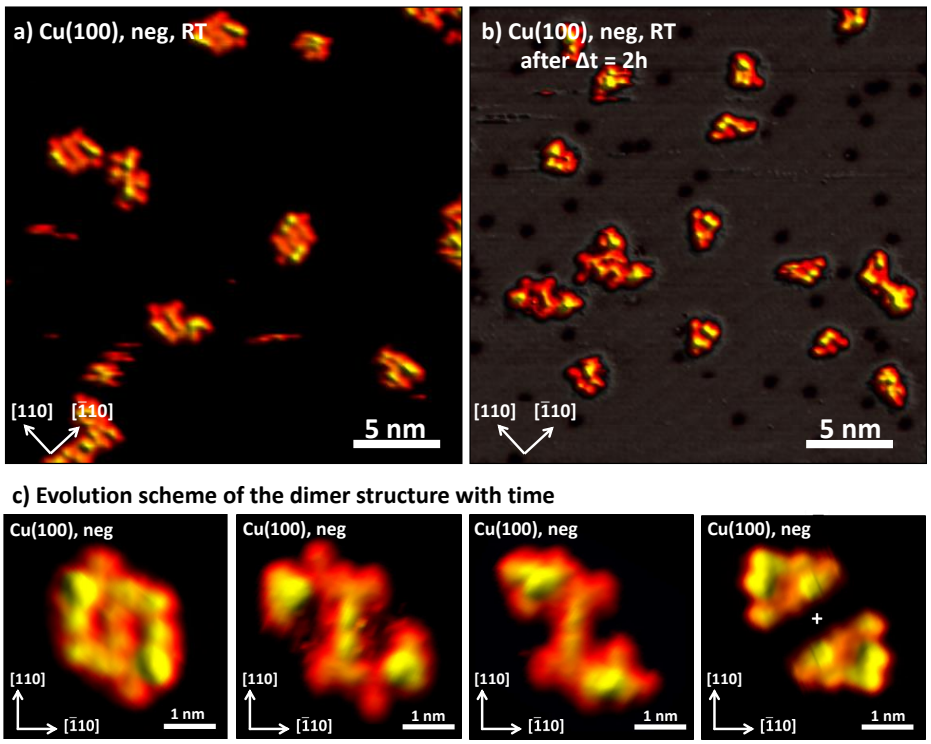

Fig. 5.9 **(a)** Negatively charged Bradykinin deposited on Cu(100) forming the known dimer structures. **(b)** With ongoing time Δt the dimers decay into single molecular structures. **(c)** Schematic evolution of the dimer break up with intermediate structures found on the surface.

peptide ion beams (Fig. 5.9 a). These structures are adsorbed in two perpendicular $\langle 110 \rangle$-directions and provide two bright double lobes with a two-fold symmetry.

Interestingly, within a few hours, the dimers appear to break up into single molecules with a triangular shape and their long side parallel to the $\langle 100 \rangle$-direction (Fig. 5.9 b). This was never observed in several measurements of bradykinin in positive mode. Based on their geometry, two of these single entities could constitute the (100)-dimer. Therefore they are ascribed to single molecules. Compared to the single molecular structures observed on the Cu(110) surface, these structures exhibit a different shape, but they possess a similar bright double lobe feature in the [110]-direction and a second lobe at the other end. Due to the four-fold symmetry of the Cu(100) surface, this monomer is found in four configurations rotated by 90°.

During the transition from dimers into single molecule structures, intermediate dimer structures are observed in several images showing snapshots of the unfolding process of the dimer (Fig. 5.9 c). These intermediate states evidence that the molecules are connected by a small branch in $\langle 110 \rangle$-direction and that the bright

lobes are rotated outwards from the structure. Furthermore, it shows that the decay into monomers proceeds through folding as well.

This unfolding process of the dimer reveals an additional direct bond between two monomers in contrast to the MD simulations where two hydrogen bonds between the NH group of the N-terminal arginine and the oxygen atom of the phenylalanine connect the two monomers. This central bond rather fits to the drawn folding scheme in Fig. 5.3, in which the molecules are connected via the branch labeled with ④. In this feature the arginine with the C-terminal is located. Exactly at that one group the gas phase deprotonated ion differs from the neutralized positive mode bradykinin. Thus, it is possible that the deprotonated carboxylic group generates the same structure, but at the same time offers a reactive site, while the dimers are stable for several days when positively charged molecules with protonated C-terminal are deposited. It is known that deprotonated carboxylic groups prefer to form bonds to Cu adatoms.[165–167] In this view, the dimer might break up due to the reaction of the carboxylic group with copper, forming two individual Cu-BK complexes.

In order to get an indication whether a reaction due to the deprotonation took place, the molecules deposited in positive mode can be deprotonated by temperature treatment, a reaction typically used in the afore mentioned literature.[165–167] Therefore, the various samples with positively deposited peptides, were annealed at 120°C for a few minutes.

After the annealing of the Cu(110) sample, single molecular structures were still present but due to the O-adsorption induced reconstruction of the surface,[224,225] it was difficult to resolve them with submolecular resolution. Accordingly, it was not possible to judge whether their configuration has changed. The annealing of the Cu(100) surface with the dimers resulted in the decay into a manifold of single molecular entities with no majority configuration. In contrast, the dimers on the Au(111) surface were preserved after annealing and no change besides a lower coverage was observed. The annealing of the Cu(111) surface, on which dimers were observed at LT, resulted in triangular structures stable at RT (Fig. 5.10 a). These structures showed the same characteristic features as the triangular structure of the negatively charged Bradykinin on Cu(100) after decaying into monomers. Due to the three-fold symmetry of the surface the structures are found in three directions and exhibit an equilateral triangular shape instead of two directions and a right-angled triangular shape, as on the Cu(100) surface. However, the distances between the characteristic lobes are approximately the same, as indicated by the blue circles in Fig. 5.10 b).

This shows that a reaction took place related to the copper surface, since on the

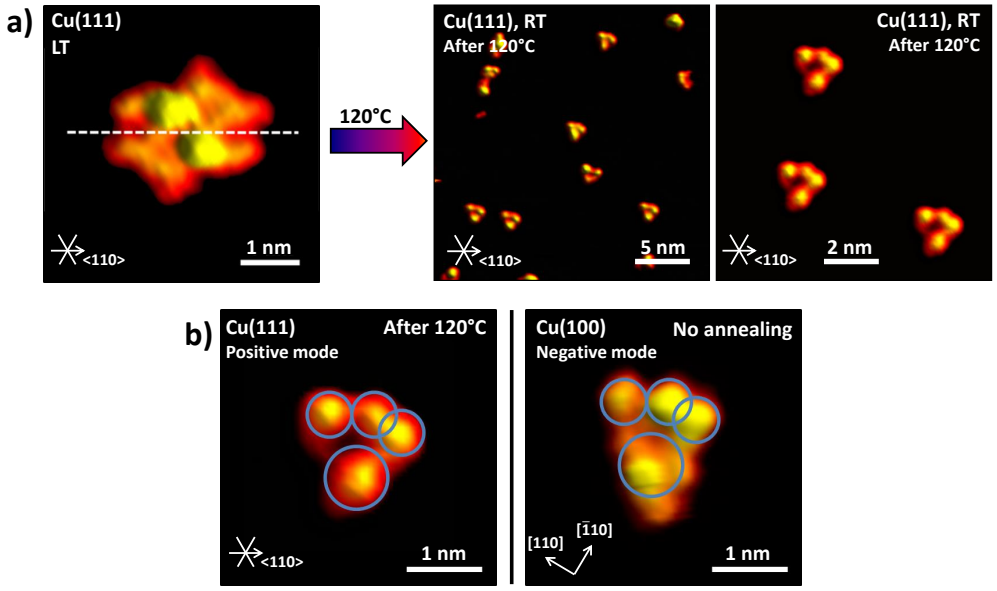

Fig. 5.10 **(a)** After annealing at 120°C of the Cu(111) sample with positively charged Bradykinin, the dimer structures decayed into single molecules. **(b)** The triangular shape of the molecule is similar to the features observed after the deposition of negatively charge species on Cu(100).

gold surface, the structures were preserved and not affected by the temperature treatment. The differences in appearance after annealing on the copper surfaces might be related to the different interactions of the surface with the molecules. In the case of the Cu(110) surface, the interaction between the single molecules and the surface is already very strong. Thus an annealing led to no significant change of the conformation of the molecules. This is different on the Cu(100) surface. Here, the interaction is weaker allowing a reorganization of the molecules after annealing. The decay of the dimers into the many different single structures shows, on the contrary, that they react with a copper adatom but cannot engage a low energy configuration due to the low mobility on the Cu(100) surface. This is different on the Cu(111) surface as it provides a lower interaction. Upon annealing, the molecules react with the surface and have mobility to adjust themselves into a low energy conformation, which is in this case the triangular structure similar to what was observed on Cu(100) after negative ion deposition.

As this conformation is observed only after annealing of the positive charged species and the deposition of the negative charge species on copper surfaces, it supports the hypothesis that a reaction with a copper atom took place. On the Cu(100) surface, it is induced by the deposition of the deprotonated species and the availability of Cu adatoms at the surface while on the Cu(111) surface, the

necessary conditions were evoked by the annealing. The slight difference between the monomer structures as shown in Fig. 5.10 b) can be understood by the difference in surface structure underneath. Nevertheless, the fact that such similar structures are observed on different surfaces for a molecule offering a huge variety of conformations, shows that the Cu-coordination is the dominating binding motif, overcoming the unspecific binding to the surface.

5.5 Summary & Conclusion

We have studied the deposition of a natural peptide with a total of nine amino acids and a mass of 1060 Da on different surfaces by employing electrospray ion beam deposition. Several conformations starting from single isolated structures to dimers and hierarchical self-assemblies of dimers are observed by STM as a function of the molecule-surface interaction. By applying a 2D folding processes, these structures could be related to each other, allowing a high resolution insight into the folding processes of peptides in 2D for the first time.

Furthermore, the observed features are connected to the amino acid chain by applying a combination of MD simulations and DFT calculations. In this way the problem of simulating a huge molecule is solved as MD simulations presented the molecular structure and DFT calculated the corresponding electronic structure. This enabled a comparison with the experimental data obtained and the assignment of the amino acids to the lobes. Since the lobes on the different surfaces were equivalent, also the other structures are identified based on these simulations.

This method, experimentally and theoretically, facilitates to evaluate folding processes on surfaces locally for single amino acids chains. The simple exchange of certain amino acids might allow to tune the structure formation. Thereby also the functionality of the molecule can be influenced rationally. This is shown by the deposition of positively and negatively charged peptides on the Cu(100) surface. Whereas the positively charged peptides formed stable dimer structures, the peptides deposited in negative mode are reactive and decay after a short time from the same initial dimer structures into single triangular monomers. The triangular monomers were also yielded after the annealing of the positively deposited peptides on Cu(111). This correlation is only explained by the incorporation of a metal atom into the structure induced by a thermal deprotonation of the C-terminal.

These results illustrate the vast functionality and strong potential this class of molecules are offering but also the possibilities which are enabled by ES-IBD. The technique not only promotes the deposition of such large nonvolatile molecules. It also allows to create reactive species in the gas phase, which upon deposition

develop their function. Together with the evaluation of amino acid chains for certain folding patterns, surfaces with novel catalytic and chemical functionalities might be created.

Summary & Perspectives

Before electrospray ionization (ESI) and matrix assisted laser desorption ionization (MALDI) were available, only small molecules could be analyzed by mass spectrometry as larger molecules were fragmented by ionization techniques like electron impact or chemical ionization. The utilization of ESI and MALDI for mass spectrometry bears comparison with a revolution as they facilitate the precise identification and characterization of biological non-volatile molecules. They were thus strongly involved in the development of the field of proteomics, which studies the structure, function and interactions of the entireness of proteins produced by the genes of a particular cell, tissue, or organism.[226]

More than two decades later, a similar problem in the field of controlled nanostructure growth has to be faced as it is desirable to deposit large functional molecules on surfaces intactly and under perfectly controlled conditions. Due to the fact that large functional molecules tend to be non-volatile or thermally fragile, it hinders the conventional vacuum processing by evaporation. A solution to this problem could be electrospray ion beam deposition (ES-IBD), which could be seen as a derivative development from ESI mass spectrometry, additionally enabling the deposition of the ionized species.

In this thesis the vast potential of this new method is shown: We saw that ES-IBD could introduce fundamentally new aspects to materials synthesis by thin film growth. Structures of non-volatile molecules are grown with molecular precision and characterized on the atomic scale with scanning tunneling microscopy (STM) in ultrahigh vacuum (UHV). In this process, ES-IBD offers many new parameters, at a high level of control, which were not accessible in deposition techniques before. For instance, the influence of the charge state and the deposition energy or the difference of single molecule and cluster deposition could be observed. These parameters do not only play an important role on the outcome of a deposition but can furthermore all be measured and actively influenced during the deposition. Moreover, ES-IBD enables to study the structure formation of complex molecules with many functionalities and many conformational degrees of freedom at a level

of precision that is only available to UHV techniques.

In order to demonstrate the capabilities of ES-IBD, a broad range of molecules was deposited on different surfaces, starting from non-volatile synthesized species with different properties, to biological species. The growth of thin films and ordered molecular layers revealed the equivalence to conventional MBE growth. Crystalline layer growth of non-volatile amphiphilic molecules as well as island growth from organic salts was demonstrated. On the basis of these deposition experiments the crucial influence of clusters in the ion beam for the material flux was presented. The influence of the clusters was further revealed by the deposition of Reichardt's dye showing differences in the coverage between mass-selected and non-mass-selected deposition. Furthermore, it was discovered that the chemical state of that molecule is an important factor for the deposition result, as neutral molecules from clusters self-assemble into ordered structures while mass-selected molecules had a very high mobility and were not imaged. Annealing of the mass-selected ion deposited resulted in the reaction into a new molecule and demonstrated the possibilities for a controlled surface chemistry which profits from the high selectivity of the method. ES-IBD can also handle delicate species what is shown by the deposition of hexaynes, very reactive molecules due to the six succeeding triple bonds in the structure. Moreover, this molecule manifested that molecular engineering is necessary in order to adjust the self-assembly into the desired way as well as to be compatible to the ES-IBD method.

In addition to the growth of layers and ordered structures, ES-IBD in combination with microscopy provides amazing performance as an analytical tool to study complex single molecular entities at unprecedented resolution. In particular, the study of biomolecules, as peptides and proteins, is presented in the two last parts of the thesis. Both chapters deal with the conformation of these large objects and how it can be influenced rationally. On the larger length scale, ES-IBD provides the possibility to select a certain conformation of a protein under the influence of the charged state and transfer the conformation onto the surface. On the smaller scale, the conformation is mainly affected by the interaction with the surface and with the molecule itself. The deposition of a peptide results in ordered structures on different surfaces. As all structures could be related to each other an insight into a surface induced folding is given on the atomic level.

Perspectives

The experiments presented in this work offer a multitude of connecting points for future research, branching into three major directions: (1) the improvement of the ES-IBD technology, (2) the application of the present technology for the

investigation of complex organic adsorbates with high resolution methods, and finally (3) the study of the unique possibilities of hyperthermal surface chemistry with molecular ion beams.

Having understood the characteristics of ES-IBD for deposition with exemplary molecules and the surface chemistry, one can go further for technological relevant systems as for example layers of organic semiconductors for transistors, displays or solar cells. The performance of these devices, fabricated with a highly controlled system such as ES-IBD, could be improved as solvent residues and contaminations can be completely excluded. Furthermore, new molecules providing additional functionalities can be used. By controlling the conformation of large molecules, the morphology as well as the structure of the thin film might be adjusted resulting in improved properties.

However, the ES-IBD system in the current state is far away from being relevant for industrial applications, since the deposition spot size is too small or ion currents are too low, correspondingly. However if samples of wafer size can be handled at relevant time scales the system becomes relevant. An important requirement towards this aim, is the enhancement of the ion currents in the range of μA. We have shown that there is still a lot of room for improvement. Already small changes at the source interface can affect the ion current transmission strongly. Through utilizing the hydrodynamics occurring at the transfer capillary by shaping the inlet, a 100% ion transmission was achieved.[99] It might be even improved by applying ion optics already at the interface or improving the hydrodynamic properties further. However, the transmission is limited by the space charge of the ion cloud and has to be considered for the transfer but also for the following ion optics when the ion beam currents increase. Furthermore, new ion sources with a better ionization efficiency can be used, for instance AC-ESI[227] or electrosonic spray ionization (ESSI).[228]

Until the system does not reach these benchmarks, it remains an instrument for scientific research, which nevertheless is perfectly suited for the investigation of single non-volatile molecules in a highly controlled environment. In this perspective, first technological relevant molecules were deposited for their investigation on the atomic scale.

Recently, we worked with N3 dye molecules on a TiO_2 anatase (101) surface (Fig. S.1), a system which is applied in dye-sensitized solar cells (DSSC). We found supramolecular clusters and various configurations with different electronic properties of which only some of them might contribute to the charge injection. This study of the structural and electronic properties on the atomic scale can help to understand and improve solar cells further by shaping the electronic landscape of

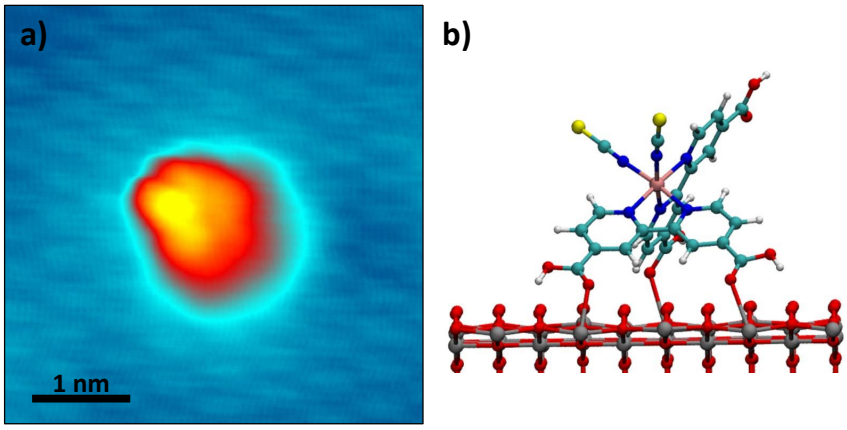

Fig. S.1 **(a)** STM image of an individual N3 dye molecule on an atomically resolved TiO_2 anatase (101) surface deposited with ES-IBD. **(b)** Corresponding DFT model of the adsorption geometry in which the three carboxyl groups bind via the unidentate mode.

the molecule – surface interface through proper modification of the dye molecule. Through this precise control of the relation between substrate, molecular, and electronic structure new surfaces and materials might become eligible for DSSC's.

Furthermore, the new parameters, which are offered by ES-IBD like charge state selection, deposition energy or fragmentation can also be used to modify the molecule upon deposition and create new functional surfaces by exploiting hyperthermal, chemical reactions. Through these parameters the handling of extremely reactive molecules is enabled and allows for controlled non-equilibrium covalent bond formation. In combination with scanning probe microscopy, these newly created materials can be resolved spatially and analyzed on the atomic scale. But a full understanding will also require additional chemical characterization like secondary ion mass spectrometry (SIMS) or desorption ionization induced by neutral cluster impact (DINeC).[108]

The high resolution of molecules on the surface is also important in order to study the conformation of complex molecules. As it is shown, the polymer properties like stiffness can be influenced and transfered onto the surface in the form of structure properties. This is of technological relevance as surface properties can be adjusted through the deposition process alone.

With regards to proteins, which were so far only randomly distributed on the surface, the question arises whether the secondary structure elements like the α-helix or the β-sheet can be stabilized within the gas phase and transferred onto the surface. Or there are maybe other secondary structure motifs which are preferred in 2D, what could be revealed by ES-IBD and STM.

Moreover, the reverse examination of biological strcutures may also be possible. The deposition of folded proteins or even protein complexes and their analysis with STM under the influence of temperature treatment or tip induced strain, might enable to follow the unfolding process in analogy to the recent nuclear magnetic resonance (NMR) study.[62] In contrast to that work, the unfolding dynamics and stability of an individual protein would be recorded for a specific local disturbance.

A different ansatz for steering the conformation is attempted by using small amino acid chains. The rational systematic molecular design by exchanging only arts of the sequence or even one single amino acid enables access to fine tune the interaction of the surface with the peptide as well as the interaction with itself or other peptides. Moreover, the functionality of the peptides and of the self-assembled structures can be adjusted and controlled in small steps whereas involved structure modifications are directly imaged with STM. The high resolution of the STM might be also used to sequence the peptide chains and identify single amino acids through characteristic spectra obtained by scanning tunneling spectroscopy (STS). Here, ES-IBD in combination with STM could be used in purely analytical capacity revealing properties otherwise unaccessible.

These ambitious goals make it necessary to integrate further characterization methods like high resolution low temperature STM with ES-IBD. Therefore, our suitcase transfer method has to be improved so that samples from the deposition facility can be efficiently brought to analytic facilities without breaking the vacuum. Important thereby are fast and clean transfers of high reliability to ensure the cleanliness of the samples. A new version of the vacuum suitcase is currently

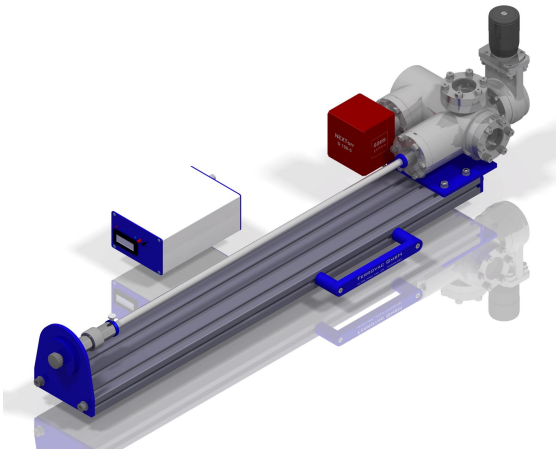

Fig. S.2 The new model of the UHV suitcase, enabling fast and clean transfers between the ES-IBD setup for deposition and other analytic UHV instruments in our department.

designed and shown in Fig. S.2. In contrast to the old version it consists of a wobble stick, which enables to place the sample into a holder in the deposition chamber and leave it there. This ensures a better vacuum during deposition as the valve to the connecting chamber between suitcase and deposition chamber can be closed. Furthermore, with an attached cryopump at the connecting chamber there is no need to bake it, saving precious experimental time.

Reviewing the capacities and prospects of ES-IBD, I would not be surprised to see many more setups in academic environment in the future and eventually also in technology.

Appendix A - Cluster Ion Beam

A.1 Concentration dependence of SDS

The mass spectra of SDS in dependence of the concentration in Chap. 2 in Fig. 2.1 is shown on a linear scale up to 3500 Th. When the same graph is plotted on the logarithmic scale up to 7000 Th, an increase of an unresolved region above 3500 Th with concentration can be observed (Fig. A1). This intensity corresponds to large clusters whose portion increases upon rising the concentration and would be not seen in a linear plotted mass spectra.

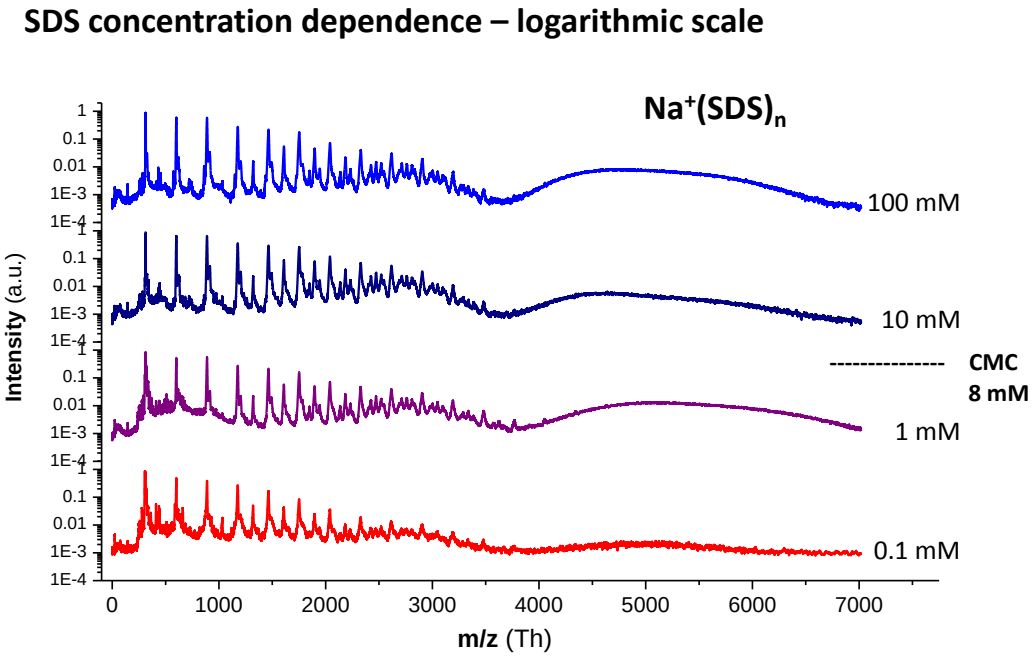

Fig. A1 Mass spectra of SDS of different concentration on the logarithmic scale. With increasing concentration the unresolved region above 3500 Th increases.

A.2 Quantification of the Material and Charge Content in the Ion Beam

Two independent methods were applied to quantify material and charge content in the electrospray ion beams. The first approach is based on the analysis of the mass spectra, which gives the relative material and charge content for the resolvable charge states of the ion beam. The second method relates the net deposited charge to the material content observed on the sample surface to get an average m/z - value.

A.2.1 Analysis of the mass spectra

The cluster beams of SDS and SoCit consist of several neutral organic salt molecules with one or several added or removed Na^+ charge carriers each. This gives rise to several series of peaks in the mass spectra each belonging to a charge state. Some peaks in these series for different clusters can overlap at the same m/z, for instance the cluster $Na^+(SDS)_2$ is found at the same position as its double sized, doubly charged counterpart $Na_2^+(SDS)_4$. While the latter cluster conveys the double amount of material and charge, both are registered as one single count in the mass spectrum. This illustrates that judging material and charge content by the intensities can be extremely misleading.

A cluster mass spectrum $J(M)$ can be intuitively dissected into separate spectra for each charge state $J_z(M)$, with their sum representing the full spectrum

$$J(M) = \sum_{z=1}^{z_{max}} J_z(M)$$

with $M \equiv m/z$ the mass-to-charge-ratio. In such a single charge state peak series J_z all ions have the same defined charge state z and thus the material content can be calculated. To use this quantification for a measured mass spectrum with several charge state series, all peaks have to be identified and additionally the intensity in the mixed charge state peaks must be divided up between the contained charge states.

An easy way to do this is to fit the entire mass spectrum with an appropriate function, in which a relation for the intensity distribution within each charge state is contained. Here, we represent a cluster series by a series of equidistant Gaussian peaks, which follow an envelope, which is of Gaussian shape as well. Several of these series added up give a complete mass spectrum, which can be fitted to the

data:

$$J(M) = \sum_{z=1}^{z_{\max}} \sum_{n=1}^{n_{\max}} J_z \cdot g(n, c_z, w_z) \cdot g\left(M, \frac{m_{n,z}}{z}, \frac{m_{n,z}}{Rz}\right)$$

with $m_{n,z} = m_{\mathrm{Na}} \cdot z + m_{\mathrm{SDS}} \cdot n$, the mass of a peak with n SDS molecules and z charges and $g(x, x_0, \sigma) = \frac{1}{(\sigma\sqrt{2\pi})} \exp\left[-\frac{1}{2}(\frac{x-x_0}{\sigma})^2\right]$ the Gaussian distribution. The intensity J_z, the center position c_z and the width w_z for each charge state series are fitted. The difference in peak width is introduced in the model through a parameter $R \equiv m/\Delta m$, which is fitted as well.

Considering charge states up to $z = 5$ would result in 16 free parameters, three for each charge state and the resolution. However, as long as the peak series can be distinguished from each other, the parameters triplets for each series are mostly independent and the fit will be of good quality. But with our resolution peaks above $z = 5$ cannot be identified and thus the result would become arbitrary.

Also, simply using a least square fit would underestimate the low intensity peaks of the high charge states. The fit was thus carried out on the logarithm of the data, which transforms all intensity values into the same order of magnitude. The results are summarized in Fig. A2. With rising charge state, the intensity J_z decreases, while the center position c_z of the envelope and its width w_z (in number of peaks) rises (Fig. A2 a). Displayed on a m/z-scale the picture is almost the same, only the envelope width is roughly constant with large fluctuations (Fig. A2 c).

With these parameters each charge state series can be plotted as a separate spectrum as shown in Fig. 3(a) in the main article. The full spectrum assembled from the charge states resembles the measured spectrum.

a)

Parameters for the envelope function for each charge state z found by fitting: intensity J_z, center position c_z and width w_z

z	J_z	c_z	w_z
1	35	2.7	1.9
2	13	11	2.7
3	3.6	18	2.7
4	2.9	34	5.8
5	2.6	43	5.1

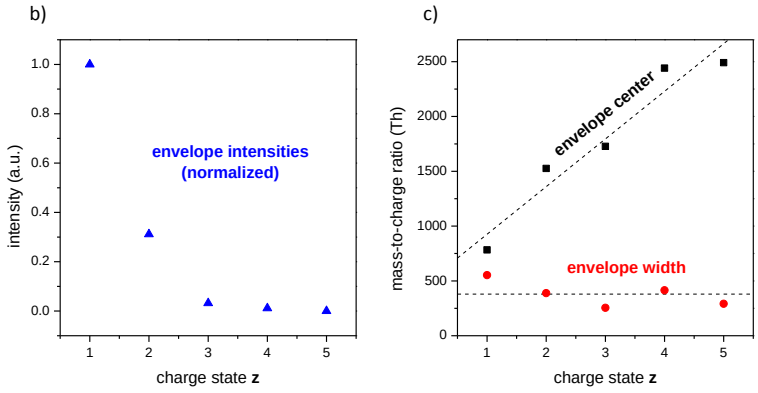

Fig. A2 Parameters for the envelope function as a function of charge state z found by fitting: **(a)** table showing the envelope center and width in number of peaks, **(b)** graph with normalized envelope intensity, **(c)** envelope center and width in units of m/z.

A.2.2 Calculation of the relative material and charge amount

The relative material and charge content of the ion beam can now be calculated from the fitted mass spectra by summing up the intensities of the peaks multiplied by their material or charge content respectively.

The original time-of-flight spectrum was measured as counts per time as histogram of constant width bins. Our standard calibration procedure transforms time-of-flight spectra into a function of m/z, on which the fit is performed. However, the calibration does not renormalize the intensities with respect to the non-linear recalibration. For a typical mass spectrometry application this is often not necessary, however, when intensities are compared by fitting a continuous function on the discrete mass spectrum, the relation of the integrals over time-of-flight and m/z must be taken into account. This can be done post ex. From the calibration function $M(t) = A_0(t - t_0)^2$ follows for the bin width ΔM

$$\Delta M(M) = A_0 \Delta t \left(2\sqrt{\frac{M}{A_0}} + \Delta t \right).$$

The method is valid since the peak area of a Gaussian peak scales linearly with its height. The post ex intensity correction disturbs the Gaussian envelopes slightly, however, since those were chosen arbitrarily as a crude approximation of the intensity distribution, this is acceptable. If a more suitable intensity envelope function is available, the calibration of the intensities should be made in accordance with this function.

Now the relative material amount $N(z)$ and charge amount $Q(z)$ for each charge state can be written as

$$N(z) = \sum_{n=1}^{n_{max}} \frac{n \cdot J_z \cdot g(n, c_z, w_z)}{\Delta M(M_{\text{cluster}}(n, z))} \tag{A.1}$$

$$Q(z) = \sum_{n=1}^{n_{max}} \frac{z \cdot J_z \cdot g(n, c_z, w_z)}{\Delta M(M_{\text{cluster}}(n, z))} \tag{A.2}$$

with $M_{\text{cluster}}(n, z) = \frac{m_0 + n\Delta m}{ze}$ the m/z of the n-th cluster of the charge state z series. The results displayed in the main article in Fig. 3(b) show that the low charge states contribute more charge than material while for the high charge states it is the opposite. Most importantly this calculation shows that the very low intensity peaks can be responsible for a significant amount of material. With this method - maybe in a refined version - this material to charge relation can be quantified from mass spectra.

A.2.3 Estimation of the material and charge content of the unresolved intensity

From the resolved part of the mass spectra (0-3500 Th), the relative material and charge content of each individual charge state can be estimated. The unresolved region (>3500 Th) has to be excluded as it cannot be fitted. Nevertheless, a significant material or charge amount can be contributed by this part of the ion beam.

A first indication is the integrated intensity[c] of the mass spectrum (Fig. 2.4), which shows that approximately 9 % of the counts are found in the unresolved region. Assuming that in the high m/z region larger clusters are present, the overall average m/z-ratio $\langle M_{tot} \rangle$ might be affected. To elvaluate the contribution of the low and high m/z regions, $\langle M_{tot} \rangle$ can be written as follows:

$$\langle M_{tot} \rangle = \frac{N_{tot}}{Q_{tot}} = \frac{N_{lo} + N_{hi}}{Q_{lo} + Q_{hi}} \tag{A.3}$$

with N the number of molecules and Q the contained charge of the low, high and whole m/z region. Expanding Eq. (A.3) with Q_{lo}/Q_{lo} and Q_{hi}/Q_{hi}

$$\langle M_{tot} \rangle = \frac{N_{lo}}{Q_{lo} + Q_{hi}} \cdot \frac{Q_{lo}}{Q_{lo}} + \frac{N_{hi}}{Q_{lo} + Q_{hi}} \cdot \frac{Q_{hi}}{Q_{hi}} \tag{A.4}$$

the average m/z ratio of the low $\langle M_{lo} \rangle = N_{lo}/Q_{lo}$ and high $\langle M_{hi} \rangle = N_{hi}/Q_{hi}$ m/z-region can be gained:

$$\langle M_{tot} \rangle = \frac{\langle M_{\mathrm{lo}} \rangle \cdot Q_{lo} + \langle M_{\mathrm{hi}} \rangle \cdot Q_{hi}}{Q_{lo} + Q_{hi}} \tag{A.5}$$

The relative charge Q is related to the relative amount of clusters $j_{lo/hi}$ normalized with a factor γ, to yield $Q_{lo} + Q_{hi} = 1$:

$$Q_{lo/hi} = j_{lo/hi} \cdot z_{lo/hi} \cdot \gamma$$

This equation inserted in Eq. (A.5) results in a relation for $\langle M_{tot} \rangle$ which is only dependent the average m/z value, the average charge state $\bar{z}$ and the relative intensity j of the low and high m/z region of the mass spectra:

$$\langle M_{tot} \rangle = \frac{\langle M_{\mathrm{lo}} \rangle \cdot j_{lo} \cdot \bar{z}_{lo} + \langle M_{\mathrm{hi}} \rangle \cdot j_{hi} \cdot \bar{z}_{hi}}{j_{lo} \cdot \bar{z}_{lo} + j_{hi} \cdot \bar{z}_{hi}} \tag{A.6}$$

[c]Integrated counts, normalized to the bin width.

Using the relative intensities from the integrated mass spectrum (Fig. 2.4 for $j_{\mathrm{lo/hi}}$ and knowing $\langle M_{\mathrm{lo}} \rangle$ and $\langle M_{\mathrm{hi}} \rangle$), the missing parameter to evaluate Eq. (A.6) in order to find $\bar{z}_{hi}$ is the average charge state of the resolved region $\bar{z}_{lo}$. This value can be calculated, again using the fitted parameters. Equivalent to Eq. (A.1) and (A.2) we can write the relative number of clusters per charge state:

$$n(z) = \sum_{n=1}^{n_{max}} \frac{J_z \cdot g(n, c_z, w_z)}{\Delta M(M_{\mathrm{cluster}})}$$

It follows that the average charge state $\bar{z}$ can be calculated as

$$\bar{z} = \frac{\sum_{z=1}^{z_{max}} z \cdot n(z)}{\sum_{z=1}^{z_{max}} n(z)}$$

where we find a value of $\bar{z}_{lo} = 1.54$ for the low m/z region with $z_{max} = 5$.

A.3 X-ray Diffraction of SDS layers

High-resolution X-ray powder diffraction (XRPD) data of the samples were collected at room temperature on a laboratory powder diffractometer (D-8, Bruker, Cu-Kα_1 radiation from a primary Ge(111), Johanson-type monochromator; Lynx-Eye position-sensitive detector (PSD) with an opening angle of 3.5°) in Bragg-Brentano geometry with the sample carefully loaded on low background Si-911 sample holders of 40 mm diameter. Data were taken from 5.0°... 90.0° in steps of 0.008° in 2θ for 12 hours total. The sample was rotated during measurement for better particle statistics. All data reduction was done with TOPAS (Bruker AXS). The peak profile and lattice parameters were determined by whole powder pattern fitting (WPPF) according to the Le Bail method[134] using the fundamental parameter (FP) approach of TOPAS.[229] Due to the fact that the geometry of the Lynx-Eye PSD is not fully characterized by FP's, fine tuning of the available parameters was performed by using refined values of the FP's from a precise measurement of the NIST line profile standard SRM 660a (LaB_6) over the full two theta range of the diffractometer. For the modeling of the background, Chebychev polynomials were employed.

Using WPPF, a binomial intensity distribution of the Bragg peaks belonging to SDS was found, suggesting two different SDS phases with slightly different lattice parameters. Owing to the large a-axis of SDS, all individual Bragg refections at low diffraction angle belong to (h00) refections, while mixed indices occur only in fully overlapping refections at higher diffraction angle, reducing the reliability of the WPPF for lattice parameters other than a to a precision of 0.01 nm.[230]

Nevertheless, the refinement converged to reasonable numbers (1st SDS phase: a_1 = 4.0259 nm, b_1 = 0.476 nm, c_1 = 0.824 nm. β_1 = 93.491°; 2nd SDS phase: a_2 = 4.0786 nm, b_2 = 0.477 nm, c_2 = 0.835 nm, β_2 = 93.442°).

The XRPD measurement and analysis were performed by Prof. Robert E. Dinnebier, Max-Planck-Institute for Solid State Research, as collaboration in this project

Appendix B - Electronic Structure of Bradykinin

In order to find the molecular structure of the single bradykinin peptide on the Cu(110) surface, we performed several MD simulations in the same way as for the dimer structure on Cu(100) and shown in Chap. 5.3 on page 114. In this way, two different conformations were found so far, which did not fit the structures observed with STM. But electronic structure calculations with DFT of these molecular arrangements showed for both of them a similar distribution of the density of states although the conformation is different. In Fig. B1 these structures are depicted with the first 10 unoccupied orbitals. Both structures reveal similar electronic states at the N-terminal of the molecule where the arginine and the two proline groups are located and at the C-terminal arginine. The intensity observed in-

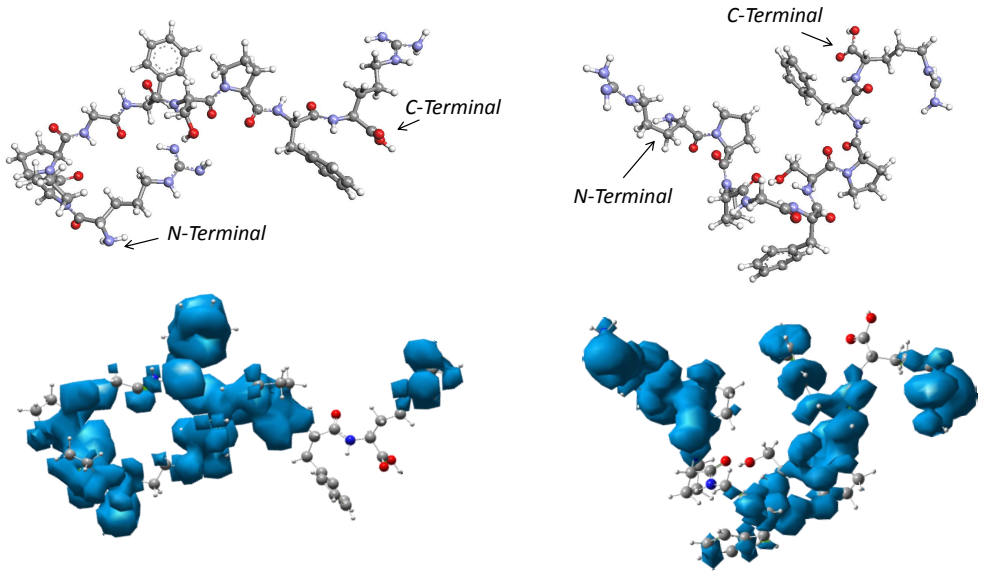

Fig. B1 DFT calculations of the first 10 occupied orbitals of single bradykinin structures obtained by MD simulations on a Cu(110) surface.

between is located at the two phenylalanine groups, which however show slight deviations due to the different conformation.

This electronic structure is also in good agreement to the one of the dimer molecule in Fig. 5.6 on page 116. Hence, it is demonstrated that the electronic structure is mainly coupled to the amino acid sequence and largely independent of the conformation of the molecule. It can be understood as the molecule is already so large that the conformational changes on the nanometer scale do not strongly affect the electronic structure.

Bibliography

[1] Suntola, T. *Atomic Layer Epitaxy, Handbook of Thin Film Process Technology* (Institute of Physics (IOP) Publishing Inc., 1994).

[2] Herman, M. A. & Sitte, H. *Molecular beam epitaxy: fundamentals and current status*, vol. 7 (Springer-Verlag, 1996), springer series in materials science edn.

[3] Parker, E. H. C. *The Technology and physics of molecular beam epitaxy* (Plenum Press, 1985).

[4] Brune, H. Microscopic view of epitaxial metal growth: nucleation and aggregation. *Surface Science Reports* **31**, 121–229 (1998).

[5] Barth, J. V., Costantini, G. & Kern, K. Engineering atomic and molecular nanostructures at surfaces. *Nature* **437**, 671 – 679 (2005).

[6] Forrest, S. R. The path to ubiquitous and low-cost organic electronic appliances on plastic. *Nature* **428**, 911 (2004).

[7] Bittner, A. Clusters on soft matter surfaces. *Surface Science Reports* **61**, 383 – 428 (2006).

[8] Franchetti, V., Solka, B. H., Baitinger, W. E., Amy, J. W. & Cooks, R. G. Soft landing of ions as a means of surface modification. *Int. J. Mass Spectrom. Ion Processes* **23**, 29–35 (1977).

[9] Miller, S. A., Luo, H., Pachuta, S. J. & Cooks, R. G. Soft-landing of polyatomic ions at fluorinated self-assembled monolayer surfaces. *Science* **275**, 1447–1450 (1997).

[10] Laskin, J., Wang, P. & Hadjar, O. Soft-landing of peptide ions onto self-assembled monolayer surfaces: An overview. *Phys. Chem. Chem. Phys.* **10**, 1079 – 1090 (2008).

[11] Rauschenbach, S., Stadler, F. L., Lunedei, E., Malinowski, N., Koltsov, S., Costantini, G. & Kern, K. Electrospray ion beam deposition of clusters and biomolecules. *Small* **2**, 540–547 (2006).

[12] Rauschenbach, S. *et al.* Electrospray ion beam deposition: Soft-landing and fragmentation of functional molecules at solid surfaces. *ACS Nano* **3**, 2901 (2009).

[13] Moore, G. E. Cramming more components onto integrated circuits. *Electronics Magazine* **38**, 114–117 (1965).

[14] Hutcheson, G. D. Moore's law: The history and economics of an observation that changed the world. *The Electrochemical Society Interface* **14**, 17–21 (2005).

[15] Gargini, P. The international technology roadmap for semiconductors (itrs): ldquo;past, present and future rdquo;. In *GaAs IC Symposium, 2000. 22nd Annual*, 3–5 (2000).

[16] Pimpin, A. & Srituravanich, W. Review on micro- and nanolithography techniques and their applications. *Engineering Journal,* **16,1** (2012).

[17] Bratton, D., Yang, D., Dai, J. & Ober, C. K. Recent progress in high resolution lithography. *Polymers for Advanced Technologies* **17**, 94–103 (2006).

[18] Jaeger, R. C. *Introduction to Microelectronic Fabrication*, vol. V (Addison Wesley Pub Co Inc., 1998).

[19] Chandril, S. *In Situ Structural and Compositional Analysis Using Rheed Electrons Induced X-Rays* (BiblioBazaar, 2011).

[20] Braun, W. *Applied RHEED. Reflection High-Energy Electron Diffraction During Crystal Growth* (1999).

[21] Takashi Ito, S. O. Pushing the limits of lithography. *Nature* **406**, 1027–1031 (2000).

[22] Beaujuge, P. M. & Frechet, J. M. J. Molecular design and ordering effects in π-functional materials for transistor and solar cell applications. *J. Am. Chem. Soc.,* **133 (50)**, 20009–20029 (2011).

[23] Henson, Z. B., Müllen, K. & Bazan, G. C. Design strategies for organic semiconductors beyond the molecular formula. *Nat. Chem.* **4**, 699–704 (2012).

[24] Gu, G., Parthasarathy, G. & Forrest, S. R. A metal-free, full-color stacked organic light-emitting device. *Appl. Phys. Lett.,* **74**, 306 (1999).

[25] Ong, B. S., Wu, Y., Liu, P. & Gardner, S. High-performance semiconducting polythiophenes for organic thin-film transistors. *J. Am. Chem. Soc.* **126 (11)**, 3378–3379 (2004).

[26] Hagfeldt, A. & Grätzel, M. Molecular photovoltaics. *Accounts of Chemical Research* **33**, 269–277 (2000).

[27] Günes, S., Neugebauer, H. & Sariciftci, N. S. Conjugated polymer-based organic solar cells. *Chemical Reviews* **107**, 1324–1338 (2007).

[28] Lindsay, S. M. & Ratner, M. A. Molecular transport junctions: Clearing mists. *Adv. Mater.* **19**, 23–31 (2007).

[29] Seufert, K., Bocquet, M. . L., Auwärter, W., Weber-Bargioni, A., Reichert, J., Lorente, N. & Barth, J. V. Cis-dicarbonyl binding at cobalt and iron porphyrins with saddle-shape conformation. *Nat. Chem.* **3**, 114–119 (2011).

[30] Fabris, S. *et al.* Oxygen dissociation by concerted action of di-iron centers in metal-organic coordination networks at surfaces: Modeling non-heme iron enzymes. *Nano Letters* **11**, 5414–5420 (2011).

[31] Evans, O. R. & Lin, W. Rational design of nonlinear optical materials based on 2d coordination networks. *Chemistry of Materials* **13**, 3009–3017 (2001).

[32] Grätzel, M. Recent advances in sensitized mesoscopic solar cells. *Accounts of Chemical Research* **42**, 1788–1798 (2009).

[33] Binnig, G. & Rohrer, H. Scanning tunneling microscopy - from birth to adolescence (nobel lecture). *Angew. Chem. Int. Ed. Engl.,* **26**, 606–614 (1987).

[34] Wiesendanger, R. *Scanning Probe Microscopy and Spectroscopy: Methods and Applications.* (Cambridge University Press, 1994).

[35] Stipe, B. C., Rezaei, M. A. & Ho, W. Single-molecule vibrational spectroscopy and microscopy. *Science* **280**, 1732–1735 (1998).

[36] Ruska, E. The development of the electron microscope and of electron microscopy (nobel lecture). *Angew. Chem. Int. Ed. Engl.* **26**, 595–605 (1987).

[37] Williams, D. B. & Carter, C. B. *The Transmission Electron Microscope* (Springer-Verlag, 1996).

[38] Gross, L., Mohn, F., Moll, N., Liljeroth, P. & Meyer, G. The chemical structure of a molecule resolved by atomic force microscopy. *Science* **325**, 1110 (2009).

[39] Gross, L., Moll, N., Mohn, F., Curioni, A., Meyer, G., Hanke, F. & Persson, M. High-resolution molecular orbital imaging using a p-wave stm tip. *Phys. Rev. Lett.* **107**, 086101 (2011).

[40] Theobald, J. A., Oxtoby, N. S., Phillips, M. A., Champness, N. R. & Beton, P. H. Controlling molecular deposition and layer structure with supramolecular surface assemblies. *Nature* **424**, 1029–1031 (2003).

[41] Pawin, G., Wong, K. L., Kwon, K.-Y. & Bartels, L. A homomolecular porous network at a cu(111) surface. *Science* **313**, 961–962 (2006).

[42] Schlickum, U. *et al.* Chiral kagomé lattice from simple ditopic molecular bricks. *J. Am. Chem. Soc.* **130(35)**, 11778–82 (2008).

[43] Stepanow, S. *et al.* Steering molecular organization and host-guest interactions using two-dimensional nanoporous coordination systems. *Nat. Mater.* **3**, 229–233 (2004).

[44] Tait, S. L., Langner, A., Lin, N., Chandrasekar, R., Fuhr, O., Ruben, M. & Kern, K. Assembling isostructural metal-organic coordination architectures on cu(100), ag(100) and ag(111) substrates. *Chem. Phys. Chem.* **9**, 2495–2499 (2008).

[45] Schlickum, U. *et al.* Metal-organic honeycomb nanomeshes with tunable cavity size. *Nano Lett.* **7 (12)**, 3813–3817 (2007).

[46] Kley, C. S., Cechal, J., Kumagai, T., Schramm, F., Ruben, M., Stepanow, S. & Kern, K. Highly adaptable two-dimensional metal-organic coordination networks on metal surfaces. *J. Am. Chem. Soc.* **134**, 6072–6075 (2012).

[47] Grill, L., Dyer, M., Lafferentz, L., Persson, M., Peters, M. V. & Hecht, S. Nano-architectures by covalent assembly of molecular building blocks. *Nature Nanotechn.* **2**, 687–691 (2007).

[48] Zwaneveld, N. A. A., Pawlak, R., Abel, M., Catalin, D., Gigmes, D., Bertin, D. & Porte, L. Organized formation of 2d extended covalent organic frameworks at surfaces. *J. Am. Chem. Soc.* **130**, 6678–6679 (2008).

[49] Otero, G. *et al.* Fullerenes from aromatic precursors by surface-catalysed cyclodehydrogenation. *Nature* **454**, 865 (2008).

[50] Iski, E. V., Yitamben, E. N., Gao, L. & Guisinger, N. P. Graphene at the atomic-scale: Synthesis, characterization and modification. *Adv. Funct. Mater.* doi: 10.1002/adfm.201203421 (2013).

[51] Cai, J. *et al.* Atomically precise bottom-up fabrication of graphene nanoribbons. *Nature* **466**, 470–473 (2010).

[52] Whitesides, G. M. The 'right' size in nanobiotechnology. *Nature Biotechnology* **21**, 1161 (2003).

[53] Steitz, T. A. From the structure and function of the ribosome to new antibiotics (nobel lecture). *Angew. Chem. Int. Ed.* **49**, 4381–4398 (2010).

[54] Ramakrishnan, V. Unraveling the structure of the ribosome (nobel lecture). *Angew. Chem. Int. Ed.* **49**, 4355 – 4380 (2010).

[55] Deisenhofer, J. & Michel, H. The photosynthetic reaction centre from the purple bacterium rhodopseudomonas viridis (nobel lecture). *The EMBO Journal* **8**, 2149–2170 (1989).

[56] Drexler, K. E. *Engines of Creation, The Coming Era of Nanotechnology* (Anchor Books, New York, 1986).

[57] Duchesne, J. *The structure and properties of biomolecules and biological systems* (1964).

[58] Hansma, H., Kim, K., Laney, D., Garcia, R., Argaman, M., Allen, M. & Parsons, S. Properties of biomolecules measured from atomic force microscope images: A review. *Journal of Structural Biology* **119**, 99 – 108 (1997).

[59] Moody, M. F. *Structural Biology Using Electrons and X-rays: An Introduction for Biologists* (Academic Press, 2011).

[60] Henderson, R. The potential and limitations of neutrons, electrons and x-rays for atomic resolution microscopy of unstained biological molecules. *Q. Rev. Biophys.* **28(2)**, 171–93 (1995).

[61] Wüthrich, K. Nmr studies of structure and function of biological macromolecules (nobel lecture). *Angew. Chem. Int. Ed.* **42**, 3340–3363 (2003).

[62] Jaremko, M. *et al.* Cold denaturation of a protein dimer monitored at atomic resolution. *Nature Chemical Biology* **9**, 264–270 (2013).

[63] Bustamante, C., Vesenka, J., Tang, C. L., Rees, W., Guthold, M. & Kellers, R. Circular dna molecules imaged in air by scanning force microscopy. *Biochemistry* **31**, 22–26 (1992).

[64] Czajkowsky, D. M., Iwamoto, H. & Shao, Z. Atomic force microscopy in structural biology: from the subcellular to the submolecular. *Journal of Electron Microscopy* **49**, 395–406 (2000).

[65] Deng, Z., Thontasen, N., Malinowski, N., Rinke, G., Harnau, L., Rauschenbach, S. & Kern, K. A close look at proteins: Submolecular resolution of two- and three-dimensionally folded cytochrome c at surfaces. *Nano Lett.* **12**, 2452–2458 (2012).

[66] Wu, C. C., Sturm, J. C., Register, R. A. & Thompson, M. E. Integrated three-color organic light-emitting devices. *Appl. Phys. Lett.* **69**, 3117 (1996).

[67] Fenn, J. B., Mann, M., Meng, C. K., Wong, S. F. & Whitehouse, C. M. Electrospray ionization for mass-spectrometry of large biomolecules. *Science* **246**, 64–71 (1989).

[68] Benjamin, D. R., Robinson, C. V., Hendrick, J. P., Hartl, F. U. & Dobson, C. M. Mass spectrometry of ribosomes and ribosomal subunits. *Proc. Natl. Acad. Sci. USA* **95**, 7391–7395 (1998).

[69] Rostom, A. A. *et al.* Detection and selective dissociation of intact ribosomes in a mass spectrometer. *Proc. Natl. Acad. Sci. U.S.A.* **97**, 5185–5190 (2000).

[70] Fuerstenau, S. D., Benner, W. H., Thomas, J. J., Brugidou, C., Bothner, B. & Siuzdak, G. Mass spectrometry of an intact virus. *Angew. Chem.* **113**, 559–562 (2001).

[71] Tsekouras, A. A., Iedema, M. J. & Cowina, J. P. Soft-landed ion diffusion studies on vapor-deposited hydrocarbon films. *J. Chem. Phys.,* **111**, 2222 (1999).

[72] Kaiser, B., Bernhardt, T. M., Stegemann, B., Opitz, J. & Rademann, K. Interaction of mass selected antimony clusters with hopg. *Nuclear Instruments and Methods in Physics Research B* **157**, 155–161 (1999).

[73] Feng, B. B., Wunschel, D. S., Masselon, C. D., Pasa-Tolic, L. & Smith, R. D. Retrieval of dna using soft-landing after mass analysis by esi-fticr for enzymatic manipulation. *J. Am. Chem. Soc.* **121**, 8961–8962 (1999).

[74] Alvarez, J., Futrell, J. & Laskin, J. Soft-landing of peptides onto self-assembled monolayer surfaces. *J. Phys. Chem. A* **110**, 1678–1687 (2006).

[75] Wang, P. & Laskin, J. Helical peptide arrays on self-assembled monolayer surfaces through soft and reactive landing of mass-selected ions. *Angew. Chem., Int. Ed.* **47**, 6678–668 (2008).

[76] Johnson, G. E., Wang, C., Priest, T. & Laskin, J. Monodisperse au11 clusters prepared by soft landing of mass selected ions. *Anal. Chem.* **83**, 8069–8072 (2011).

[77] Karas, M., Bachmann, D., Bahr, U. & F., H. Matrix-assisted ultraviolet-laser desorption of nonvolatile compounds. *Int. J. Mass Spectrom. Ion Processes* **78**, 53–68 (1987).

[78] Smith, S. A., Blake, T. A., Ifa, D. R., Cooks, R. G. & Zheng, O. Y. Dual-source mass spectrometer with MALDI-LIT-ESI configuration. *Journal of Proteome Research* **6**, 837–845 (2007).

[79] Dole, M., Cox, H. L. & J., G. Electrospray mass-spectroscopy. *Advances in Chemistry Series* **125**, 73–84 (1973).

[80] Fenn, J. B., Mann, M., Meng, C. K., Wong, S. F. & Whitehouse, C. M. Electrospray ionization-principles and practice. *Mass Spectrometry Reviews* **9**, 37–70 (1990).

[81] Wilm, M. & Mann, M. Analytical properties of the nanoelectrospray ion source. *Anal. Chem.* **68**, 1–8 (1996).

[82] Kelly, R. T., Page, J. S., Luo, Q., Moore, R. J., Orton, D. J., Tang, K. & Smith, R. D. Chemically etched open tubular and monolithic emitters for nanoelectrospray ionization mass spectrometry. *Anal. Chem.* **78**, 7796–7801 (2006).

[83] de la Mora, J. F. The fluid dynamics of taylor cones. *Annu. Rev. Fluid Mech.* **39**, 217–243 (2007).

[84] Konermann, L., Ahadi, E., Rodriguez, A. D. & Vahidi, S. Unraveling the mechanism of electrospray ionization. *Anal. Chem.* **85**, 2–9 (2013).

[85] Rayleigh, L. Xx. on the equilibrium of liquid conducting masses charged with electricity. *Philosophical Magazine Series 5* **14**, 184–186 (1882).

[86] Nguyen, S. & Fenn, J. B. Gas-phase ions of solute species from charged droplets of solutions. *Proc. Natl. Acad. Sci. U.S.A.* **104**, 1111–1117 (2007).

[87] Hogan, C. J., Carroll, J. A., Rohrs, H. W., Biswas, P. & Gross, M. L. Combined charged residue-field emission model of macromolecular electrospray ionization. *Anal. Chem.* **81**, 369–377 (2009).

[88] Konermann, L., Rodriguez, A. D. & Liu, J. On the formation of highly charged gaseous ions from unfolded proteins by electrospray ionization. *Anal. Chem.* **84**, 6798–6804 (2012).

[89] Iribarne, J. V. & Thomson, B. A. On the evaporation of small ions from charged droplets. *J. Chem. Phys.* **64**, 2287 (1976).

[90] Dole, M., Mack, L. L., Hines, R. L., Mobley, R. C., Ferguson, L. D. & Alice, M. B. Molecular beams of macroions. *J. Chem. Phys.* **49**, 2240 (1968).

[91] Iavarone, A. T. & Williams, E. R. Mechanism of charging and supercharging molecules in electrospray ionization. *J. Am. Chem. Soc.* **125**, 2319 (2003).

[92] Kebarle, P. & Verkerk, U. H. Electrospray: from ions in solution to ions in the gas phase: what we know now. *Mass Spectrometry Reviews* **28**, 898–917 (2009).

[93] Ahadi, E. & Konermann, L. Modeling the behavior of coarse-grained polymer chains in charged water droplets: Implications for the mechanism of electrospray ionization. *J. Phys. Chem. B* **116**, 104 (2012).

[94] Page, J. S., Kelly, R. T., Tang, K. & Smith, R. D. Ionization and transmission efficiency in an electrospray ionization-mass spectrometry interface. *J. Am. Soc. Mass Spectrom.* **18**, 1582–1590 (2007).

[95] Page, J. S., Tang, K., Kelly, R. T. & Smith, R. D. Subambient pressure ionization with nanoelectrospray source and interface for improved sensitivity in mass spectrometry. *Anal. Chem.* **80**, 1800–1805 (2008).

[96] Kelly, R. T., Tolmachev, A. V., Page, J. S., Tang, K. & Smith, R. D. The ion funnel: Theory, implementations, and applications. *Mass Spectrometry Reviews* **29**, 294 (2010).

[97] Tang, K. *et al.* High-sensitivity ion mobility spectrometry/mass spectrometry using electrodynamic ion funnel interfaces. *Anal. Chem.* **77**, 3330–3339 (2005).

[98] Juraschek, R., Dulcks, T. & Karas, M. Nanoelectrospray - more than just a minimized-flow electrospray ionization source. *J. Am. Soc. Mass Spectrom.* **10**, 300–308 (1999).

[99] Pauly, M. *et al.* A hydrodynamically optimized nano-electrospray ionization atmospheric pressure source and interface with 100% vacuum transmission. *submitted* (2013).

[100] Gerlich, D. *Inhomogenous RF Fields: A Versatile Tool for the Study of Processes with Slow Ions* (John Wiley and Son, Inc., 1992).

[101] Shaffer, S., Tang, K., Anderson, G., Prior, D., Udseth, H. & Smith, R. A novel ion funnel for focusing ions at elevated pressure using electrospray ionization mass spectrometry. *Rapid Commun. Mass Spectrom.* **11**, 1813–1817 (1997).

[102] Cermak, I. Compact radio-frequency power supply for ion and particle guides and traps. *Rev. Sci. Instrum.* **76**, 063302 (2005).

[103] Wiley, W. C. & McLaren, I. H. Time-of-flight mass spectrometer with improved resolution. *Rev. Sci. Instr.* **26**, 1150–1157 (1955).

[104] Kahle, S. *et al.* The quantum magnetism of individual manganese-12-acetate molecular magnets anchored at surfaces. *Nano Lett.* **12**, 518–521 (2012).

[105] Cech, N. B. & Enke, C. G. Practical implications of some recent studies in electrospray ionization fundamentals. *Mass Spectrom. Rev.* **20**, 362–387 (2001).

[106] Bromann, K., Felix, C., Brune, H., Harbich, W., Monot, R., Buttet, J. & Kern, K. Controlled decadeposition of size-selected silver nanoclusters. *Science* **274**, 956–958 (1996).

[107] Cheng, H. P. & Landman, U. Controlled deposition, soft landing, and glass-formation in nanocluster-surface collisions. *Science* **260**, 1304–1307 (1993).

[108] Gebhardt, C. R., Tomsic, A., Schröder, H., Dürr, M. & Kompa, K. L. Matrix-free formation of gas-phase biomolecular ions by soft cluster-induced desorption. *Angew. Chem. Int. Ed.* **48**, 4162–4165 (2009).

[109] Alivisatos, A. Nanocrystals: building blocks for modern materials design. *Endeavour* **21**, 56 (1997).

[110] Sanchez, A., Abbet, S., Heiz, U., Schneider, W. D., Hakkinen, H., Barnett, R. N. & Landman, U. When gold is not noble: Nanoscale gold catalysts. *J. Phys. Chem. A* **103**, 9573–9578 (1999).

[111] Milani, P. & S., I. *Cluster Beam Synthesis and Nanostructured Materials* (Springer, 1999).

[112] Bromann, K., Brune, H., Felix, C., Harbich, W., Monot, R., Buttet, J. & Kern, K. Hard and soft landing of mass selected Ag clusters on Pt(111). *Surface Science* **377**, 1051–1055 (1997).

[113] Böttcher, A., Weis, P., Bihlmeier, A. & Kappes, M. M. C58 on hopg: Soft-landing adsorption and thermal desorption. *Phys. Chem. Chem. Phys.* **6**, 5213–5217 (2004).

[114] Talapin, D. V., Lee, J., Kovalenko, M. V. & Shevchenko, E. V. Prospects of colloidal nanocrystals for electronic and optoelectronic application. *Chem. Rev.* **110**, 389–458 (2010).

[115] Gamero-Castano, M. & de la Mora, J. F. Mechanisms of electrospray ionization of singly and multiply charged salt clusters. *Analytica Chimica Acta* **406**, 67–91 (2000).

[116] Lenggoro, I. W., Xia, B., Okuyama, K. & de la Mora, J. F. Sizing of colloidal nanoparticles by electrospray and differential mobility analyzer methods. *Langmuir* **18**, 4584–4591 (2002).

[117] Meng, C. & Fenn, J. B. Formation of charged clusters during electrospray ionization of organic solute species. *Organic Mass Spectrometry* **26** (1991).

[118] O'Shea, J. N., Taylor, J. B., Swarbrick, J. C., Magnano, G., Mayor, L. C. & Schulte, K. Electrospray deposition of carbon nanotubes in vacuum. *Nanotechnology* **18**, 4 (2007).

[119] Satterley, C. J. *et al.* Electrospray deposition of fullerenes in ultra-high vacuum: in-situ scanning tunneling microscopy and photoemission spectroscopy. *Nanotechnology* **18**, 455304 (2007).

[120] Kane, B. E. Levitated spinning graphene flakes in an electric quadrupole ion trap. *Phys. Rev. B* **82**, 115441 (2010).

[121] Zhang, D. X. & Cooks, R. G. Doubly charged cluster ions $[(NaCl)_m(Na)_2]^{2+}$: magic numbers, dissociation, and structure. *Intern. J. of Mass Spectrom.* **196**, 667–684 (2000).

[122] Zhou, S. L. & Hamburger, M. Formation of sodium cluster ions in electrospray mass spectrometry. *Rapid Commun. Mass Spectrom.* **10**, 797–800 (1996).

[123] Sharon, M., Ilag, L. L. & Robinson, C. V. Evidence for micellar structure in the gas phase. *J. Am. Chem. Soc.* **129**, 8740–8746 (2007).

[124] Rauschenbach, S. *et al.* Crystalline inverted membranes grown on surfaces by electrospray ion beam deposition in vacuum. *Adv. Mater.* **24**, 2761–2767 (2012).

[125] Horcas, I. WSXM: A software for scanning probe microscopy and a tool for nanotechnology. *Rev. Sci. Instr.* **78**, 013705 (2007).

[126] Williams, R. J., Phillips, J. N. & Mysels, K. J. The critical micelle concentration of sodium lauryl sulphate at 25°c. *Trans. Faraday Soc.* **51**, 728–737 (1955).

[127] Bales, B. L., Messina, L., Vidal, A., Peric, M. & Nascimento, O. R. Precision relative aggregation number determinations of SDS micelles using a spin probe. a model of micelle surface hydration. *J. Phys. Chem. B* **102**, 10347–10358 (1998).

[128] Wang, Y., Larsson, D. S. D. & van der Spoel, D. Encapsulation of myoglobin in a cetyl trimethylammonium bromide micelle in vacuo: A simulation study. *Biochemistry* **48**, 1006–1015 (2009).

[129] van der Spoel, D., Marklund, E. G., Larsson, D. S. D. & Caleman, C. Proteins, lipids, and water in the gas phase. *Macromolecular Bioscience* **11**, 50–59 (2011).

[130] Jaynes, E. T. *Probability theory* (Cambridge University Press, 2006).

[131] Martin, T. Shells of atoms. *Physics Reports* **273**, 199–241 (1996).

[132] Smith, L. A., Duncan, A., Thomson, G. B., Roberts, K. J., Machin, D. & McLeod, G. Crystallisation of sodium dodecyl sulphate from aqueous solution: phase identification, crystal morphology, surface chemistry and kinetic interface roughening. *Journal of Crystal Growth* **263**, 480 (2004).

[133] Smith, L. A., Thomson, G. B., Roberts, K. J., Machin, D. & McLeod, G. Modeling the crystal morphology of alkali-metal alkyl surfactants: Sodium and rubidium dodecyl sulfates. *Crystal Growth and Design* **5**, 2164 (2005).

[134] Bail, A. L., Duroy, H. & Fourquet, J. L. Ab-initio structure determination of lisbwo$_6$ by x-ray powder diffraction. *Mater. Res. Bull.* **23**, 447 (1988).

[135] Schudt, E. & Weitz, G. *Landolt-Börnstein - Group III Condensed Matter Numerical Data and Functional Relationships in Science and Technology*, vol. 5: Structure Data of Organic Crystals (SpringerMaterials - The Landolt-Börnstein Database).

[136] Johnson, G. E., Lysonski, M. & Laskin, J. In situ reactivity and tof-sims analysis of surfaces prepared by soft and reactive landing of mass-selected ions. *Anal. Chem.* **82**, 5718–5727 (2010).

[137] Schlemmer, S., Wellert, S., Windisch, F., Grimm, M., Barth, S. & Gerlich, D. Interactions of electrons and molecules with a single trapped nanoparticle. *Appl. Phys. A* **78**, 629–636 (2004).

[138] Grimm, M. *et al.* New setup to study trapped nano-particles using synchrotron radiation. *AIP Conf. Proc.* **705**, 1062–1065 (2004).

[139] Hanay, M. S. *et al.* Single-protein nanomechanical mass spectrometry in real time. *Nature Nanotechnology* **7**, 602–608 (2012).

[140] Jensen, K., Kim, K. & Zettl, A. An atomic-resolution nanomechanical mass sensor. *Nature Nanotechnology* **3**, 533–537 (2008).

[141] Dmitriev, A., Lin, N., Weckesser, J., Barth, J. V. & Kern, K. Supramolecular assemblies of trimesic acid on a cu(100) surface. *J. Phys. Chem. B* **106**, 6907–6912 (2002).

[142] Griessl, S., Lackinger, M., Edelwirth, M., Hietschold, M. & Heckl, W. M. Self-assembled two-dimensional molecular host-guest architectures from trimesic acid. *Single Molecules* **3**, 25–31 (2002).

[143] Messina, P., Dmitriev, A., Lin, N., Spillmann, H., Abel, M., Barth, J. V. & Kern, K. Direct observation of chiral metal-organic complexes assembled on a cu(100) surface. *J. Am. Chem. Soc.* **124**, 14000–14001 (2002).

[144] Langner, A., Tait, S. L., Lin, N., Rajadurai, C., Ruben, M. & Kern, K. Self-recognition and self-selection in multicomponent supramolecular coordination networks on surfaces. *Proc. Natl. Acad. Sci. U.S.A.* **104 (46)**, 17927 – 17930 (2007).

[145] Côté, A. P., Benin, A. I., Ockwig, N. W., O'Keeffe, M., Matzger, A. J. & Yaghi, O. M. Porous, crystalline, covalent organic frameworks. *Science* **310**, 1166 – 1170 (2005).

[146] Nitzan, A. & Ratner, M. A. Electron transport in molecular wire junctions. *Science* **300**, 1384 – 1389 (2003).

[147] Amsharov, K., Abdurakhmanova, N., Stepanow, S., Rauschenbach, S., Jansen, M. & Kern, K. Towards the isomer-specific synthesis of higher fullerenes and buckybowls by the surface-catalyzed cyclodehydrogenation of aromatic precursors. *Angew. Chem.* **122**, 9582–9586 (2010).

[148] Monnier, F. & Taillefer, M. Catalytic C-C, C-N, and C-O Ullmann-Type Coupling Reactions: Copper Makes a Difference. *Angew. Chem. Int. Ed.* **47**, 3096–3099 (2008).

[149] Reichardt. *Solvents and Solvent Effects in Organic Chemistry* (VCH: Weinheim, Germany, 1988).

[150] Reichardt, C. Solvents and solvent effects: An introduction. *Organic Process Research & Development* **11**, 105–113 (2007).

[151] Reichardt, C. Solvatochromism, thermochromism, piezochromism, halochromism, and chiro-solvatochromism of pyridinium n- phenoxide betaine dyes. *Chem. Soc. Rev.* 147 (1992).

[152] Onida, B., Fiorilli, S., Borello, L., Viscardi, G., Macquarrie, D. & Garrone, E. Mechanism of the optical response of mesoporous silica impregnated with reichardts dye to nh3 and other gases. *J. Phys. Chem. B* **108**, 16617–16620 (2004).

[153] Blum, P., Mohr, G. J., Matern, K., Reichert, J. & Spichiger-Keller, U. E. Optical alcohol sensor using lipophilic reichardt's dyes in polymer membranes. *Anal. Chim. Acta* **473**, 269–275 (2001).

[154] Dickert, F. L., Geiger, U., Lieberzeit, P. & Reutner, U. Solvatochromic betaine dyes as optochemical sensor materials: detection of polar and non-polar vapors. *Sens. Actuators* **70**, 263 (2000).

[155] Crowther, D. & Liu, X. Covalent immobilization of solvatochromic dyes. *J. Chem. Soc., Chem. Commun.* **23**, 2445 (1995).

[156] Car, R. & Parrinello, M. Unified approach for molecular dynamics and density-functional theory. *Phys. Rev. Lett.* **55**, 2471 (1985).

[157] Vladimirova, M. *et al.* Supramolecular self-assembly and selective step decoration on the au(111) surface. *Europhys. Lett.* **56**, 254–260 (2001).

[158] Perdew, J. P. & Wang, Y. Accurate and simple analytic representation of the electron-gas correlation energy. *Phys. Rev. B* **45**, 13244 – 13249 (1992).

[159] Troullier, N. & Martins, J. L. Efficient pseudopotentials for plane-wave calculations. *Phys. Rev. B* **43**, 1993–2006 (1991).

[160] Giannozzi, P. *et al.* Quantum espresso: a modular and open-source software project for quantum simulations of materials. *Journal of Physics: Condensed Matter* **21**, 395502 (19pp) (2009).

[161] Vanderbilt, D. Soft self-consistent pseudopotentials in a generalized eigenvalue formalism. *Phys. Rev. B* **41**, 7892–7895 (1990).

[162] Perdew, J. P., Burke, K. & Ernzerhof, M. Generalized gradient approximation made simple. *Phys. Rev. Lett.* **77**, 3865–3868 (1996).

[163] Dion, M., Rydberg, H., Schröder, E., Langreth, D. C. & Lundqvist, B. I. Van der waals density functional for general geometries. *Phys. Rev. Lett.* **92**, 246401 (2004).

[164] Berner, S., Brunner, M., Ramoino, L., Suzuki, H., Güntherodt, H.-J. & Jung, T. Time evolution analysis of a 2d solid-gas equilibrium: a model system for molecular adsorption and diffusion. *Chem. Phys. Lett.* **348**, 175 – 181 (2001).

[165] Lin, N., Dmitriev, A., Weckesser, J., Barth, J. V. & Kern, K. Real-time single-molecule imaging of the formation and dynamics of coordination compounds. *Angew. Chem. Int. Ed.* **41**, 4779–4783 (2002).

[166] Barth, J., Weckesser, J., Lin, N., Dmitriev, A. & Kern, K. Supramolecular architectures and nanostructures at metal surfaces. *Appl. Phys. A* **76**, 645–652 (2003).

[167] Perry, C., Haq, S., Frederick, B. & Richardson, N. Face specificity and the role of metal adatoms in molecular reorientation at surfaces. *Surface Science* **409**, 512 – 520 (1998).

[168] Private communications with the group of Prof. Frauenrath, EPFL.

[169] Hoheisel, T. N. & Frauenrath, H. A convenient negishi protocol for the synthesis of glycosylated oligo(ethynylene)s. *Org. Lett.* **10**, 4525–4528 (2008).

[170] Barone, V., Hod, O. & Scuseria, G. E. Electronic structure and stability of semiconducting graphene nanoribbons. *Nano Letters* **6**, 2748–2754 (2006).

[171] Son, Y.-W., Cohen, M. L. & Louie, S. G. Half-metallic graphene nanoribbons. *Nature* **444**, 347–349 (2006).

[172] Hoheisel, T. N., Schrettl, S., Szilluweit, R. & Frauenrath, H. Nanostructured carbonaceous materials from molecular precursors. *Angew. Chem. Int. Ed.* **49**, 6496–6515 (2010).

[173] Takami, T. *et al.* Periodic structure of a single sheet of a clothlike macromolecule (atomic cloth) studied by scanning tunneling microscopy. *Angew. Chem. Int. Ed.* **36**, 2755–2757 (1997).

[174] Miura, A. *et al.* Light- and stm-tip-induced formation of one-dimensional and two-dimensional organic nanostructures. *Langmuir* **19**, 6474–6482 (2003).

[175] Aggeli, A. *et al.* Hierarchical self-assembly of chiral rod-like molecules as a model for peptide beta-sheet tapes, ribbons, fibrils, and fibers. *Proc. Natl. Acad. Sci. U.S.A.* **98**, 11857–11862 (2001).

[176] Petsko, G. A. & Ringe, D. *Protein Structure and Function* (New Science Press Ltd, London, 2004).

[177] Yates, J. R. Mass spectrometry and the age of the proteome. *J. Mass Spectrom.* **33**, 1–19 (1998).

[178] Yates, J. R. Mass spectral analysis in proteomics. *Annu. Rev. Biophys. Biomol. Struct.* **33**, 297–316 (2004).

[179] Rout, M. P., Aitchison, J. D., Suprapto, A., Hjertaas, K., Zhao, Y. M. & Chait, B. T. The yeast nuclear pore complex: Composition, architecture, and transport mechanism. *J. Cell Biol.* **148**, 635–651 (2000).

[180] Shelimov, K. B., Clemmer, D. E., Hudgins, R. R. & Jarrold, M. F. Protein structure in vacuo: Gas-phase conformations of bpti and cytochrome c. *J. Am. Chem. Soc.* **119**, 2240–2248 (1997).

[181] Clemmer, D. E., Hudgins, R. R. & Jarrold, M. F. Naked protein conformations - cytochrome-c in the gas-phase. *J. Am. Chem. Soc.* **117**, 10141–10142 (1995).

[182] Warnke, S., von Helden, G. & Pagel, K. Protein structure in the gas phase: The influence of side-chain microsolvation. *J. Am. Chem. Soc.* **135**, 1177–1180 (2013).

[183] Hall, Z. & Robinson, C. V. Do charge state signatures guarantee protein conformations? *J. Am. Soc. Mass Spectrom.* **23**, 1161–1168 (2012).

[184] Brady, J. J., Judge, E. J. & Levis, R. J. Nonresonant femtosecond laser vaporization of aqueous protein preserves folded structure. *Proc. Natl. Acad. Sci. U.S.A.* **108**, 12217–12222 (2011).

[185] Gellman, S. H. Foldamers: A manifesto. *Acc. Chem. Res.* **31**, 173–180 (1998).

[186] Gobbo, C., Li, M., Mali, K. S., van Esch, J. H. & Feyter, S. D. Preprogrammed 2d folding of conformationally flexible oligoamides: Foldamers with multiple turn elements. *ACS Nano* **6**, 10684–10698 (2012).

[187] Jain, R. K. & Hamilton, A. D. Protein surface recognition by synthetic receptors based on a tetraphenylporphyrin scaffold. *Org. Lett.* **2**, 1721–1723 (2000).

[188] Wolynes, P. G. Biomolecular folding in vacuo!!!(?). *Proc. Natl. Acad. Sci. USA* **92**, 2426–2427 (1995).

[189] Tkatchenko, A., Rossi, M., Blum, V., Ireta, J. & Scheffler, M. Unraveling the stability of polypeptide helices: Critical role of van der waals interactions. *Phys. Rev. Lett.* **106**, 118102 (2011).

[190] Harnau, L., Winkler, R. G. & Reineker, P. Dynamic structure factor of semiflexible macromolecules in dilute solution. *J. Chem. Phys.* **104**, 6355 (1996).

[191] Toan, N. M., Ha, B.-Y. & Thirumalai, D. *Polyelectrolyte and Polyampholyte Effects in Synthetic and Biological Macromolecules, in Ionic Interactions in Natural and Synthetic Macromolecules, eds A. Ciferri and A. Perico* (John Wiley and Sons, Hoboken, 2012).

[192] Huheey, J. A., Keiter, E. A. & Keiter, R. L. *Inorganic Chemistry - Principles of Structure and Reactivity* (HarperCollins College, 1993).

[193] Kaatze, U. Complex permittivity of water as a function of frequency and temperature. *J. Chem. Eng. Data* **34**, 371–374 (1989).

[194] Rockwood, A. L., Busman, M. & Smith, R. D. Coulombic effects in the dissociation of large highly charged ions. *Intern. J. of Mass Spectrom. Ion Proc.* **111**, 103–129 (1991).

[195] Schnier, P. D., Gross, D. S. & Williams, E. R. Electrostatic forces and dielectric polarizability of multiply protonated gas-phase cytochrome c ions probed by ion/molecule chemistry. *J. Am. Chem. Soc.* **110**, 6747–6757 (1995).

[196] Lazaridis, T., Archontis, G. & Karplus, M. Enthalpic contribution to protein stability: Insights from atom-based calculations and statistical mechanics. *Adv. Protein Chem.* **47**, 231–306 (1995).

[197] Koppenol, W. H., Rush, J. D., Mills, J. D. & Margolias, E. The dipole moment of cytochrome c. *Mol. Biol. Evol.* **8**, 545–558 (1991).

[198] Mao, Y., Woenckhaus, J., Kolafa, J., Ratner, M. A. & Jarrold, M. F. Thermal unfolding of unsolvated cytochrome c:? experiment and molecular dynamics simulations. *J. Am. Chem. Soc.* **121**, 2712–2721 (1999).

[199] Mao, X., Wang, Y., Liu, L., Niu, L., Yang, Y. & Wang, C. Molecular-level evidence of the surface-induced transformation of peptide structures revealed by scanning tunneling microscopy. *Langmuir* **25**, 8849–8853 (2009).

[200] Breuker, K. Segmental charge distributions of cytochrome c on transfer into the gas phase. *Int. J. Mass Spectrom.* **253**, 249 (2006).

[201] Steinberg, M. Z., Elber, R., McLafferty, F. W., Gerber, R. B. & Breuker, K. Early structural evolution of native cytochrome c after solvent removal. *Chem. Bio. Chem.* **13**, 2417 (2008).

[202] Dill, K. A. & MacCallum, J. L. The protein-folding problem, 50 years on. *Science* **338**, 1042–1046 (2012).

[203] Elrod-Erickson, M., Benson, T. E. & Pabo, C. O. High-resolution structures of variant zif268-dna complexes: implications for understanding zinc finger-dna recognition. *Structure* **6**, 451–464 (1998).

[204] Krishna, S. S., Majumdar, I. & Grishin, N. V. Structural classification of zinc fingers. *Nucleic Acids Research* **31**, 532–550 (2003).

[205] Bessette, P. H., Aslund, F., Beckwith, J. & Georgiou, G. Efficient folding of proteins with multiple disulfide bonds in the escherichia coli cytoplasm. *Proc. Natl. Acad. Sci. U.S.A.* **96**, 13703–13708 (1999).

[206] Kadokura, H. & Beckwith, J. The expanding world of oxidative protein folding. *Nature Cell Biology* **3**, E247 – E249 (2001).

[207] Selkoe, D. J. Folding proteins in fatal ways. *Nature* **426**, 900–904 (2003).

[208] Stefani, M. Protein folding and misfolding on surfaces. *Int. J. Mol. Sci.* **9**, 2515–2542 (2008).

[209] Sarikaya, M., Tamerler, C., Jen, A. K. Y., Schulten, K. & Baneyx, F. Molecular biomimetics: Nanotechnology through biology. *Nature Materials* **2**, 577–585 (2003).

[210] Carbone, C. *et al.* Self-assembled nanometer-scale magnetic networks on surfaces: Fundamental interactions and functional properties. *Adv. Funct. Mater.* **21**, 1212–1228 (2011).

[211] Lingenfelder, M., Tomba, G., Costantini, G., Colombi Ciacchi, L., De Vita, A. & Kern, K. Tracking the chiral recognition of adsorbed dipeptides at the single-molecule level. *Angew. Chem. Int. Ed.* **119**, 4576–4579 (2007).

[212] Barlow, S. & Raval, R. Complex organic molecules at metal surfaces: bonding, organisation and chirality. *Surface Science Reports* **50**, 201 – 341 (2003).

[213] Whitehouse, C. *et al.* Adsorption and self-assembly of peptides on mica substrates. *Angew. Chem. Int. Ed.* **44**, 1965–1968 (2005).

[214] Bas, M., Adams, V., Suvorava, T., Niehues, T., Hoffmann, T. K. & Kojd, G. Nonallergic angioedema: Role of bradykinin. *Allergy* **62**, 842–856 (2007).

[215] Classen, T. *et al.* Templated growth of metal-organic coordination chains at surfaces. *Angew. Chem. Int. Ed.* **44**, 6142–6145 (2005).

[216] Zhong, D., Blömker, T., Wedeking, K., Chi, L., Erker, G. & Fuchs, H. Surface-mounted molecular rotors with variable functional groups and rotation radii. *Nano Lett.,* **9**, 4387–4391 (2009).

[217] Saywell, A. *et al.* Conformation and packing of porphyrin polymer chains deposited using electrospray on a gold surface. *Angew. Chem. Int. Ed.* **49**, 9136–9139 (2010).

[218] Lafferentz, L., Ample, F., Yu, H., Hecht, S., Joachim, C. & Grill, L. Conductance of a single conjugated polymer as a continuous function of its length. *Science* **323**, 1193–1197 (2009).

[219] Kohn, W., Becke, A. D. & Parr, R. G. Density functional theory of electronic structure. *J. Phys. Chem.* **100**, 12974–12980 (1996).

[220] Bocquet, M.-L. & Wang, B. Metal-organic interaction probed by first principles stm simulations. *Progress in Surface Science* **85**, 435–459 (2010).

[221] Fan, H. & Mark, A. E. Refinement of homology-based protein structures by molecular dynamics simulation techniques. *Protein Sci.* **13(1)**, 211–220 (2004).

[222] Chen, J. & Brooks, C. L. Can molecular dynamics simulations provide high-resolution refinement of protein structure? *Proteins: Structure, Function, and Bioinformatics* **67**, 922–930 (2007).

[223] Neese, F. The orca program system. *WIREs Comput. Mol. Sci.* **2**, 73–78 (2012).

[224] Moritz, W., Zuschke, R., Pflanz, S., Wever, J. & Wolf, D. Adsorption induced reconstruction of the cu(110) surface. *Surface Science* **272**, 94–101 (1992).

[225] Uehara, Y., Matsumoto, T. & Ushioda, S. Identification of o atoms on a cu110 surface by scanning tunneling microscope light emission spectra. *Phys. Rev. B* **66**, 075413 (2002).

[226] Anderson, N. L. & Anderson, N. G. Proteome and proteomics: New technologies, new concepts, and new words. *Electrophoresis* **19**, 1853–1861 (1998).

[227] Chetwani, N., Cassou, C. A., Go, D. B. & Changa, H.-C. High-frequency ac electrospray ionization source for mass spectrometry of biomolecules. *J. Am. Soc. Mass Spectrom.* **21**, 1852–1856 (2010).

[228] Takáts, Z., Wiseman, J. M., Gologan, B. & Cooks, R. G. Electrosonic spray ionization. a gentle technique for generating folded proteins and protein complexes in the gas phase and for studying ion-molecule reactions at atmospheric pressure. *Anal. Chem.* **76**, 4050–4058 (2004).

[229] Cheary, R. W., Coelho, A. A. & Cline, J. P. Fundamental parameters line profile fitting in laboratory diffractometers. *J. Res. Natl. Inst. Stand. Technol.* **109**, 1–25 (2004).

[230] Usui, H. Electrochemical self-assembly synthesis of zinc oxide nanoparticles and lamellar-structured organic/inorganic hybrids by electrodeposition in surfactant solution. *Electrochim. Acta* **56**, 3934–3940 (2011).

Acknowledgment

Without the contribution of many people, this thesis could have been not written in the way it is. Be it in the interpretation of the results, the support in the lab, the nice atmosphere in the institute or the spontaneous get-together's after work.

First of all, I would like to express my gratitude to my thesis director Prof. Dr. Klaus Kern for giving me the opportunity to work in his lab on such an interesting field in nanoscience as well as for making it possible to continue for one further year.

I would like to thank the PhD committee. In particular, the referees Dr. Leonard Grill, Prof. Francesco Stellacci, and Prof. Ernst Meyer who agreed to evaluate the thesis. Furthermore I like to thank Prof. Andreas Mortensen, the jury president, who took the job over and managed the room change in the last moment.

At this moment of accomplishment, I am deeply indebted and grateful to my supervisor Dr. Stephan Rauschenbach for his support, enthusiasm, patience, expertise, inspiration, and his great efforts to explain things clearly and simply. He always had an open door and I could always address him with my requests. So it happened that I had breakfast, lunch, or dinner together with his family Sabine, Emil and Elsa who never seem to be bothered about that. Well, the price was that I had to read stories for Emil and Elsa...

A big portion of the presented results evolved from the collaboration with Priv.-Doz. Dr. Ludger Hanau who performed all the MD simulations of the protein as well as of the peptide. I thank him for his effort and the fruitful discussions and meetings we had which were from time to time quite spontaneously. Due to this collaboration we understood a way more.

The same holds for my office mate Dr. Rico Gutzler who contributed the Bradykinin DFT results and was always available to discuss these and also other things in the office or during a coffee break.

Special thanks goes also to the great ES-IBD team which changed over the last years. I started with Dr. Zhitao Deng and Dr. Nicha Thontasen who introduced me to the lab in the beginning and showed me their tricks. I also want to thank the internship students Lucy Hilsenbek, Jonathan Blohm, and Hannah Ochner who supported me in the lab during their time here. In particular, I want to thank Hannah Ochner who not just worked with me in the lab but also proofread some

chapters and can bake delicious muffins. I also like to express my gratitude to Dr. Matthias Pauly with whom we have improved the source which enabled us to obtain the majority of the presented results. Some results were also obtained together with Alyasan Albarghash during his master project and who brought the Arab Spring into the lab. Recently Dr. Girjesh Dubey and Sabine Abb joined the lab. Their support and encouragement helped me a lot during my time of writing the thesis and preparing the exam.

I gratefully acknowledge our collaborators Dr. Giula Tomba and Dr. Andrea Floris for the theoretical support and the fruitful discussions without ever meeting each other. For providing us the exciting hexaine molecules and a great deal of discussion I like to thank Stephen Schrettl, Dr. Tobias Hoheisel, and Prof. Holger Frauenrath.

I thank all the members of the institute for the nice atmosphere. In particular, I want to mention our lunch group who everyday wanted to be rounded up by a phone call at 12:07 initiated by our office. During the years a lot of people have left and joined the group, especially I want to acknowledge: Dr. Theresa Lutz, Dr. Nasiba White, Dr. Sebastian Stepanov, Christoph Große, Carola Straßer, Dr. Doris Grumelli, and Benjamin Wurster.

Furthermore I want to thank the "Männerabend" team Eike Schäfer-Nolte, Tobias Herden, Christian Dette and Christopher Kley for the more or less spontaneous evenings. Particularly, I am deeply grateful to Christopher with whom I started to work in the institute and who gave me shelter in his apartment for the first two weeks in Stuttgart. Since then a deep friendship developed leading to the nice "Männerabend" events, shared research project and culminating in being witness to my marriage.

This leads me directly to the next person I am deeply indebted to, my fidanzata Roberta Caterino. She supported and encourage me every time I needed it, especially in the last weeks during the writing process. In these days she always took the long way from Munich to Stuttgart and also managed it to serve freshly made pasta in the institute late in the evening. *Ascoltami, volevo solo dirti che tu sei il massimo per me... una vacanza che non se ne va, un frigo pieno di gelati alla spiaggia, la soluzione se qualcosa va storto, e così bella che non vorrei mai farne a meno...*

Finally, I thank my family for supporting me throughout all my studies at the university. Besonderen Dank möchte ich, neben meinen Eltern Dr. Klaus und Brigitte Rinke, meiner Tante Christina Jahn widmen.

Curriculum Vitae

Name	Gordon Rinke
Address	Senefelderstr. 71a 70176 Stuttgart Germany
Birth	09 December 1982 in Schwerin, Germany
eMail	g.rinke@fkf.mpg.de
Telephone	+49-711-689-1730

EDUCATION

May 09 – July 13	**Doctoral Studies (PhD)** Ecole Polytechnique Federale de Lausanne, Switzerland *Doctoral School: Materials Science and Engineering* Max-Planck Institute for Solid State Research Stuttgart, Nanoscale Science Department, Prof. Dr. K. Kern
Apr 07 – Apr 09	**Master of Science (M.Sc.)** RWTH Aachen University, Germany *Program in Materials Science* Research Center Jülich, Institute of Bio- and Nanosystems 1, Prof. Dr. D. Grützmacher
Sep 03 – Mar 07	**Bachelor of Science (B.Sc.)** RWTH Aachen University, Germany *Program in Materials Science* Institut für Werkstoffe der Elektrotechnik 2, Prof. Dr. R. Waser
June 2002	**University-entrance diploma**
1993 – 2002	Grammar School Bergstadt Gymnasium Lüdenscheid

WORK EXPERIENCE

Nov 12 – Feb 12	**Tutorial** "Experimentelle Physik für Naturwissenschaftler", University of Stuttgart
Apr 08 – Apr 09	**Student research assistant** IBN-1, Research Center Jülich (MBE, AFM, SEM)
Mar 07 – Mar 08	**Student research assistant** IWE II, RWTH Aachen University (CSD, CMP, XRD, SEM, PFM, Tutorial)
2002 – 2003	**Civil Service** Patient Transport Ambulance, Deutsches Rotes Kreuz Lüdenscheid

CONFERENCES & SEMINARS

March 2013	DPG Conference Regensburg *"The molecular structure of a nine amino acid peptide at metal surfaces in vacuum"*, (Talk)
April, 17th 2012	Invited Talk, Pacific Northwest National Laboratory (PNNL) Richland, WA *"The structure of complex molecules at surfaces deposited from electrospray ion beams"*,
April, 2012	MRS Spring Meeting San Francisco *"Crystalline Organic Films by High Flux Electrospray Ion Beam Deposition of Nonvolatile Molecular Clusters"*, (Talk)
March 2011	DPG Conference Dresden *"Scanning Tunneling Microscopy of Proteins in Ultrahigh Vacuum"*, (Talk), *"Electrospray Ion Beam Deposition for Scanning Tunneling Microscopy Studies in Ultra-high Vacuum"*, (Poster)
March 2010	DPG Conference Regensburg *"In-situ Ion Beam Deposition of Molecules and Nanoparticles"*, (Poster)

PUBLICATIONS

- Rinke, G.; Albarghash, A.; Hanau, L.; Gutzler, R.; Rauschenbach, S. & Kern, K; "Conformation control by charge state dependent deposition of unfolded proteins", *in preparation*

- Rinke, G.; Rauschenbach, S.; Harnau, L. & Kern, K.; "Clusters and Nanoparticles in Electrospray Ion Beams", *in preparation*

- Pauly, M.; Sroka, M.; Reiss, J.; Rinke, G.; Albarghash, A.; Vogelgesang, R.; Hahne, H.; Kuster, B.; Sesterhenn, J.; Kern, K. & Rauschenbach, S.; "A Hydrodynamically Optimized Nano-Electrospray Ionization Atmospheric Pressure Source and Interface with 100% Vacuum Transmission", *submitted* (2013)

- Rauschenbach, S.; Reiss, J.; Pauly, M.; Sroka, M.; Rinke, G.; Vogelgesang, R.; Kuester, A.; Sesterhenn, J. & Kern, K.; Max- Planck-Gesellschaft zur Foerderung der Wissenschaften e.V., "*Device For Transferring Ions From High To Low Pressure Atmosphere, System And Use*", European Patent EP12156326.6, (Feb. 2012)

- Deng, Z.; Thontasen, N.; Malinowski, N.; Rinke, G.; Harnau, L.; Rauschenbach, S. & Kern, K.; "A Close Look at Proteins: Submolecular Resolution of Two- and Three-Dimensionally Folded Cytochrome-C at Surfaces", *Nano Letters*, **12** (5), 2452-2458 (2012)

- Rauschenbach, S.; Rinke, G.; Malinowski, N.;Weitz, R. T.; Thontasen, N.; Deng, Z.; Lutz, T.; de Almeida Rollo, P. M.; Costantini, G.; Harnau, L. & Kern, K.; "Crystalline Inverted Membranes Grown on Surfaces by Electrospray Ion Beam Deposition in Vacuum", *Advanced Materials*, **24**, 2761-2767 (2012)

- Kahle, S.; Deng, Z.; Malinowski, N.; Tonnoir, C.; Forment-Aliaga, A.; Thontasen, N.; Rinke, G.; Le, D.; Turkowski, V.; Rahman, T. S.; Rauschenbach, S.; Ternes, M. & Kern, K.; "The Quantum Magnetism of Individual Manganese-12-Acetate Molecular Magnets Anchored at Surfaces" *Nano Letters*, **12**, 518-521 (2012)

- Rinke, G.; Mussler,G.; Gerharz, J.; Moers, J. & Grützmacher, D.; "Growth of germanium dots on template silicon substrates with diffusion-altered holes" *Europhysics Letters*, **85**, 58002 (2009)